Politecnico di Torino

ScuDo
Scuola di Dottorato ~ Doctoral School
WHAT YOU ARE, TAKES YOU FAR

Doctoral Dissertation
Doctoral Program in Mechanical Engineering (36^{th}cycle)

Multiscale finite element models for the analysis, design and optimisation of variable stiffness composites

By

Alberto Racionero Sánchez-Majano

******

Supervisor(s):
Prof. Alfonso Pagani
Prof. Marco Petrolo

Doctoral Examination Committee:
Prof. Maria Cinefra, Referee, Politecnico di Bari
Prof. Riccardo Vescovini, Referee, Politecnico di Milano

Politecnico di Torino
2024

Declaration

I hereby declare that, the contents and organization of this dissertation constitute my own original work and does not compromise in any way the rights of third parties, including those relating to the security of personal data.

Alberto Racionero Sánchez-Majano
2024

* This dissertation is presented in partial fulfillment of the requirements for **Ph.D. degree** in the Graduate School of Politecnico di Torino (ScuDo).

A todas las personas que me han acompañado hasta aquí.

Acknowledgements

First, I sincerely thank Professor Alfonso Pagani for trusting me and giving me the opportunity to develop this thesis and for the time dedicated to me over these years. His knowledge and guidance have been fundamental to my professional and personal growth. I also want to show my gratitude to Professor Marco Petrolo for his insights and suggestions, which helped me grow as a researcher. The precision and professionalism with which he faces each task are inspirational. I want to take this opportunity to thank Professor Erasmo Carrera. It was always a pleasure listening to him when I had the chance to come into his office. His insight, knowledge of mechanics, and passion for research have always been captivating. I also thank Professor Enrico Zappino and Professor Matteo Filippi for their continuous and invaluable help whenever I came to their office looking for programming advice.

I also owe my gratitude to Prof. Maryam Shakiba for hosting me at Virginia Polytechnic Institute and State University. The three months I spent in Blacksburg allowed me to learn about new research topics and get to know new friends and colleagues at Patton Hall.

I would like to thank the people at MUL2, both current and former, for helping create an enjoyable and productive workplace environment. A special mention has to be given to Dr. Alberto García de Miguel, Dr. Ibrahim Kaleel, Dr. Manish Nagaraj, and Dr. Riccardo Augello for their help during my first steps in the group. I have been extremely fortunate to become friends with Marco, Rodolfo, Mattia, and Rebecca. Thank you for making each day spent at the office worth it.

I also thank my friends from Alcázar for supporting me during these years. It was great coming back home and finding that nothing changed between us despite the distance. In addition, I want to show my gratitude to the Spanish friends I have made over the last three years. Thank you for all the memories in Turin.

This research was carried out within the project PRE-ECO: A new paradigm to re-engineering printed composites, funded by the European Research Council under the European Union's Horizon 2020 research and innovation programme (Grant Agreement No. 850437).

Last, this thesis would not have been possible without the tremendous support of my parents. I would like to thank them for their continued encouragement and for cherishing every small milestone along the way.

Abstract

The irruption of Automated Fibre Placement (AFP) has permitted the conceiving of new composite materials in which the fibres are no longer straight but can follow curvilinear paths. These are known as variable angle tow (VAT) or tow-steered composites. Although beneficial, this new class of composites leads to new modelling challenges. In this context, and due to these materials' hierarchical and multiscale behaviour, advanced numerical methods need to be conceived to analyse, design and optimise them thoroughly.

Different modelling techniques are utilised accordingly because of the interaction between the scales in composites. For instance, at the component level, it is common to use classical lamination theories that predict the structure's global performance well. However, as soon as the engineer needs to investigate what is happening at the innermost scales, the fidelity of the analysis tools must be increased. At this stage, more computationally demanding models are required.

Due to the changes in the modelling strategies, new governing equations need to be generated for each scale. To avoid generating ad hoc equations for all the composite scales, one can employ the Carrera Unified Formulation (CUF). CUF permits deriving the governing equations for an arbitrary structural theory without making any *a priori* assumption. Based on CUF, this thesis derived numerical solutions based on the Finite Element Method (FEM) to investigate the component, layer and fibre scale of VAT composites. In detail, the component and fibre scales were modelled by coupling CUF with classic FEM. In contrast, novel embedded CUF-FEM models have been developed to study the layer scale. This new approach permits the analysis of complex configurations with no mesh and geometry limitations.

Apart from generating numerical models, the fabrication process of tow-steered structures was of interest. In particular, the defects arising during the fabrication and their ultimate influence on the mechanical behaviour of the structure were investigated. Since these components are manufactured with hierarchical materials such as fibre-reinforced composites, defects can occur at different scales, i.e., fibre-matrix and layer levels. Furthermore, defects can be subdivided into uncertainty and deterministic flaws. Examples of the latter are the fibre volume fraction variability and misalignments. In

contrast, gaps and overlaps are deterministic defects, as we can predict their position by simulating the AFP manufacturing process.

Last, the optimisation of the mechanical performance of VAT components was addressed. In detail, the fundamental frequency, buckling load, vertical deflection, strain concentration factor, and strength were optimised. These characteristics were tailored considering a defect-free laminate. Additionally, the effect of the manufacturing condition, i.e. defect-free or in the presence of gaps and overlaps, on the fundamental frequency optimisation was tackled.

Contents

List of Figures

List of Tables

Chapter 1

Introduction

1.1 Motivation

During the past decades, composite materials have increased their popularity in engineering applications thanks to their higher stiffness and strength as well as their lighter weight compared with metallic alloys. Although the aerospace industry represents the main end user, composites are nowadays extensively employed in the automotive, civil, biomedical and energy engineering fields. Concerning the aerospace sector, the two biggest companies, Airbus and Boeing, have increased the presence of composites in their commercial aircraft since the 1970s decade. Indeed, in their latest releases, the A350 and B787 respectively, composites represent more than 50% of the aircraft weight.

Composite are materials that comprise two or more constituents that have different mechanical and chemical properties, which combined exhibit properties that differ from those of the individual components. A classic example are the fibre-reinforced polymers, which combine the high stiffness of fibres and the ductile properties of the polymer matrix. Some of the most spread fibres are carbon, glass and aramid. In engineering applications, composites are used to conceive layups or textiles [1]. These can be manufactured for a broad variety of shapes in a more automated process. From the designer standpoint, composite materials offer a larger number of design parameters, or design variables, compared to traditional metallic alloys. Some of them can be the material selection, the volume ratio between fibre and matrix, the total number of plies and their orientations. As a consequence, a composite structure is more versatile and can be better optimised for different load cases, leading to lighter and more cost-efficient designs.

As mentioned before, the orientation of the composite ply is a common design variable in the optimisation process of a composite structure. Since the introduction of

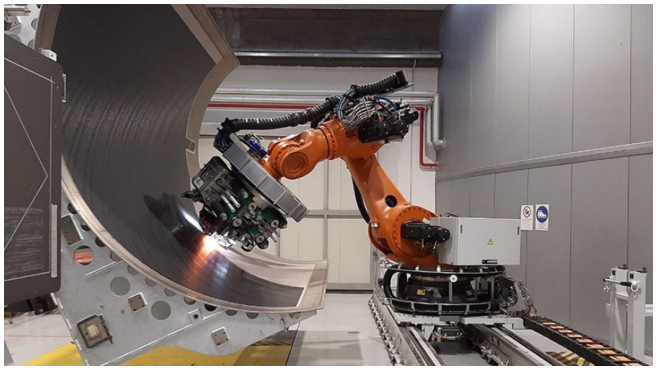

(a)

(b)

Figure 1.1 Examples of (a) AFP and (b) ATL machines by MTorres©.

composites in the industry, the fibre orientation has been supposed to remain constant within the layer. By simply modifying the stacking sequence of a component, the structural weight could be reduced and the mechanical performance be enhanced compared to a metallic part. However, the designer would not be exploiting all the potential of composites.

Thanks to the irruption of new manufacturing technologies such as Automated Fibre Placement (AFP), or Automated Tape Laying (ATL), new families of composites can be conceived. Examples of AFP and ATL machines, from MTorres©, are illustrated in Fig. 1.1. Specifically, with these new fabrication processes, engineers can conceive composite structures in which the fibre orientation can vary within the layer [2]. In this manner, the in-plane stiffness of the individual layer is no longer constant across the ply. This is the principal moto of tow-steered composites.

Variable stiffness composites (VSC) permit to redistribute the load carrying capacity within the layer. This is possible thanks to the consideration of multiple design variables used to generate a curvilinear fibre path, as in Fig. 1.2, instead of just one, as occurred in straight-fibre composites. In this regard, the elastic properties vary point-wise within the ply of the VSC. By considering additional design variables,

Figure 1.2 Variable stiffness lower wing skin piece manufactured by iCOMAT©.

variable angle tow (VAT) have the potential to further improve the performance of composite structures compared to their straight-fibre counterparts.

The possibility to design low-weight and high-performance structures comes with the price of uncertainty and modelling assumptions. A multiscale approach must be adopted to comprehend the mechanical response of composite structures under different working and environmental conditions. Therefore, the structural analysis is usually decoupled into a series of models that address the physics of the involved scale [3]. For instance, the arrangement of the constituents at the microscale, also referred to as fibre-matrix scale in this thesis, affect the effective properties of the homogenised material. Then, the layups and textiles that conform the test coupons are included in structural models at the mesoscale, which is known as layer scale in this document too. Last, the dynamic response, buckling performance, stiffness and strength of the structural components is studied at the macroscale with simulation tools such as the Finite Element Method (FEM). In this numerical framework, the constitutive information gathered at each scale is commonly propagated following a bottom-up approach, that is, from the fibre-matrix scale up to the final structure [4]. Nonetheless, many of the models involved in this process were initially derived for the analysis of metallic structures, especially at the larger scales. As a consequence, engineers tend to be suspicious of the simulations and huge amount of resources is devoted to experimental campaigns throughout the design process. The pyramidal diagram of the virtual testing of composites is illustrated in Fig. 1.3, from [5]. In this framework, the ideal scenario is to boost the development of reliable and efficient models for composites which will increase the confidence in the simulation.

The main limitation of the metal-oriented simulation tools is the inability to predict accurately the stress state of the structure. Conversely to components made of out isotropic materials, in composite structures, transverse and shear deformations play

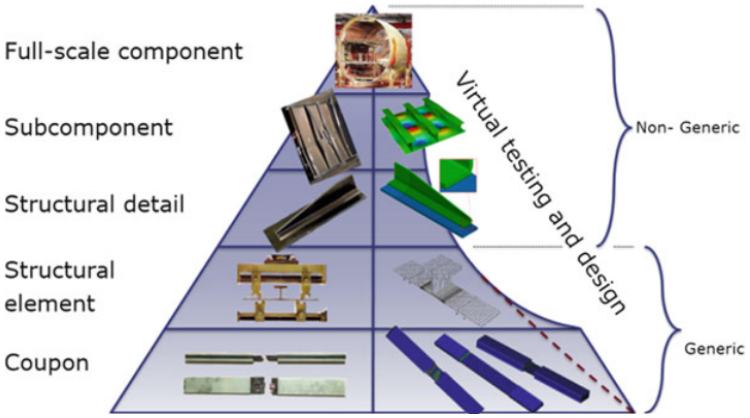

Figure 1.3 Pyramidal diagram of multiscale testing of composite materials. Adapted with permission from Falzon and Tan [5].

a major role in the mechanical performance, especially in the failure mechanisms. Being able to capture precisely the failure onset and the subsequent propagation needs an analysis tool capable of giving an accurate approximation of the strain and stress fields at the different scales involved. Therefore, it becomes mandatory to establish a numerical framework capable of providing high accuracy with a cost-effective computational cost.

1.2 State of the art

1.2.1 Variable stiffness pioneers and theories for laminated structures

The new fabrication processes brought the emergence of novel families of composites, namely VAT, in which fibres are steered following curvilinear paths, thus enabling additional design possibilities. However, the concept of VSC is not new. Indeed, in the early 1990s, Leissa and Martin [6] investigated how nonuniformly spaced fibres affect the free vibration and buckling characteristics of straight-fibre composites. They found that these two aspects could be improved by as much as 21 and 38%, respectively. Kuo et al. [7] succeeded in the experimental and numerical testing of flexible composites presenting continuous fibre with sinusoidal patterns. The experimental results showed good agreement with the theoretical predictions for the constitutive relations for the longitudinal and transverse tensile behaviour. The strength and buckling performance of perforated plates was addressed by Hyer and Lee [8]. They found improvements in the failure loads over classical composites. Then, Gürdal and Olmedo [9–11] proposed a linearly varying fibre path depending on the in-plane coordinates. A parametric

analysis of the in-plane stiffness and buckling was carried out by modifying the parameters that define the fibre path. They demonstrated that increases in the critical load up to 80% were possible with the variable stiffness concept.

The previous works employed the Classical Laminated Plate Theory (CLPT) [12], which is a generalisation of the Kirchhoff-Love plate theory [13] for multi-layered structures. Some of them [7, 9, 10] used closed-form solutions, while others [11] solved numerically the set of partial differential equations. In addition, the work by Hyer and Lee [8] utilised the FEM to solve the numerical problem and CLPT as the structural theory. Other structural theories have been developed to account for the shear stress components. This is the case of the First Shear Order Deformation Theory (FSDT) that extends the Reissner [14] and Mindlin [15] formulations. Typically, commercial codes employ these formulations. However, their applicability is limited to a narrow range of applications, e.g., when dealing with thin-walled structures and without local effects. Contrariwise, more accurate shell formulations are required when a prediction of the transverse stresses are needed. For doing so, several high-order two-dimensional (2D) formulations were derived. As an example, Reddy [16] conceived a simple high-order theory for laminated composite structures. Besides, Reddy and Liu [17] proposed a shear model that considered a parabolic distribution of transverse shear deformation in the thickness direction. Carrera [18, 19] established the unified formulation (CUF) to generate various refined shell theories. Cinefra and Carrera [20] performed linear analyses of cylindrical composite structures using shell finite elements and different through-the-thickness kinematics.

1.2.2 Multiscale models for composites

Composites are hierarchic materials. This means that the overall behaviour of a structure depends on what is happening at the innermost scales and how it propagates to upper levels. Capturing all the details at the finer scales in the numerical simulation of a large structure is not feasible because of the enormous computational cost it would require. Doing that would be similar to performing Direct Numerical Simulations (DNS) in Computational Fluid Dynamics. Therefore, another strategy needs to be chosen. In this regard, multiscale modelling facilitates the treatment of this numerical problem. Typically, a multi-step approach is followed to solve the problem, considering the different length scales. Through this method, all the analyses are linked from the constituent level to the whole operating structure, thus creating a bottom-up flow of information, as depicted by Llorca *et al.* [4]. In this manner, the microstructural level is solved by computational micromechanics to retrieve accurate constitutive models useful for the structural study at the mesoscale level, as presented in [21, 22].

Focusing on the innermost scales, micromechanical models constitute helpful tools to predict how the presence of voids, the fibre arrangement, fibre volume fraction, or the constituents' geometry affect the overall response of the homogenised equivalent material. In recent decades, a plethora of analytical, semi-analytical and numerical methods have been developed, demonstrating the continuous evolution of this research field. Many of these methods assume that the fibre arrangement follows a periodic pattern, recalling the Repeating Unit Cell (RUC) concept. Some examples of analytical formulae are the rule of mixtures [23], Rosen and Hashin upper and lower bounds [24], Hashin and Shtrikman [25], the elasticity-based cell method [26], or the Mori-Tanaka method [27]. More advanced solutions have been proposed by other authors based on semi-analytical methods. The Method of Cells (MOC) [28], the Generalised Method of Cells (GMC) [29] and the High-Fidelity Method of Cells (HFGMC) [30] are some examples, and they are suitable for more general cases. Last, another widely spread approach consists in applying adequate boundary tractions or displacements to a Representative Volume Element (RVE) and subsequently performing conventional analyses to calculate the elastic properties, as proposed in [31]. Additionally, recent works use experiments and commercial software to retrieve the homogenised features of RVE models, as in [32].

From the mesoscale standpoint, research efforts have been made towards the simulation of textile composites rather than variable stiffness. For instance, some studies performed a two-step homogenisation based on GMC to calculate the homogenised elastic properties of woven composites [33]. Other popular methods are the voxel-based FEM, which drastically alleviates the pre-processing time for unit cell generation. As a counterpart, voxel-based methods usually provide inaccurate stress fields, especially along the interfaces [34]. In the case of VSC, the mesoscale analysis have been devoted to the characterisation and modelling of defects.

1.2.3 Manufacturing of variable stiffness composites and defect modelling

As commented before, VAT structures are generally manufactured by AFP machines because of their high deposition rate. In this process, bands of fibres, referred to as tows, are placed on a mould. Usually, several tows are laid down altogether in a single pass of the AFP machine head. This band of tows is called a course. The centreline of the course is placed along the designed curvilinear path. Nonetheless, to avoid the presence of defects, there exists a limitation on the minimum turning radius of the AFP machine head. Heinecke and Willberg [35] gathered in their review the whole spectrum of manufacturing defects induced by the AFP process, some of which

are available in Chapter 4. Considering the defects within the numerical model is paramount to better understand the mechanical behaviour of a composite structure. Depending on how defects are taken into account, their modelling strategies can be divided into intrusive and non-intrusive techniques. The work by Blom *et al.* [36] pioneered the gap modelling. They proposed a mesh refinement to thoroughly capture the fibre-free regions and assign them the elastic properties of the resin. Similarly, Falcó *et al.* [37, 38] developed a procedure capable of generating structured meshes. In this manner, a better geometric description of the tow-drop areas was achieved.

The Continuous Tow Shearing (CTS) [39] manufacturing technique, developed during the last decade, theoretically avoids the presence of gaps and overlaps. CTS steers the tows by shearing instead of bending, as AFP does. This results in thickness variations, which can be modelled following the strategies proposed by Kim *et al.* [40]. The first strategy keeps the thickness constant, which can be used to verify closed-form solutions. The second is employed when different fibre paths are identical and shifted along a shifting direction. The third option considers the presence of several fibre paths whose tow width is adjusted and, therefore, the thickness increases in order to keep the cross-sectional area constant. Once the fibre paths are defined and chosen the modelling approach for the thickness variations, a 3D model is generated transforming a 2D shell model. Following these strategies, Lincoln *et al.* [41] studied the sensitivity to imperfections in variable stiffness cylinders manufactured with CTS. McInnes *et al.* [42] compared the usage of 2D shell elements against 3D shell elements for the analysis of CTS-manufactured VAT cylinders. They demonstrated the need of 3D continuum shell elements, allowing for greater fidelity representing the geometry of a CTS structure. In addition, the 3D shell models need a lower mesh resolution while maintaining the solution accuracy in comparison to 2D meshes of the same in-plane resolution.

Intrusive techniques can be devoted to void modelling too. Several works have been carried out in the last years. For instance, Dill *et al.* [43] investigated the influence of voids on the stress concentration factor by introducing a small disk, consisting of orthotropic plies, at the centre of the laminate. Another strategy was proposed by Huang and Talreja [44], in which flattened cylindrical voids were placed at the interface of a unidirectional composite in an RVE.

The non-intrusive techniques (NIT) preserve the mesh utilised for the simulation of the defect-free structure and vary the properties in those elements where flaws exist. One of the most extended NIT is the Defect Layer Method (DLM), introduced by Fayazbakhsh *et al.* [45], and employed in the modelling of gaps and overlaps. In DLM, the first step is identifying the gap or overlap areas within the lamina depending on the coverage percentage. A 0% coverage means a complete gap strategy, yielding

a constant thickness ply, whereas 100% implies a complete overlap presenting non-uniform thickness distribution. Once they are located, the properties of the FE vary according to the defect area percentage. DLM showed a great agreement with the results presented by Blom *et al.* [36]. In addition, Akbarzadeh *et al.* [46] showed the effects of transverse shear deformation and the consideration of manufacturing defects in the numerical model. By coupling DLM with CLPT, FSDT and third-order shear deformation theory (TSDT), they demonstrated that for relatively thick plates major discrepancies arise between CLPT and TSDT. Noevere and Collier [47] utilised DLM in an interface developed to couple the path created by CGTech's Verticut Composite Programming and HyperSizer by Collier Research Corporation. The interface allows passing the data generated by the fibre deposition simulation to the FE solver to perform the stress analysis employing shell models. DLM has also been considered for the non-linear buckling analysis of tow-steered plates in the work by Marouene *et al.* [48]. They showed great correspondence between experimental and numerical results and demonstrating, once again, that overlaps increase both the in-plane stiffness and buckling load up to a 40% and 69% with regard to a complete gap strategy.

Butler *et al.* [49] successfully modelled defects related to fibre misalignments namely, homogeneous ply angle perturbation, prismatic and non-prismatic in-plane fibre waviness. The first was modelled as a random perturbation following a Gaussian distribution of null mean and a certain standard deviation. The second was applied across the structure by means of a wave function including three random parameters that define the location, amplitude and width of the defect. The prismatic and non-prismatic waviness followed truncated Gaussian and uniform distributions for the parameters mentioned above. The effect of these flaws was investigated by employing the Multilevel Monte Carlo (MLMC) approach, see Giles [50], in which hierarchic mesh refinements are performed to reduce the variance of the estimator. Ferreira *et al.* [51] established another way for modelling waviness. They modelled the waviness of non-crimp fabric composites utilising straight mesoscale 3D elements in which the material mechanical properties are modified according to the actual fibre direction instead of reproducing the actual wave with curved elements, as in the case of [52].

At the microscale level, as far as the author concern, just a small number of paper have modelled voids using NIT. One of these studies was conducted by Van Den Broucke *et al.* [53]. They investigated a woven geometry and assumed a linear increase in the laminate thickness with voids as well as the presence of voids in resin rich regions between the yarns. Choudhry *et al.* [54] took voids into account through multiplication of the matrix properties by a void compensation factor, which is calculated as a weighted sum of the matrix and void volume fraction.

Other NIT that are becoming trendy are the stochastic fields [55]. Indeed, they are employed in this thesis to map defects at the different layers involved in a laminate. A thorough explanation and mathematical description of the two random field techniques utilised are available in Section 4.3.1. The great advantage of these fields is that they can easily account for defects and propagate them through the different scales involved in a structure. For instance, in this thesis, uncertainty defects occurring at the layer and fibre-matrix scale are considered first individually and, subsequently, altogether. The effect of spatially varying material elastic properties has been studied. As an example, Scarth *et al.* [56] considered the influence of material elastic properties on the free vibration and buckling. Similarly, van den Broek *et al.* [57] studied the impact of Young modulus and thickness variability on the buckling performance of plates and shells. Murugan *et al.* [58] investigated the influence of uncertain material elastic properties on the reaction forces of an helicopter hub. Choi *et al.* [59] performed stochastic progressive failure analysis of composites. They assumed that the the material strengths used in the failure criteria and the fracture energies varied spatially. This uncertainty increased the scattering of the strength in the specimens, specially in matrix tension damage. Mesoscale manufacturing defects modelled as random fields have been also investigated. Scarth and Adhikari [60] included misalignments in laminated plates and studied their influence on the lamination parameters. Similarly, Balokas *et al.* [61] investigated the impact of yarn distortion and waviness on the stiffness and strength of braided composites. van den Broek *et al.* [62] addressed the influence of fibre misalignments on the post-buckling behaviour and enhancing the structural performance. Uncertainty at the microscale level has also been of interest. In particular, Dey *et al.* [63] considered spatial variation of the elastic properties of fibre and matrix, and evaluated their influence on the structural natural frequencies. They showed that considering uncertainty at the microscale broadens the margins compared to the macroscale defected structure while keeping the same degree of stochasticity, i.e., the same standard deviation. Guimarães *et al.* [64] investigated how the fibre volume fraction variability affects the flutter velocity, flutter frequency and the total mass of straight-fibre and tow-steered plates. Moreover, they employed Polynomial Chaos Expansion (PCE) as response surface model to accelerate the uncertainty quantification analysis. The mathematical background of PCE is available in Section 4.3.2 of this thesis.

1.2.4 Optimisation of variable stiffness composites

The last topic in which this work focuses is the structural optimisation of composites structures and, in particular, VAT components. Composite materials offer additional

possibilities to tailor the mechanical behaviour of the structure by varying the number of layers and the fibre orientation of the single ply. This design flexibility has captivated the attention of engineers who conceived new design strategies to exploit the full potential of composites. These methods rely on the mathematical background of calculus and, specifically, on optimisation theory. The scope of this thesis is not delving into the mathematics of optimisation, but retrieve the better possible layups for certain applications and investigate the effect that structural theories have on the optimum result. If the reader is interested in a thorough explanation of the optimisation elements and mathematical fundamentals, the author suggests the books by Haftka and Gürdal [65], and by Martins and Ning [66]. It was indeed Haftka who, in his seminal work with Walsh [67], introduced integer programming for the stacking sequence optimisation for buckling of straight-fibre laminates. After that, Le Riche and Haftka [68] proposed an integer-valued Genetic Algorithm (GA) to maximise the buckling load. In this work, 0°, $\pm 45^\circ$ and 90° plies were encoded to perform the genetic operators. The same authors then proposed an improved version of GA for the minimum thickness design of composite laminates [69]. One of the advantages of GA is that is eases the coding of manufacturing constraints, or design rules, gathered in the work by Irisarri *et al.* [70]. Despite this advantage, integer-valued GA leads to non-convex problems, which are cumbersome to face in structural optimisation. To circumvent this issue, Fukunaga and Sekine derived a strategy based on lamination parameters [71]. The equations of the lamination parameters impose constraints on the design space of the lamination parameters to determine the feasible convex region where laminate configurations exist. In aeroelastic tailoring enabled design it is common to split the optimisation process in two steps. Because of the large numbers of design variables, the first subproblem utilises gradient-based optimisation. This step provides a distribution of the patch thicknesses and directional stiffness that satisfy the safety margins in a series of multidisciplinary criteria. During this phase, the design variables are the shell thicknesses, stringer dimensions and stacking sequences in terms of lamination parameters. Note that these magnitudes are continuous and, therefore, gradient-based algorithms are utilised. The second subproblem is a discrete optimisation process that transforms the previous stiffness distribution into one that satisfies all the design and manufacturing rules. In particular, the process that has just been described is the one conducted by Embraer for their regional jet portfolio and is depicted in the work by Silva *et al.* [72]. In the latter work [72], manufacturing design rules are applied using the formulation derived by Macquart *et al.* [73, 74]. A similar two-step optimisation process is followed at Airbus, as mentioned in the work by Ntourmas *et al.* [75]. Catapano and Montemurro [76] used a bi-level multiscale approach for the optimum design of sandwich plates based on polar parameters [77].

In the first level, they determine the optimal geometry of the unit cell of the sandwich core and the geometric parameters of the laminated skins. The second level scheme provides the optimal layup of the skins.

The optimisation above techniques were initially applied to retrieve the optimal layups of straight-fibre laminates, but they were extended to VAT structures. For instance, Serhat and Basdogan [78] utilised laminations parameters to predict the optimal fibre paths and imposed manufacturability by calculating the curvature radius point-wise. Khani *et al.* [79] extended to VAT laminates the approach implemented by IJsselmuiden *et al.* [80]. In these works, their authors derived a conservative failure envelope, based on Tsai-Wu failure criterion [81], that guarantees a failure-free region of the lamination parameter space regardless of the fibre orientations involved in the layup sequence. In the case of VAT [79], the lamination parameters for each node of the FE model was considered as design variables. The two-level approach based on polar parameters has also been extended to optimise VAT structures. Indeed, Catapano *et al.* [82] applied it to the optimisation of VAT components manufactured by Fused Filament Fabrication and Continuous Filament Fabrication.

In straight-fibre composites, the available orientations are limited to a fixed number and, hence, integer-valued problems arose. Contrariwise, in tow-steered composites, the parameters involved in the fibre path definition are continuous. Therefore, encoding is unnecessary if employing GA or other evolutionary algorithm like Particle Swarm Optimisation (PSO). Nik *et al.* [83] used a surrogate model to mimic the in-plane stiffness and buckling load of VSC plates and used it as the objective function of the optimisation problem, which was solved by GA. Later, Nik *et al.* [84] proceeded accordingly to their previous work embedding the gaps and overlaps originated during the AFP process. Vijayachandran *et al.* [85] conducted a multi-objective optimisation where the in-plane stiffness, buckling load and mass were the objectives. They used Bezier's curves to model the fibre paths and Artificial Neural Network (ANN) as surrogate model for the aforementioned magnitudes, and GA as the optimiser. In addition, Vijayachandran and Waas [86] proceeded as in [85] to minimise the stress concentration around a cutout. Groh and Weaver [87] developed a procedure devoted to the weight minimisation of plates manufactured by CTS. In this case, the weight is not only related to the number of layers, but also to the fibre path design parameters because of the coupling between the steering angle and thickness due to CTS. They used GA and included static failure and buckling requirements as optimisation constraints. PSO has also been considered as evolutionary algorithm for structural optimisation. Singh and Kapania [88] maximised the buckling load of curvilinearly stiffened VAT plates, in which the design variables were the fibre path definition angles and the parameters employed to define the shape of the stiffeners. Similarly, PSO was utilised by Zhao

and Kapania [89] to optimise the the buckling load of VSC laminates with a cutout imposing maximum curvature and parallel fibre path constraints.

It is worth mentioning that all of the above works employed ESL models based on CLPT or FSDT approaches for both the analysis and optimisation of VSC composites. Many of them relied on the FEM to solve the mechanical problem. Nevertheless, semi-analytical methods have also been devoted to the study of VAT, see for instance the works by Vescovini *et al.* [90–92]. However, to the author's knowledge, very little or no research has been devoted to the optimisation of VAT structures modelled by an LW approach. Only few works have investigated the behaviour of tow-steered structures using various structural theories. As an example, Demasi *et al.* [93] implemented 2D ESL, Zig-Zag and LW CUF models for the stress analysis of thick VAT laminates, while Viglietti *et al.* [94] carried out free vibration analysis using variable kinematic models.

1.3 Outline

This thesis is composed of seven chapters that depict the development of a platform that uses high-order numerical models that considers the defects, both uncertain and deterministic, that arise during manufacturing consideration and their effect on the mechanical performance of tow-steered composites. Moreover, the structural optimisation of the latter is also addressed, paying special attention to the effect of the selected structural theory on the retrieved optimal solution. The general layout of the document is as follows:

- **Chapter 2** introduces the high-order 1D and 2D models adopted in this research. The presented methodology is formulated with the CUF formalism. In the CUF framework, the kinematics of beam, plate and shell are expressed as the generic expansion of the generalised displacements utilising arbitrary cross-section and thickness functions. Depending on the selected function type and order, various beam, plate and shell theories may be derived. In this work, Taylor, Lagrange and Hierarchical Legendre polynomials are considered. When laminated VAT structures are analysed, Equivalent Single Layer and Layer-wise modelling approaches will be used. According to CUF and introducing the FEM, the governing equations can be written in a general and compact form in terms of Fundamental Nuclei, which are the building block of the proposed theory by exploiting the Principle of Virtual Displacements.

- **Chapter 3** provides the theoretical background for the numerical models developed to study the meso and microscale. The Component-Wise approach is

utilised for such purpose. In this regard, the different constituents are modelled using the same family of finite elements, precisely 1D elements. On the one hand, mesoscale models are generated through the novel Embedded Component-Wise approach, which facilitates the meshing operations and further reduces the computational cost. On the other hand, microscale models are derived by combining the Mechanics of Structure Genome and CUF. In this case, a non-isoparametric strategy is used to capture perfectly the curved geometry of the fibres and inclusions over the beam's cross-section.

- **Chapter 4** is devoted to the defects that arise during the fabrication of variable stiffness composites. First, the main flaws due to the AFP steering process are described. Second, the turning radius limitation is depicted along with analytical formulae to calculate it. Subsequently, uncertainty defect modelling is discussed. The Polynomial Chaos Expansion used to quantify the influence of randomly distributed defects on the mechanical performance is reported too. Last, the AFP manufacturing process is simulated in order to include the gaps and overlaps that appear in the numerical model. The defects are mapped in the FEM model through the Defect Layer Method.

- **Chapter 5** describes the components required to pose mathematically the optimisation problem. Then, a classification depending on a series of criteria is made. Such criteria include: (i) how the objective and constraint function are evaluated, (ii) the search method that is used, and (iii) the kind of algorithms that are utilised to solve the optimisation problem. Last, the functioning of a Genetic Algorithm works is available.

- **Chapter 6** discusses some of the results obtained. The interest is primarily focused on the efficiency and reliability of the proposed methodology to study the different scales involved in the analysis of variable stiffness composite structures. The effect of uncertainty defects propagated through the scales on the mechanical performance is addressed. In addition, the effect of the selected structural theory on the retrieved optimal solution is investigated for a series of structural optimisation problems. This is conducted by considering pristine and defected variable angle tow plates as well as manufacturing limitations.

- **Chapter 7** summarises the present work and draws the concluding remarks highlighting the major outcomes of this thesis. Some research ideas are proposed for future investigations relying on the developments achieved throughout this PhD.

- **Appendix A** reports the three-dimensional Hashin failure criteria formulae used to capture the failure onset on composite structures. Besides, the computation of the safety factor used in the strength maximisation problem is depicted.

Chapter 2

Derivation of high-order 1D and 2D models using CUF

This chapter introduces the Carrera Unified Formulation (CUF) and its application in the straightforward generation of 1D (beam) and 2D (plate, shell) high-order models hierarchically and automatically within a finite element framework. In essence, CUF, using an index notation, permits the unifying of all the structural theories in a single formula and the formulation of low-to-high fidelity models in a simple manner. The fundamental concept of CUF is the introduction of theory expansion functions, in addition to standard finite element interpolation functions, to enrich the kinematic description of the beam's cross-section and plate/shell thickness. This leads to generating 1D and 2D CUF models, similar to 3D solid finite elements in terms of solution accuracy but with a considerably lower computational burden.

2.1 Preliminaries

Consider beam and plate models described in a Cartesian reference frame (x,y,z). In contrast, an orthogonal curvilinear system (α,β,z) is employed for shell geometry, as illustrated in Fig. 2.1. In the beam model, the y axis denotes the beam axis, while the cross-section lays on the $x-z$ plane. For the plate and shell models, $x-y$ and $\alpha-\beta$ correspond to the in-plane coordinates, respectively, and z denotes the through-the-thickness direction. The derivation of the following theoretical formulation is independent of the choice of the cross-section or thickness.

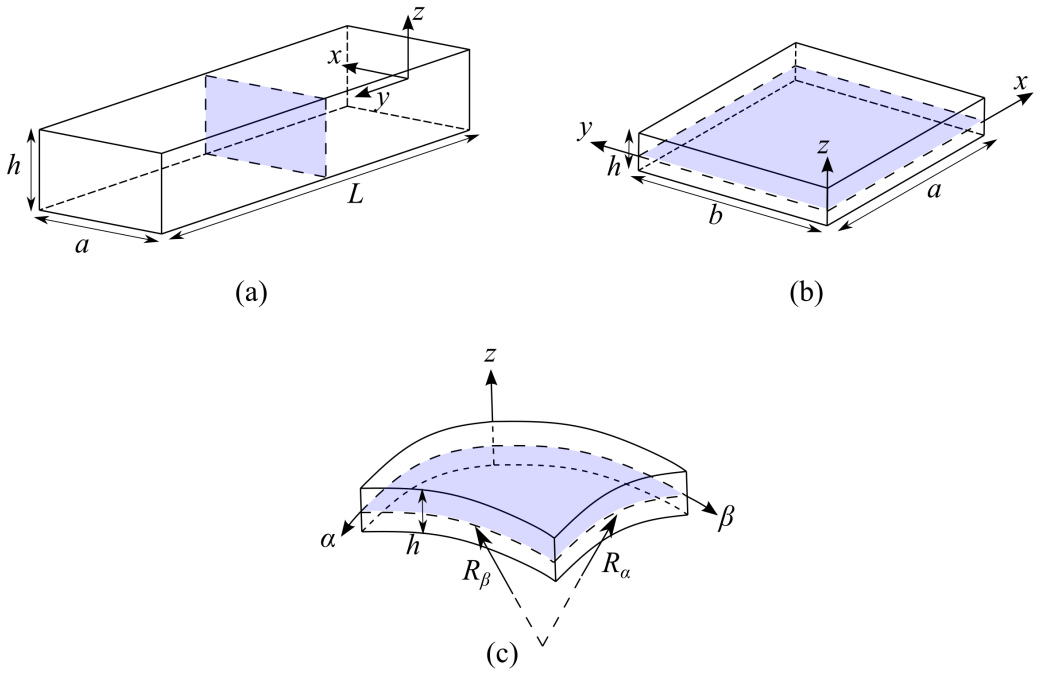

Figure 2.1 Representative geometry and reference system of (a) beam, (b) plate and (c) doubly-curved shell.

The 3D stationary displacement field of an arbitrary point within the structural domain can be expressed as follows:

$$\begin{aligned} \text{Beam, Plate:} \quad & \mathbf{u}^k(x,y,z) = \{u_x^k u_y^k u_z^k\}^T \\ \text{Shell:} \quad & \mathbf{u}^k(\alpha,\beta,z) = \{u_\alpha^k u_\beta^k u_z^k\}^T \end{aligned} \tag{2.1}$$

in which the superscript k refers to the k^{th} layer in the case that a laminated structure is considered, and T denotes the transpose operator. The strain, $\boldsymbol{\varepsilon}$, and stress, $\boldsymbol{\sigma}$, tensors are expressed in the Voigt notation as:

$$\begin{aligned} \text{Beam, Plate:} \quad & \boldsymbol{\varepsilon}^k = \{\varepsilon_{xx}^k \ \varepsilon_{yy}^k \ \varepsilon_{zz}^k \ 2\varepsilon_{xz}^k \ 2\varepsilon_{yz}^k \ 2\varepsilon_{xy}^k\}^T \\ & \boldsymbol{\sigma}^k = \{\sigma_{xx}^k \ \sigma_{yy}^k \ \sigma_{zz}^k \ \sigma_{xz}^k \ \sigma_{yz}^k \ \sigma_{xy}^k\}^T \\ \text{Shell:} \quad & \boldsymbol{\varepsilon}^k = \{\varepsilon_{\alpha\alpha}^k \ \varepsilon_{\beta\beta}^k \ \varepsilon_{zz}^k \ 2\varepsilon_{\alpha z}^k \ 2\varepsilon_{\beta z}^k \ 2\varepsilon_{\alpha\beta}^k\}^T \\ & \boldsymbol{\sigma}^k = \{\sigma_{\alpha\alpha}^k \ \sigma_{\beta\beta}^k \ \sigma_{zz}^k \ \sigma_{\alpha z}^k \ \sigma_{\beta z}^k \ \sigma_{\alpha\beta}^k\}^T \end{aligned} \tag{2.2}$$

In the proposed methodology, small displacements are assumed. Therefore, the geometrical relations between strains and displacements will only consider the linear

differential operator $\mathbf{B}$, which is a 6×3 matrix containing the following terms:

$$\text{Beam, Plate:}\quad \mathbf{B}=\begin{pmatrix} \partial_x & 0 & 0 \\ 0 & \partial_y & 0 \\ 0 & 0 & \partial_z \\ \partial_z & 0 & \partial_x \\ 0 & \partial_z & \partial_y \\ \partial_y & \partial_x & 0 \end{pmatrix}$$

$$\text{Shell:}\quad \mathbf{B}=\begin{pmatrix} \frac{\partial_\alpha}{H_\alpha} & 0 & \frac{1}{H_\alpha R_\alpha} \\ 0 & \frac{\partial_\beta}{H_\beta} & \frac{1}{H_\beta R_\beta} \\ 0 & 0 & \partial_z \\ \partial_z - \frac{1}{H_\alpha R_\alpha} & 0 & \frac{\partial_\alpha}{H_\alpha} \\ 0 & \partial_z - \frac{1}{H_\beta R_\beta} & \frac{\partial_\beta}{H_\beta} \\ \frac{\partial_\beta}{H_\beta} & \frac{\partial_\alpha}{H_\alpha} & 0 \end{pmatrix} \tag{2.3}$$

where $\partial_x = \frac{\partial(\cdot)}{\partial x}$, that is, the derivative with respect to the x direction. The same applies for α, β, y and z directions. Thus, the displacement-strain relation can be written as:

$$\boldsymbol{\varepsilon}^k = \mathbf{B}\mathbf{u}^k \tag{2.4}$$

The stress-strain relation may be expressed by employing the material properties. As far as material non-linearities are not considered in this work, Hooke's law states in vectorial form:

$$\boldsymbol{\sigma}^k = \mathbf{C}^k\boldsymbol{\varepsilon}^k \tag{2.5}$$

in which $\mathbf{C}^k$ is the material linear elastic matrix. In the case of orthotropic materials, e.g., straight-fibre carbon/epoxy unidirectional lamina, $\mathbf{C}^k$ reads in the material reference system as:

$$\mathbf{C}^k = \begin{bmatrix} C_{11}^k & C_{12}^k & C_{13}^k & 0 & 0 & 0 \\ & C_{22}^k & C_{23}^k & 0 & 0 & 0 \\ & & C_{33}^k & 0 & 0 & 0 \\ & & & C_{44}^k & 0 & 0 \\ & & & & C_{55}^k & 0 \\ sym & & & & & C_{66}^k \end{bmatrix} \tag{2.6}$$

where the C_{ij}^k coefficients depend on the Young moduli E, the Poison's ratio ν and the shear moduli G, and the fibre angle orientation θ. Note that 1 denotes the fibre

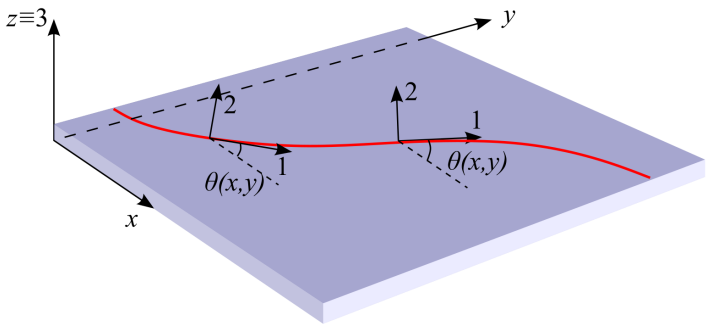

Figure 2.2 Variation of the material reference system with respect to the global reference system in the case of a VAT lamina. Direction 1 corresponds to the fibre direction while 2 and 3 represent the transverse directions.

direction in the material reference frame. In contrast, the 2 direction is transverse to the fibre direction in the plane of the lamina, and 3 is perpendicular to the plane of the lamina.

In laminated composite structures, the material reference frame is rotated with respect to the global reference system by the fibre orientation θ, which, in the case of tow-steered composites, depends on the in-plane coordinates, i.e., $\theta(x,y)$ or $\theta(\alpha,\beta)$. As a result,

$$\boldsymbol{\sigma}^k = \tilde{\mathbf{C}}^k \boldsymbol{\varepsilon}^k \tag{2.7}$$

where:

$$\tilde{\mathbf{C}}^k = \mathbf{T}\mathbf{C}^k\mathbf{T}^T \tag{2.8}$$

being $\mathbf{T}$ the rotation matrix [12]. In the case of variable stiffness composites, $\mathbf{T}$ will depend on the in-plane coordinates, i.e., $\mathbf{T}(x,y)$ or $\mathbf{T}(\alpha,\beta)$. An illustrative example of how the material reference system varies with the in-plane coordinates is available in Fig. 2.2.

2.2 Carrera Unified Formulation

For decades, many efforts have been dedicated to the derivation of advanced theories able to tackle various structural problems. To solve some of the issues related to classical approaches, CUF was introduced as a generator of structural theories for beams, plates and shells [95]. In the CUF formalism, the 3D field of displacements

can be expressed as:

$$\begin{aligned}
\text{Beam:} \quad & \mathbf{u}^k(x,y,z) = F_\tau^k(x,z)\mathbf{u}_\tau^k(y) \quad \tau = 1,...,M \\
\text{Plate:} \quad & \mathbf{u}^k(x,y,z) = F_\tau^k(z)\mathbf{u}_\tau^k(x,y) \quad \tau = 1,...,M \\
\text{Shell:} \quad & \mathbf{u}^k(\alpha,\beta,z) = F_\tau^k(z)\mathbf{u}_\tau^k(\alpha,\beta) \quad \tau = 1,...,M
\end{aligned} \tag{2.9}$$

where F_τ denotes a set of arbitrary expansion functions depending on the cross-section coordinates, x and z, in the case of beam models, and on the thickness coordinate z when plate and shell models are considered; $\mathbf{u}_\tau$ represents the vector containing the generalised displacements and M denotes the number of expansion terms. Precisely, the selection of F_τ and M are the inputs of the analysis and define the structural theory adopted for the model. In recent years, three families of expansion functions have emerged as ideal options due to their inherent capabilities: the Taylor Expansion (TE) [96], Lagrange Expansion (LE) [97] and Hierarchical Legendre Expansion (HLE) [98]. Considering the modelling of laminated composite structures, two approaches are devised, namely Equivalent Single Layer (ESL) and Layer-Wise (LW). In this document, ESL models are derived using TE, whereas LW is obtained by employing LE. Throughout this thesis, the acronyms TEN and LEN indicate the use of Taylor and Lagrange expansions of N^{th} order assumed for the $x-z$ cross-section or thickness direction z, respectively.

TE class considers the Taylor series of the $x-z$ cross-section or the z direction as F_τ. Therefore, it results in a hierarchic basis where the order N is user-defined. As an example, the first-order TE (TE 1) for 1D and 2D models can be written as:

$$\begin{aligned}
& & u_x &= u_{x_1} + xu_{x_2} + zu_{x_3} \\
& \text{1D:} & u_y &= u_{y_1} + xu_{y_2} + zu_{y_3} \\
& & u_z &= u_{z_1} + xu_{z_2} + zu_{z_3} \\
& & u_x &= u_{x_1} + zu_{x_2} \\
& \text{2D:} & u_y &= u_{y_1} + zu_{y_2} \\
& & u_z &= u_{z_1} + zu_{z_2}
\end{aligned} \tag{2.10}$$

As one can appreciate, classical beam, plate and shell models can be derived by selectively removing some of the terms of the first-order expansion. If interested, the reader can find further information about TE in [99, 100].

The LE family uses Lagrange polynomials to build 1D and 2D high-order structural theories, and the isoparametric formulation is exploited to deal with intricate geometries. In the case of beams, LE is employed as F_τ to describe the cross-section geometry, while in the case of plates and shells, LE is used along the thickness di-

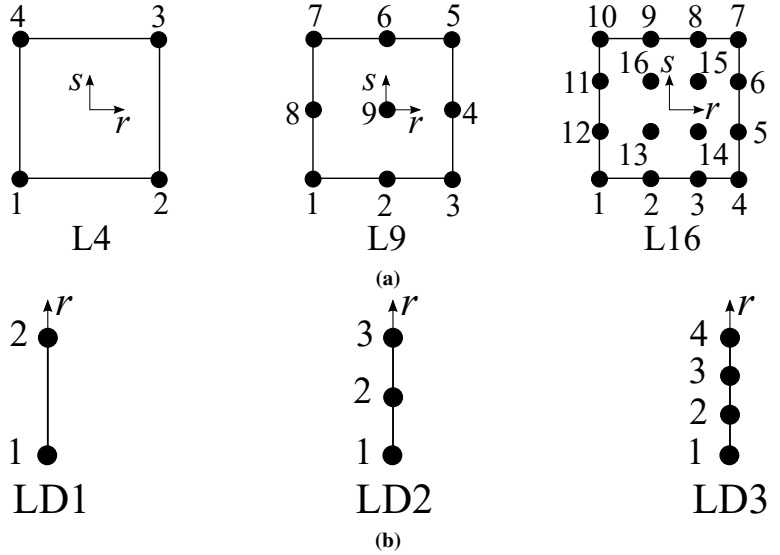

Figure 2.3 Lagrange expansions on the: (a) cross-section, (b) thickness, for 1D and 2D models, respectively.

rection. Throughout this work, three sets of Lagrange polynomials have been used for both 1D and 2D models. These are illustrated in Fig. 2.3. Concretely, four-point (L4), nine-point (L9) and sixteen-point (L16) polynomials have been employed to describe the beam's cross-section. The polynomial order of L4, L9 and L16 is bi-linear, bi-quadratic and bi-cubic, respectively. In the case of 2D models, the acronym LDN, that is, Lagrange expansion Displacement-based of N^{th} order, is assumed. In this case, LD1, LD2 and LD3 refer to using linear, quadratic and cubic Lagrange expansion functions, respectively. They are used along the thickness direction to describe linear to high-order kinematics. For the sake of clarity, the interpolation functions of an L4 beam model are reported in the following:

$$F_\tau = \frac{1}{4}\left(1 - r_\tau r\right)\left(1 - s_\tau s\right) \quad \tau = 1,2,3,4 \tag{2.11}$$

in which r and s represent the natural coordinates and vary from -1 to 1. At the same time, r_τ and s_τ are the coordinates of the four points whose numbering and location in the natural reference frame are depicted in Fig. 2.3. Note that LE uses pure displacements unknowns, i.e., it only has displacements as degrees of freedom.

The HLE class employs Legendre polynomials to generate 1D high-order theories. This set of interpolation functions was originally defined by Szabó and Babuška [101] for the p-version of the Finite Element Method. They are based on an orthogonal basis and constitute a fully hierarchical set. The Legendre polynomials can be obtained

recurrently as:

$$\begin{aligned} L_0 &= 1 \\ L_1 &= \xi \\ L_k &= \frac{2k-1}{k}\xi L_{k-1}(\xi) - \frac{k-1}{k}\xi L_{k-2}(\xi) \quad k = 2,3,... \end{aligned} \tag{2.12}$$

The roots of L_k coincide with the Gauss points, and the resultant polynomial set constitutes an orthonormal basis. The set of interpolation functions in the 1D case can be expressed as:

$$\begin{aligned} \tilde{L}_1 &= \frac{1}{2}(1-r) \\ \tilde{L}_2 &= \frac{1}{2}(1+r) \\ \tilde{L}_k &= \phi_{k-1}(r) \quad k = 3,4,...,p+1 \end{aligned} \tag{2.13}$$

where $\phi_j(r)$ are the normalised integrals of L_k:

$$\phi_j(r) = \sqrt{\frac{2j-1}{j}} \int_{-1}^{r} L_{j-1}(\xi) d\xi \quad j = 2,3,4,... \tag{2.14}$$

In Eq. (2.13), $\tilde{L}_1$ and $\tilde{L}_2$ are linear function ranging from 0 to 1 in the natural domain, that is, $r \in [-1,1]$. Thus, they are referred to as nodal modes. The $\tilde{L}_k$ functions are higher-order polynomials that vanish at the edges of the interval and are known as internal modes.

The orthogonality of the Legendre set of functions is defined as:

$$\int_{-1}^{1} \frac{d\tilde{L}_i}{dr} \frac{d\tilde{L}_j}{dr} dr = \delta_{ij}, \quad \text{for } i \geq 3 \text{ and } j \geq 1 \tag{2.15}$$

where δ_{ij} is the Kronecker's delta.

Generalising the above procedure, one can expand to quadrilateral $[-1,1] \times [-1,1]$ domains and obtain a 2D set of interpolating polynomials. In a 2D domain, it is possible to define three classes of expansions, namely, nodal, side and internal, constructed by the product of the 1D Legendre polynomials. Figure 2.4 shows examples of the HLE functions.

Nodal expansions They are the same as the bi-linear Lagrange expansion (L4), reported in Eq. (2.11).

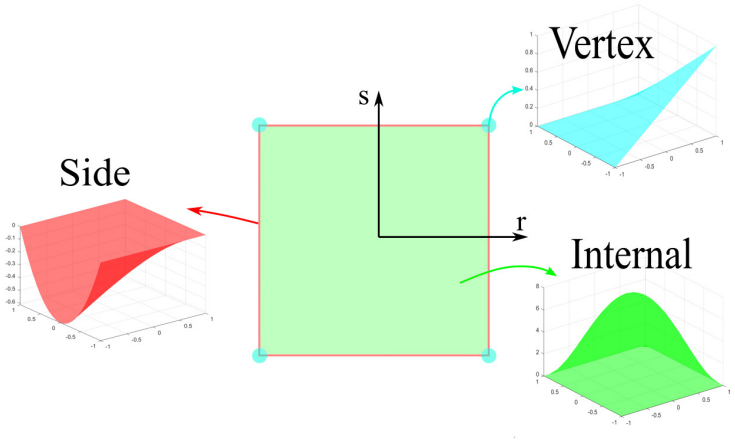

Figure 2.4 Types of HLE expansion functions.

Side expansion They are defined for polynomial order greater or equal to 2 ($p \geq 2$). Their functions are:

$$\begin{aligned} F_\tau(r,s) &= \frac{1}{2}(1-s)\phi_p(r) \quad \tau = 5,9,13,18,... \\ F_\tau(r,s) &= \frac{1}{2}(1+r)\phi_p(s) \quad \tau = 6,10,14,19,... \\ F_\tau(r,s) &= \frac{1}{2}(1+s)\phi_p(r) \quad \tau = 7,11,15,20,... \\ F_\tau(r,s) &= \frac{1}{2}(1-r)\phi_p(s) \quad \tau = 8,12,16,21,... \end{aligned} \tag{2.16}$$

Internal expansion They are defined for $p \geq 4$, and a given polynomial set includes $(p-2)(p-3)/2$ functions. They are obtained as a product of the 1D Legendre modes $\tilde{L}_k$ from Eq. (2.13):

$$F_\tau(r,s) = \phi_{p_1}(r)\phi_{p_2}(s) \quad p_1,p_2 = 2,3,4... \text{ and } p = p_1 + p_2 \tag{2.17}$$

For example, the set of internal functions when $p = 6$ are:

$$\begin{aligned} F_{28}(r,s) &= \phi_4(r)\phi_2(s) \\ F_{29}(r,s) &= \phi_3(r)\phi_3(s) \\ F_{30}(r,s) &= \phi_2(r)\phi_4(s) \end{aligned} \tag{2.18}$$

HLE gather the features of other refined beam theories. On the one hand, the displacement field can be enriched hierarchically, as for TE models. On the other hand, HLE allows the discretisation of the cross-section into subdomains, as for LE models. The advantage of HLE models is that the cross-section can be discretised just once,

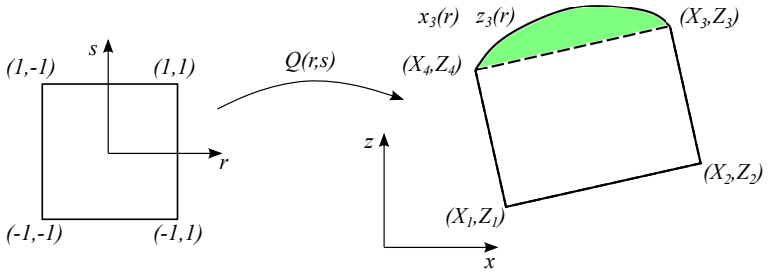

Figure 2.5 Jacobian transformation of the quadrilateral domains of a generic cross-section.

and the convergence is achieved by systematically increasing the polynomial order p [101]. Therefore, there is no need for remeshing.

2.3 Cross-section mapping

Standard isoparametric elements utilise the same set of interpolating functions to characterise the geometry and displacements. When dealing with curved geometries, the isoparametric elements introduce a numerical error due to the inability to capture the exact geometry. In the case of large domains, this error might be unacceptably large and non-isoparametric techniques become mandatory.

First, let us consider the Jacobian transformation of a quadrilateral domain, defined in the natural (r,s) plane, into the global coordinate system (x,z) represented in Fig. 2.5, in which one side is curved. The mapping functions are written as follows:

$$\begin{aligned} x &= Q_x(r,s), \\ z &= Q_z(r,s) \end{aligned} \tag{2.19}$$

Some mapping techniques involve first- and second-order approximations, which involve the L4 and L9 inteporlating functions. Nevertheless, they still introduce numerical error. To mitigate it, the blending function method (BFM), introduced by Gordon and Hall [102], is employed. BFM makes it possible to describe the actual geometry of the domain of interest, thus ensuring that the exact domain is integrated in the energy terms. In this thesis, the BFM is used to derive non-isoparametric HLE domains which are able to represent with high accuracy the surface of arbitrary curved cross-sections.

In the quadrilateral domain illustrated in Fig. 2.5, the curved edge can be described mathematically in the 2D space by a pair of parametric functions $x = x_3(r)$ and $z = z_3(r)$. For instance, if cubic polynomials are employed to describe the geometry,

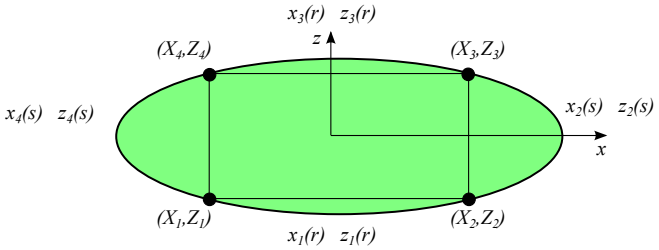

Figure 2.6 Mapping of the cross-section domain by BFM.

one can write the following relations:

$$\begin{aligned} x_3(r) &= a_x + b_x r + c_x r^2 + d_x r^3, \\ z_3(r) &= a_z + b_z r + c_z r^2 + d_z r^3 \end{aligned} \tag{2.20}$$

which guarantee the conditions:

$$\begin{aligned} x_3(-1) = X_3 \;\; x_3(1) = X_4 \\ z_3(-1) = Z_3 \;\; z_3(1) = Z_4 \end{aligned} \tag{2.21}$$

In this context, the mapping functions are expressed as follows:

$$\begin{aligned} x = Q_x(r,s) &= F_\tau(r,s)X_\tau + \left(x_3(r) - \left(\frac{1+r}{2}X_3 + \frac{1-r}{2}X_4 \right) \right) \frac{1+s}{2} \\ z = Q_z(r,s) &= F_\tau(r,s)Z_\tau + \left(z_3(r) - \left(\frac{1+r}{2}Z_3 + \frac{1-r}{2}Z_4 \right) \right) \frac{1+s}{2} \end{aligned} \tag{2.22}$$

where X_τ and Z_τ correspond to the vertex of the quadrilateral domain in the global coordinate system, and $\tau = 1,...,4$. The first term of the right hand side corresponds to the first-order mapping, The subsequent term adds the area between $z_3(r)$ and the straight line between vertices 3 and 4, highlighted in Fig. 2.5. The term $(1+s)/2$ denotes the blending function as it is added to vanish the transformation at the opposite edge of the quadrilateral domain.

If the blending operation is applied to all the four sides of the quadrilateral domain, one obtains the following:

$$\begin{aligned} x = Q_x(r,s) &= \frac{1-s}{2}x_1(r) + \frac{1+r}{2}x_2(s) + \frac{1+s}{2}x_3(r) + \frac{1-r}{2}x_4(s) - F_\tau(r,s)X_\tau, \\ z = Q_z(r,s) &= \frac{1-s}{2}z_1(r) + \frac{1+r}{2}z_2(s) + \frac{1+s}{2}z_3(r) + \frac{1-r}{2}z_4(s) - F_\tau(r,s)Z_\tau. \end{aligned} \tag{2.23}$$

Note that each side is represented by parametric functions x_i and z_i, being $i = 1,...,4$, as depicted in Fig. 2.6.

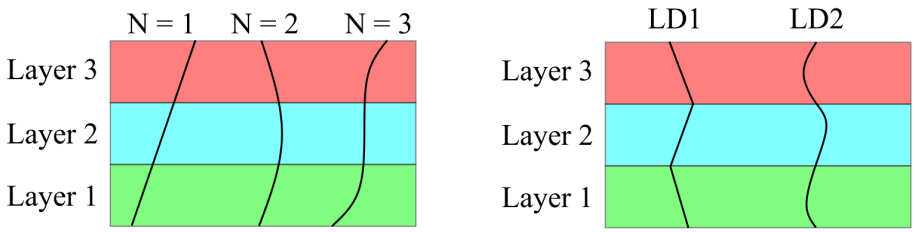

(a) ESL **(b)** LW

Figure 2.7 ESL and LW behaviours of the primary variables in the thickness direction of a 2D model.

From the beam modelling perspective, this approach permits to decouple the discretisation of the cross-section from the order of the structural theory. In this manner, the surface of any curved section can be modelled a priori, and the order of the HLE can be chosen according to the level of accuracy desired. Therefore, no computational effort is wasted to capture the desired geometry.

2.4 Modelling of laminated composite structures

There exists two approaches when modelling laminated composite structures, namely Equivalent Single Layer (ESL) and Layer-Wise (LW). The ESL approach considers the cross-section as a single domain in which the expansion functions F_τ are defined, and the stresses are computed considering the resulting strains in each layer of the displacement-based models. Therefore, the stiffness matrix is derived through the homogenisation technique of the properties of each layer by summing all the contributions for each layer. It is known that multi-layered structures are heterogeneous. In this regard, ESL models lead to continuous transverse strains along the thickness, and discontinuous transverse stresses at the layer interfaces [103]. Despite this drawback, ESL approaches are still employed for many applications due to their simplicity and fairly good performance. Indeed, ESL theories provide a good approximation for global responses such as buckling loads, fundamental frequencies and transverse deflections, but tend to provide inaccurate 3D stress distribution predictions.

On the opposite side, LW theories consider the displacement field within each material layer. Thus, the continuity of the displacements at the interface is guaranteed, although not automatically [104]. With LW models, the strain and stress distributions are evaluated thoroughly. Throughout this thesis, LW models are derived by using LD as F_τ, which posses pure displacement degrees of freedom. In addition, the continuity of displacements is guaranteed because we place these expansion function at the

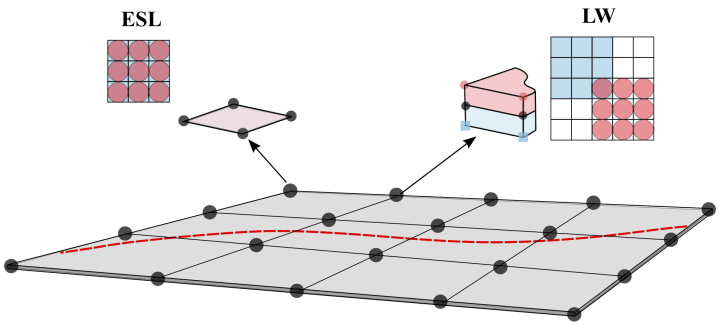

Figure 2.8 Differences in the assembly procedure of ESL and LW models.

top and bottom of each layer. This is illustrated in Fig. 2.7. For completeness, the differences in the assembly procedure of ESL and LW for a 2D structure are depicted in Fig. 2.8.

2.5 The Finite Element Method

The Finite Element Method (FEM) is employed to solve the structural problem thanks to its versatility in modelling complex geometries as well as different boundary and loading conditions. Regardless of the beam, plate or shell model kinematics, FEM is used to discretise the generalised displacement vector along the y-axis in beams, or the in-plane coordinates, (x,y) or (α,β), when plates or shells are considered, respectively. The generalised displacement vector can be written as follows:

$$\begin{aligned} \text{Beam:} \quad & \mathbf{u}^k_\tau(y) = N_i(y)\mathbf{q}^k_{\tau i} \quad i = 1,...,N_n \\ \text{Plate:} \quad & \mathbf{u}^k_\tau(x,y) = N_i(x,y)\mathbf{q}^k_{\tau i} \quad i = 1,...,N_n \\ \text{Shell:} \quad & \mathbf{u}^k_\tau(\alpha,\beta) = N_i(\alpha,\beta)\mathbf{q}^k_{\tau i} \quad i = 1,...,N_n \end{aligned} \tag{2.24}$$

in which N_i represents the shape functions, $\mathbf{q}_{\tau i}$ are the unknowns nodal variables, N_n stands for the number of nodes per element and i indicates summation. When modelling beam structures, 1D FE with two (B2), three (B3) and four (B4) nodes, that is, linear, quadratic and cubic approximations along the beam axis, are used. In the case of plates and shells, 2D FE with four (Q4), nine (Q9) and sixteen (Q16) nodes are adopted as shape functions for the $x-y$ and $\alpha-\beta$ planes.

CUF and FEM can be combined by substituting Eq. (2.24) into Eq. (2.9), yielding as a result the following expression for the 3D field of displacements:

$$\begin{aligned}
&\text{Beam:} && \mathbf{u}^k_\tau(y) = F^k_\tau(x,z)N_i(y)\mathbf{q}^k_{\tau i} \quad \tau = 1,...,M \quad i = 1,...,N_n \\
&\text{Plate:} && \mathbf{u}^k_\tau(x,y) = F^k_\tau(z)N_i(x,y)\mathbf{q}^k_{\tau i} \quad \tau = 1,...,M \quad i = 1,...,N_n \\
&\text{Shell:} && \mathbf{u}^k_\tau(\alpha,\beta) = F^k_\tau(z)N_i(\alpha,\beta)\mathbf{q}^k_{\tau i} \quad \tau = 1,...,M \quad i = 1,...,N_n
\end{aligned} \tag{2.25}$$

For the sake of completeness, Fig. 2.9 depicts the CUF and FEM model approximation of 1D and 2D structures.

2.6 Derivation of the governing equations

In the calculus of variation, a variational statement is formulated to find the stationary solutions of an integral problem. In detail, in solid mechanics, the variational formulation minimises the total potential energy of a structure, which sums the contributions of the internal and external energies. In this context, to derive the governing equations of a linear elastic problem, the Principle of Virtual Displacements (PVD) is used. It states that for all kinematically admissible virtual displacements, a body is in equilibrium if the work done by the internal stresses equals the work done by the external loads:

$$\delta\mathscr{L}_{int} = \delta\mathscr{L}_{ext} - \delta\mathscr{L}_{ine} \tag{2.26}$$

in which $\delta\mathscr{L}_{int}$, $\delta\mathscr{L}_{ext}$ and $\delta\mathscr{L}_{ine}$ represent the virtual variations of the strain energy, the external loads and the inertia loads, respectively.

The virtual variation of the internal work corresponds to the elastic strain energy and is defined as:

$$\delta\mathscr{L}_{int} = \int_V \delta\boldsymbol{\varepsilon}^T\boldsymbol{\sigma}dV, \tag{2.27}$$

where V is the volume of the body. The external work includes the contribution of surface loads, $\mathbf{P}_S$, line loads, $\mathbf{P}_l$, and point loads, $\mathbf{P}$,

$$\delta\mathscr{L}_{ext} = \int_S \delta\mathbf{u}^T\mathbf{P}_S dS + \int_l \delta\mathbf{u}^T\mathbf{P}_l dl + \delta\mathbf{u}^T\mathbf{P}. \tag{2.28}$$

The virtual variation of the inertial loads is defined as:

$$\delta\mathscr{L}_{ine} = \int_V \delta\mathbf{u}^T\rho\ddot{\mathbf{u}}dV \tag{2.29}$$

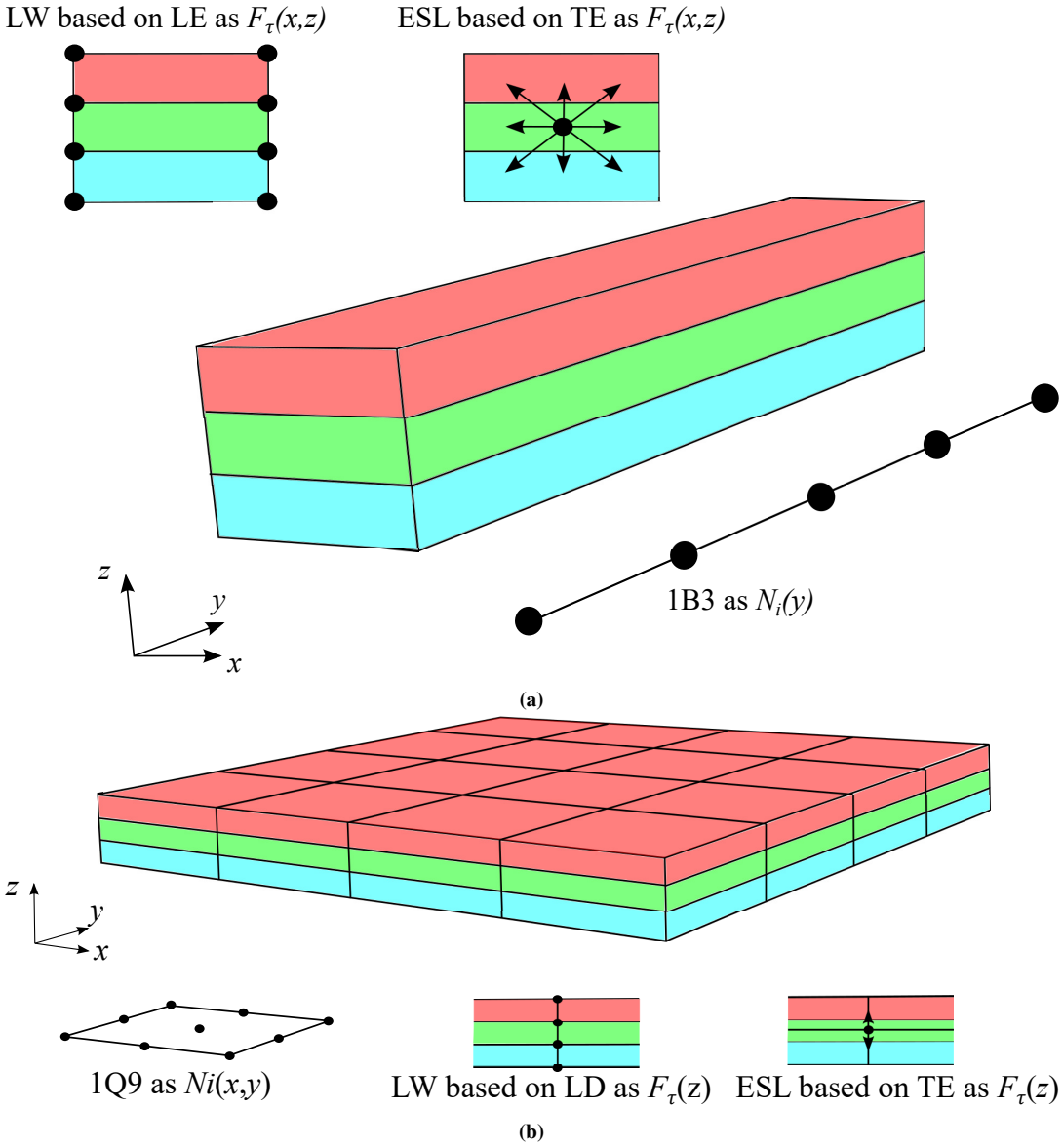

Figure 2.9 CUF and FEM representation of (a) 1D and (b) 2D model approximation.

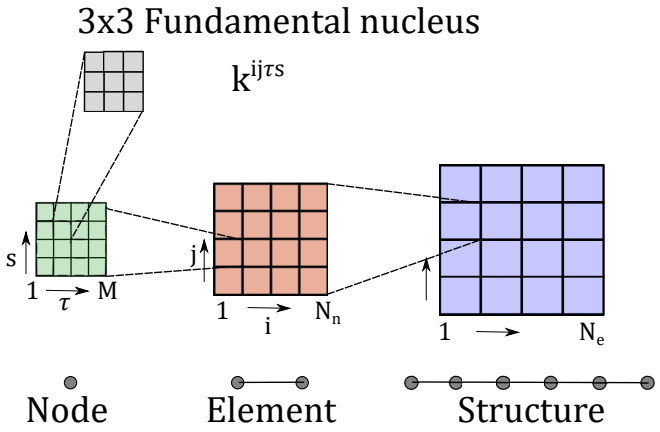

Figure 2.10 CUF assembly technique.

in which ρ is the material density and $\ddot{\mathbf{u}}$ is the acceleration vector. As a result, the PVD can be written as:

$$\int_V \delta\boldsymbol{\varepsilon}^T \boldsymbol{\sigma} dV + \int_V \delta\mathbf{u}^T \rho \ddot{\mathbf{u}} dV = \int_S \delta\mathbf{u}^T \mathbf{P}_S dS + \int_l \delta\mathbf{u}^T \mathbf{P}_l dl + \delta\mathbf{u}^T \mathbf{P}. \tag{2.30}$$

Introducing Eqs. (2.25), (2.3), rewriting the Hooke's law as $\boldsymbol{\sigma} = \tilde{\mathbf{C}}\mathbf{B}(N_i F_\tau)\mathbf{q}_{\tau i}$, and considering the virtual displacements as $\delta\mathbf{u} = N_j F_s \delta\mathbf{q}_{sj}$, the governing equations from Eq. (2.30) reads as:

$$\begin{aligned} &\delta\mathbf{q}_{sj}^T \left[\int_V \mathbf{B}(N_j F_s)^T \tilde{\mathbf{C}}\mathbf{B}(N_i F_\tau) dV\right] \mathbf{q}_{\tau i} + \delta\mathbf{q}_{sj}^T \left[\int_V \rho \mathbf{I} N_i N_j F_\tau F_s dV\right] \ddot{\mathbf{q}}_{\tau i} = \\ &\delta\mathbf{q}_{sj}^T \int_S N_j F_s \mathbf{P}_S dS + \delta\mathbf{q}_{sj}^T \int_l N_j F_s \mathbf{P}_l dl + \delta\mathbf{q}_{sj}^T \mathbf{P}, \end{aligned} \tag{2.31}$$

where $\mathbf{I}$ is the 3×3 identity matrix. This expression can be written in a compact form as:

$$\delta\mathbf{q}_{sj}^T \mathbf{k}^{ij\tau s} \mathbf{q}_{\tau i} + \delta\mathbf{q}_{sj}^T \mathbf{m}^{ij\tau s} \ddot{\mathbf{q}}_{\tau i} = \delta\mathbf{q}_{sj}^T \mathbf{F}_{sj} \tag{2.32}$$

in which:

$$\begin{aligned} \mathbf{k}^{ij\tau s} &= \int_V \mathbf{B}(N_j F_s)^T \tilde{\mathbf{C}}\mathbf{B}(N_i F_\tau) dV \\ \mathbf{m}^{ij\tau s} &= \int_V \rho \mathbf{I} N_i N_j F_\tau F_s dV \end{aligned} \tag{2.33}$$

are the 3×3 fundamental nucleus of the stiffness and mass matrices, respectively. Note that the formal expressions of $\mathbf{k}^{ij\tau s}$ and $\mathbf{m}^{ij\tau s}$ remain constant regardless of the structural theory or FE chosen. Indeed, this is where the main potentiality of CUF resides [95]. From a coding point of view, any structural model can be created by looping through the four indices τ, s, i and j. This procedure is illustrated in Fig. 2.10. For the case of orthotropic materials with a generic orientation of the fibres in space,

the global components of the elasticity tensor $\tilde{\mathbf{C}}$ are computed by means of the rotation matrix without affecting the definition of the FNs. Thus, the components of the $\mathbf{k}^{ij\tau s}$ nucleus can be written as:

$$
\begin{aligned}
k_{xx}^{ij\tau s} &= \int_V \tilde{C}_{11}\partial_x(N_jF_s)\partial_x(N_iF_\tau)dV + \int_V \tilde{C}_{16}\partial_x(N_jF_s)\partial_y(N_iF_\tau)dV \\
&+ \int_V \tilde{C}_{44}\partial_z(N_jF_s)\partial_z(N_iF_\tau)dV + \int_V \tilde{C}_{16}\partial_y(N_jF_s)\partial_x(N_iF_\tau)dV \\
&+ \int_V \tilde{C}_{66}\partial_y(N_jF_s)\partial_y(N_iF_\tau)dV \\
k_{xy}^{ij\tau s} &= \int_V \tilde{C}_{12}\partial_x(N_jF_s)\partial_y(N_iF_\tau)dV + \int_V \tilde{C}_{16}\partial_x(N_jF_s)\partial_x(N_iF_\tau)dV \\
&+ \int_V \tilde{C}_{45}\partial_z(N_jF_s)\partial_z(N_iF_\tau)dV + \int_V \tilde{C}_{26}\partial_y(N_jF_s)\partial_y(N_iF_\tau)dV \\
&+ \int_V \tilde{C}_{66}\partial_y(N_jF_s)\partial_x(N_iF_\tau)dV \\
k_{xz}^{ij\tau s} &= \int_V \tilde{C}_{13}\partial_x(N_jF_s)\partial_z(N_iF_\tau)dV + \int_V \tilde{C}_{44}\partial_z(N_jF_s)\partial_x(N_iF_\tau)dV \\
&+ \int_V \tilde{C}_{45}\partial_z(N_jF_s)\partial_y(N_iF_\tau)dV + \int_V \tilde{C}_{36}\partial_y(N_jF_s)\partial_z(N_iF_\tau)dV \\
k_{yx}^{ij\tau s} &= \int_V \tilde{C}_{12}\partial_y(N_jF_s)\partial_x(N_iF_\tau)dV + \int_V \tilde{C}_{26}\partial_y(N_jF_s)\partial_y(N_iF_\tau)dV \\
&+ \int_V \tilde{C}_{45}\partial_z(N_jF_s)\partial_z(N_iF_\tau)dV + \int_V \tilde{C}_{16}\partial_x(N_jF_s)\partial_x(N_iF_\tau)dV \\
&+ \int_V \tilde{C}_{66}\partial_x(N_jF_s)\partial_y(N_iF_\tau)dV \\
k_{yy}^{ij\tau s} &= \int_V \tilde{C}_{22}\partial_y(N_jF_s)\partial_y(N_iF_\tau)dV + \int_V \tilde{C}_{26}\partial_y(N_jF_s)\partial_x(N_iF_\tau)dV \\
&+ \int_V \tilde{C}_{26}\partial_x(N_jF_s)\partial_y(N_iF_\tau)dV + \int_V \tilde{C}_{66}\partial_x(N_jF_s)\partial_x(N_iF_\tau)dV \\
&+ \int_V \tilde{C}_{55}\partial_z(N_jF_s)\partial_z(N_iF_\tau)dV \\
k_{yz}^{ij\tau s} &= \int_V \tilde{C}_{23}\partial_y(N_jF_s)\partial_z(N_iF_\tau)dV + \int_V \tilde{C}_{45}\partial_z(N_jF_s)\partial_x(N_iF_\tau)dV \\
&+ \int_V \tilde{C}_{55}\partial_z(N_jF_s)\partial_y(N_iF_\tau)dV + \int_V \tilde{C}_{36}\partial_x(N_jF_s)\partial_z(N_iF_\tau)dV \\
k_{zx}^{ij\tau s} &= \int_V \tilde{C}_{13}\partial_z(N_jF_s)\partial_x(N_iF_\tau)dV + \int_V \tilde{C}_{36}\partial_z(N_jF_s)\partial_y(N_iF_\tau)dV \\
&+ \int_V \tilde{C}_{44}\partial_x(N_jF_s)\partial_z(N_iF_\tau)dV + \int_V \tilde{C}_{45}\partial_y(N_jF_s)\partial_z(N_iF_\tau)dV
\end{aligned}
\tag{2.34}
$$

$$
\begin{aligned}
k_{zy}^{ij\tau s} &= \int_V \tilde{C}_{23}\partial_z(N_jF_s)\partial_y(N_iF_\tau)dV + \int_V \tilde{C}_{36}\partial_z(N_jF_s)\partial_x(N_iF_\tau)dV \\
&+ \int_V \tilde{C}_{45}\partial_x(N_jF_s)\partial_z(N_iF_\tau)dV + \int_V \tilde{C}_{55}\partial_y(N_jF_s)\partial_z(N_iF_\tau)dV \\
k_{zz}^{ij\tau s} &= \int_V \tilde{C}_{36}\partial_z(N_jF_s)\partial_z(N_iF_\tau)dV + \int_V \tilde{C}_{44}\partial_x(N_jF_s)\partial_x(N_iF_\tau)dV \\
&+ \int_V \tilde{C}_{45}\partial_x(N_jF_s)\partial_y(N_iF_\tau)dV + \int_V \tilde{C}_{45}\partial_y(N_jF_s)\partial_x(N_iF_\tau)dV \\
&+ \int_V \tilde{C}_{55}\partial_y(N_jF_s)\partial_y(N_iF_\tau)dV
\end{aligned}
\tag{2.35}
$$

The individual expressions of each component of the stiffness FN can be written for beam and plate elements by accordingly using their respective shape and expansion functions. Recall that in the case of beam models, the displacement field can be expressed as $\mathbf{u} = N_i(y)F_\tau(x,z)\mathbf{u}_\tau$. Substituting that expression into the $k_{xx}^{ij\tau s}$ component, one has:

$$
\begin{aligned}
k_{xx}^{ij\tau s} &= \int_V \tilde{C}_{11}N_jF_{s,x}N_iF_{\tau,x}dV + \int_V \tilde{C}_{16}N_jF_{s,x}N_{i,y}F_\tau dV \\
&+ \int_V \tilde{C}_{44}N_jF_{s,z}N_iF_{\tau,z}dV + \int_V \tilde{C}_{16}N_{j,y}F_sN_iF_{\tau,x}dV \\
&+ \int_V \tilde{C}_{66}N_{j,y}F_sN_{i,y}F_\tau dV
\end{aligned}
\tag{2.36}
$$

Conversely, in the case of plate models, the displacement field reads as $\mathbf{u} = N_i(x,y)F_\tau(z)\mathbf{u}_\tau$. In this context, $k_{xx}^{ij\tau s}$ can be expressed as:

$$
\begin{aligned}
k_{xx}^{ij\tau s} &= \int_V \tilde{C}_{11}N_{j,x}F_sN_{i,x}F_\tau dV + \int_V \tilde{C}_{16}N_{j,x}F_sN_{i,y}F_\tau dV \\
&+ \int_V \tilde{C}_{44}N_jF_{s,z}N_iF_{\tau,z}dV + \int_V \tilde{C}_{16}N_{j,y}F_sN_{i,x}F_\tau dV \\
&+ \int_V \tilde{C}_{66}N_{j,y}F_sN_{i,y}F_\tau dV.
\end{aligned}
\tag{2.37}
$$

Note that in the above equations, the comma in the suffix denotes partial derivative.

Later, in Section 2.9, numerical integration will be discussed. As of now, the reader should know that when straight-fibre composites are considered, the $\tilde{\mathbf{C}}$ matrix is constant within the lamina and can be extracted from the integral. However, in the case of tow-steered composites, the lamination angle is no longer constant in each ply, and thus $\tilde{\mathbf{C}}$ needs to be kept within the integral.

2.7 Free vibration analysis

The undamped free vibration problem can be written as follows:

$$\mathbf{M}\ddot{\mathbf{q}} + \mathbf{K}\mathbf{q} = 0 \tag{2.38}$$

where $\mathbf{M}$ and $\mathbf{K}$ are the structure's mass and stiffness matrices, respectively. They are obtained by looping over the FN's indices i, j, τ and s of the single FE. By imposing an harmonic solution as $\mathbf{q} = \tilde{\mathbf{q}} e^{i\omega t}$, Eq. (2.38) is expressed as the following eigenvalue problem:

$$\left(\mathbf{K} - \omega_i^2 \mathbf{M}\right) \tilde{\mathbf{q}}_i = 0 \tag{2.39}$$

where ω_i and $\tilde{\mathbf{q}}_i$ are the i^{th} natural frequency and eigenvector, respectively.

2.8 Buckling analysis

The buckling analysis consists of solving the following equation:

$$|\mathbf{K}_T| = 0, \tag{2.40}$$

in which $\mathbf{K}_T$ is the tangent stiffness matrix of the structure. The expression for this matrix is derived by linearising the virtual variation of the internal strain energy:

$$\delta^2(\mathscr{L}_{int}) = \int_V \delta\left(\delta\boldsymbol{\varepsilon}^T \boldsymbol{\sigma}\right) dV = \int_V \left[\delta\left(\delta\boldsymbol{\varepsilon}^T\right)\boldsymbol{\sigma} + \delta\boldsymbol{\varepsilon}^T \delta\boldsymbol{\sigma}\right] dV \tag{2.41}$$

Substituting Eq. (2.25), the constitutive law, and the geometrical relations between strains and displacements, the previous equation can be rewritten as follows:

$$\delta^2(\mathscr{L}_{int}) = \delta\mathbf{q}_{sj}^T \mathbf{k}_T^{ij\tau s} \delta\mathbf{q}_{\tau i} = \delta\mathbf{q}_{sj}^T \left(\mathbf{k}^{ij\tau s} + \mathbf{k}_\sigma^{ij\tau s} + \mathbf{k}_{T_1}^{ij\tau s}\right) \delta\mathbf{q}_{\tau i} \tag{2.42}$$

where $\mathbf{k}_\sigma^{ij\tau s}$ and $\mathbf{k}_{T_1}^{ij\tau s}$ denote the 3×3 FN of the geometric stiffness matrix and the nonlinear contribution to the tangent matrix, respectively. The former strictly depends on the internal stress state of the structure. It is worth recalling that the stress state depends on the model's accuracy. This thesis does not report the equations that allow computing the tangent stiffness matrix but can be found in [105]. Linearised buckling analyses are performed under the following assumptions:

- The pre-buckling deformation can be neglected.
- The initial stress remains constant and varies neither in magnitude nor in direction during buckling.

- At bifurcation, the equilibrium states are infinitesimally adjacent so that a linearisation is possible.

Under these hypothesis, the buckling load can then be defined via a scalar load factor λ such that $\boldsymbol{\sigma} = \lambda \boldsymbol{\sigma}_0$. At bifurcation, there exists a critical value λ_{cr} of the load factor for which an equilibrium configuration exists where:

$$|\mathbf{K} + \lambda_{cr}\mathbf{K}_\sigma| = 0 \tag{2.43}$$

in which $\mathbf{K}_\sigma$ denotes the assembled geometric stiffness matrix of the structure.

2.9 Numerical calculation of FE integrals considering VAT composites

In the case of materials whose properties do not vary spatially, as it would happen with isotropic materials or straight-fibre composites, the components of the material stiffness matrix are constant within the integration volume V and they can be removed from the integrals in Eq. (2.34).

The integration of the FN integrals for the 1D case foresees the calculation of two integrals: one in the beam axis direction, and another over the beam's cross-section. In this context, the fourth term of $k_{xx}^{ij\tau s}$ can be split into:

$$\tilde{C}_{16} \int_A F_{\tau,x} F_s dA \int_l N_{j,y} N_i dy \tag{2.44}$$

where A is the cross-section area, and l is the length of the beam. If normalised coordinates ξ and ν are accounted for the cross-section, and η is considered for the beam axis, the above integral can be computed independently of the actual geometry of the beam. For instance, if a quadrilateral subdomain is considered over the cross-section, the following arises:

$$\int_A F_{\tau,x} F_s dx dz = \int_{-1}^{1} \int_{-1}^{1} F_{\tau,\xi} F_s |J^{2D}| d\xi d\eta \tag{2.45}$$

where $|J^{2D}|$ is the Jacobian determinant of the transformation. Partial derivatives have to be computed with respect to the normalised coordinates according to the chain rule as follows:

$$\begin{aligned} \frac{\partial F_\tau}{\partial x} &= \frac{\partial F_\tau}{\partial \xi}\frac{\partial \xi}{\partial x} + \frac{\partial F_\tau}{\partial \nu}\frac{\partial \nu}{\partial x} \\ \frac{\partial F_\tau}{\partial z} &= \frac{\partial F_\tau}{\partial \xi}\frac{\partial \xi}{\partial z} + \frac{\partial F_\tau}{\partial \nu}\frac{\partial \nu}{\partial z} \end{aligned} \tag{2.46}$$

The evaluation of Eq. (2.46) requires knowing $\xi = \xi(x,z)$ and $\nu = \nu(x,z)$. These explicit relations are often difficult to establish and, therefore, it is preferable to use the chain rule as:

$$\begin{aligned} \frac{\partial F_\tau}{\partial \xi} &= \frac{\partial F_\tau}{\partial x}\frac{\partial x}{\partial \xi} + \frac{\partial F_\tau}{\partial z}\frac{\partial z}{\partial \xi} \\ \frac{\partial F_\tau}{\partial \nu} &= \frac{\partial F_\tau}{\partial x}\frac{\partial x}{\partial \nu} + \frac{\partial F_\tau}{\partial z}\frac{\partial z}{\partial \nu} \end{aligned} \tag{2.47}$$

Equation (2.47) can be rewritten in matrix form as follows:

$$\left\{ \begin{matrix} \frac{\partial F_\tau}{\partial \xi} \\ \frac{\partial F_\tau}{\partial \nu} \end{matrix} \right\} = \underbrace{\left[\begin{matrix} \frac{\partial x}{\partial \xi} & \frac{\partial z}{\partial \xi} \\ \frac{\partial x}{\partial \nu} & \frac{\partial z}{\partial \nu} \end{matrix} \right]}_{J^{2D}} \left\{ \begin{matrix} \frac{\partial F_\tau}{\partial x} \\ \frac{\partial F_\tau}{\partial z} \end{matrix} \right\} \tag{2.48}$$

Note that the steps above can compute the derivatives and Jacobian involving F_s terms.

Similarly, the integral of the shape functions along the beam axis from Eq. (2.44) can be computed as:

$$\int_l N_{j,y} N_i dy \tag{2.49}$$

where the term $N_{j,y}$ is computed as follows:

$$\frac{dN_j}{dy} = \frac{dN_j}{d\eta}\frac{d\eta}{dy} = \frac{1}{|J^{1D}|}\frac{dN_j}{d\eta} \tag{2.50}$$

being $|J^{1D}| = l/2$ is the Jacobian of the 1D transformation. Therefore, Eq. (2.49) can be computed in the natural reference frame in the following form:

$$\int_l N_{j,y} N_i dy = \int_{-1}^{1} N_{j,\eta} \frac{1}{|J^{1D}|} N_i |J^{1D}| d\eta = \int_{-1}^{1} N_{j,\eta} N_i d\eta \tag{2.51}$$

Then, by substituting Eqs. (2.45) and (2.51) into Eq. (2.44), the fourth term of $k_{xx}^{ij\tau s}$ is rewritten as follows:

$$\tilde{C}_{16} \int_{-1}^{1}\int_{-1}^{1} F_{\tau,\xi} F_s |J^{2D}| d\xi d\eta \int_{-1}^{1} N_{j,\eta} N_i d\eta \tag{2.52}$$

In the case of 2D models, when calculating the FN integrals, the domain is split into the structure's midplane and the thickness direction. In this regard, the fourth term of $k_{xx}^{ij\tau s}$ of Eq. (2.34) can be written as follows:

$$\tilde{C}_{16} \int_t F_\tau F_s dz \int_\Omega N_{j,y} N_{i,x} d\Omega \tag{2.53}$$

where t is the thickness, and Ω is the midplane area. The normalised coordinates ξ and η are accounted for the midplane, and ν is considered for the thickness direction. If a quadrilateral element is utilised for the midplane discretisation, the following arises:

$$\int_{\Omega} N_{j,y} N_{i,x} dxdy = \int_{-1}^{1}\int_{-1}^{1} N_{j,\eta} N_{i,\xi} |J^{2D}| d\xi d\eta \tag{2.54}$$

The partial derivatives need to be calculated with respect to the normalised coordinates through the chain rule as follows:

$$\begin{aligned} \frac{\partial N_i}{\partial x} &= \frac{\partial N_i}{\partial \xi}\frac{\partial \xi}{\partial x} + \frac{\partial N_i}{\partial \eta}\frac{\partial \eta}{\partial x} \\ \frac{\partial N_i}{\partial y} &= \frac{\partial N_i}{\partial \xi}\frac{\partial \xi}{\partial y} + \frac{\partial N_i}{\partial \nu}\frac{\partial \nu}{\partial y} \end{aligned} \tag{2.55}$$

which requires knowing $\xi = \xi(x,y)$ and $\eta = \eta(x,y)$ beforehand. Knowing those explicit relations is seldom easy and, thus, is preferable to use the chain rule as:

$$\begin{Bmatrix} \frac{\partial N_i}{\partial \xi} \\ \frac{\partial N_i}{\partial \eta} \end{Bmatrix} = \underbrace{\begin{bmatrix} \frac{\partial x}{\partial \xi} & \frac{\partial y}{\partial \xi} \\ \frac{\partial x}{\partial \eta} & \frac{\partial y}{\partial \eta} \end{bmatrix}}_{J^{2D}} \begin{Bmatrix} \frac{\partial N_i}{\partial x} \\ \frac{\partial N_i}{\partial y} \end{Bmatrix} \tag{2.56}$$

These derivation above can be implemented straightforwardly for the case of N_j.

The integral of the expansion functions along the plate thickness from Eq. (2.53) is computed as:

$$\int_{l} F_\tau F_s dz = \int_{-1}^{1} F_\tau F_s |J^{1D}| d\nu \tag{2.57}$$

being $|J^{1D}| = t/2$ the Jacobian of the 1D transformation in the thickness direction. Last, by incorporating Eqs. (2.54) and (2.57) into Eq. (2.53), one has:

$$\tilde{C}_{16} \int_{-1}^{1} F_\tau F_s |J^{1D}| d\nu \int_{-1}^{1}\int_{-1}^{1} N_{j,\eta} N_{i,\xi} |J^{2D}| d\xi d\eta \tag{2.58}$$

2.9.1 Gaussian quadrature

The Gaussian quadrature approximates the integral of a function in the $\xi \in [-1,1]$ domain with the sum of the values of the function evaluated at the i^{th} Gauss point, $f(\xi_i)$, multiplied by a weight w_i. This reads mathematically as:

$$\int_{-1}^{1} f(\xi) d\xi \approx \sum_{i=0}^{n_{gp}} w_i f(\xi_i) \tag{2.59}$$

in which n_{gp} denotes the number of Gauss points where the function f is evaluated. The Gauss quadrature can also be extended for the integration over surfaces:

$$\int_{-1}^{1}\int_{-1}^{1} f(\xi,\eta)d\xi d\eta \approx \sum_{i=1}^{n_{gp}^{i}}\sum_{m=1}^{n_{gp}^{m}} w_i w_m f(\xi_i,\eta_m) \tag{2.60}$$

As the reader can observe, the above expressions present an approximation sign $\approx$. However, this sign can turn into an equal if the appropriate number of Gauss points is used and the integrand functions is a polynomial. Given a number of Gauss points n_{gp}, a polynomial of order at most $(2n_{gp}-1)$ is integrated exactly. As a consequence, given a polynomial function of order p, the minimum number of Gauss points necessary to calculate exactly the integral is given by:

$$n_{gp} = 1 + \left\lfloor \frac{p}{2} \right\rfloor \tag{2.61}$$

where $\lfloor\cdot\rfloor$ indicates the floor function. The Gauss point can be defined as the roots of the Legendre polynomials:

$$P_n(z) = \frac{1}{2\pi i}\oint (1-2tz+t^2)^{-1/2} t^{-n-1} dt \tag{2.62}$$

and the weights are derived using the following equation:

$$w_i = \frac{2}{(1-x_i^2)[P_n'(x_i)]^2} \tag{2.63}$$

Following the previous reasoning, the computation of the integrals from Eqs. (2.52) and (2.58) is made as follows:

1D case:

$$\begin{aligned}
&\tilde{C}_{16}\int_A F_{\tau,x}F_s dA \int_l N_i N_{j,y} dl = \\
&\tilde{C}_{16}\int_{-1}^{1}\int_{-1}^{1} F_{\tau,\xi}F_s |J^{2D}| d\xi d\nu \int_{-1}^{1} N_i N_{j,\eta} |J^{1D}| d\eta \approx \\
&\tilde{C}_{16}\sum_{l=1}^{n_{gp}^{l}}\sum_{n=1}^{n_{gp}^{n}} F_{\tau,\xi}(\xi_l,\nu_n) F_s(\xi_l,\nu_n) |J^{2D}(\xi_l,\nu_n)| w_l w_n \\
&\sum_{m=1}^{n_{gp}^{m}} N_i(\eta_m) N_{j,\eta}(\eta_m) |J^{1D}(\eta_m)| w_m
\end{aligned} \tag{2.64}$$

2D case:

$$\begin{aligned}
&\tilde{C}_{16}\int_t F_\tau F_s dz \int_\Omega N_{i,x}N_{j,y}d\Omega = \\
&\tilde{C}_{16}\int_{-1}^{1} F_\tau F_s |J^{1D}| d\nu \int_{-1}^{1}\int_{-1}^{1} N_{i,\xi}N_{j,\eta}|J^{2D}|d\xi d\eta \approx \\
&\tilde{C}_{16}\sum_{n=1}^{n_{gp}^n} F_\tau(\nu_n)F_s(\nu_n)|J^{1D}(\nu_n)|w_n \\
&\sum_{l=1}^{n_{gp}^l}\sum_{m=1}^{n_{gp}^m} N_{i,\xi}(\xi_l,\eta_m)N_{j,\eta}(\xi_l,\eta_m)|J^{2D}(\xi_l,\eta_m)|w_l w_m
\end{aligned} \tag{2.65}$$

The calculation of the above integrals will be exact depending on the number of Gauss points used for each of the integrals. If the 1D case uses as F_τ bi-linear Lagrange polynomials, the maximum polynomial order of an integral in the cross-section is provided by $\int_A F_\tau F_s dA$, and equals four. Therefore, $n_{gp}^l = n_{gp}^n = 2$ are necessary to compute exactly the integral over the cross-section. If the 1D model uses as N_i cubic Lagrange polynomials, the maximum polynomial order is given by $\int_l N_i N_j dl$ and equals six. Hence, a total of $n_{gp}^m = 4$ Gauss points are needed to compute the exact value of the integral along the beam axis. A similar reasoning is made when 2D structures are involved.

So far, the effect of VAT composites on the computation of the integrals has not been discussed, as the coefficients of the material stiffness matrix have been assumed constant across the volume of integration. In the case of tow-steered composites, these coefficients vary pointwise across the in-plane domain and need to be included into the integrals, yielding:

$$\begin{aligned}
&\text{1D case:} \quad \int_V \tilde{C}_{16}(x,y)F_{\tau,x}F_s N_i N_{j,y} dV \\
&\text{2D case:} \quad \int_V \tilde{C}_{16}(x,y)F_\tau F_s N_{i,x}N_{j,y}dV = \int_t F_\tau F_s dz \int_\Omega \tilde{C}_{16}(x,y)N_{i,x}N_{j,y}d\Omega
\end{aligned} \tag{2.66}$$

Note that in the 1D case, the integral cannot be split into beam axis and cross-section integrals given the dependency of $\tilde{C}_{16}$ on the x and y coordinates, which are related to the cross-section and beam axis integrals, respectively. Thus, for the 1D case a 3D integral needs to be performed. On the opposite side, when a 2D model is considered, the through-the-thickness integrals can be computed independently from the midplane integrals, which includes the material stiffness matrix coefficient. The numerical

computation of the integrals is carried out by Gaussian quadrature as follows:

$$
\begin{aligned}
&\text{1D case:}\\
&\int_{-1}^{1}\int_{-1}^{1}\int_{-1}^{1} F_{\tau,\xi}\tilde{C}_{16}F_s N_i N_{j,\eta}|J^{2D}||J^{1D}|d\eta d\xi d\nu \approx\\
&\sum_{l=1}^{n_{gp}^{l}}\sum_{n=1}^{n_{gp}^{n}}\sum_{m=1}^{n_{gp}^{m}} \tilde{C}_{16}(\xi_l,\eta_m,\nu_n)F_{\tau,\xi}(\xi_l,\nu_n)F_s(\xi_l,\nu_n)N_i(\eta_m)N_{j,\eta}(\eta_m)\\
&|J^{2D}(\xi_l,\nu_n)||J^{1D}(\eta_m)|w_l w_n w_m\\
&\text{2D case:}\\
&\int_{-1}^{1} F_\tau F_s|J^{1D}|d\nu \int_{-1}^{1}\int_{-1}^{1} \tilde{C}_{16}N_{i,\xi}N_{j,\eta}|J^{2D}|d\xi d\eta \approx\\
&\sum_{n=1}^{n_{gp}^{n}} F_\tau(\nu_n)F_s(\nu_n)|J^{1D}(\nu_n)|w_n\\
&\sum_{l=1}^{n_{gp}^{l}}\sum_{m=1}^{n_{gp}^{m}} \tilde{C}_{16}(\xi_l,\eta_m)N_{i,\xi}(\xi_l,\eta_m)N_{j,\eta}(\xi_l,\eta_m)|J^{2D}(\xi_l,\eta_m)|w_l w_m
\end{aligned}
\tag{2.67}
$$

An adequate number of Gauss points are needed to calculate exactly the integrals. The number of points depends on the order of the polynomial function one aims to integrate. In the case of classical laminates, the number of points is easily determined by knowing the order of the shape and expansion functions used. However, when VAT laminates are involved, apart from the shape and expansion functions, one has to consider the material stiffness coefficient, which order is not known a priori. These coefficients depend on the rotation matrix $\mathbf{T}(x,y)$, which involves trigonometric functions of the local fibre orientation and is evaluated at the Gauss integration points. Besides, the fibre orientation follows a polynomial law. This means that the Gauss integration will always be approximative and never exact since the Gauss approximation is exact only for polynomial functions. Therefore, the number of Gauss points needs to be increased to better approximate the integrals. Based on the author's experience, the number of integration points for the VAT case is $n_{gp}^{\mathrm{VAT}} = n_{gp}^{\mathrm{CL}} + 2$, being n_{gp}^{CL} the number of Gauss points for classical laminates, which is obtained from Eq. (2.61).

Chapter 3

High-order multiple scales modelling

This chapter is devoted to the mathematical derivation of high-order models for composite multiscale applications. In particular, embedded finite element mesoscale and microscale models based on the Mechanics of Structure Genome (MSG) are described and incorporated within the CUF framework. These multiscale techniques rely on the Component-Wise (CW) approach introduced in [106]. The CW strategy permits alleviating the computational cost related to multi-component and/or multiscale structures. In classical modelling strategies, different structural components are modelled through various element types, e.g., beams, shells or solids. Instead, the CW method allows modelling all the multiple constituents with the same kind of finite element. In particular, this research foresees the usage of 1D FE. The CW approach enables the tuning of the capabilities of the model by (i) choosing the component that requires a more detailed model and (ii) setting the order of the structural model to be used. In addition, the FE mathematical models can be built using only physical boundaries, as beam axes or plate/shell reference surfaces are no longer necessary.

3.1 Embedded mesoscale models

Despite the significant advancement in FE modelling, the classic CW approach foresees the continuity of the displacements at the constituents interface by properly discretising the shared nodes of the different components, as illustrated in Fig 3.1a. On the other hand, with the embedded CW, the constituents' meshes do not need to match. Instead, a differentiation between host and embedded elements is considered, as shown in Fig. 3.1b. These aspects are explained in the following.

The classical embedded finite element method superimposes an embedded mesh onto a host grid without modifying the volume of the host element to account for the space that the embedded mesh occupies. The classical FE method is based on energy

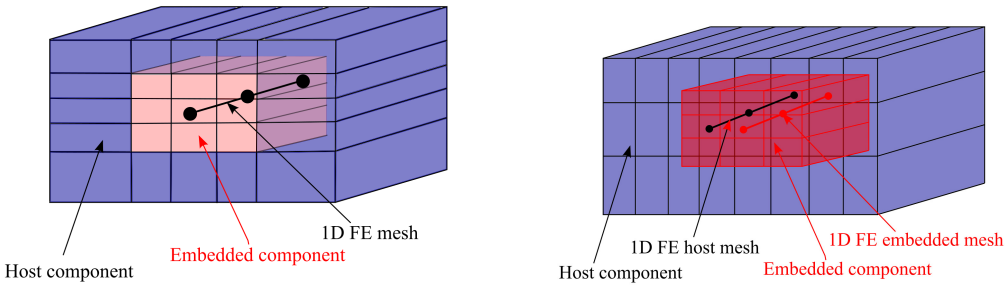

(a) Conforming mesh. **(b)** Host and embedded meshes.

Figure 3.1 Representation of a generic reinforced structure using two meshing approaches: (a) Conforming meshes and (b) Host (black) and embedded (red) meshes. In (a), both constituents share the same FE discretisation and cross-section, whereas in (b), two different FE meshes and cross-sections are used.

methods in which the internal energy of an element is approximated by an integral of the strain energy over the element volume. The same occurs when approximating the inertial energy, in which the mesh mass is calculated as a volume integral of the material density. Because of the extra volume of the embedded element, there is an increase in inertia and strain energy, which lately affects the system solution [107]. In this regard, the integral over the host component should not consider the volume occupied by the embedded part to avoid volume redundancy. Therefore, the virtual variations of the internal and inertial energies from Eqs. (2.27) and (2.29) can be reformulated as:

$$\delta\mathscr{L}_{\text{int}} = \underbrace{\int_{V_H} \delta\boldsymbol{\varepsilon}^{h^T}\boldsymbol{\sigma}^h dV_H}_{\text{Host strain energy}} + \underbrace{\int_{V_E} \delta\boldsymbol{\varepsilon}^{e^T}\boldsymbol{\sigma}^e dV_E}_{\text{Embedded strain energy}} - \underbrace{\int_{V_E} \delta\boldsymbol{\varepsilon}^{h^T}\boldsymbol{\sigma}^h dV_E}_{\text{Redundant host strain energy}}, \tag{3.1}$$

$$\delta\mathscr{L}_{\text{ine}} = \underbrace{\int_{V_H} \delta\mathbf{u}^{h^T}\rho^h\ddot{\mathbf{u}}^h dV_H}_{\text{Host kinetic energy}} + \underbrace{\int_{V_E} \delta\mathbf{u}^{e^T}\rho^e\ddot{\mathbf{u}}^e dV_E}_{\text{Embedded kinetic energy}} - \underbrace{\int_{V_E} \delta\mathbf{u}^{h^T}\rho^h\ddot{\mathbf{u}}^h dV_E}_{\text{Redundant host kinetic energy}}. \tag{3.2}$$

The displacement degrees of freedom of the embedded elements must be tied to those of the host element to avoid slipping between the host and embedded nodes. For doing so, the displacements in the embedded nodes are interpolated from the displacements of the host nodes via the host shape and expansion functions as:

$$\mathbf{u}^e_{e_j} = \sum_k N_i^{h_k}(y_{e_j}) F_\tau^{h_k}(x_{e_j}, z_{e_j})\mathbf{u}^h_{h_k}, \tag{3.3}$$

where h_k is the k^{th} node of the host grid, and e_j is the j^{th} node of the embedded grid. $N_i^{h_k}$ and $F_\tau^{h_k}$ are the shape function and expansion function of h_k, and $(x_{e_j}, y_{e_j}, z_{e_j})$ are

the coordinates of e_j. Equation (3.3) can be rewritten in a compact form as follows:

$$\mathbf{u}^e = \mathbf{w}^T \mathbf{u}^h. \tag{3.4}$$

where $\mathbf{u}^e$ and $\mathbf{u}^h$ are the displacement unknown vectors of the embedded and host parts, respectively, and $\mathbf{w}$ is the assembled interpolation matrix resulting from Eq. (3.3). Rearranging Eqs. (3.1) and (3.2), and recalling that $\boldsymbol{\sigma}^h = \mathbf{C}^h \boldsymbol{\varepsilon}^h$ and $\boldsymbol{\sigma}^e = \mathbf{C}^e \boldsymbol{\varepsilon}^e$, yields:

$$\begin{aligned}
&\delta \mathscr{L}_{\text{int}} = \int_{V_H} \delta \boldsymbol{\varepsilon}^{h^T} \mathbf{C}^h \boldsymbol{\varepsilon}^h dV_H + \int_{V_E} \delta \boldsymbol{\varepsilon}^{e^T} (\mathbf{C}^e - \mathbf{C}^h) \boldsymbol{\varepsilon}^e dV_E = \\
&\delta \mathbf{u}_{sj}^{h^T} \int_{V_H} \mathbf{B}(N_j^h F_s^h) \mathbf{C}^h \mathbf{B}(N_i^h F_\tau^h) \mathbf{u}_{\tau i}^h dV_H + \delta \mathbf{u}_{sj}^{e^T} \int_{V_E} \mathbf{B}(N_j^e F_s^e)(\mathbf{C}^h - \mathbf{C}^e) \mathbf{B}(N_i^e F_\tau^e) \mathbf{u}_{\tau i}^e dV_E = \\
&\delta \mathbf{u}_{sj}^{h^T} \mathbf{k}^{h,ij\tau s} \mathbf{u}_{\tau i}^h + \delta \mathbf{u}_{sj}^{e^T} \mathbf{k}^{e,ij\tau s} \mathbf{u}_{\tau i}^e,
\end{aligned} \tag{3.5}$$

$$\begin{aligned}
&\delta \mathscr{L}_{\text{ine}} = \int_{V_H} \delta \mathbf{u}^{h^T} \rho^h \ddot{\mathbf{u}}^h dV_H + \int_{V_E} \delta \mathbf{u}^{e^T} (\rho^e - \rho^h) \ddot{\mathbf{u}}^e dV_E = \\
&\delta \mathbf{u}_{sj}^{h^T} \int_{V_H} \mathbf{I} N_i^h N_j^h F_\tau^h F_s^h \rho^h \ddot{\mathbf{u}}_{\tau i}^h dV_H + \delta \mathbf{u}_{sj}^{e^T} \int_{V_E} \mathbf{I} N_i^e N_j^e F_\tau^e F_s^e (\rho^e - \rho^h) \ddot{\mathbf{u}}_{\tau i}^e dV_E = \\
&\delta \mathbf{u}_{sj}^{h^T} \mathbf{m}^{h,ij\tau s} \ddot{\mathbf{u}}_{\tau i}^h + \delta \mathbf{u}_{sj}^{e^T} \mathbf{m}^{e,ij\tau s} \ddot{\mathbf{u}}_{\tau i}^e,
\end{aligned} \tag{3.6}$$

in which $\mathbf{k}^{h,ij\tau s}$, $\mathbf{k}^{e,ij\tau s}$, $\mathbf{m}^{h,ij\tau s}$ and $\mathbf{m}^{e,ij\tau s}$ are the stiffness and mass FN of the host and embedded components, respectively. Equations (3.5) and (3.6) can be expanded through the τ and s expansion indices, and the i and j FE indices to obtain the following expressions regarding the whole structure under consideration:

$$\delta \mathscr{L}_{\text{int}} = \delta \mathbf{u}^{h^T} \mathbf{K}^h \mathbf{u}^h + \delta \mathbf{u}^{e^T} \mathbf{K}^e \mathbf{u}^e \tag{3.7}$$

$$\delta \mathscr{L}_{\text{ine}} = \delta \mathbf{u}^{h^T} \mathbf{M}^h \ddot{\mathbf{u}}^h + \delta \mathbf{u}^{e^T} \mathbf{M}^e \ddot{\mathbf{u}}^e \tag{3.8}$$

Introducing Eq. (3.4) into Eqs. (3.7) and (3.8), the virtual variation of the internal and inertial work can be expressed as follows:

$$\delta \mathscr{L}_{\text{int}} = \delta \mathbf{u}^{h^T} \left(\mathbf{K}^h + \mathbf{w} \mathbf{K}^e \mathbf{w}^T \right) \mathbf{u}^h \tag{3.9}$$

$$\delta \mathscr{L}_{\text{ine}} = \delta \mathbf{u}^{h^T} \left(\mathbf{M}^h + \mathbf{w} \mathbf{M}^e \mathbf{w}^T \right) \ddot{\mathbf{u}}^h \tag{3.10}$$

Concerning the external forces acting on the whole structure, these will be applied directly to the host constituent unless volumetric forces are acting on the structure. Therefore, the virtual work of the external loading can be written as follows:

$$\delta \mathscr{L}_{\text{ext}} = \int_{V_H} \delta \mathbf{u}_{sj}^{h^T} \mathbf{P} N_j F_s |_{(x_p, y_p, z_p)} dV_H = \delta \mathbf{u}^{h^T} \mathbf{F}^{ext} \tag{3.11}$$

Last, considering all the terms stemming from the PVD applied to host and embedded components, one can get the following expression:

$$\left(\mathbf{M}^h + \mathbf{w}\mathbf{M}^e\mathbf{w}^T\right)\ddot{\mathbf{u}}^h + \left(\mathbf{K}^h + \mathbf{w}\mathbf{K}^e\mathbf{w}^T\right)\mathbf{u}^h = \mathbf{F}^{ext} \tag{3.12}$$

The methodology depicted above can be used to analyse tow-steered composite structures at the mesoscale. For instance, the actual fibre courses are described through beam elements embedded into a matrix region modelled by 1D or 2D elements. Figure 3.2 illustrates the fibre course-matrix ensemble, where the matrix acts as the host, and the fibre is the embedded component. The embedded CW is useful for predicting stress states in regions where gaps exist with no mesh limitations or the need for cumbersome meshing operations. Note that although 1D or 2D elements can be used as host grids, an L or LD expansion must be used to achieve a 3D-like representation of the host constituent, respectively. For instance, in Fig. 3.2, the matrix is modelled by straight 1D elements with Lagrange expansion, while the embedded fibre utilises curved 1D elements and Lagrange expansion. Current efforts are devoted to coupling host elements using LE and embedded employing TE to reduce the computational burden further. Of course, classic 3D FE can also be employed as the host grid.

3.2 Microscale models

This section is devoted to deriving the MSG governing equations for purely elastic heterogeneous solids. First, the assumptions of micromechanical analyses and the variational asymptotic method are applied to the repeated unit cell (RUC) problem. Subsequently, 1D high-order models are employed to solve the RUC problem, which in this thesis concerns the fibre-matrix scale. Later, an extension to tackle the thermoelasticity problem is reported. Note that tensorial notation is preferred to vectorial notation as operations between tensors and vectors are easier to describe.

3.2.1 Variational asymptotic method for the unit cell problem

Micromechanical analyses rely on a series of assumptions. The first one is that the size of the RUC is significantly smaller than the dimension of the global structure. This can be posed mathematically as $\mathbf{y} = \mathbf{x}/\delta$, with δ being a scaling parameter that characterises the size of the RUC, and $\mathbf{y}$ and $\mathbf{x}$ are the local and global reference systems of the RUC, respectively. The second assumption is that the loading and boundary conditions associated with the macroscale problem do not affect the effective material properties provided by the RUC analysis at the microscale. In addition,

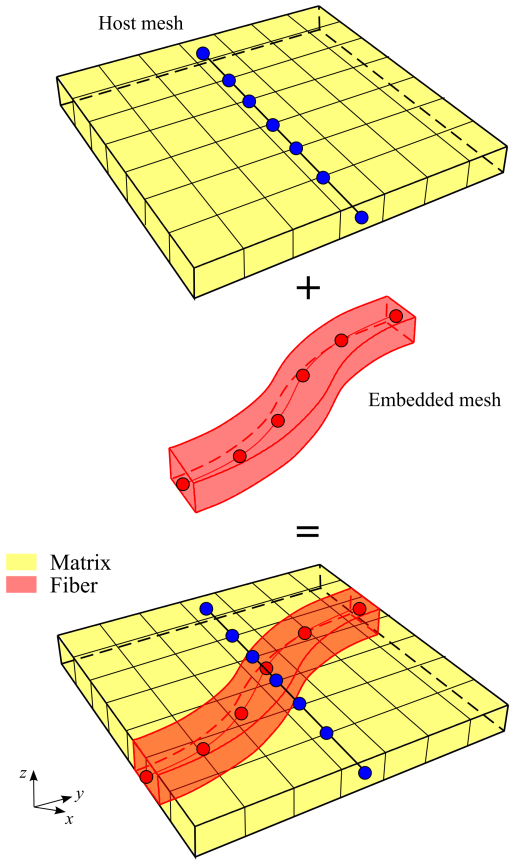

Figure 3.2 Representation of a fibre course embedded into a matrix component.

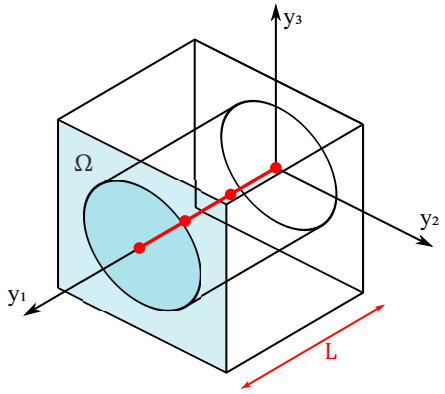

Figure 3.3 Local coordinate system for RUC problem.

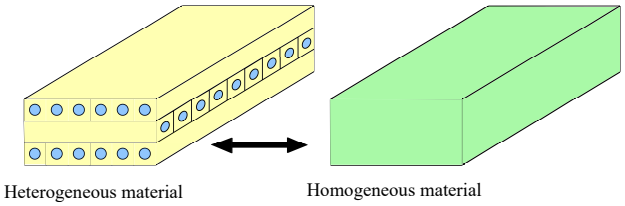

Figure 3.4 Representation of heterogeneous and homogenised material. The former accounts for the fibre and matrix material properties, whilst the latter uses the effective material properties.

the local solutions have an average value over the RUC corresponding to the global solution of the upper-scale problem. In the case of the displacement field $\mathbf{u}(\mathbf{x},\mathbf{y})$, this assumption reads as:

$$\bar{\mathbf{u}}(\mathbf{x}) = \frac{1}{V}\int_V \mathbf{u}(\mathbf{x};\mathbf{y})dV \tag{3.13}$$

where $\bar{\mathbf{u}}$ is the averaged displacements vector, which only depends on the global coordinates, $\mathbf{u}(\mathbf{x};\mathbf{y})$ is the local field of displacements, which depends on both global and local coordinates, and V is the volume associated to the RUC. Furthermore, periodic boundary conditions are applied to guarantee the compatibility of deformations relative to the neighbouring RUCs. They can be expressed as:

$$\begin{aligned} u_i(x_1,x_2,x_3;0,y_2,y_3) &= u_i(x_1+L_1,x_2,x_3;L_1,y_2,y_3) \\ u_i(x_1,x_2,x_3;y_1,0,y_3) &= u_i(x_1,x_2+L_2,x_3;y_1,L_2,y_3) \\ u_i(x_1,x_2,x_3;y_1,y_2,0) &= u_i(x_1,x_2,x_3+L_3;y_1,y_2,L_3), \end{aligned} \tag{3.14}$$

where L_i is the characteristic dimension of the RUC in the y_i direction as illustrated in Fig. 3.3.

According to MSG [108], by minimising the difference between the strain energies of the heterogeneous material and the homogenised one, shown in Fig. 3.4, one can retrieve the solution to the stationary value problem, expressed as the following

functional:

$$\Pi = \frac{1}{2}\left\langle C_{ijkl}\varepsilon_{ij}\varepsilon_{kl}\right\rangle - \frac{1}{2}\left(C^{*}_{ijkl}\bar{\varepsilon}_{ij}\bar{\varepsilon}_{kl}\right) \tag{3.15}$$

in which the first term refers to the strain energy of the heterogeneous composite represented by the RUC, whereas the second one is that of the homogenised material, and $\langle\cdot\rangle$ denotes the volume average. C_{ijkl} and ε_{ij} are the fourth-order elastic tensor and the second-order strain tensor, respectively. Likewise, C^{*}_{ijkl} and $\bar{\varepsilon}_{ij}$ are the fourth-order elastic tensor and second-order strain tensor of the homogenised material, respectively.

One can formulate the variational statement over a single RUC to not solve the stationary problem for every point in the global system $\mathbf{x}$. In this regard, one can express the field of displacements $\mathbf{u}$ as the sum of the global displacement $\bar{\mathbf{u}}$ plus the difference as:

$$\mathbf{u}(\mathbf{x};\mathbf{y}) = \bar{\mathbf{u}}(\mathbf{x}) + \delta\chi(\mathbf{x};\mathbf{y}), \tag{3.16}$$

where χ denotes the fluctuation functions about the global displacement and is scaled down by a δ factor.

Because of the differences in the coordinate systems of the scales that are relevant to the multiscale problem, one needs to calculate the derivative of a field of the type $\mathbf{u}(\mathbf{x},\mathbf{y})$ as:

$$\frac{\partial \mathbf{u}}{\partial x_j} + \frac{1}{\delta}\frac{\partial \mathbf{u}}{\partial y_j} \tag{3.17}$$

Thus, applying Eq. (3.17) to the derivatives of Eq. (3.16), the strain variables can be expressed as:

$$\varepsilon_{ij}(\mathbf{x};\mathbf{y}) = \bar{\varepsilon}_{ij}(\mathbf{x}) + \chi_{(i,j)}(\mathbf{x};\mathbf{y}) \tag{3.18}$$

in which

$$\bar{\varepsilon}_{ij}(\mathbf{x}) = \frac{1}{2}\left(\frac{\partial \bar{u}_i(\mathbf{x})}{\partial x_j} + \frac{\partial \bar{u}_j(\mathbf{x})}{\partial x_i}\right) \tag{3.19}$$

and

$$\chi_{(i,j)}(\mathbf{x};\mathbf{y}) = \frac{1}{2}\left(\frac{\partial \chi_i(\mathbf{x};\mathbf{y})}{\partial y_j} + \frac{\partial \chi_j(\mathbf{x};\mathbf{y})}{\partial y_i}\right) \tag{3.20}$$

Recalling Eq. (3.13), it can be written that $\bar{u}_i = \langle u_i\rangle$ and $\bar{\varepsilon}_{ij} = \langle\varepsilon_{ij}\rangle$. This implies that $\langle\chi_i\rangle = 0$ and $\langle\chi_{(i,j)}\rangle = 0$. Subsequently, employing the field of displacements and strain from Eqs. (3.16) and (3.18), and assuming the second term of (3.15) as constant, the unknown fluctuation terms can be retrieved by minimising the following functional:

$$\Pi^{*} = \frac{1}{2}\left\langle C_{ijkl}\left[\bar{\varepsilon}_{ij} + \chi_{(i,j)}\right]\left[\bar{\varepsilon}_{kl} + \chi_{(k,l)}\right]\right\rangle \tag{3.21}$$

3.2.2 Unified high-order finite beam elements for the unit cell problem

MSG can be utilised to solve a 3D problem with different elements varying over the three directions, such as particle-reinforced composites, or a 2D problem in which the phases vary within the plane, such as fibre-reinforced composites. Figure illustrates the local coordinate system of the RUC, using a square-pack microstructure as an example. The beam axis, with length L, coincides with the fibre direction y_1, while the $y_2 - y_3$ plane identifies the cross-section of the beam model Ω. In this research, 1D CUF-based models are employed to solve the RUC problem by assuming that the fluctuation unknowns can be expanded over the cross-section through arbitrary expansions F_τ depending on the cross-sectional coordinates as follows:

$$\chi(\mathbf{x}; y_1, y_2, y_3) = F_\tau(y_2, y_3)\chi_\tau(\mathbf{x}; y_1) \quad \tau = 1, ..., M \tag{3.22}$$

being M the number of expansion terms considered in the kinematic model.

The problem in the beam axis direction y_1 is solved by employing FEM. In this work, the fibre direction is discretised through 1D standard elements. Therefore, the generalised fluctuations unknowns $\chi_\tau(\mathbf{x}; y_1)$ are interpolated with Lagrange shape functions N_i on the y_1 direction as:

$$\chi_\tau(\mathbf{x}; y_1) = N_i(y_1)\chi_{\tau i}(\mathbf{x}) \quad i = 1, ..., N \tag{3.23}$$

where N represents the number of beam nodes and $\chi_{\tau i}(\mathbf{x})$ is the nodal unknown vector.

The global strains in the Voigt notation are written as:

$$\bar{\boldsymbol{\varepsilon}}^T = \{\bar{\varepsilon}_{11} \;\; \bar{\varepsilon}_{22} \;\; \bar{\varepsilon}_{33} \;\; 2\bar{\varepsilon}_{13} \;\; 2\bar{\varepsilon}_{23} \;\; 2\bar{\varepsilon}_{12}\} \tag{3.24}$$

and, thus, it is allowed to express the geometrical relations

$$\boldsymbol{\varepsilon} = \bar{\boldsymbol{\varepsilon}} + \mathbf{B}\chi, \tag{3.25}$$

being $\mathbf{B}$ the differential operator defined in Eq. (2.3).

Subsequently, stresses and strains are related, for the purely elastic case, by the Hooke's law as:

$$\boldsymbol{\sigma} = \mathbf{C}\boldsymbol{\varepsilon} \tag{3.26}$$

where $\mathbf{C}$ is the 6×6 material matrix condensed from the fourth-order tensor C_{ijkl}.

The functional in Eq. (3.21) can be rewritten as:

$$\Pi^* = \frac{1}{2}\int_V (\bar{\boldsymbol{\varepsilon}} + \mathbf{B}\chi)^T \mathbf{C}\,(\bar{\boldsymbol{\varepsilon}} + \mathbf{B}\chi)\,dV \tag{3.27}$$

Periodic boundary conditions are applied to the RUC. In detail, these are applied on the sides of the cross-section ($\chi_\tau^+ = \chi_\tau^-$) and on the sections orthogonal to the fibre direction ($\chi_{\tau 1} = \chi_{\tau n}$). Then, substituting Eq. (3.23) into Eq. (3.22), and the latter into Eq. (3.27), the functional Π^* reads in CUF form as:

$$\Pi^* = \frac{1}{2}\left(\chi_{sj}^T \mathbf{E}^{\tau sij}\chi_{\tau i} + 2\chi_{sj}^T \mathbf{D}_{h\varepsilon}^{sj}\bar{\boldsymbol{\varepsilon}} + \bar{\boldsymbol{\varepsilon}}^T \mathbf{D}_{\varepsilon\varepsilon}\bar{\boldsymbol{\varepsilon}}\right) \tag{3.28}$$

where

$$\mathbf{E}^{\tau sij} = \int_\Omega\int_l (\mathbf{B}(F_s N_j \mathbf{I}))^T \mathbf{C}\mathbf{B}(F_\tau N_i \mathbf{I})\,d\Omega dy_1 \qquad \mathbf{D}_{h\varepsilon}^{sj} = \int_\Omega\int_l (\mathbf{B}(F_s N_j \mathbf{I}))^T \mathbf{C}\,d\Omega dy_1$$
$$\mathbf{D}_{\varepsilon\varepsilon} = \int_V \mathbf{C}\,dV \tag{3.29}$$

being $\mathbf{I}$ the 3×3 identity matrix. $\mathbf{E}^{\tau sij}$ and $\mathbf{D}_{h\varepsilon}^{sj}$ are the 3×3 and 3×6 fundamental nuclei of the purely elastic RUC problem, which contain the complete details related to the structural problem. In addition, $\mathbf{D}_{\varepsilon\varepsilon}$ is the averaged stiffness matrix of the material. Lately, one can calculate the assembled $\mathbf{E}$ and $\mathbf{D}_{h\varepsilon}$ matrices for the RUC problem by looping throughout the τ, s, i and j indices. The explicit equations of the $\mathbf{E}^{\tau sij}$ FN are already available in Eq. (2.34). The extended form of the eighteen components of $\mathbf{D}_{h\varepsilon}^{sj}$ are reported in the following:

$$\begin{aligned}
D_{h\varepsilon,11}^{sj} &= C_{11}\int_l N_j dy_1 \int_A F_{s,x} dA + C_{16}\int_l N_{j,y} dy_1 \int_A F_s dA \\
D_{h\varepsilon,12}^{sj} &= C_{12}\int_l N_j dy_1 \int_A F_{s,x} dA + C_{26}\int_l N_{j,y} dy_1 \int_A F_s dA \\
D_{h\varepsilon,13}^{sj} &= C_{13}\int_l N_j dy_1 \int_A F_{s,x} dA + C_{36}\int_l N_{j,y} dy_1 \int_A F_s dA \\
D_{h\varepsilon,14}^{sj} &= C_{44}\int_l N_j dy_1 \int_A F_{s,z} dA \qquad D_{h\varepsilon,15}^{sj} = C_{45}\int_l N_j dy_1 \int_A F_{s,z} dA \\
D_{h\varepsilon,16}^{sj} &= C_{16}\int_l N_j dy_1 \int_A F_{s,x} dA + C_{66}\int_l N_{j,y} dy_1 \int_A F_s dA \\
D_{h\varepsilon,21}^{sj} &= C_{12}\int_l N_{j,y} dy_1 \int_A F_s dA + C_{16}\int_l N_j dy_1 \int_A F_{s,x} dA \\
D_{h\varepsilon,22}^{sj} &= C_{22}\int_l N_{j,y} dy_1 \int_A F_s dA + C_{26}\int_l N_j dy_1 \int_A F_{s,x} dA \\
D_{h\varepsilon,23}^{sj} &= C_{23}\int_l N_{j,y} dy_1 \int_A F_s dA + C_{36}\int_l N_j dy_1 \int_A F_{s,x} dA
\end{aligned} \tag{3.30}$$

$$
\begin{aligned}
D^{sj}_{h\varepsilon,24} &= C_{45}\int_l N_j dy_1 \int_A F_{s,z} dA \quad D^{sj}_{h\varepsilon,25} = C_{55}\int_l N_j dy_1 \int_A F_{s,z} dA \\
D^{sj}_{h\varepsilon,26} &= C_{26}\int_l N_{j,y} dy_1 \int_A F_s dA + C_{66}\int_l N_j dy_1 \int_A F_{s,x} dA \\
D^{sj}_{h\varepsilon,31} &= C_{13}\int_l N_j dy_1 \int_A F_{s,z} dA \quad D^{sj}_{h\varepsilon,32} = C_{23}\int_l N_j dy_1 \int_A F_{s,z} dA \\
D^{sj}_{h\varepsilon,33} &= C_{33}\int_l N_j dy_1 \int_A F_{s,z} dA \\
D^{sj}_{h\varepsilon,34} &= C_{44}\int_l N_j dy_1 \int_A F_{s,x} dA + C_{45}\int_l N_{j,y} dy_1 \int_A F_s dA \\
D^{sj}_{h\varepsilon,35} &= C_{45}\int_l N_j dy_1 \int_A F_{s,x} dA + C_{55}\int_l N_{j,y} dy_1 \int_A F_s dA \\
D^{sj}_{h\varepsilon,36} &= C_{36}\int_l N_j dy_1 \int_A F_{s,z} dA
\end{aligned}
\tag{3.31}
$$

The fluctuation unknowns that minimise the functional in Eq. (3.28) can be computed by solving the linear system of equations:

$$\mathbf{E}\boldsymbol{\chi} = -\mathbf{D}_{h\varepsilon}\bar{\boldsymbol{\varepsilon}} \tag{3.32}$$

Assuming that the fluctuation is linearly proportional to $\bar{\boldsymbol{\varepsilon}}$, i.e.:

$$\boldsymbol{\chi} = \boldsymbol{\chi}_0\bar{\boldsymbol{\varepsilon}} \tag{3.33}$$

and plugging it into Eq. (3.32), one obtains the following linear system:

$$\mathbf{E}\boldsymbol{\chi}_0 = -\mathbf{D}_{h\varepsilon} \tag{3.34}$$

where $\boldsymbol{\chi}_0$ is a 3×6 matrix. Last, substituting Eq. (3.33) into Eq. (3.27), one can calculate

$$\Pi^* = \frac{1}{2}\bar{\boldsymbol{\varepsilon}}^T\mathbf{C}^*\bar{\boldsymbol{\varepsilon}} \tag{3.35}$$

being

$$\mathbf{C}^* = \frac{1}{\Omega}\left[\boldsymbol{\chi}_0^T\mathbf{D}_{h\varepsilon} + \mathbf{D}_{\varepsilon\varepsilon}\right] \tag{3.36}$$

where $\bar{\boldsymbol{\varepsilon}}$ denotes the global strains and $\mathbf{C}^*$ is the matrix containing the elastic coefficients of the equivalent material. Moreover, $\mathbf{D}_{h\varepsilon}$ and $\mathbf{D}_{\varepsilon\varepsilon}$ are the assembled arrays of their aforementioned fundamental nuclei.

By reintroducing the fluctuation solutions into the geometrical and constitutive relations, the local fields over the RUC can be derived. Recall that the complete

solution to the fluctuation function is:

$$\chi = \chi_0 \bar{\boldsymbol{\varepsilon}} \tag{3.37}$$

As a consequence, the local strain field becomes:

$$\boldsymbol{\varepsilon} = \bar{\boldsymbol{\varepsilon}} + \mathbf{B}(F_\tau N_i \chi), \tag{3.38}$$

and using Hooke's law, the local stress field of the original heterogeneous material is computed as:

$$\boldsymbol{\sigma} = \mathbf{C}\boldsymbol{\varepsilon} \tag{3.39}$$

3.2.3 Extension to the thermo-elastic unit cell problem

The mathematical derivation of the thermo-elastic unit cell equations is made in this part. Note the hypothesis mentioned in Section 3.2.1 holds. Of course, additional terms due to the thermal effects must be included in the functional from Eq. (3.15). Indeed, it now reads as follows:

$$\Pi = \frac{1}{2}\left\langle C_{ijkl}\varepsilon_{ij}\varepsilon_{kl} + 2\beta_{ij}\varepsilon_{ij}\theta + c_v\frac{\theta^2}{T_0}\right\rangle - \frac{1}{2}\left(C^*_{ijkl}\bar{\varepsilon}_{ij}\bar{\varepsilon}_{kl} + 2\beta^*_{ij}\bar{\varepsilon}_{ij}\theta + c^*_v\frac{\theta^2}{T_0}\right) \tag{3.40}$$

where β_{ij} is the second-order thermal strain tensor, T_0 is the reference temperature at which there exists a stress-free condition, c_v is the specific heat per unit volume at constant volume, and θ represents the difference between the current temperature and T_0.

Following the procedure from Eq. (3.16) to Eq. (3.20), Eq. (3.21) can be rewritten as:

$$\Pi^* = \frac{1}{2}\left\langle C_{ijkl}\left[\bar{\varepsilon}_{ij} + \chi_{(i,j)}\right]\left[\bar{\varepsilon}_{kl} + \chi_{(k,l)}\right] + 2\beta_{ij}\left[\bar{\varepsilon}_{ij} + \chi_{(i,j)}\right]\theta + c_v\frac{\theta^2}{T_0}\right\rangle \tag{3.41}$$

Utilising the coupling between MSG and CUF, depicted in Eqs. (3.22) and (3.23), and recalling that in the thermo-elastic problem, stresses and strains are related by Hooke's law as:

$$\boldsymbol{\sigma} = \mathbf{C}\boldsymbol{\varepsilon} + \boldsymbol{\beta}\theta \tag{3.42}$$

where $\boldsymbol{\beta}$ is a 6×1 matrix condensed from the second-order tensor β_{ij}.

In this context, Eq. (3.27) contains additional terms, and arises as:

$$\Pi^* = \frac{1}{2}\int_V \left[(\bar{\boldsymbol{\varepsilon}} + \mathbf{B}\chi)^T\,\mathbf{C}\,(\bar{\boldsymbol{\varepsilon}} + \mathbf{B}\chi) + 2\boldsymbol{\beta}(\bar{\boldsymbol{\varepsilon}} + \mathbf{B}\chi)\theta + c_v\frac{\theta^2}{T_0}\right] dV \tag{3.43}$$

which can be written in CUF form as:

$$\Pi^* = \frac{1}{2}\left(\chi_{sj}^T \mathbf{E}^{\tau sij}\chi_{\tau i} + 2\chi_{sj}^T \mathbf{D}_{h\varepsilon}^{sj}\bar{\boldsymbol{\varepsilon}} + \bar{\boldsymbol{\varepsilon}}^T \mathbf{D}_{\varepsilon\varepsilon}\bar{\boldsymbol{\varepsilon}} + 2\chi_{sj}^T \mathbf{D}_{h\theta}^{sj}\theta + 2\bar{\boldsymbol{\varepsilon}}^T \mathbf{D}_{\varepsilon\theta}\theta + D_{\theta\theta}\frac{\theta^2}{T_0}\right) \tag{3.44}$$

The equation above provides additional fundamental nuclei and volume integrals, reported in the following:

$$\mathbf{D}_{h\theta}^{sj} = \int_\Omega \int_l (\mathbf{B}(F_s N_j \mathbf{I}))^T \boldsymbol{\beta} d\Omega dy_1 \qquad \mathbf{D}_{\varepsilon\theta} = \int_V \boldsymbol{\beta} dV \qquad D_{\theta\theta} = \int_V c_v dV \tag{3.45}$$

$\mathbf{D}_{h\theta}^{sj}$ is the 3×1 FN due to the thermal effects, and $\mathbf{D}_{\varepsilon\theta}$ and $D_{\theta\theta}$ are the average thermal stiffness matrix and averaged specific heat of the material, respectively. Moreover, $\mathbf{D}_{h\theta}$ is the assembled matrix for the thermoelastic RUC problem obtained by looping on the s and j indices. The extended expression of $\mathbf{D}_{h\theta}^{sj}$ is:

$$\begin{aligned}
D_{h\theta,11}^{sj} &= \beta_{11}\int_l N_{j,y_1} dy_1 \int_\Omega F_s d\Omega + \beta_{13}\int_l N_j dy_1 \int_\Omega F_{s,y_3} d\Omega + \beta_{12}\int_l N_j dy_1 \int_\Omega F_{s,y_2} d\Omega \\
D_{h\theta,21}^{sj} &= \beta_{22}\int_l N_j dy_1 \int_\Omega F_{s,y_2} d\Omega + \beta_{23}\int_l N_j dy_1 \int_\Omega F_{s,y_3} d\Omega + \beta_{12}\int_l N_{j,y_1} dy_1 \int_\Omega F_s d\Omega \\
D_{h\theta,31}^{sj} &= \beta_{33}\int_l N_j dy_1 \int_\Omega F_{s,y_3} d\Omega + \beta_{23}\int_l N_j dy_1 \int_\Omega F_{s,y_2} d\Omega + \beta_{12}\int_l N_{j,y_1} dy_1 \int_\Omega F_s d\Omega
\end{aligned} \tag{3.46}$$

The fluctuation unknowns that minimise the functional from Eq. (3.44) can be computed by solving the linear system of equations:

$$\mathbf{E}\chi = -\mathbf{D}_{h\varepsilon}\bar{\boldsymbol{\varepsilon}} - \mathbf{D}_{h\theta}\theta \tag{3.47}$$

Assuming that the fluctuation is linearly proportional to $\bar{\boldsymbol{\varepsilon}}$ and θ, i.e.:

$$\chi = \chi_0\bar{\boldsymbol{\varepsilon}} + \chi_\theta\theta \tag{3.48}$$

and substituting it into Eq. (3.47), one gets the following linear system:

$$\begin{cases} \mathbf{E}\chi_0 = -\mathbf{D}_{h\varepsilon} \\ \mathbf{E}\chi_\theta = -\mathbf{D}_{h\theta} \end{cases} \tag{3.49}$$

where the term χ_θ is a 3×1 matrix. Last, plugging Eq. (3.48) into Eq. (3.43), one can calculate

$$\Pi^* = \frac{1}{2}\bar{\boldsymbol{\varepsilon}}^T \mathbf{C}^*\bar{\boldsymbol{\varepsilon}} + \bar{\boldsymbol{\varepsilon}}^T\bar{\boldsymbol{\beta}}\theta + \frac{1}{2}\bar{c}_v\frac{\theta^2}{T_0} \tag{3.50}$$

being

$$\mathbf{C}^* = \frac{1}{\Omega}\left[\chi_0^T \mathbf{D}_{h\varepsilon} + \mathbf{D}_{\varepsilon\varepsilon}\right] \quad \bar{\boldsymbol{\beta}} = \frac{1}{\Omega}\left[\frac{1}{2}(\mathbf{D}_{h\varepsilon}^T \chi_\theta + \chi_0^T \mathbf{D}_{h\theta}) + \mathbf{D}_{\varepsilon\theta}\right]$$
$$\bar{c}_v = \frac{1}{\Omega}\left[\chi_\theta^T \mathbf{D}_{h\theta} T_0 + \mathbf{D}_{\theta\theta}\right] \tag{3.51}$$

where $\bar{\boldsymbol{\beta}}$ is the effective thermal stress coefficients vector and $\bar{c}_v$ is the effective specific heat. Moreover, $\mathbf{D}_{h\theta}$, $\mathbf{D}_{\varepsilon\theta}$ and $\mathbf{D}_{\theta\theta}$ are the assembled arrays of their aforementioned fundamental nuclei. The effective coefficients of thermal expansion can be retrieved as:

$$\bar{\boldsymbol{\alpha}} = -\mathbf{C}^{*-1}\bar{\boldsymbol{\beta}} \tag{3.52}$$

By reintroducing the fluctuation solutions into the geometrical and constitutive relations, the local fields over the RUC can be derived. Recall that the complete solution to the fluctuation function is:

$$\chi = \chi_0 \bar{\boldsymbol{\varepsilon}} + \chi_\theta \theta \tag{3.53}$$

Consequently, the local strain field becomes:

$$\boldsymbol{\varepsilon} = \bar{\boldsymbol{\varepsilon}} + \mathbf{B}(F_\tau N_i \chi), \tag{3.54}$$

and using Hooke's law, the local stress field of the original heterogeneous material is computed as:

$$\boldsymbol{\sigma} = \mathbf{C}\boldsymbol{\varepsilon} + \boldsymbol{\beta}\theta \tag{3.55}$$

Chapter 4

Defect modelling

The presence of defects is almost unavoidable during the manufacturing process of composites. Since they are hierarchic and heterogeneous materials, flaws can be present at different scales. In this regard, some flaws can be witnessed by the naked eye, while others require specific machinery to be appreciated. In addition, the occurrence of some defects cannot be predicted by engineers and, thus, should be treated as uncertain. Instead, by simulating the fabrication process, the engineers can foresee where flaws are likely to occur.

This chapter presents the most common defects that appear during the AFP steering process and manufacturing limitations. Subsequently, a distinction between uncertainty and deterministic defects is made. The modelling techniques used to include these two families in the numerical framework are discussed. Moreover, an uncertainty quantification technique such as Polynomial Chaos Expansion is introduced after describing how uncertainty defects are modelled.

4.1 Defect classification

This section introduces the manufacturing defects that arise during the fabrication of VAT composites by the Automated Fibre Placement (AFP) technique and how they can be modelled within FE method. These are enlisted and briefly depicted in the following:

Angle deviation It occurs when the AFP machine deviates from the guiding curves that serve as a reference and is mainly due to the chosen course width. Consequently, broader fibre courses imply larger angle deviations, and narrower ones increase the manufacturing time. Therefore, a trade-off between quality and fabrication time is needed.

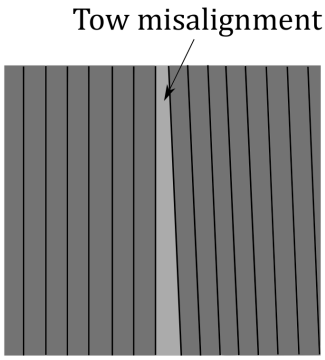

Figure 4.1 Example of tow misalignment generating a gap during AFP process.

Tow misalignment It is caused by an inaccurate positioning of the deposition head due to inertial effects on the machine structure and process speed. A graphical representation is available in Fig. 4.1.

Waviness It can occur in- and out-of-plane within the ply. The former is produced by the steering of the fibres and the presence of complex surfaces. The latter is affected by tooling as well as fibre steering. The out-of-plane waviness harms the composite parts' strength and stiffness.

Gap and overlap They are the most common and studied defects that occur in AFP-manufactured parts. They are related to both the processability of the material and the machine parameters. Besides, the quality of the material also affects the tow width, which could fluctuate. A 0% overlap strategy means that only gaps will occur within the ply. A 100% overlap implies that only overlaps will be present. These two strategies can be referred to as full-gap or full-overlap, respectively. These two defects are illustrated in Fig. 4.2. As shown there, a coverage percentage between 0% and 100% implies a combination of gaps and overlaps.

Twisting It is a defect that barely happens thanks to the sophisticated process control and material quality employed during manufacturing. Nevertheless, when it happens, it will be within the material supply and payout system of the AFP end effector due to the movement of the AFP machine along the fibre path. It might also be caused during the steering of the fibres, and, as a consequence, gaps will arise close to the twisted tows, as represented in Fig. 4.3.

Bridging and crowning They occur because of a lack of pre-tension within the tows, which allows the AFP machine to place tows on concave and convex surfaces. Bridging happens when fibres are deposited on concave geometries, while crowning appears when steering over convex surfaces. In this regard, the fibre tow pre-stress needs to

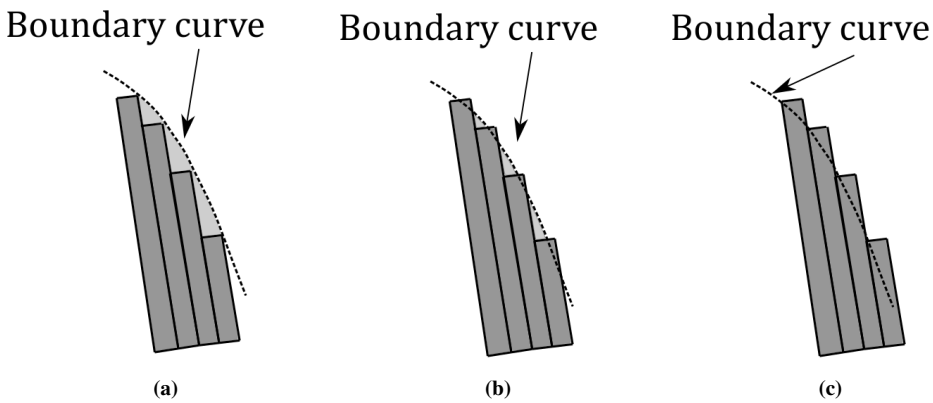

Figure 4.2 Different coverage strategies: (a) Full-gap. (b) 50% gap and 50% overlap. (c) Full-overlap.

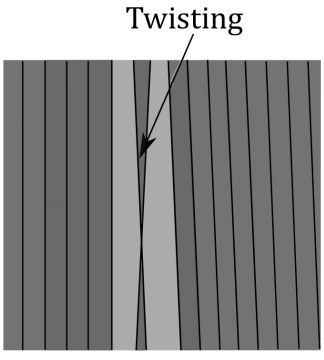

Figure 4.3 Twisted tow induced by the AFP process.

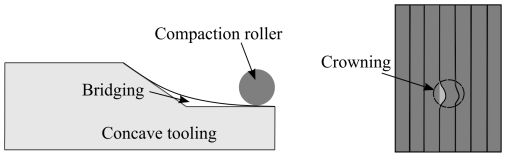

Figure 4.4 Bridging and crowning defects within a ply.

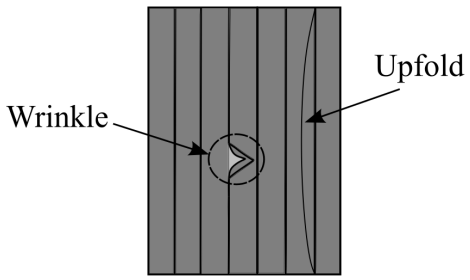

Figure 4.5 Wrinkle and upfold within a ply.

be monitored and adjusted throughout the entire fibre/fed system. Figure 4.4 shows a schematic representation of these two defects.

Tow wrinkling and upfolding They arise when the adhesion between the pre-impregnated tow and the tool surface fails. They may also stem from fibre steering. The edges of the fibre course present different curvature radii, i.e., one side lengthens while the other compresses. Therefore, the tensile and compressive stress within the tow may lead to eventual fold up or wrinkle, as represented in Fig. 4.5.

Voids and inclusions The already present voids in the raw material can be reduced to a small extent by compaction during the AFP process. In this context, an insufficient compaction of the tows increases the chances of entraping air. Likewise, small or large gaps and overlaps promote void formation.

Residual stresses and process-induced imperfections (PID) These defects are induced during the curing phase and arise in the cured part. Besides fibre steering, gaps and overlaps facilitate the emergence of residual stresses and PID.

Fuzz formation It is caused by shredded material at the edges of a narrow tow. Each part of the AFP machine that contacts the fibre tows interacts with the fibre constituent. In detail, the friction with the tow edges leads to an accumulation of fuzz that may contaminate the laminate during fibre placement. Fuzz formation might be due to fluctuations in the width of the fibre tow. A graphical representation is available in Fig. 4.6.

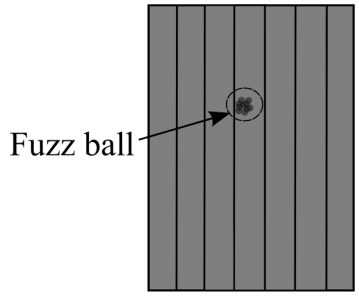

Figure 4.6 Fuzz ball within a ply.

4.2 Manufacturing limitations

Apart from the previous defects, other manufacturing quantities are paramount when designing VAT components. The first that is considered in this document is the minimum turning radius of the AFP machine $r_{\min}$, which is usually enforced through a constraint in the optimisation problem as:

$$-\frac{1}{r_{\min}} \leq \kappa \leq \frac{1}{r_{\min}} \tag{4.1}$$

An analytic expression to calculate the curvature of a generic tow-angle distribution was derived by Brooks and Martins [109] and is depicted in the following. Let us consider a 2D unit tangent vector $\overrightarrow{t}$ to a fibre path $\theta(x,y)$, see Fig. 4.7, as:

$$\overrightarrow{t}(\theta) = \cos(\theta)\hat{\mathbf{i}} + \sin(\theta)\hat{\mathbf{j}}. \tag{4.2}$$

Then, performing the curl operator over the vector field $\overrightarrow{t}$ and keeping the only non-zero vector component gives:

$$\kappa(x,y) = (\nabla \times \overrightarrow{t}(\theta)) \cdot \hat{\mathbf{k}} = \frac{\partial \theta}{\partial x}\cos(\theta) + \frac{\partial \theta}{\partial y}\sin(\theta) = \nabla\theta \cdot \overrightarrow{t}(\theta), \tag{4.3}$$

which can be evaluated to assess whether a design is manufacturable or not. Note that $\hat{\mathbf{i}}$, $\hat{\mathbf{j}}$ and $\hat{\mathbf{k}}$ denote the unitary vectors of a Cartesian reference frame. Besides, θ's explicit dependence on x and y is omitted for conciseness.

If one considers the expression of the linear variability of the fibre orientation angle proposed by Olmedo and Gürdal [10] and assuming $\phi = 0°$, Eq. (4.3) can be rewritten as follows:

$$\kappa(x) = \operatorname{sgn}(x)\frac{T_1 - T_0}{d}\cos\left(T_0 + \frac{T_1 - T_0}{d}x\right) \tag{4.4}$$

in which $\mathrm{sgn}(\cdot)$ denotes the sign function.

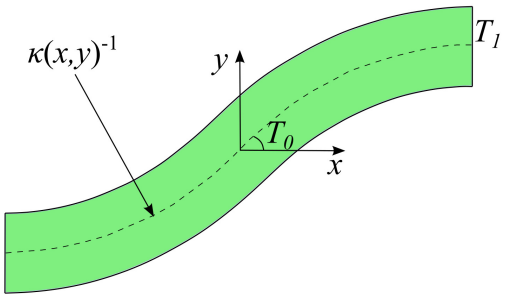

Figure 4.7 Illustration of the AFP turning radius in a linearly varying fibre path at a certain (x,y) in-plane location.

4.3 Uncertainty defects and quantification

4.3.1 Stochastic fields

Composite structures are not exempt from flaws arising during the fabrication process. For instance, the composite material may present variability of their intrinsic properties such as different Young's modulus, shear modulus or material strengths. Other can be strictly related to the manufacturing process, such as an unexpected void content due to some pressure variation when the composite part was in the autoclave. Additional geometrical features that can present variability are the ply thickness, the presence of fibre waviness or misalignments, or even variability in the direction of the applied loads.

In order to consider these possible variations, they have to be included in the numerical model, which can be done using stochastic fields. They are n-dimensional fields that spread a parameter in space following a specific probability distribution. Several techniques exist that can be used for the computation of random fields. Spanos and Zeldin [110] wrote a thorough review in the late 90s, which gathered some of the most extended methodologies, such as the Covariance Matrix Decomposition (CMD), spectral method, the auto-regressive moving-average (ARMA) method, noise shower method, scale refinement method and turning band method.

In this research, the CMD [111] was considered first, thanks to its straightforwardness in generating stochastic fields. CMD just needs a correlation function and a correlation length. It starts with the generation of the covariance matrix $\mathbb{C}$ through a

correlation function, which is commonly based on an exponential function as follows:

$$\begin{aligned}\mathbb{C}(\mathbf{x},\mathbf{x}') &= e^{-\frac{|x_i - x_i'|}{L_{ci}}} \\ \mathbb{C}(\mathbf{x},\mathbf{x}') &= e^{-\frac{||x - x'||}{L_{ci}}},\end{aligned} \tag{4.5}$$

in which L_{ci} is the correlation length in the i^{th} direction. Note that the numerator at the exponentials refers to the distance between the reference points in which random variables are to be computed. In the case of flat structures such as plates, the numerator corresponds to the Euclidean distance. However, in the case of shells, the geodesic distance is more representative of the structure.

Using CMD, stochastic fields are calculated through the multiplication of a matrix with a random vector:

$$\mathbf{h} = \mathbf{L}\boldsymbol{\xi} \tag{4.6}$$

where $\mathbf{L}$ is a decomposed version of the correlation matrix $\mathbf{R}$ and $\boldsymbol{\xi}$ a vector with zero mean and a unit variance. The correlation matrix is generated as follows:

$$R_{ij} = \frac{\text{cov}(h_i, h_j)}{\sigma_i \sigma_j} \rightarrow \mathbf{R} = \begin{bmatrix} 1 & \mathbb{C}(\mathbf{x}_1,\mathbf{x}_2) & \dots & \mathbb{C}(\mathbf{x}_1,\mathbf{x}_n) \\ \mathbb{C}(\mathbf{x}_2,\mathbf{x}_1) & 1 & \dots & \mathbb{C}(\mathbf{x}_2,\mathbf{x}_n) \\ \vdots & & \ddots & \vdots \\ \mathbb{C}(\mathbf{x}_n,\mathbf{x}_1) & \mathbb{C}(\mathbf{x}_n,\mathbf{x}_2) & \dots 1 & \end{bmatrix} \tag{4.7}$$

in which $\mathbb{C}(\mathbf{x}_i,\mathbf{x}_j) = \mathbb{C}(\mathbf{x}_j,\mathbf{x}_i)$. Then, taking the definition of the covariance:

$$\text{cov}[h_i, h_j] = \mathbb{E}[h_i h_j] - \mathbb{E}[h_i]\mathbb{E}[h_j] \tag{4.8}$$

and recalling that the field has a null mean, it is possible to show that $\mathbf{R}$ can be decomposed into two matrices:

$$\mathbf{R} = \text{cov}[\mathbf{h},\mathbf{h}] = \mathbb{E}(\mathbf{h},\mathbf{h}^T) - 0 \cdot 0 = \mathbb{E}(\mathbf{L}\boldsymbol{\xi}\,(\mathbf{L}\boldsymbol{\xi})^T) = \mathbf{L}\mathbb{E}(\boldsymbol{\xi}\,\boldsymbol{\xi}^T)\mathbf{L}^T = \mathbf{L}\mathbf{L}^T \tag{4.9}$$

Because $\mathbf{R}$ is symmetric and positive semi-definite, it can be decomposed using eigendecomposition in the form of:

$$\mathbf{R} = \mathbf{Q}\boldsymbol{\Lambda}\mathbf{Q}^T \tag{4.10}$$

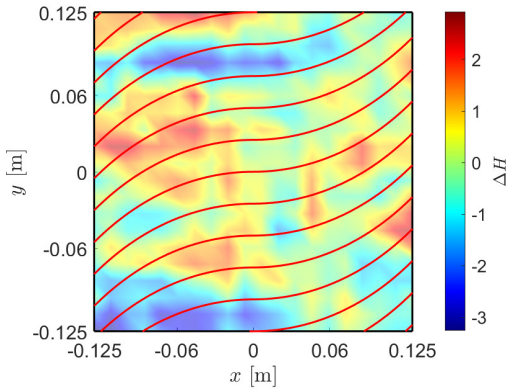

Figure 4.8 Example of a generic random field generated by CMD over a $[\langle 0,45\rangle]$ VAT ply. The correlation lengths are $L_{cx} = 0.125$ m and $L_{cy} = 0.025$ m, and field standard deviation $\sigma_H = 1.5$.

where $\mathbf{\Lambda}$ is a diagonal matrix containing the eigenvalues of $\mathbf{R}$, and $\mathbf{Q}$ contains the eigenvectors of the matrix. Therefore, $\mathbf{L}$ can be extracted as follows:

$$\mathbf{R} = \mathbf{Q}\tilde{\mathbf{\Lambda}}\tilde{\mathbf{\Lambda}}\mathbf{Q}^T = \mathbf{L}\mathbf{L}^T \rightarrow \mathbf{L} = \mathbf{Q}\tilde{\mathbf{\Lambda}} \tag{4.11}$$

being $\tilde{\mathbf{\Lambda}} = \text{diag}(\sqrt{\lambda})$, and λ the eigenvalues of $\mathbf{R}$. In this manner, utilising the decomposed correlation matrix $\mathbf{L}$, it is possible to generate random fields employing Eq. (4.6) as:

$$H_i = \tilde{H} + \sigma_H L_{ij} \xi_j \tag{4.12}$$

where H_i is the value of the random field at point i, $\tilde{H}$ and σ_H are the mean value and standard deviation of the field. An illustrative example of a random field generated by CMD over a $[\langle 0,45\rangle]$ VAT ply is available in Fig. 4.8. The covariance matrix is generated using the first kernel reported in Eq. (4.5), and the correlation lengths are $L_{cx} = 0.125$ and $L_{cy} = 0.025$ m, and standard deviation $\sigma_H = 1.5$.

A similar procedure to CMD is the Karhunen-Loève expansion (KLE) [112], which can be seen as a particular case of the orthogonal series expansion where the orthogonal functions are the eigenfunctions of a Fredholm integral equation of the second kind with the autocovariance function as the kernel. In this case, the stochastic field can be expressed as:

$$H(\mathbf{x};\omega) = \tilde{H} + \Delta H(\mathbf{x};\omega), \tag{4.13}$$

in which ω represents the stochastic nature of the field, $\tilde{H}$ is the mean value of the field, and ΔH denotes the Gaussian variation of the random field about its mean. This

last term can be expressed as a truncated series including M terms as follows:

$$\Delta H(\mathbf{x};\omega) = \sum_{i=1}^{M} \xi_i(\omega)\sqrt{\lambda_i}\varphi_i(\mathbf{x}), \tag{4.14}$$

where $\xi_i(\omega)$ is a set of zero-mean independent Gaussian random variables, and λ_i and φ_i are the eigenvalues and eigenfunctions of the Fredholm integral:

$$\int \mathbb{C}(\mathbf{x},\mathbf{x}')\varphi_i(\mathbf{x}')d\mathbf{x}' = \lambda_i\varphi_i(\mathbf{x}) \tag{4.15}$$

Depending on the kernel, analytical solutions can be derived. For instance, for a squared plate and using as kernel:

$$\mathbb{C}(x,y;x',y') = \sigma_H^2 e^{-\frac{|x-x'|}{L_{cx}}-\frac{|y-y'|}{L_{cy}}}, \tag{4.16}$$

one can write that the f_n eigenfunction as the following product:

$$\varphi_n(x,y) = \varphi_i^{(1)}(x)\varphi_j^{(2)}(y) \tag{4.17}$$

and

$$\lambda_n = \lambda_i^{(1)}\lambda_j^{(2)}. \tag{4.18}$$

Substituting Eqs. (4.16), (4.17) and (4.18) into Eq. (4.15), reads as:

$$\lambda_i^{(1)}\lambda_j^{(2)}\varphi_i^{(1)}(x)\varphi_j^{(2)}(y) = \int_{-L_{cx}/2}^{L_{cx}/2} e^{-\frac{|x-x'|}{L_{cx}}}\varphi_i^{(1)}(x)dx' \int_{-L_{cy}/2}^{L_{cy}/2} e^{-\frac{|y-y'|}{L_{cy}}}\varphi_j^{(2)}(y)dy', \tag{4.19}$$

whose solution is the product of the individual solutions of the following two equations:

$$\begin{aligned} \lambda_i^{(1)}\varphi_i^{(1)} &= \int_{-L_{cx}/2}^{L_{cx}/2} e^{-\frac{|x-x'|}{L_{cx}}}\varphi_i^{(1)}(x)dx' \\ \lambda_j^{(2)}\varphi_j^{(2)}(y) &= \int_{-L_{cy}/2}^{L_{cy}/2} e^{-\frac{|y-y'|}{L_{cy}}}\varphi_j^{(2)}(y)dy' \end{aligned} \tag{4.20}$$

The solution of the first equation has the following eigenvalues:

$$\lambda_i^{(1)} = \frac{2/L_{cx}}{\omega_i^2 + (1/L_{cx})^2}, \tag{4.21}$$

and eigenfunctions:

$$\begin{aligned} \varphi_i^{(1)}(x) &= \frac{\cos(\omega_i x)}{\sqrt{a+\frac{\sin(2\omega_i a)}{2\omega_i}}} \quad \text{for } i \text{ odd} \\ \varphi_i^{(1)}(x) &= \frac{\sin(\omega_i x)}{\sqrt{a-\frac{\sin(2\omega_i a)}{2\omega_i}}} \quad \text{for } i \text{ even} \end{aligned} \tag{4.22}$$

being a the semi-length of the x domain, and ω_i the solution of the transcendental equation:

$$\begin{aligned} \frac{1}{L_{cx}} - \omega_i \tan(\omega_i a) = 0 \quad \text{for } i \text{ odd} \\ \omega_i + \frac{1}{L_{cx}} \tan(\omega_i a) = 0 \quad \text{for } i \text{ even} \end{aligned} \tag{4.23}$$

Note that the same procedure is made to solve for $\lambda_j^{(2)}$ and $\varphi_j^{(2)}(y)$. Of course, L_{cx} and a must be substituted by L_{cy} and the semi-length in the y domain, respectively. If more complex geometries or more complex kernels are considered in the stochastic analysis, Eq. (4.15) can be solved numerically employing the FEM as explained in the book by Ghanem and Spanos [112]. Additionally, other numerical methods to generate KLE are depicted in the work by Betz *et al.* [113]. Last, an example of a stochastic field generated by KLE is represented in Fig. 4.9. In detail, the first fifteen eigenvalues, the first and second eigenfunctions and the stochastic field over a $[\langle 0,45 \rangle]$ VAT lamina are illustrated. The covariance kernel from Eq. (4.16) with $L_{cx} = 0.125$ and $L_{cy} = 0.025$ m, and a standard deviation $\sigma_H = 1.5$ are considered.

To conclude this section, it is worth mentioning that the above methods are limited to simulating Gaussian random fields. If needed, these methods may readily be extended to simulating non-Gaussian fields as a translation process, which is defined using a nonlinear transformation of an underlying Gaussian stochastic field of the form [114, 115]

$$Z(\mathbf{x};\omega) = g(Y(\mathbf{x};\omega)) = F^{-1}[\Phi(Y(\mathbf{x};\omega))] \tag{4.24}$$

in which $Z(\mathbf{x};\omega)$ is a non-Gaussian random field with marginal Cumulative Distribution Function (CDF) F, Φ is the standard Gaussian CDF, $Y(\mathbf{x};\omega)$ is an underlying Gaussian field, and g denotes a nonlinear *memoryless* transformation.

4.3.2 Polynomial Chaos Expansion

Addressing the uncertainty in the mechanical performance of composite materials is becoming an increasingly important field, as reliability analysis tends to be performed after designing a component. However, the cost of dealing with uncertainty is the large

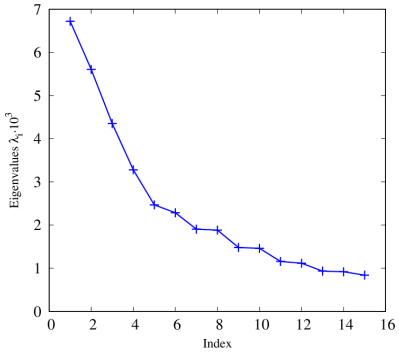

(a) Eigenvalues

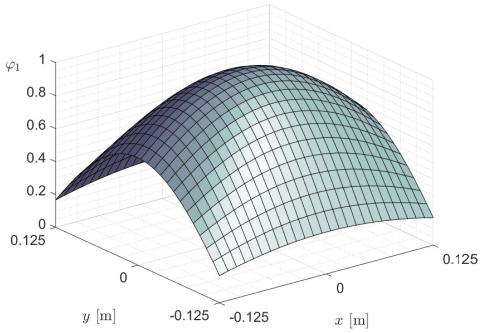

(b) First eigenfunction

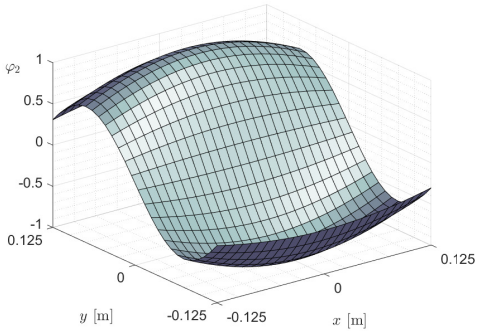

(c) Second eigenfunction

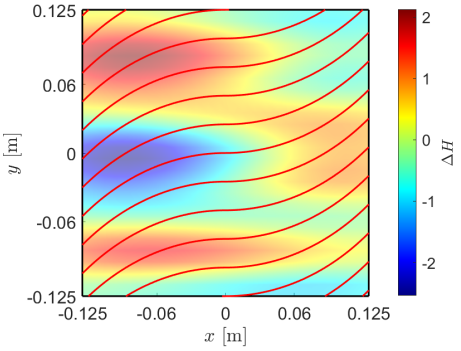

(d) Random field

Figure 4.9 (a) First fifteen eigenvalues, (b) first and (c) second eigenfunctions, and (d) random field generated by KLE over a $[\langle 0,45 \rangle]$ ply. The correlation lengths are $L_{cx} = 0.125$ m and $L_{cy} = 0.025$ m, and field standard deviation $\sigma_H = 1.5$.

amount of data needed. This information is commonly obtained through Monte Carlo simulations, which repeatedly evaluate expensive computational models.

Metamodels, or surrogate models, attempt to decrease the cost of uncertainty analyses by substituting expensive computational models with inexpensive surrogates. Throughout the decades, a plethora of methods have been employed to characterise uncertainty, among which Polynomial regression, Kriging processes [116], Radial Basis functions [117], Support Vector regression [118] and Polynomial Chaos expansion (PCE) [112]. The latter is considered in this thesis to accelerate the uncertainty quantification of the buckling response of VAT affected by spatially varying waviness and fibre volume fraction. The mathematical foundations of PCE are depicted in the following. PCE can be generally expressed as:

$$Y(\xi_1,\xi_2,...,\xi_r) = a_0\Gamma_0 + \sum_{i=1}^{\infty} a_{1i}\Gamma_1(\xi_{i1}(\omega)) + \sum_{i=1}^{\infty}\sum_{j=1}^{i} a_{i1i2}\Gamma_2(\xi_{i1}(\omega)\xi_{i2}(\omega)) + ... \tag{4.25}$$

where $\xi_{i1}(\omega)$ is a set of independent standard Gaussian variables and $\Gamma_p(\xi_{i1}(\omega),...,\xi_{ip}(\omega))$ is a set of multivariate Hermite polynomials of order p; $a_{i1},...,a_{ip}$ are deterministic coefficients and ω represents the random nature of the magnitudes involved. Equation (4.25) can be rewritten as:

$$Y(\xi_1,\xi_2,...,\xi_n) = \sum_{i=0}^{r} \beta_i \psi_i(\xi_i(\omega)) \tag{4.26}$$

in which β_i and $\psi_i(\xi_i(\omega))$ are equivalent to $a_{i1},...,a_{ip}$ and $\Gamma_p(\xi_{i1}(\omega),...,\xi_{ip}(\omega))$, respectively. It is worth mentioning that, depending on the nature of the uncertainty quantities involved, i.e., Gaussian, uniform, beta distribution, and so forth, the polynomial basis varies as depicted in [119]. The number of terms involved in a PCE up to order p are calculated as:

$$N = \frac{(r+p)!}{r!p!} \tag{4.27}$$

being r the number of variables involved, and p the degree of the polynomial. An interesting feature of PCE is that thanks to the orthonormality of the polynomial basis, the first two statistical moments, namely the mean value and standard deviation, are encoded within the PCE coefficients. The mean value $\tilde{Y}$ and variance σ_Y^2 of the stochastic process Y can be calculated using the following expressions:

$$\begin{aligned} \tilde{Y} &= \beta_0 \\ \sigma_Y^2 &= \sum_{i=1}^{r} \beta_i^2. \end{aligned} \tag{4.28}$$

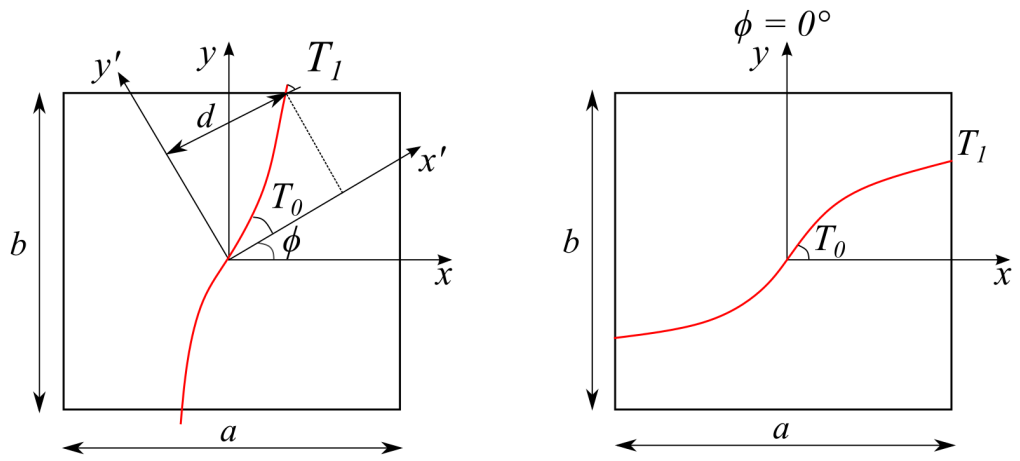

Figure 4.10 Representation of a linearly varying fibre path. (a) General case. (b) $\phi = 0°$.

In this thesis, the PCE independent variables $\xi_i(\omega)$ correspond to the standard Gaussian terms considered in the KLE, reported in Eq. (4.14).

4.4 Deterministic defects

As opposed to the imperfections depicted in the previous section, the presence and location of deterministic defects can be predicted by modelling the material deposition process. This is referred to as manufacturing process simulation and can be used to foresee where gaps and overlaps are likely to occur in the case of tow-steered composites.

In this investigation, the linear fibre variation proposed by Olmedo and Gürdal [10] is considered. The linear variation can be expressed as:

$$\theta(x') = \phi + T_0 + \frac{T_1 - T_0}{d}|x'| \tag{4.29}$$

in which T_0 and T_1 are the fibre orientations at $x' = 0$ and $x' = d$, respectively, and d is the length along which the fibre orientation varies from T_0 to T_1; last, ϕ is the fibre rotation path angle and defines the axis along which the courses are steered, i.e., x-axis, y-axis, or a combination of both since $x' = x\cos\phi + y\sin\phi$. It is commonly found that $\phi = 0°$ or $\phi = 90°$, and in those cases, d equals the semi-width, $a/2$, or semi-length, $b/2$, of the plate, respectively. All these parameters are represented in Fig. 4.10 for a better understanding.

In order to visualise the fibre deposition process, it is necessary to obtain an analytic equation that provides the in-plane position of the fibre courses. In this regard, the

centre line of a fibre course can be calculated as follows:

$$\frac{dy}{dx} = \tan\theta \tag{4.30}$$

in which θ takes the expression from Eq. (4.29). Assuming $\phi = 0^\circ$, and therefore $d = a/2$, the solution to the previous differential equation reads as:

$$y(x) = \begin{cases} \frac{a}{2(T_0-T_1)}\left[\ln(\cos T_0) + \ln\left(\cos\left(-T_0 + 2T_1 + \frac{2(T_1-T_0)}{a}x\right)\right)\right] & -a \le x \le -\frac{a}{2} \\ \frac{a}{2(T_1-T_0)}\left[-\ln(\cos T_0) + \ln\left(\cos\left(T_0 + \frac{2(T_0-T_1)}{a}x\right)\right)\right] & -\frac{a}{2} \le x \le 0 \\ \frac{a}{2(T_0-T_1)}\left[-\ln(\cos T_0) + \ln\left(\cos\left(T_0 + \frac{2(T_1-T_0)}{a}x\right)\right)\right] & 0 \le x \le \frac{a}{2} \\ \frac{a}{2(T_1-T_0)}\left[\ln(\cos T_0) + \ln\left(\cos\left(-T_0 + 2T_1 + \frac{2(T_0-T_1)}{a}x\right)\right)\right] & \frac{a}{2} \le x \le a \end{cases} \tag{4.31}$$

Note that Eq. (4.31) provides the equations for the fibre path for the outer regions of the considered plate. This is needed because in cases where $\phi \neq 0^\circ$, portions of the fibre course will lay outside the plate domain. In this manner, one constructs the so-called *manufacturing mesh*.

Let us focus on a single fibre course being steered. A course comprises several tows. The number of tows, n_{tow}, laid down by the AFP head can vary. Most AFP machines can simultaneously place eight, twelve, sixteen, twenty-four or thirty-two tows. Since each of these tows has a fixed width, w_{tow}, the width of the single course can be calculated as $w_{course} = n_{tow} w_{tow}$. Therefore, to model a single tow, one needs to consider not only the course reference path from Eq. (4.31) but also its left and right edges. These features are illustrated in Fig. 4.11. Their analytical expressions are:

$$\begin{aligned} \text{Left edge:} \quad & \begin{cases} x_l = x - p_l \sin\theta(x) \\ y_l = y + p_l \cos\theta(x) \end{cases} \\ \text{Right edge:} \quad & \begin{cases} x_r = x + p_l \sin\theta(x) \\ y_r = y - p_l \cos\theta(x) \end{cases} \end{aligned} \tag{4.32}$$

Recall that the previous set of equations was derived for the case when $\phi = 0^\circ$. If the chosen VAT design considered $\phi \neq 0^\circ$, Eq. (4.32) can be rewritten as:

$$\begin{aligned} \text{Left edge:} \quad & \begin{cases} x_l^\phi = x_l \cos\phi - y_l \sin\phi \\ y_l^\phi = x_l \sin\phi + y_l \cos\phi \end{cases} \\ \text{Right edge:} \quad & \begin{cases} x_r^\phi = x_r \cos\phi - y_r \sin\phi \\ y_r^\phi = x_r \sin\phi + y_r \cos\phi \end{cases} \end{aligned} \tag{4.33}$$

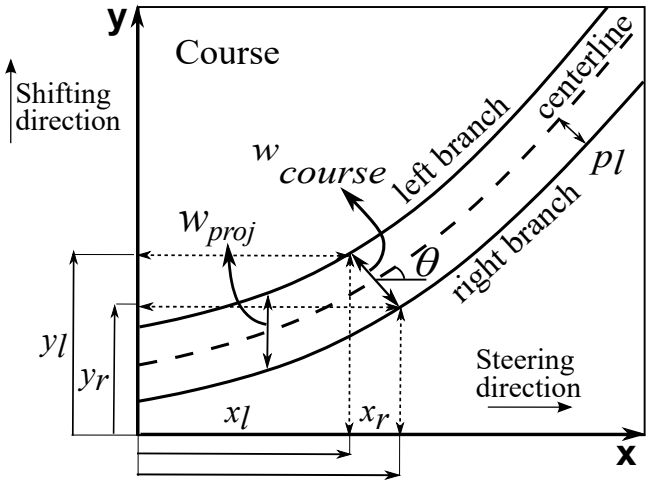

Figure 4.11 Schematic representation of how the projected vertical width varies with the steering process.

Table 4.1 Defects arising within the plate depending on the fibre parameters and the manufacturing strategy.

Condition	Contact at edge	Contact at centre
$\lvert\cos T_0\rvert > \lvert\cos T_1\rvert$	Gap at centre	Overlap at edges
$\lvert\cos T_1\rvert > \lvert\cos T_0\rvert$	Overlap at centre	Gap at edges

Focusing on a generic fibre course, one can observe that the vertical projection of the course width diminishes or increases, depending on the T_0 and T_1 fibre path angles. The projected width can be calculated as:

$$w_{proj} = \frac{w_{course}}{\cos\theta}, \tag{4.34}$$

and can be visualised in Fig. 4.11. Steering fibre bands along a fixed direction and shifting the AFP head perpendicularly to generate the subsequent fibre course leads to gaps and/or overlaps. The location where they appear depends on the fibre path definition angles, T_0 and T_1, and the steering strategy. For instance, one can impose contact between two adjacent courses at the plate's edge or centre. Figure 4.12 illustrates the case of a $[\langle 0,45\rangle]$ plate in which the fibre courses touch at the edge, Fig. 4.12a, and at the centre of the plate, see Fig. 4.12b. The yellow area highlights a gap area, whereas the green one indicates an overlap area.

Depending on the chosen fibre orientation parameters and the region where the fibre courses contact each other, one will find gaps and overlaps at the edge or centre of the plate. These conditions are summarised in Table 4.1. The previous flaws affect large areas because the course width is kept constant throughout the deposition process. In order to reduce the defect area, the course width has to decrease or increase

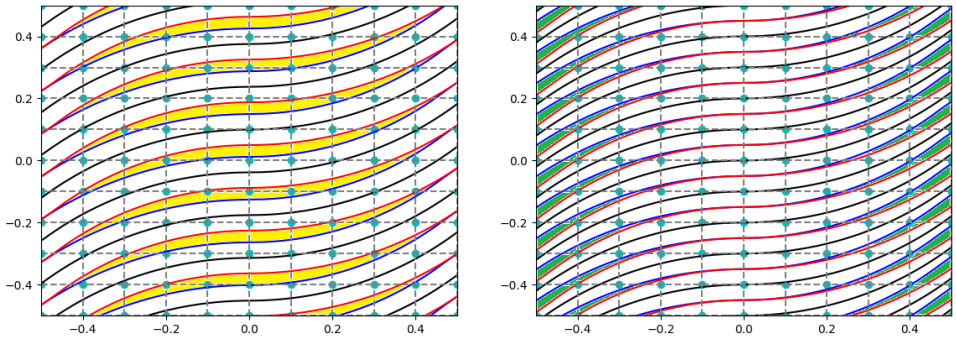

(a) Gaps **(b)** Overlaps

Figure 4.12 Example of a plate with $[\langle 0,45 \rangle]$ stacking sequence with full gap (a) and full overlap (b) manufacturing strategy.

whenever a course intersects the successive one, or it does not reach the precedent course's edge, respectively. The increase or decrease of the course width is achieved by cutting an individual tow and restarting its deposition. This comports the generation of small triangular defected regions, as observed in Fig. 4.13.

It is worth recalling that the described methodology was derived only for linearly varying fibre paths. However, if other variability strategies are utilised, the former procedure should be tweaked as the solution to the differential equation in Eq. (4.30) will be different.

4.5 Coupling manufacturing process simulation and FEM

So far, the concept of manufacturing mesh has been utilised to create the fibre courses that compose the laminated VAT plate, and depending on the chosen manufacturing strategy, one can obtain a 100% gap- or 100% overlap-defected plate. Foreseeing the position of such defects makes it possible to calculate the percentage of defects within a layer. This percentage is computed by tessellating the plate domain into a series of rectangular partitions and computing the defected area within each subdomain. This process is repeated for each layer comprising the laminated VAT component.

After calculating the defect area of each manufacturing subdomain, it is necessary to map these defects onto the FE mesh. For simplicity, in this study, the manufacturing and FE grids are divided into the same number of subdomains. Therefore, there is a one-to-one relation between the manufacturing and FE meshes.

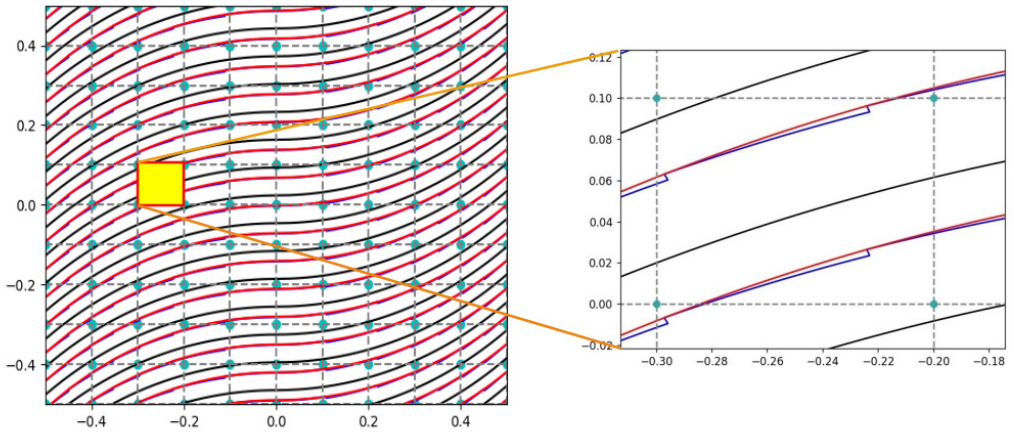

(a) Gaps

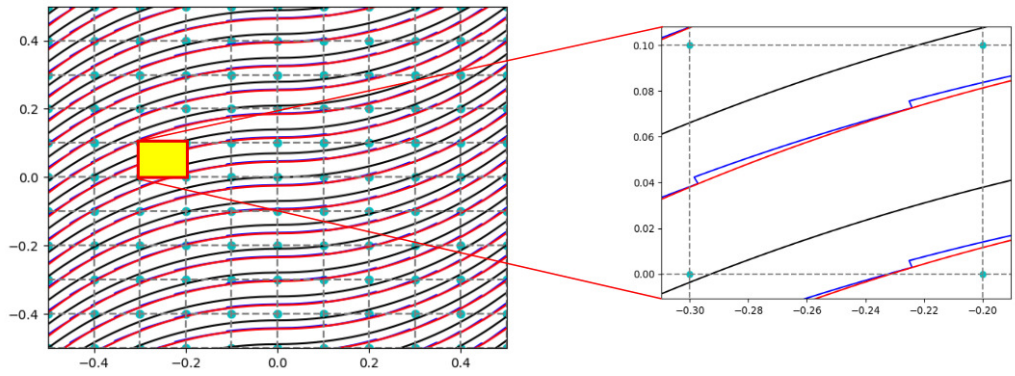

(b) Overlaps

Figure 4.13 Gap and overlap defect correction over a $[\langle 0,45 \rangle]$ ply. The zoomed areas show the triangular gaps and overlaps that are generated.

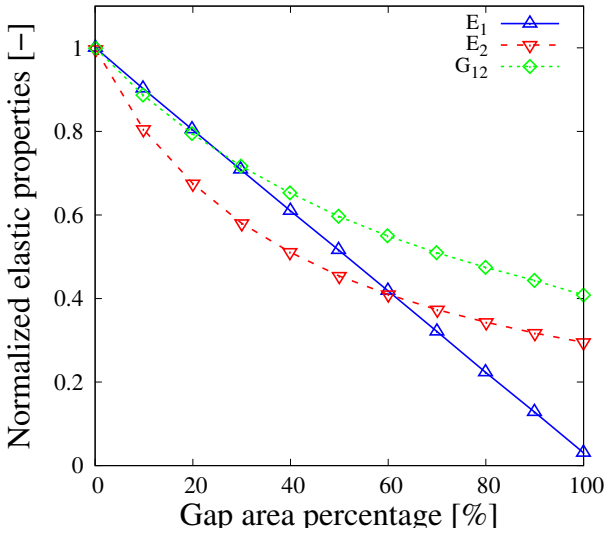

Figure 4.14 Normalised elastic properties with respect to the gap percentage area of the gap-modified defect layer. Adapted with permission from Fayazbakhsh *et al.* [45].

The Defect Layer Method (DLM), introduced by Fayazbakhsh *et al.* [45], is used to modify the relative properties of each FE. In the case of a full-gap strategy, the material elastic properties are penalised according to the laws shown in Fig. 4.14, whereas the modified density, ρ_{mod}, is calculated using the rule of mixtures as:

$$\rho_{\text{mod}} = \rho_{\text{resin}} A_{\text{gap}} + \rho_{\text{tow}}(1 - A_{\text{gap}}) \tag{4.35}$$

where A_{gap} is the gap defect area within the FE, and ρ_{resin} and ρ_{tow} are the resin and pre-impregnated tow densities, respectively. Conversely, when a full-overlap design is chosen, the material properties are kept the same as in the pre-impregnated material, and each FE's thickness is increased proportionally to the overlap area within the FE. Experiments showed that two superimposing tows do not lead to a twofold thickness increase due to the compaction pressure in the autoclave [120]. Therefore, the thickness increase is topped up by 95% of the original thickness. In this manner, the modified thickness t_{mod} is calculated as:

$$t_{\text{mod}} = 0.95 t_{\text{ply}}(1 + A_{\text{overlap}}) \tag{4.36}$$

in which A_{overlap} is the overlap defect area within the FE, and t_{ply} is the nominal thickness of the pre-impregnated tow. As an illustrative example, Fig. 4.15 shows each FE's fibre courses and the gap and overlap area.

As the reader can infer, when using DLM to model gaps, a multimaterial plate model is generated. In that model, the individual ply thicknesses are invariant and

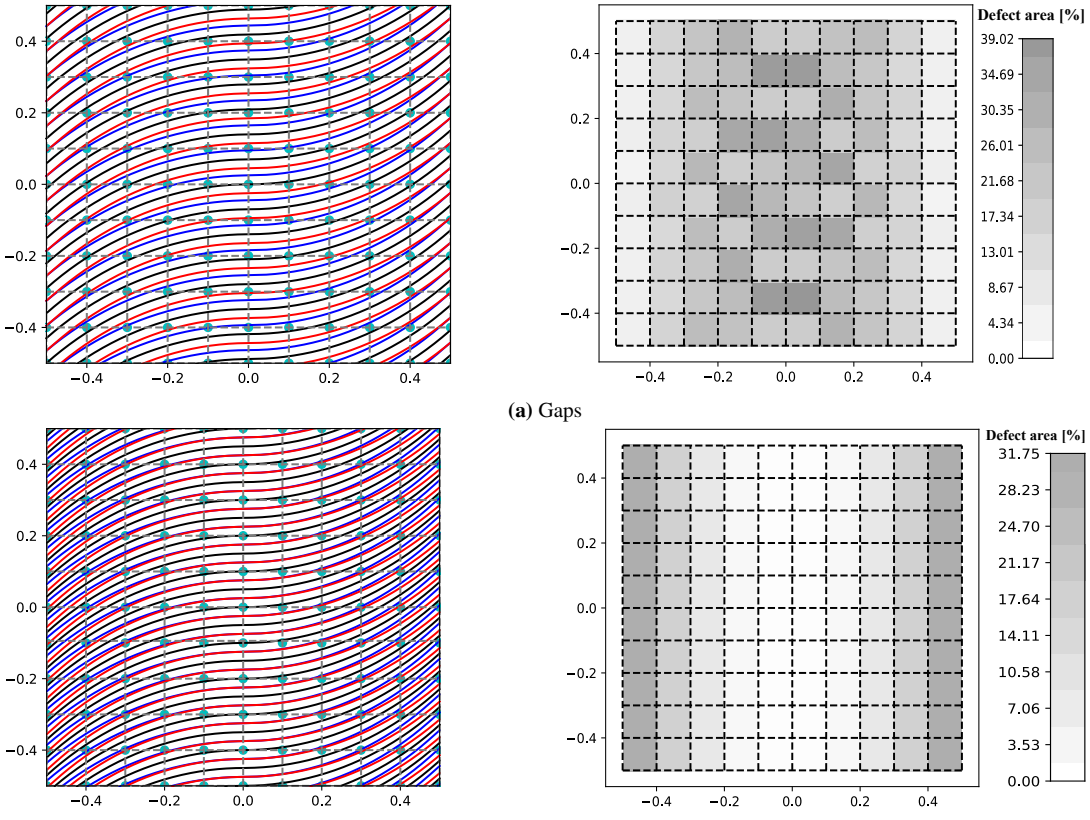

(a) Gaps

(b) Overlaps

Figure 4.15 Gap and overlap defect correction over a $[\langle 0,45 \rangle]$ ply. The greyscale map shows the defect area within each FE.

equal to those of the defect-free laminated component. Therefore, LW models can be easily developed by modifying the material properties of each FE in the in-plane and thickness directions, as appreciated in Fig. 4.16a. In contrast, when modelling overlaps with DLM, the thickness of each FE and layer varies spatially. Currently, new methodologies are being studied to develop full LW plates with the presence of overlaps. However, in the framework of this thesis, high-order ESL models are preferred to model this kind of defect. In this regard, the integration domain along the thickness for an ESL model varies for each FE. Indeed, with the present approach, generating an LW model accounting for overlaps is a cumbersome task because of the stair-like through-the-thickness discretisation required; see Fig. 4.16b. LW overlap modelling encompasses a significant increase in DOF that might not report additional benefits in the prediction of global responses of the structure, such as buckling load or fundamental frequency, which tend to be quantities of interest during the optimisation phase.

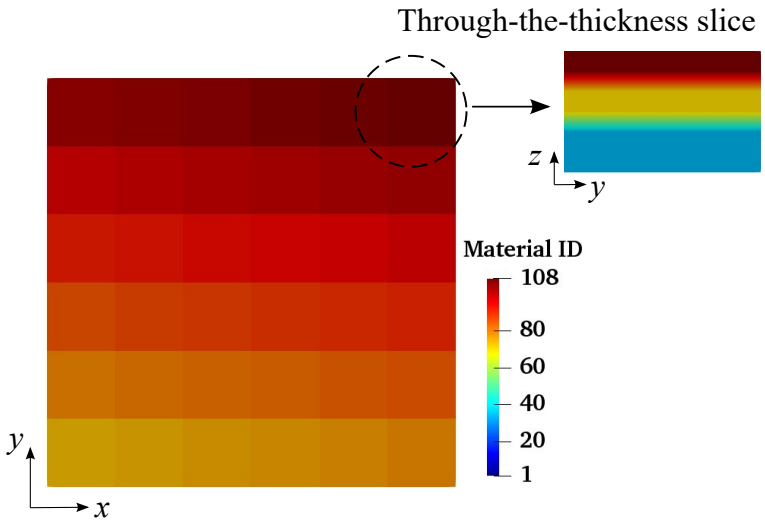

(a) Gap modelling

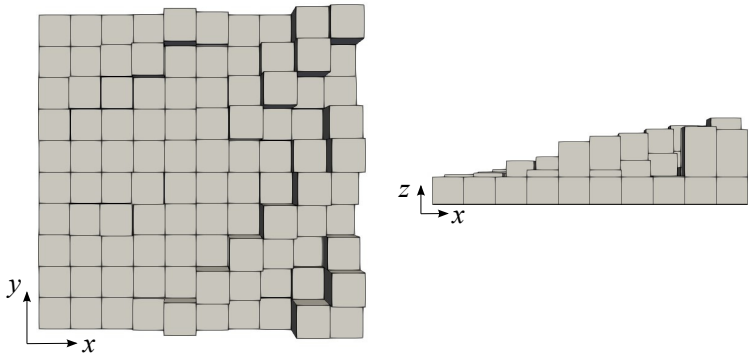

(b) Overlap modelling

Figure 4.16 Gap and overlap models resulting from coupling between DLM and FE.

Chapter 5

The optimisation problem

This chapter describes the main components needed to establish an optimisation problem. A description of the necessary features is made until construction of the mathematical statement. Then, the optimisation problem can be classified according to different criteria. These comprise how the functions involved are evaluated, i.e., direct simulations or surrogate models; whether a local or global search strategy is conducted; and the algorithm classification, depending on how the iterative process is handled.

5.1 Optimisation problem formulation

Optimisation problems are present in various everyday-activities, such as economics, management, manufacturing, physics, biology and, of course, engineering [121, 122]. Concerning the latter, this research is devoted to the structural design optimisation of variable stiffness composite structures, with a special focus on how the different structural theories chosen to analyse the aforementioned components affect the optimum solution in a series of linear static applications.

In the design optimisation process, the engineers have to translate their intent to a mathematical statement that can be solved by an optimization algorithm. To generate this statement, the designer needs to describe the problem and establish all the goals and requirements. It is also essential to identify all the possible inputs and outputs of the analysis, as well as its limitations.

The first step is to identify the design variables that describe the system. These must not depend on each other or any other parameter, and the optimiser must be free to choose the values of the design variables independently. In this manner, the design variables are input parameters that remain constant throughout the analysis process. Depending on the nature of the design variables, they can be defined as continuous

or discrete. Continuous variables are real numbers that are allowed to vary within a specified range. Conversely, a variable is referred to as discrete when it is allowed to take only a predefined number of values. The latter is common in structural sizing problems. For instance, in the optimisation of composite laminates, specific thickness values of the plies are available by the material suppliers.

The second step is the definition of the objective function, which is the quantity that determines whether a design is better than other. Depending on the problem, the objective function can be minimised or maximised. For instance, in the aeronautic sector, a structural engineer might want to minimise the structural weight of an aircraft, whereas an operation engineer would try to maximise the range of a vehicle. The selection of the objective function is not trivial. In many applications, optimising a certain feature could lead to a poor performance on another one. In this regard, it is not obvious which one of these features is the most appropriate to consider as objective function, as the trade-off will depend on the end-user preferences. The consideration of multiple objective functions within a single optimisation process is referred to as multiobjective optimisation. This is a topic that goes beyond the scope of this work, although it should be considered in future research activities.

The last step towards the definition of the optimisation problem is the identification of the constraints. The constraints are functions of the design variables that one wants to restrict in some way. As in the case of the objective function, the constraints are computed through models whose complexity can vary, i.e., from simple equations up to Finite Element or Computational Fluid Dynamic solvers. The feasible region is the set of points that fulfil all constraints, and one aims to minimise the objective function within this feasible design space.

Constraints can be divided into two categories: equality and inequality constraints. The former restricts a function to being equal to a fixed value, while the latter requires the function to be less or equal to a certain value. In addition, inequality constraints can be active or inactive at the optimum point. Active means that the constraint is equal to the fixed value, whereas an inactive one implies that the function is less than the certain value. In this regard, if one of the constraints is inactive at the optimum, this constraint could have been removed from the problem with no change in its solution. However, knowing this information in advance is a difficult task.

After having introduced the design variables, objective function and constraints, one can include them in an optimisation problem statement. Mathematically, the

optimisation problem is formulated as follows:

$$\min_{\mathbf{x}} \; f(\mathbf{x}) \;\; \text{s.t.} \begin{cases} g_i(\mathbf{x}) \leq 0 \;\; i = 1,...,n_g \\ h_j(\mathbf{x}) = 0 \;\; j = 1,...,n_h \\ \mathbf{x}_L \leq \mathbf{x} \leq \mathbf{x}_U \end{cases} \tag{5.1}$$

where $f(\mathbf{x})$ is the objective function that aims to be minimised; $g_i(\mathbf{x})$ and $h_j(\mathbf{x})$ are the inequality and equality constraints, respectively; and $\mathbf{x}_L$ and $\mathbf{x}_U$ are the lower and upper limits of the design variables $\mathbf{x}$.

5.2 Optimisation problem classification

Optimisation algorithms can be classified depending on a series of attributes, and no single optimisation algorithm is effective or appropriate for all possible optimisation problems. In this work, different strategies have been considered to solve the structural optimisation problems. According to [66], one can subdivide the strategies in terms of the function evaluation, algorithm and search method as:

- Function evaluation: { Direct / Surrogate model
- Search method: { Local / Global
- Algorithm: { Mathematical / Heuristic

5.2.1 Function evaluation

Concerning the function evaluation, it can be done directly by solving the numerical models involved in the system. That is, in the case of structural optimisation, the output will be provided by the FE solver. In this research, the direct simulations are performed by using the in-house CUF-based FE solver. Another possible way to evaluate the functions involved is by building a surrogate model, or metamodel, that mimics the desired output, whether it is the objective or a constraint function. This strategy might be preferred when computationally demanding simulations are involved, as it could be the case of buckling or fundamental frequency optimisation, in which different structural matrices have to be calculated prior to solving an eigenvalue problem. In particular, in this work, a metamodel based on polynomial functions was utilised to optimise the fundamental frequency and buckling of tow-steered plates. These

results are available in Sections 6.5.1 and 6.5.2, respectively, while the mathematical background is depicted in the following.

Although in this manuscript polynomial expressions are used to construct a surrogate model, other mathematical instruments can be used to solve the optimisation problem. That is the case of Artificial Neural Networks (ANN) [85], Kriging processes [123], Polynomial Chaos Expansion [112] or Radial Basis Functions [124]. The mathematical derivation of how the polynomial surrogate model is created will consider a second-order polynomial, although it can be easily extended to higher orders. The expression for the second-order polynomial can be expressed as:

$$f(\mathbf{x}) = \xi_0 + \sum_{i=1}^{n} \xi_i x_i + \sum_{i=1}^{n} \sum_{j=i+1}^{n} \xi_{ij} x_i x_j + \sum_{i=1}^{n} \xi_{ii} x_i^2 \tag{5.2}$$

where ξ_0, ξ_i and ξ_{ij} are the polynomial coefficients, x_i are the independent variables and n the number of independent variables. To fit the surrogate model to the data set, the least squares method is used to calculate the polynomial coefficients. If a total of N_s samples are employed to construct the surrogate model and two design variables, $n = 2$, are considered, the regression problem reads as:

$$\mathbf{f} = \boldsymbol{\Psi}\boldsymbol{\xi} \tag{5.3}$$

in which $\mathbf{f}$ is a $N_s \times 1$ column vector containing the data samples of the function that one aims to mimic, $\boldsymbol{\xi}$ contains the coefficients of the polynomial and $\boldsymbol{\Psi}$ is a matrix with the N_s values of the design variables, i.e.:

$$\boldsymbol{\Psi} = \begin{bmatrix} 1 & x_{11} & x_{12} & x_{11}x_{12} & x_{11}^2 & x_{12}^2 \\ 1 & x_{21} & x_{22} & x_{21}x_{22} & x_{21}^2 & x_{22}^2 \\ \vdots & \vdots & \vdots & \vdots & \vdots & \vdots \\ 1 & x_{N_s1} & x_{N_s2} & x_{N_s1}x_{N_s2} & x_{N_s1}^2 & x_{N_s2}^2 \end{bmatrix}, \tag{5.4}$$

which, in general, is not a square matrix [125]. Therefore, the coefficient vector can be calculated as:

$$\boldsymbol{\xi} = (\boldsymbol{\Psi}^T\boldsymbol{\Psi})^{-1}\boldsymbol{\Psi}^T\mathbf{f} \tag{5.5}$$

5.2.2 Search method

The classification in terms of the search method is related to the way in which the design space is explored. On the one hand, the local search starts from a single point and forms a sequence of points that hopefully converges into a local optimum. On the contrary, global search algorithms try to investigate the whole design space aiming to

find the global optimum. Despite its name, a global search method does not guarantee that any optimum found is a global one.

It is a common that gradient-based algorithms are recalled as local search and gradient-free algorithms as global search. However, this is a mistake and they should be viewed as independent attributes. As an example, a global search can be performed to provide starting points for a gradient-based strategy. Likewise, some gradient-free algorithms are based on local search strategies.

The selection of search type is essentially related to the modality of the design space. A local search is be sufficient if the design space is unimodal, as it will converge to the global optimum. Contrariwise, if the design space is multimodal, a local search will converge to an optimum that might be local. A global search increases the chances of converging to a global optimum, although is not guaranteed by any means.

5.2.3 Optimisation algorithm

Regarding how the iterative process associated to the optimization algorithm is conducted as well as the optimality criteria, these can be divided in gradient-based and heuristic.

Gradient-based are based on mathematical principles associated to the iterative procedure and the optimality criteria. On the contrary, gradient-free algorithms can be subdivided into mathematical and heuristic in terms of optimality criteria and iterative process. In this context, the mathematical gradient-free algorithms are referred to as derivative-free algorithms. Heuristic gradient-free algorithms consider a large variety of nature-inspired algorithms, such as Genetic Algorithm (GA) and Particle Swarm Optimisation (PSO). In the case of heuristic algorithms, the optimality criteria is an issue since they do not prove that a given point is a local optimum. This clashes with mathematical optimality criteria, which are unambiguous about optimality and converge to an optimum.

This work considers the CUF-based FE solver a black-box whose input are the fibre path orientation angles, and whose output is the objective function. In this context, one could consider choosing a gradient-based optimiser in which the calculation of the derivatives is made by finite-differences. However, when estimating the derivatives using finite-differences one faces the so-called step-size dilemma. Estimating the derivative has a truncation error of $O(h)$, or $O(h^2)$ when using second order, and one would like to choose a small step size in order to reduce this error. However, as the step size diminishes, roundoff error becomes dominant. In this manner, given the opposite trends of the truncation and roundoff errors, there is an optimal size step for which the sum of the two errors is at a minimum. In the literature, one can find different

approaches to calculate the gradients. This is the case of the Complex Step derivative approximation [126], and Algorithmic differentiation (AD) [127, 128], also known as Automatic differentiation. However, these two later methods require access to the source code.

Considering the above information about the treatment of the FE solver, and with the aim to explore the whole design space, this research employs two optimisation algorithms. First, an in-house GA is used for the fundamental frequency and buckling optimisation of variable stiffness composites plates in Sections 6.5.1 and 6.5.2. The developed GA is depicted in the following. Later, for the vertical deflection, strain concentration and strength optimisation problems, see Sections 6.5.3, 6.5.4 and 6.5.5, an optimisation algorithm incorporated in modeFrontier© [129] that combines global and local search, and balances the direct simulation and surrogate model-based optimisation. The fundamental frequency optimisation accounting for manufacturing defects in Section 6.5.6 is solved similarly to the latter three optimisation problems.

The optimisation problems that are faced in Sections 6.5.1 to 6.5.6 consider a fixed number of plies and aim to optimise the fibre path of the individual layers to minimise the objective function. Instead, if the scope of the optimisation problem is minimising the mass and the number of layers is allowed to vary, a different optimisation strategy should be pursued. In this case, the optimisation problem is categorised as a mixed-integer, and other approaches should be considered to solve it. For example, one could consider a multiobjective optimisation problem in which one of the objectives is mass minimisation and the other is fundamental frequency maximisation. Then, after studying the Pareto front, one could select the optimal configuration of its convenience.

Genetic Algorithm

GA comprise a family of gradient-free optimisation algorithms inspired by the evolution theory. They implement a repeated process of slight stochastic variations followed by selection. In each iteration, or generation, new offspring are generated from their parents. In other words, each new candidate solution is generated from solutions already evaluated. Based on their fitness, i.e.: the value of the objective functions, the better offspring are selected to become the parents of the next generation. In this context, three operators are involved in the generation of new offspring, namely: selection, crossover and mutation. A flowchart depicting the optimisation process is included in Fig. 5.1. Unlike gradient-based optimisers, GA starts with a random set of solutions, also called population. For each of the population individuals, the objective and constraint functions are evaluated. A termination criteria is then checked. If it is not satisfied, the population is modified by the aforementioned operators and a new

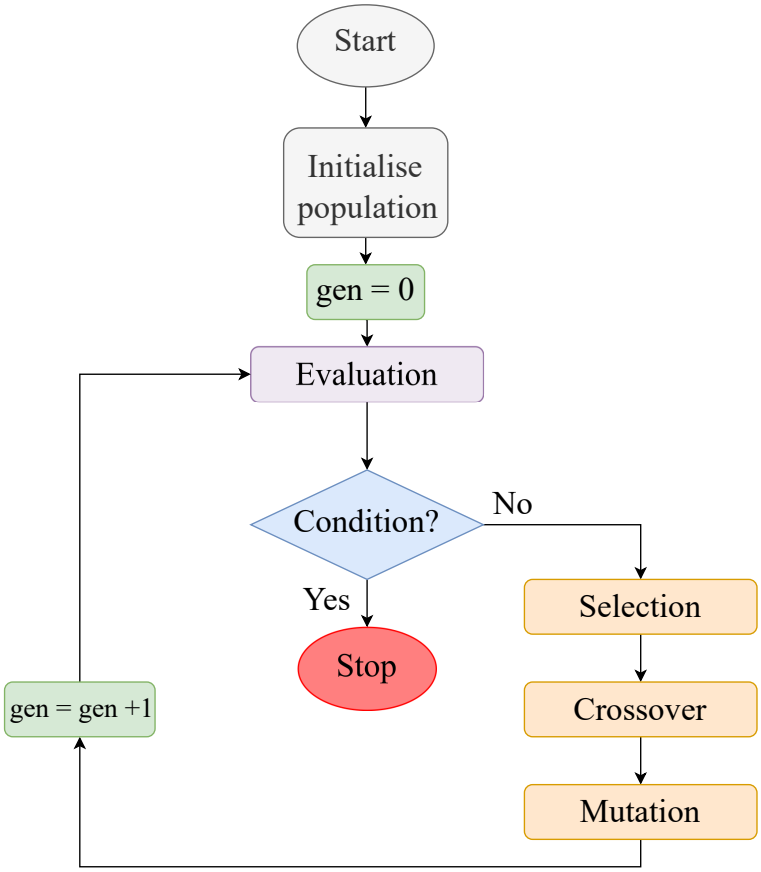

Figure 5.1 Flowchart of a generic GA.

population is created. Subsequently, the generation counter is incremented to indicate that one generation of the GA is completed.

GAs present different methods for representing the design variables. There are two broad categories: binary-encoded and real-encoded GA. The former utilises bits to represent the design variables, while real-encoded keep the same real value representation used in most other optimisation algorithms. In binary-encoded GAs, each variable is represented as a binary number with m bits. In the binary representation, each bit has a location j and a value b_j, which is either 0 or 1. To represent a real-valued variable in the finite interval $x_i \in [x_{i,L}, x_{i,U}]$, one has to divide it into $2^m - 1$ intervals, which size is given by:

$$\Delta x_i = \frac{x_{i,U} - x_{i,L}}{2^m - 1}. \tag{5.6}$$

The genetic operators will act and manipulate directly the binary representation. After these operators are applied, decoding is necessary to evaluate the objective and constraint functions of the successive generation. To decode each design variable, the following expression is used:

$$x_i = x_{i,L} + \sum_{j=0}^{m-1} b_j 2^j \Delta x_i \tag{5.7}$$

As depicted in Fig. 5.1, the first action that is needed is initialising the population. This can be made at random. When using binary encoding, one can assign each bit a 50% chance of being either 0 or 1. This can be done by generating a random number r in the [0,1] interval. If $r \leq 0.5$, the bit is set to 0 and 1 if $r > 0.5$. For a population containing n_p individuals, with n design variables and m bits being used to encode each variable, a total of $n_p \times n \times m$ bits need to be generated. On the contrary, when a real-encoded GA is used, the whole set of design variables of an individual can be obtained as follows:

$$\mathbf{x} = \mathbf{x}_L + \mathbf{r}^T (\mathbf{x}_U - \mathbf{x}_L), \tag{5.8}$$

where $\mathbf{r}$ is a vector containing random values following a uniform distribution in the $[0,1]$ range, i.e.: $r_i \sim \mathscr{U}(0,1)$. Of course, more effective methods can be employed to create the initial population that spans across the whole design space. For instance, Latin Hypercube Sampling (LHS) permits to explore the design space more effectively [130].

To characterise the individuals genotype, i.e.: the genes containing the design variables, two approaches can be followed. The first is the consideration of a set of binary strings to represent the design parameters. For instance, a set of two design

variables, x_1 and x_2, that equal 8 and 10, respectively, can be written as:

$$\underbrace{01000}_{x_1=8} \quad \underbrace{01010}_{x_2=10}. \tag{5.9}$$

The second approach directly considers the value of the design variable as it is. That is, in the aforementioned case, one will just have $x_1 = 8$ and $x_2 = 10$. This approach is referred to as real-encoded. As the reader can observe, if the binary strings are considered, coding and decoding operations will be necessary to evaluate the objective function and constraints comprised in the optimisation problem. A discussion on how the genetic operators act on the individual genotypes depending on its characterisation is available in the following.

Selection This operation selects the parents for the next generation based on their fitness performance. It is possible that an individual is selected as parent more than once, in which case it will contribute its genes to more than one child. There exists a plethora of methods for the parent selection, among which roulette and tournament selection are two of the most spread. The former chooses the parents by simulating a roulette wheel in which the area of the section of the wheel corresponding to an individual is proportional to the individual's expectation. Then, a random number is generated to select one of the sections with a probability equal to its area. Instead, the tournament selection chooses each parent by comparing the fitness function of a set of individuals and cherry-picking the one with best fitness. This two methods can be applied straightforwardly regardless of the encoding approach since they use the values of the objective function.

Crossover This operator serves to generate individuals with new genotypes in the population. As in the case of selection, there exists a number of crossover operators in the GA literature. In most of the cases, two individuals are picked from the population at random and a portion of their genes are exchanged to create new design variables combination. Single- or multiple-point crossover methods are utilised when binary-encoding is considered. In a single-point crossover operator, this is performed by randomly choosing a crossing position and exchanging all the design variables on the right side of the crossing side. Instead, when real-encoding is used, a standard method is linear crossover, which generates two or more points in the line defined by the two parent points. Another option for real-encoding is a crossover as in the binary case. All these crossover methods are devised in Fig. 5.2.

Mutation As in the case of the crossover operator, the mutation operator is also responsible for the search aspect of GA. The main purpose of the mutation is to keep

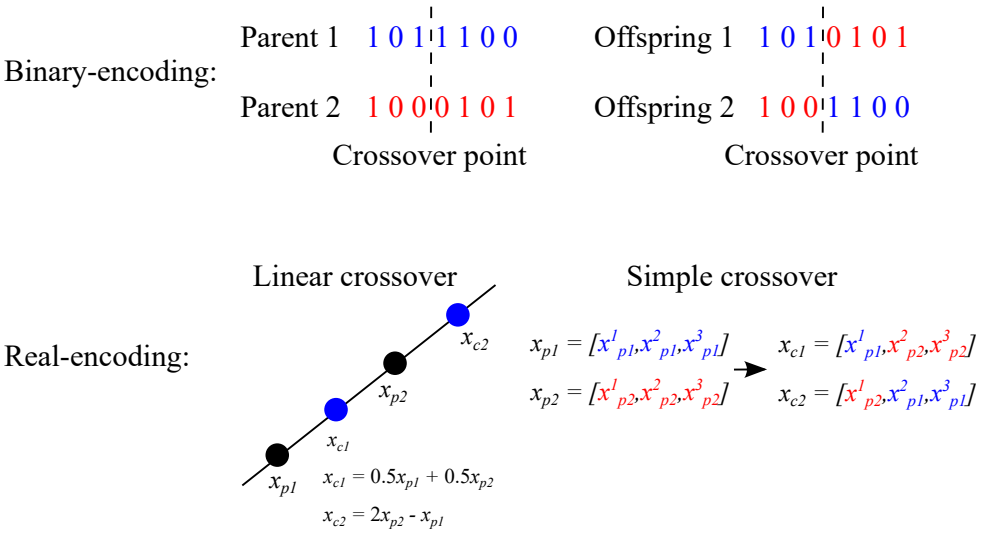

Figure 5.2 Crossover operators for binary- and real-encoded GA. The linear crossover operator foresees that parent 2 is more fit than parent 1 ($f(x_{p2}) < f(x_{p1})$).

Table 5.1 Mutation operator acting on a binary-encoded individual.

Before mutation	1	0	1	1	1	0	0
After mutation	1	0	1	1	0	0	0

diversity in the population. In the binary-encoded approach, the mutation procedure requires the creation of a random number r_i for every bit or design variable, so that $r_i \sim \mathscr{U}(0,1)$. If this random number is lower than the mutation probability p_m, then the bit or design variable is modified. In this regard, a 1 would become 0, and vice versa. This is illustrated in Table 5.1. Conversely, in the case of real-encoded design variables, the mutated design variable can be perturbed as follows:

$$x_i^{\text{mut}} = x_i + (r_i - 0.5)\Delta_i \tag{5.10}$$

where Δ_i is a predefined maximum perturbation in the i^{th} design variable.

Chapter 6

Numerical results

Based on the formulations derived in the previous chapters, this section discusses multiscale analysis, optimisation and design of VAT structures. First, the stress state at the layer scale of VAT composite plates and shells is predicted using the methodology depicted in Section 2. These results are included in [131]. Second, layer and fibre scale analyses are conducted based on the embedded CW approach described in Section 3.1. These outcomes are present in [132]. Subsequently, the application of MSG-CUF for thermo-elastic problems at the fibre-matrix scale is shown. These results were reported in [133]. A second set of results is devoted to studying the mechanical performance of VAT composites affected by uncertainty defects at different material scales. The manufacturing flaws are modelled through stochastic fields, described in Section 4.3, and propagated from the fibre scale up to the layer scale. These cases are available in [134–137]. Last, the mechanical characteristics of tow-steered composites are optimised. Not only are optimal angle distributions sought, but the effect of different structural theories on the retrieval of optimum design variables is also investigated. The optimisation results are partially included in [138, 139].

6.1 Stress state prediction of VAT plates and shells

6.1.1 Clamped VAT plate

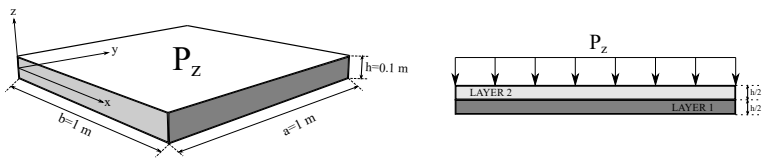

Figure 6.1 Geometry and loading condition of the clamped VAT plate.

The first numerical assessment regards a two-layered squared VAT plate introduced in Demasi et al. [93]. The plate has a width a equal to one meter, presents a width-to-thickness ratio $a/h = 10$ and has a $\theta = [\langle 90°, 45° \rangle, \langle 0°, 45° \rangle]$ stacking sequence. A pressure $p_z = 10$ kPa is applied on the top surface, whereas all the edges are clamped. Table 6.1 provides the material properties of the composite material considered in this analysis. Figure 6.1 shows the laminated structure.

Table 6.1 Material properties of the two-layered squared VAT plate from Demasi *et al.* [93].

E_1 [GPa]	$E_2 = E_3$ [GPa]	G_{12} [GPa]	G_{23} [GPa]	$\nu_{12} = \nu_{13}$ [-]	ν_{23} [-]
137.9	8.96	7.10	6.21	0.30	0.49

A convergence study is carried out first to perform accurate calculations. This analysis considers nine-node quadratic Q9 FE, while a third-order LD expansion per layer is employed in the thickness direction. Table 6.2 gathers the vertical deflection at the plate's centroid, while Fig. 6.2 presents the σ_{xz} and σ_{zz} stress components in the thickness direction at $(-0.25, -0.25)$ m. From these results, it is evident that the 14×14Q9 mesh provides converged and accurate results regarding vertical deflection u_z and stress prediction.

The effect of the structural theory on the predicted deflection and stress distribution is now addressed. A series of high-order TE-based ESL models are confronted against the reference results and those obtained with the previous LW models. Each model is discretised with a 14×14Q9 mesh. Table 6.2 enlists the vertical deflection, while Fig. 6.3 provides the transverse stress distribution. It is appreciated that low-order ESL models underestimate the vertical deflection. Indeed, at least a sixth-order structural theory is needed to predict the same deflection value as the LW-1LD3 model. Despite predicting the same value of u_z, a disagreement is found in retrieving the transverse stress components. It is appreciated in Fig. 6.3 that the ESL-TE 1 cannot predict the σ_{xz} and σ_{zz} components, which present linear trends. The ESL-TE 3 structural theory produces a quadratic distribution of σ_{xz}, but discontinuous at the layer's interface; the predicted σ_{zz} does not match that of the reference. Last, the sixth-order ESL theory

Table 6.2 Mesh convergence on the deflection at the two-layered squared plate's centroid. Each model employs a 1LD3 expansion per layer.

Mesh	DOF	$-u_z \cdot 10^6$ [m]
8×8 Q9	6069	6.37
12×12 Q9	10092	6.40
14×14 Q9	17661	6.41
16×16 Q9	22869	6.41

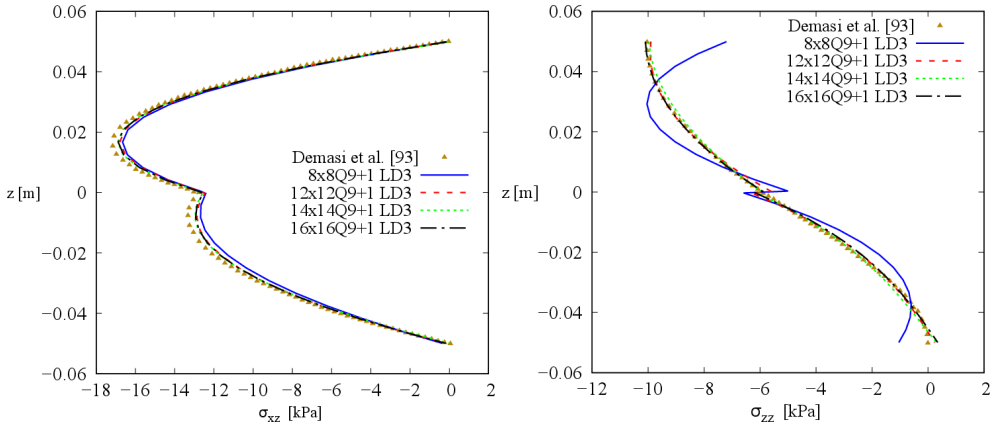

(a) σ_{xz}. **(b)** σ_{zz}.

Figure 6.2 Convergence study of the transverse stress distributions for the clamped VAT plate. Calculated through the thickness at $(-0.25, -0.25)$ m.

Table 6.3 Effect of the structural theory on the deflection at the two-layered squared plate's centroid. Each model employs a 14×14 Q9 mesh.

Model	DOF	$-u_z \cdot 10^6$ [m]
ESL-TE 1	5046	5.68
ESL-TE 3	10092	6.34
ESL-TE 4	12615	6.39
ESL-TE 6	17661	6.41
ESL-TE 7	20184	6.41
LW-1LD3	17661	6.41

of structures captures well the σ_{xz} component at the top and bottom of the laminate and struggles at the interface. Conversely, the transverse normal component perfectly matches that of the reference and the LW-1LD3 model. Last, it is appreciated that the proposed LW-1LD3 is in perfect correlation with the reference results.

6.1.2 Clamped VAT shell

The second numerical assessment concerns a six-layered clamped VAT shell component, which fibres are steered in $\theta = [0\langle 0,50\rangle, 90\langle 0,75\rangle, 45\langle 0,15\rangle]_s$. The shell's geometrical properties and boundary conditions are illustrated in Fig. 6.4, and the material properties are reported in Table 6.4.

Table 6.4 Material properties of the clamped VAT shell.

E_1 [GPa]	$E_2 = E_3$ [GPa]	G_{12} [GPa]	G_{23} [GPa]	$\nu_{12} = \nu_{13}$ [-]	ν_{23} [-]
165.0	9.00	5.60	2.80	0.34	0.50

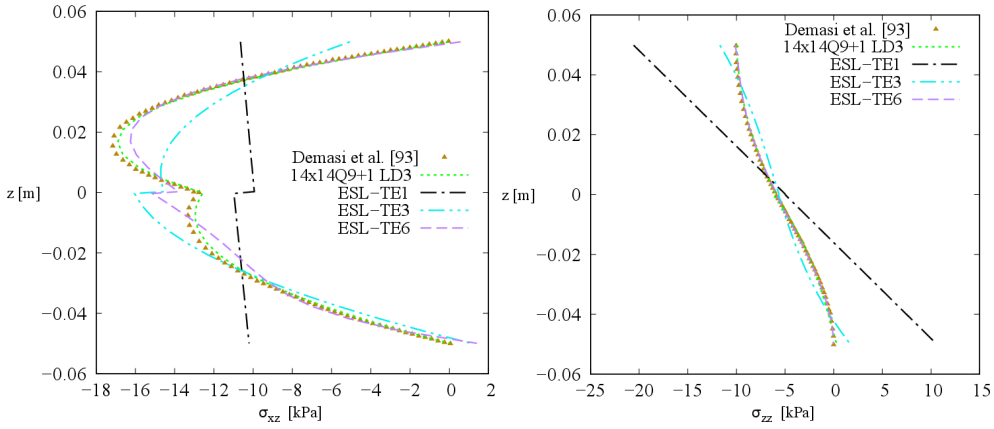

(a) σ_{xz}. **(b)** σ_{zz}.

Figure 6.3 Effect of different structural theories on the transverse stress distributions for the clamped VAT plate. Calculated through the thickness at $(-0.25, -0.25)$ m. Each model employs a 14×14Q9 mesh.

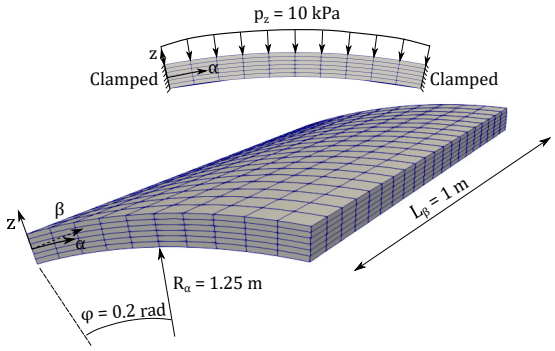

(a)

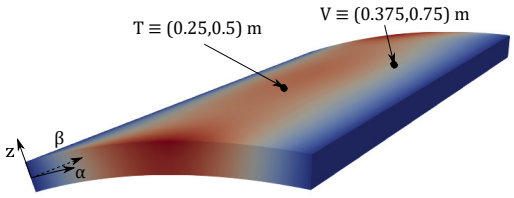

(b)

Figure 6.4 Graphical description of the clamped curved VAT panel: (a) geometry and boundary conditions; (b) points were magnitudes are measured at.

Table 6.5 Mesh convergence for the vertical displacement calculated at the centroid of the clamped VAT shell. All the meshes employ a 1LD2 expansion.

Model	DOF	$-u_z \cdot 10^6$ [m]
6×2Q9	2535	2.37
10×5Q9	9009	2.93
20×10Q9	33579	3.00
30×15Q9	73749	3.01

First, a convergence study is performed. A 1LD2 expansion per layer is employed in the thickness direction. Table 6.5 gathers the vertical deflection at the centroid of the shell. Figure 6.5 represents the $\sigma_{\alpha\alpha}$, σ_{zz}, $\sigma_{\beta z}$ and $\sigma_{\alpha\beta}$ stress components along the thickness direction at point V, see Fig. 6.4b. One can observe small discrepancies between the FE meshes regarding vertical deflection and in-plane stress components $\sigma_{\alpha\alpha}$ and $\sigma_{\alpha\beta}$. Nevertheless, these are more evident in the transverse stress components σ_{zz} and $\sigma_{\beta z}$. From these results, it is inferred that a 20×10Q9 mesh is necessary to obtain a good prediction of stresses as it produces very close results to those obtained with the 30×15Q9 discretisation.

The next step addresses the influence of the chosen structural theory on stress prediction. A series of LW-LD and ESL-TE expansions are compared against the results provided by commercial software Abaqus [140]. For this purpose, the 20×10Q9 mesh is employed, while the Abaqus model utilises 80×40×18 C3D20R quadratic solid elements. Figure 6.6 represents the stress components along the thickness at point V. It is observed that the ESL-TE models cannot capture the $\sigma_{\beta z}$ component. In contrast, the remaining stress components agree with those obtained by the 1LD2 and 1LD3 expansions. Moreover, the 1LD1 structural theory does not retrieve the transverse components well. In detail, the $\sigma_{\alpha z}$ and $\sigma_{\beta z}$ present a constant, or linearly-varying, value within the layer and do not have null value at the top and bottom of the laminate. This occurs because with the LD1 expansion, the field of displacements varies linearly within the ply, and hence, the transverse strains and stresses are constant within the layer. The same reasoning applies to compute σ_{zz}. Concerning the ESL-TE models, they accurately predict the in-plane stress components while underperforming in evaluating the transverse shear terms, especially the low-order ESL-TE 1 and ESL-TE 2 theories. Nevertheless, ESL-TE 3 and ESL-TE 4 calculate these components better as they practically satisfy the null value condition at the top and bottom. In this regard, higher-order ESL theories could eventually provide these components accurately. The Abaqus model could not provide accurate results for the transverse components. Therefore, they are not included in Figs. 6.6c to 6.6e.

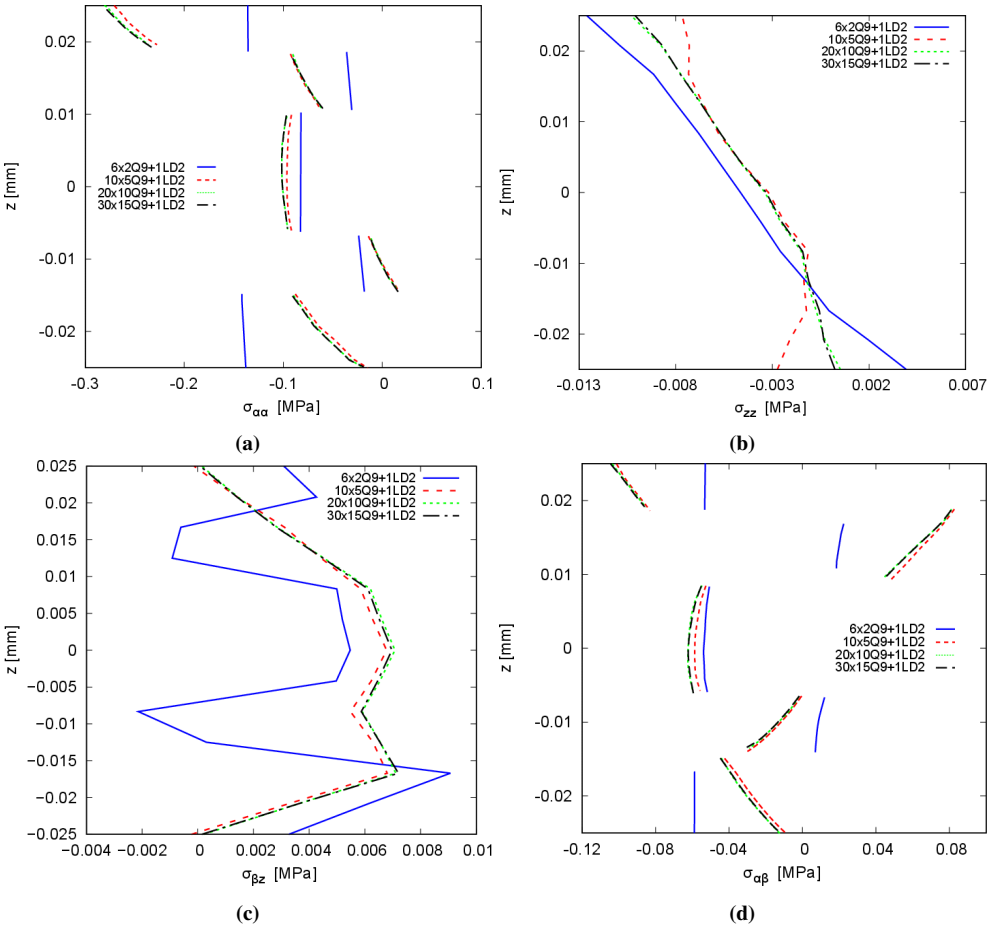

Figure 6.5 Convergence study of the stress distributions for the clamped VAT shell calculated through the thickness at point V.

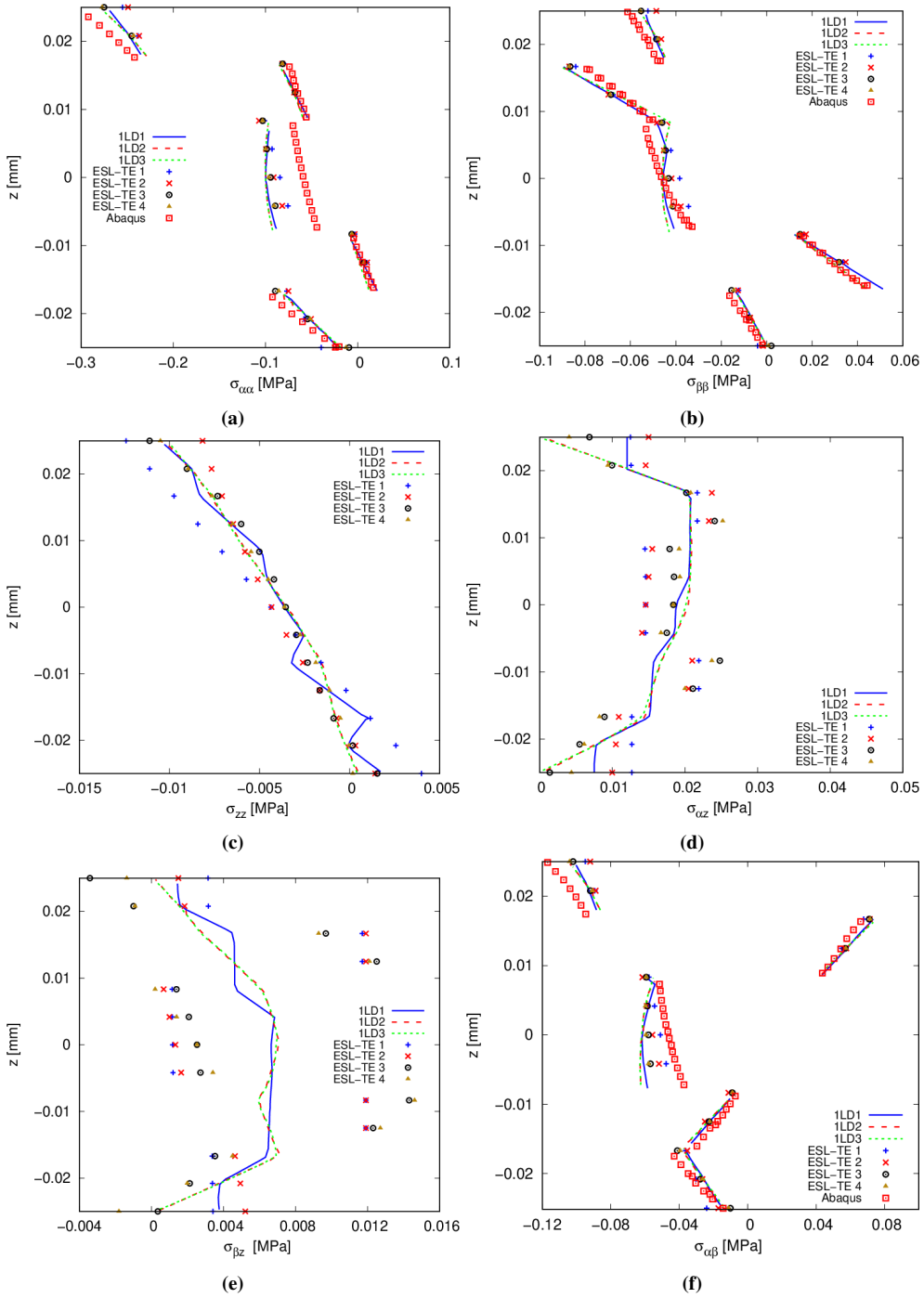

Figure 6.6 Effect of different structural theories on the stress distributions for the clamped VAT shell. Calculated through the thickness at point V. Each model employs a 20×10Q9 mesh.

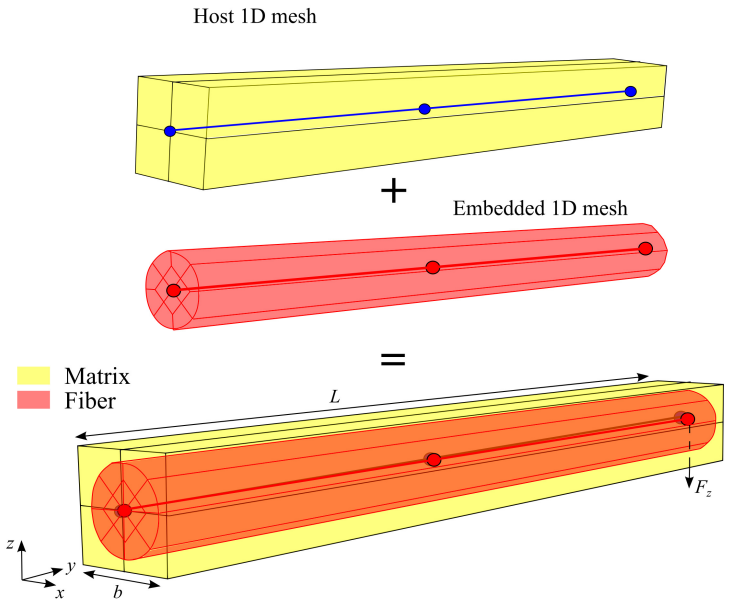

Figure 6.7 Fibre-matrix beam geometry with host and embedded meshes, dimensions and boundary conditions.

6.2 Embedded unified finite elements

The efficiency and effectiveness of the embedded CW method are showcased by comparing it against classic beam theories, commercial FE tools and the already existing CW approach [106]. The following nomenclature is adopted: H*A*B4-*X*L9+E*C*B4-*Y*L9, where A and C denote the number of cubic beam elements (B4), using Lagrange shape functions, employed to discretise the host and embedded components, respectively; X and Y represent the number of cross-sectional bi-quadratic subdomains (L9) that describe the host and embedded beam cross-section, respectively. Note that the B4 beam elements and L9 cross-sectional subdomains are selected based on the author's experience.

6.2.1 Square-pack unit cell subject to bending load

A fibre-matrix square-pack RUC subject to a bending load, taken from [141], is used to verify the proposed methodology. A graphical representation is available in Fig. 6.7. The length of the microstructure is $L = 1$ mm, whereas the width $b = 0.1$ mm, and the fibre volume fraction $V_f = 0.5027$, which implies a fibre diameter $d = 0.08$ mm. For simplicity, both constituents have been considered isotropic. The fibre Young's modulus $E = 202.04$ GPa and $\nu = 0.2128$, while those of the matrix are $E = 3.252$

GPa and $\nu = 0.355$. The structure is clamped on one end, and a concentrated load $F_z = -0.1$ N is applied at $y = L$.

The model is verified by comparing the vertical displacement, longitudinal and transverse shear stress components at different locations of the fibre-matrix ensemble obtained by various numerical models available in the literature. In detail, classic beam theories such as Euler-Bernouilli (EBBT) and Timoshenko (TBT), refined CW, based on LE and HLE, and Nastran solid models (HEXA8) are reported in Table 6.6. In addition, the distribution of the longitudinal and shear transverse stress components along the thickness are illustrated in Fig. 6.8. The solutions include Nastran HEXA8 and HLE8-CW models. These results suggest the following:

- From the displacements reported in Table 6.6, one notices that EBBT, TBT, L- and HLE-CW, and HEXA8 are more compliant numerical models than the embedded CW. The reason is twofold: (i) The embedded CW models use less FE to achieve convergence, while L- and HLE-CW employ ten cubic and quadratic elements, respectively; (ii) Both L- and HLE-CW use a cross-section discretisation that better describes the circular shape of the fibre. The former utilises a combination of nine- and six-node elements, while the latter employs a mapping strategy to characterise the fibre domain.

- The embedded CW models remarkably capture the stress field within the fibre-matrix body. The normal in-plane component σ_{yy} in Fig. 6.8a perfectly matches the HEXA8 and HLE8 results. The transverse shear σ_{yz} is perfectly captured by increasing the cross-section elements of the host beam. Indeed, the parabolic shape is retrieved when nine and sixteen L9 cross-section descriptions are utilised.

6.2.2 Global-local analysis of laminated beam

In this case, a composite cross-ply beam including fibres, matrix, and homogenised layers from [141] is modelled with the embedded CW and confronted against the literature. The total length of the beam is $L = 40$ mm, while the width and thickness are $b = 0.8$ mm and $t = 0.6$ mm, respectively. A $[0,90,0]^\circ$ layup sequence is considered, having each ply equal thickness. The fibre diameter is 0.16 mm and is as long as the length of the beam. The disposition of the fibre, matrix and homogenised layers is depicted in Fig. 6.9. The material properties of the different constituents are enlisted in Table 6.7. Note that the properties of the homogenised layers are retrieved through the rule of mixtures. A concentrated load $F_z = -1$ N is applied at $(0,L,0)$. Twelve L9

Table 6.6 Vertical displacement and stress tensor components for the different numerical models of the cantilevered fibre-matrix square-pack.

Model	Model name	DOF	u_z [mm] at $[0,L,0]$	σ_{yy} [MPa] at $[0,L/2,d/2]$	σ_{yz} [MPa] at $[-d/2,L/2,d/2]$
References					
Nastran HEXA8 fine [141]	-	296160	$-7.857\cdot10^{-2}$	$9.555\cdot10^{2}$	-0.3394
EBBT [142]	-	363	$-7.811\cdot10^{-2}$	$9.469\cdot10^{2}$	-0.1962
TBT [142]	-	605	$-7.835\cdot10^{-2}$	$9.469\cdot10^{2}$	-0.1962
12L9+8L6 [142]	-	7533	$-7.933\cdot10^{-2}$	$9.450\cdot10^{2}$	-0.2500
HLE4 [141]	-	4557	$-7.771\cdot10^{-2}$	$9.400\cdot10^{2}$	-0.3022
HLE8 [141]	-	15531	$-7.775\cdot10^{-2}$	$9.361\cdot10^{2}$	-0.3558
Present model					
H1B4-4L9+E1B4-12L9	Model 1.1	300+684	$-7.635\cdot10^{-2}$	$9.015\cdot10^{2}$	-0.2933
H2B4-4L9+E2B4-12L9	Model 1.2	525+1197	$-7.739\cdot10^{-2}$	$8.914\cdot10^{2}$	-0.5943
H3B4-4L9+E3B4-12L9	Model 1.3	750+1719	$-7.773\cdot10^{-2}$	$9.378\cdot10^{2}$	-0.2796
H4B4-4L9+E4B4-12L9	Model 1.4	975+2223	$-7.791\cdot10^{-2}$	$9.264\cdot10^{2}$	-0.2715
H5B4-4L9+E5B4-12L9	Model 1.5	1200+2736	$-7.801\cdot10^{-2}$	$9.344\cdot10^{2}$	-0.2759
H5B4-9L9+E5B4-12L9	Model 1.6	2352+2736	$-7.809\cdot10^{-2}$	$9.305\cdot10^{2}$	-0.3045
H5B4-16L9+E5B4-12L9	Model 1.7	3888+2736	$-7.816\cdot10^{-2}$	$9.330\cdot10^{2}$	-0.2825

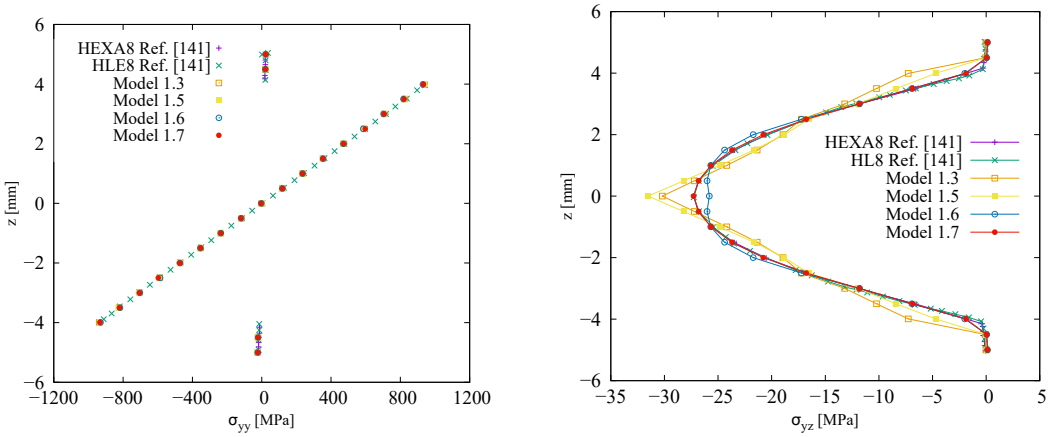

(a) σ_{yy} **(b)** σ_{yz}

Figure 6.8 Through-the-thickness stress distribution of the cantilevered square-pack at midspan.

Table 6.7 Material elastic properties of the cross-ply composite beam constituents, taken from Carrera *et al.* [141].

Constituent	E_{11} [GPa]	$E_{22}=E_{33}$ [GPa]	$\nu_{12}=\nu_{13}$ [-]	ν_{23} [-]	$G_{12}=G_{13}$	G_{23} [GPa]
Fibre	202.038	12.134	0.2128	0.2704	8.358	4.756
Matrix	3.252	3.252	0.355	0.355	1.20	1.20
Layer	103.173	5.145	0.2835	0.3124	2.107	2.353

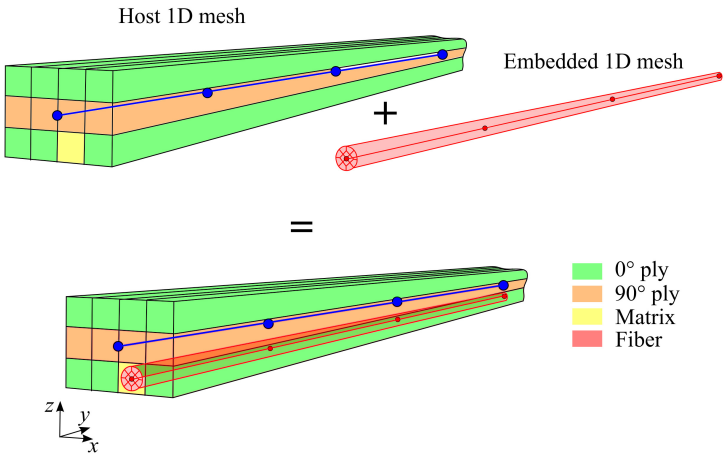

Figure 6.9 Cross-ply beam with embedded 0° fibre. The host grid considered the 0° and 90° layers as well as the matrix. The embedded grid models the fibre.

subdomains are used to characterise their cross-section for both the host and embedded components.

The vertical deflection and stresses from the literature references and the present approach are enlisted in Table 6.8. The reference results were obtained with Nastran HEXA8 solid elements and HLE-based CW models from [141]. The displacement is evaluated at the loaded end, while the stresses are measured at the fibre centroid at midspan. In addition, the through-the-thickness distributions of σ_{yy} and σ_{yz} predicted with the different models are available in Fig. 6.10. The following comments can be made:

- The displacements enlisted in Table 6.8 agree with those provided by the references. Similarly, the longitudinal stress σ_{yy} in Fig. 6.10a are well correlated with those provided by the HLE6 model from [141].

- The σ_{yz} component is illustrated in Fig. 6.10b. A good agreement is found for the homogenised layer region, that is, above $z = -0.12$ mm. Also, Models 2.1.4 and 2.1.6 of the current methodology capture the reference's trend in the fibre domain. Discrepancies at the fibre-matrix interface are observed due to the interpolation of the host displacements.

6.2.3 Non-crimp textile

A non-crimp fabric composite is analysed in the following. The material properties of the fibre tows and matrix are reported in Table 6.9. The planar dimensions of the textile are 2×2 mm and 0.24 mm thick. Each tow has an elliptical section with major

Table 6.8 Vertical displacement and stress tensor components for the different numerical models of the cantilevered cross-ply with embedded fibre at 0°.

Model	Model name	DOF	u_z [mm] at $[0,L,0]$	σ_{yy} [MPa] at $[b/8,L/2,-0.2]$	σ_{yz} [MPa] at $[b/8,L/2,-0.2]$
References					
Nastran HEXA8 [141]	-	1579653	-15.69	$-5.928\cdot10^2$	-2.147
HL2 [141]	-	5859	-10.46	$-3.717\cdot10^2$	-124.390
HLE4 [141]	-	14601	-14.98	$-5.659\cdot10^2$	-2.381
HLE6 [141]	-	29295	-14.98	$-5.659\cdot10^2$	-2.408
Present model					
H1B4-12L9+E1B4-12L9	Model 2.1	756+684	-14.96	$-5.646\cdot10^2$	-1.805
H2B4-12L9+E2B4-12L9	Model 2.2	1323+1197	-14.97	$-5.618\cdot10^2$	-1.026
H3B4-12L9+E3B4-12L9	Model 2.3	1890+1710	-14.98	$-5.605\cdot10^2$	-1.876
H4B4-12L9+E4B4-12L9	Model 2.4	2460+2223	-14.98	$-5.666\cdot10^2$	-2.287
H5B4-12L9+E5B4-12L9	Model 2.5	3024+2736	-14.98	$-5.651\cdot10^2$	-1.865
H6B4-12L9+E6B4-12L9	Model 2.6	3591+3249	-14.98	$-5.647\cdot10^2$	-2.469

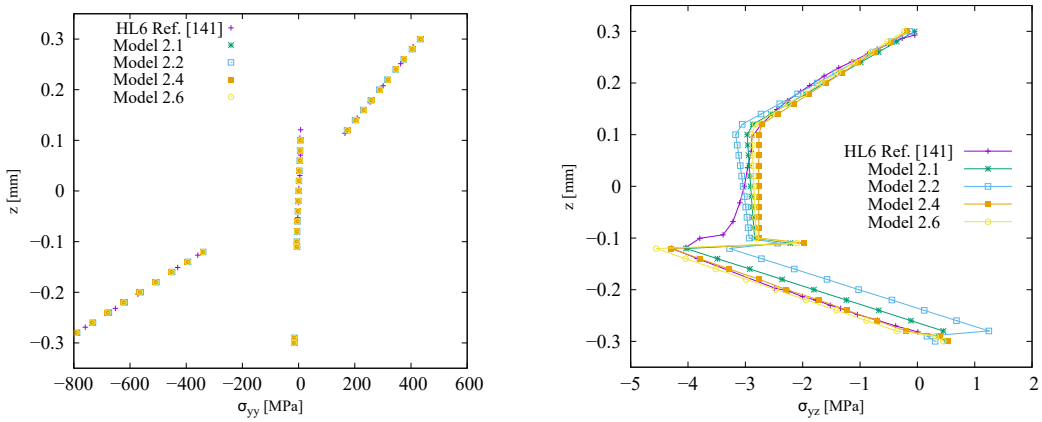

(a) σ_{yy} **(b)** σ_{yz}

Figure 6.10 Through-the-thickness stress distribution at $[b/8,L/2]$ of the cantilevered cross-ply with embedded fibre at 0°.

Table 6.9 Material elastic properties of the non-crimp fabric composite.

Constituent	E_{11} [GPa]	$E_{22}=E_{33}$ [GPa]	$\nu_{12}=\nu_{13}$ [GPa]	$G_{12}=G_{13}$ [GPa]
Tow	184.5	10.13	0.26	6.95
Matrix	3.5	3.5	0.35	1.30

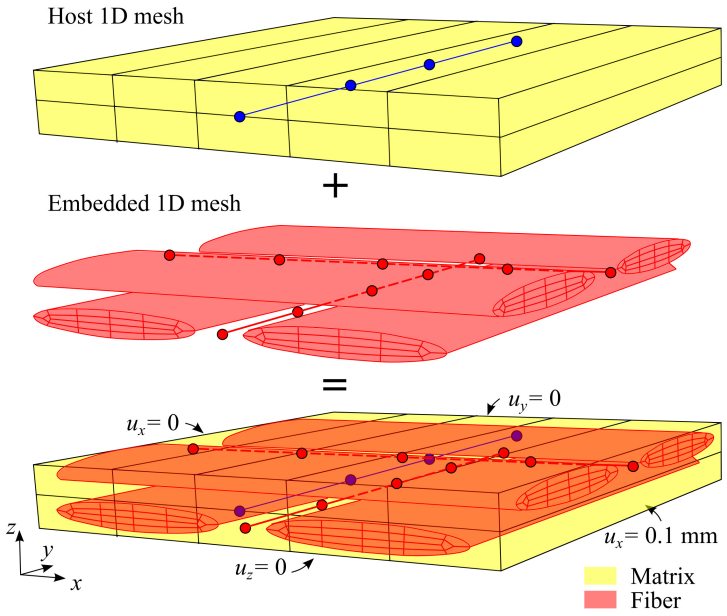

Figure 6.11 Non-crimp textile representation. The host grid represents the matrix, while the embedded one represents the warp and weft yarns.

and minor axes equal to 0.8 and 0.1 mm, respectively. Four sets of 1D embedded elements are considered, corresponding to the fibre tows in both directions, while 1D host elements are employed for the matrix constituent. The yarns in the x-axis are labelled warp yarns, while those oriented along the y-axis are referred to as weft yarns. This configuration is illustrated in Fig. 6.11.

The embedded CW model is compared with an Abaqus 3D (ABQ3D) model comprising 229040 C3D8R elements from [143]. The simulation outcomes are provided in Table 6.10 and Fig. 6.12. The displacements in Table 6.10 are evaluated at the matrix between the warp and weft yarn, while stresses are measured at the warp fibre. The results suggest the following:

- There is a good agreement between the solid ABQ3D model and the present embedded CW in terms of u_x, σ_{xx} and σ_{yy}. They present a 0.04%, -0.09% and 4.84% relative difference between ABQ3D and Model 3.4.

- The embedded CW overestimates the u_y displacement compared to the ABQ3D solution. A 22.62% relative difference between ABQ3D and Model 3.4 is found.

- Regarding the through-the-thickness stress distributions in Fig. 6.12, the embedded CW models predict perfectly the σ_{xx} stress component by ABQ3D. A slight difference in the bottom region of the warp fibre is observed in Fig. 6.12a. On the other hand, the σ_{yy} distribution differs in the matrix and the weft fibre

regions. These differences are mainly due to the overprediction of u_y in the matrix.

Table 6.10 Displacements and stresses of non-crimp fabric subject to uniaxial pulling.

Model	Model name	DOF	u_x [mm] at [0.5,0.5,0]	u_y [mm] at [0.5,0.5,0]	σ_{xx} [MPa] at [0.5,0.5,0.06]	σ_{yy} [MPa] at [2.5,7.5,0.06]
References						
ABQ3D [143]	-	756696	$7.499 \cdot 10^{-2}$	$2.272 \cdot 10^{-3}$	9191.97	94.27
Present model						
H3B4-10Q9+E3B4-22Q9	Model 3.1	1650+12120	$7.507 \cdot 10^{-2}$	$2.825 \cdot 10^{-3}$	9195.27	107.53
H4B4-10Q9+E4B4-22Q9	Model 3.2	2145+15756	$7.506 \cdot 10^{-2}$	$2.800 \cdot 10^{-3}$	9203.13	106.05
H5B4-10Q9+E5B4-22Q9	Model 3.3	2640+19392	$7.502 \cdot 10^{-2}$	$2.803 \cdot 10^{-3}$	9185.29	99.13
H5B4-20Q9+E5B4-22Q9	Model 3.4	4095+15756	$7.502 \cdot 10^{-2}$	$2.786 \cdot 10^{-3}$	9183.67	98.83

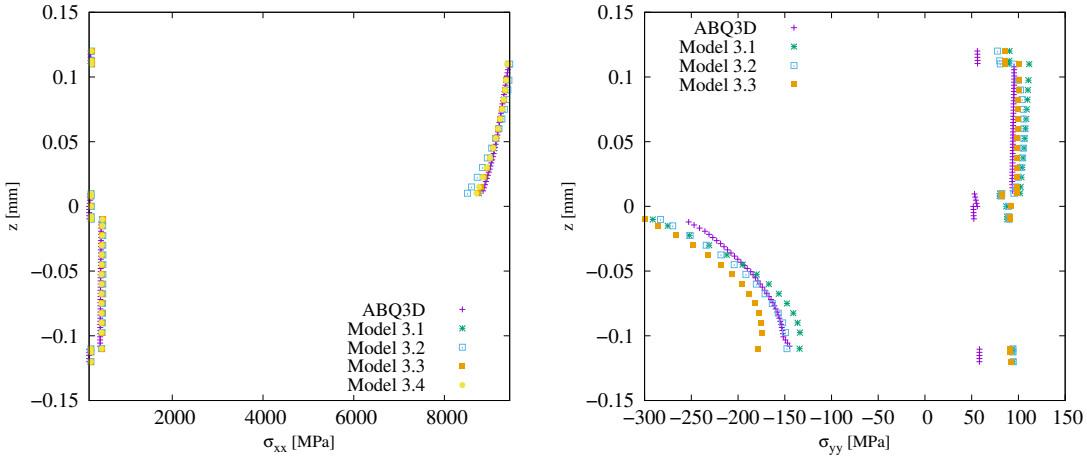

(a) σ_{xx} **(b)** σ_{yy}

Figure 6.12 Through-the-thickness stress distribution at (0.5,0.5) of the non-crimp fabric.

6.3 Thermo-elastic microscale analyses

This section tests the thermo-elastic microscale models developed in Section 3.2 against analytical, semi-analytical and established software tools such as SwiftComp [144]. Homogenised material properties for fibre- and particle-reinforced composites and stress recovery in fibre-reinforced composite microstructures are retrieved. The differences between SwiftComp and the present approach reside in the fact that the former uses 2D FE for fibre-reinforced RUC and 3D FE when particles are involved. Conversely, the proposed method uses 1D FE along the longitudinal direction and 2D expansions for the cross-section.

Table 6.11 Effective CTEs of fibre-reinforced composite B/Al square-pack provided by the literature and the present approach, considering different HLE polynomial order. The fibre volume fraction is set to 0.47.

Model	DOF	$\alpha_{11} \cdot 10^6$ [K^{-1}]	$\alpha_{22} \cdot 10^6$ [K^{-1}]
Reference solutions			
Rosen and Hashin [24]	-	10.99	16.69
VAMUCH [144]	-	10.99	16.69
Voigt [145]	-	12.09	12.09
Reuss [146]	-	16.00	16.00
MOC [28]	-	10.85	16.89
GMC [29]	-	10.85	16.88
HFGMC [30]	-	10.91	16.34
Tamma and Avila [147]	-	10.77	17.34
CUF-MSG			
HLE 2	240	11.06	16.48
HLE 4	582	11.02	16.59
HLE 6	1140	11.02	16.60
HLE 8	1914	11.02	16.61

6.3.1 Homogenisation of fibre- and particle-reinforced composites

The first numerical assessment comprises a boron fibre embedded in an aluminium matrix, referred to as B/Al hereinafter, arranged in a square-pack geometry. A linear beam element is used because the fluctuations will be invariant along the fibre direction.

The two constituents are isotropic, with $E = 379.3$ GPa, $\nu = 0.10$ and $\alpha = 8.1 \cdot 10^{-6}$ K^{-1} for the boron fibre, while the properties of the aluminium are $E = 68.3$ GPa, $\nu = 0.30$ and $23.0 \cdot 10^{-6}$ K^{-1}. The validation against analytical formulae (Rosen and Hashin [24]), Voigt [145] and Reuss [146]) as well as semi-analytical (MOC [28], GMC [29], HFGMC [30]) and numerical solutions [147]. Different HLE orders are utilised to calculate the homogenised α_{11} and α_{22}. The resulting CTEs are enlisted in Table 6.11 for a fixed fibre volume fraction equal to 47%. There is a good correlation between the proposed method and the reference results, except for Voigt and Reuss, which are alternative versions of the rule of mixtures.

The effect of the fibre volume fraction on the longitudinal and transverse CTE is illustrated in Fig. 6.13. An eighth-order HLE is used for the cross-section definition. A good agreement between CUF-MSG and the literature solutions is observed across the fibre volume range. Again, the most significant differences are found when compared to the Voigt [145] and Reuss [146] analytical solutions.

A silicon carbide fibre embedded in a copper matrix, referred to as SiC/Cu composite, is taken into account to predict the effective specific heat. The SiC/Cu RUC

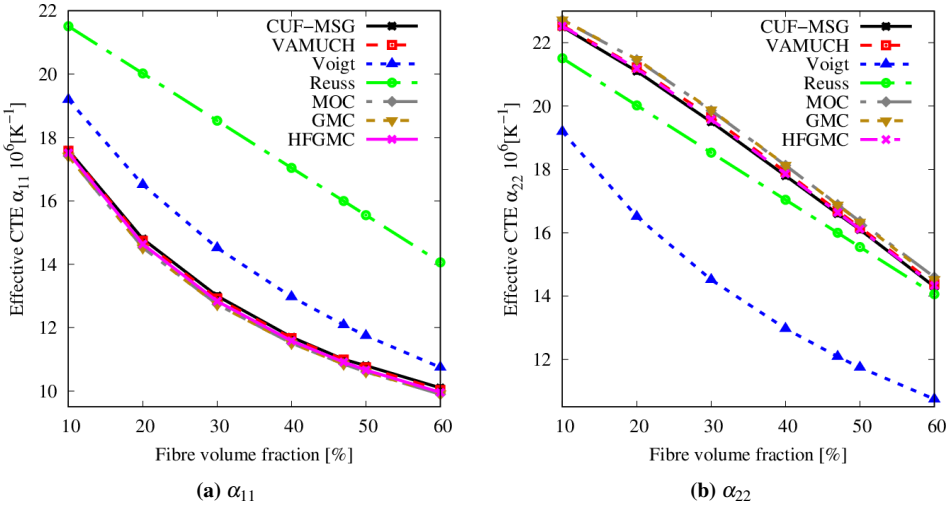

(a) α_{11} **(b)** α_{22}

Figure 6.13 Variation of the CTEs of fibre-reinforced composite B/Al square-pack with regard to the fibre volume fraction. An eighth-order HLE is used as expansion function.

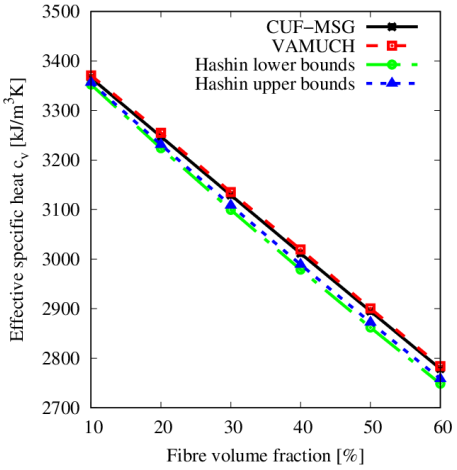

Figure 6.14 Variation of the effective specific heat of the fibre-reinforced SiC/Cu square-pack with regard to the fibre volume fraction. An eighth-order HLE is used as expansion function.

presents a square-pack fibre arrangement. The fibre and matrix are considered as isotropic materials. The SiC fibre material properties are $E = 410$ GPa, $\nu = 0.14$, $\alpha = 4.0 \cdot 10^{-6}$ K^{-1} and $c_v = 2327.73$ kJ/(m^{3}K), while the copper matrix has $E = 117$ GPa, $\nu = 0.34$, $\alpha = 22.0 \cdot 10^{-6}$ K^{-1} and $c_v = 3485.09$ kJ/(m^{3}K). Figure 6.14 presents the variation of the specific heat in a fibre volume fraction range between 10 and 60%.

The influence of the geometry of the reinforcement particles on the thermal properties is studied now. Parallelepiped and cylindrical inclusions are modelled. The latter is illustrated in Fig. 6.15. When dealing with inclusions, the constituent distribution varies over the 3D space of the RUC. Thus, six four-node cubic beam elements are utilised to capture the correct description of changes along the beam axis. The different phases are involved in the numerical model thanks to the CW capabilities.

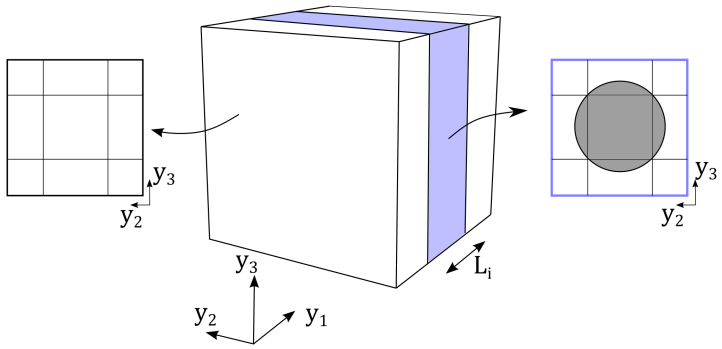

Figure 6.15 HLE beam model of cylindrical particle-reinforced RUC. L_i denotes the length of the inclusion along which the mapped circular expansion is used.

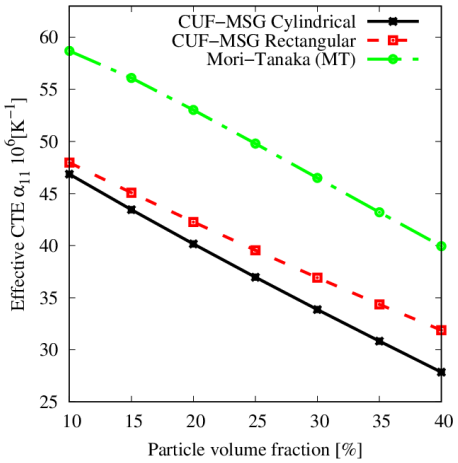

Figure 6.16 Variation of the effective longitudinal CTE α_{11} of a particle-reinforced glass/epoxy composite with regard to the particle percentage. An eighth-order HLE is used as expansion function.

A glass/epoxy particle-reinforced composite is studied first. The glass properties are $E = 72.38$ GPa, $\nu = 0.20$ and $\alpha = 5.0 \cdot 10^{-6}$ K^{-1}, while the epoxy matrix foresees $E = 2.75$ GPa, $\nu = 0.35$ and $\alpha = 54.0 \cdot 10^{-6}$ K^{-1}. The outcomes produced by both inclusion types are compared against the Mori-Tanaka (MT) method [27], which is widely used for reinforced materials. Note that MT does not consider the geometry of the reinforcement constituent. Results are included in Fig. 6.16. Minor differences between rectangular and cylindrical inclusions are observed for low particle volume fractions, while greater discrepancies arise for larger particle percentages. In addition, MT overestimates the CTE value compared to both inclusion geometries.

The effect on the geometry on the homogenised CTEs α_{11} and α_{22} is further addressed by comparing the previous geometries against a spherical inclusion modelled in SwiftComp. The results are enlisted in Table 6.12. The longitudinal CTE α_{11} of the spherical reinforcement lies between those of the cylindrical and rectangular inclusion.

Table 6.12 Effective CTEs of particle-reinforced composite glass/epoxy provided by the literature and the present approach, considering different HLE polynomial order and inclusion geometry. The particle volume fraction is set to 0.3.

Model	Expansion theory	$\alpha_{11} \cdot 10^6$ [K^{-1}]	$\alpha_{22} \cdot 10^6$ [K^{-1}]
VAMUCH Spherical [144]	-	35.50	34.97
Mori-Tanaka (MT)[27]	-	46.50	9.31
CUF-MSG Cylindrical	HLE 3	33.79	38.73
	HLE 6	33.86	38.78
	HLE 8	33.87	38.78
CUF-MSG Rectangular	HLE 3	36.85	36.80
	HLE 6	36.93	36.89
	HLE 8	36.93	36.90

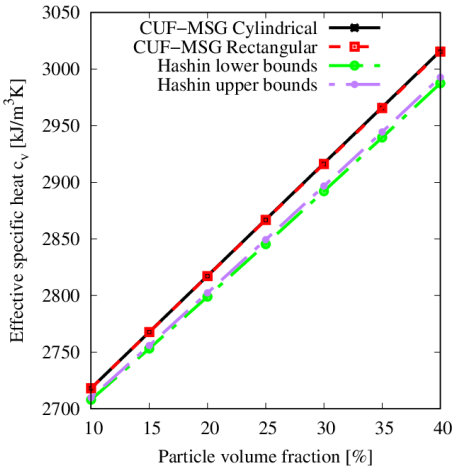

Figure 6.17 Variation of the effective specific heat of the fibre-reinforcedSteel/Al square-pack with regard to the particle volume fraction. An eighth-order HLE is used as expansion function.

On the contrary, the transverse CTE α_{22} of the spherical inclusion is lower than the ones provided by the MSG-CUF models.

The effect of the geometry of the inclusion on the effective specific heat is investigated in the following. An aluminium matrix is strengthened with a steel inclusion. The steel particle assumes $E = 200$ GPa, $\nu = 0.30$, $\alpha = 12.0 \cdot 10^{-6}$ K^{-1} and $c_v = 3609.6$ kJ/(m^{3}K), while the aluminium thermo-elastic properties are $E = 68.3$ GPa, $\nu = 0.33$, $\alpha = 23.0 \cdot 10^{-6}$ K^{-1} and $c_v = 2619.1$ kJ/(m^{3}K). The effective specific heat as a function of the particle volume fraction is represented in Fig. 6.17. It is worth noting that no difference is appreciated between the cylindrical and rectangular inclusion, as opposed to the previous inclusion study. However, slight differences are appreciated if compared to Rosen and Hashin [24] analytical method.

6.3.2 Stress recovery of fibre-reinforced composites

The local stress recovery for the different constituents at the RUC level is a complex step in microscale analysis after a load is applied to the global structure. Capturing high gradients in strain/stress solutions needs highly refined models. In the present work, high-order HLE kinematics are required to provide accurate solutions.

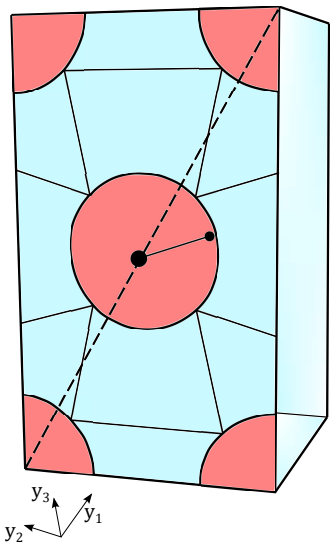

Figure 6.18 HLE beam model of an hexa-pack RUC.

The local stress state of a glass/epoxy with a hexa-pack fibre arrangement is predicted. The glass fibre is considered as isotropic with $E = 72.38$ GPa, $\nu = 0.20$ and $\alpha = 5.0 \cdot 10^{-6}$ K^{-1}. The epoxy matrix is also isotropic with $E = 2.75$ GPa, $\nu = 0.35$ and $\alpha = 55.0 \cdot 10^{-6}$ K^{-1}. The fibre volume fraction is set to 0.30. Figure 6.18 depicts the hexa-pack configuration as an HLE beam model. The cross-section is modelled through fifteen expansion subdomains, in which five correspond to the fibre and the remaining ten to the matrix.

The stress state that arises within the RUC when a unitary longitudinal strain ε_{11} and a 100 K temperature raise is represented in Fig. 6.19. An eighth-order HLE was utilised to obtain the accurate 3D stress contour. Besides, Figs. 6.19b and 6.19d show the variation of σ_{22} and σ_{23} along the diagonal highlighted in Fig. 6.18. It is appreciated that the HLE2 model cannot provide an accurate stress distribution. Indeed, it overestimates the σ_{22} and σ_{23} components as appreciated in Figs. 6.19b and 6.19d. The HLE4 provides similar results to those by the HLE6 and HLE8 models for the σ_{22} term. However, it is not sufficient to calculate accurately the transverse shear component σ_{23}. In this regard, additional side and internal expansion terms of the HLE are necessary; recall Section 2.2 and the work by Carrera *et al.* [141]. These results demonstrate that high-order HLE kinematics allow the stress gradients that occur at

the fibre-matrix interface to be captured. This is better observed for the transverse stresses where the fibre and matrix are under tension and compression states.

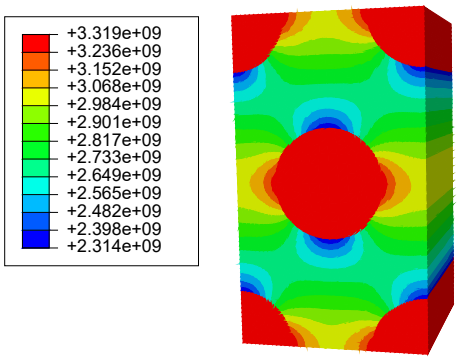

(a) σ_{22} by CUF-MSG

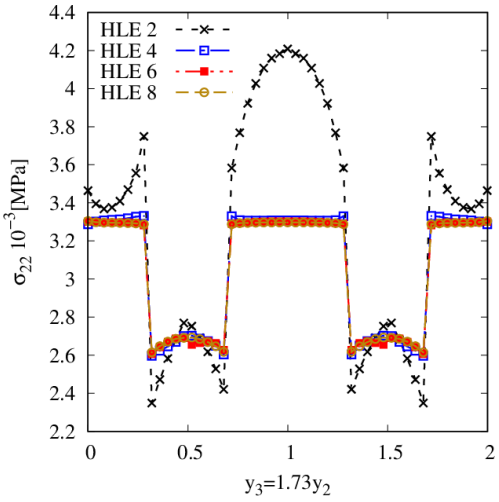

(b) σ_{22} distribution

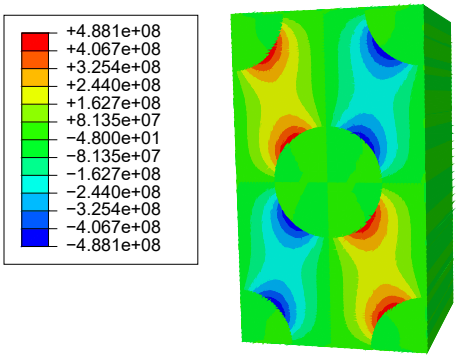

(c) σ_{23} by CUF-MSG

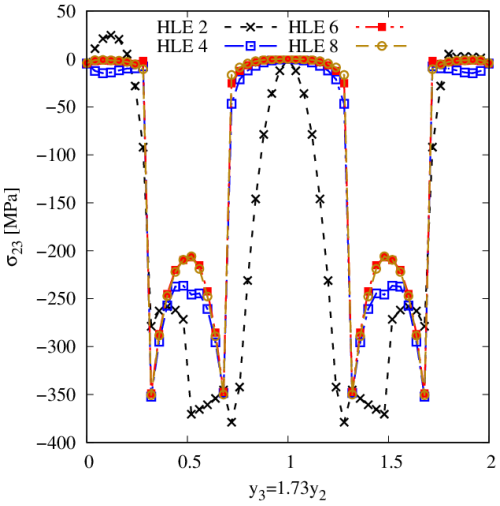

(d) σ_{23} distribution

Figure 6.19 Stress state due to a unitary longitudinal strain ε_{11} and a 100 K raise in temperature of a glass/epoxy hexa-pack. An eighth-order HLE is used as expansion function in the 3D representation.

6.4 Influence of uncertainty defects

This section provides numerical studies regarding the influence of layer and fibre scale uncertainty defects on the mechanical performance of VAT composites. In detail, the impact of fibre misalignments, or fibre waviness, on the stress state and buckling load prediction is analysed first. Secondly, the effect of fibre waviness and variability in

the fibre volume fraction on the buckling performance and fibre-matrix stress state is studied.

6.4.1 Layer scale uncertainty

Stochastic stress analysis

First, the 3D stress state and the failure modes of Hashin 3D criteria are studied when fibre misalignments are considered within the numerical model. The Correlation Matrix Decomposition (CMD) technique was considered first to generate the random fields that will map the misalignments into the integration points of the virtual model. The waviness field was supposed to have a null mean and a standard deviation $\sigma_\theta = 1.5^\circ$ according to the literature [148]. The VAT component under study was already presented in Section 6.1.1. Table 6.13 reports the considered material strengths.

Table 6.13 Material strengths used for the failure indices uncertainty analysis of the two-layered clamped plate from Section 6.1.1.

X_T [MPa]	X_C [MPa]	Y_T [MPa]	Y_C [MPa]	S_{12} [MPa]	$S_{13} = S_{23}$ [MPa]	Z_T [MPa]
2586.0	1620.0	94.0	340.50	152.66	174.54	60.0

A thousand Monte Carlo simulations were performed, and the statistical envelopes, namely mean value, 95% confidence interval and minimum-maximum range, of the stress state at point $(-0.25, -0.25)$ m are represented in Fig. 6.20. Table 6.14 contains the statistics of the stress field at $2z/h = 0.416$. It is appreciated that the mean value barely differs from the pristine solution. Additionally, the 95% confidence interval does not present a significant variation in the stress components. On the contrary, the minimum-maximum range of σ_{xx} and σ_{yy} shows a vast variability, which can be deleterious for the failure indices. The transverse stress components present a lower minimum-maximum range, which is reasonable as only in-plane waviness is considered in the numerical model.

The failure indices are represented in Fig. 6.21 along its mean value, 95% confidence interval and minimum-maximum range. Fibre failure, see Figs. 6.21a and

Table 6.14 Pristine value and statistics of the stress field evaluated at $2z/h = 0.4160$ for the $[\langle 90, 45\rangle, \langle 0, 45\rangle]$ clamped VAT plate after performing the Monte Carlo analysis.

	$\sigma_{xx} \cdot 10^{-5}$ [Pa]	$\sigma_{yy} \cdot 10^{-5}$ [Pa]	$\sigma_{zz} \cdot 10^{-5}$ [Pa]	$\sigma_{xz} \cdot 10^{-5}$ [Pa]	$\sigma_{yz} \cdot 10^{-5}$ [Pa]	$\sigma_{xy} \cdot 10^{-5}$ [Pa]
Pristine	-0.1158	-0.0729	-0.0853	-0.1661	-0.1256	0.1505
Mean value	-0.1151	-0.0727	-0.0854	-0.1661	-0.1254	0.1507
Standard deviation	0.0368	0.0085	0.0007	0.0023	0.0037	0.0118
Range	[-0.2421,0.04714]	[-0.10763,-0.03586]	[-0.08529,-0.08521]	[-0.1735,-0.1559]	[-0.1386,-0.1089]	[0.1120,0.2024]
95% C.I.	[-0.1174,-0.1128]	[-0.07324,-0.07219]	[-0.08763,-0.08258]	[-0.1662,-0.1659]	[-0.1256,-0.1252]	[0.1499,0.1514]

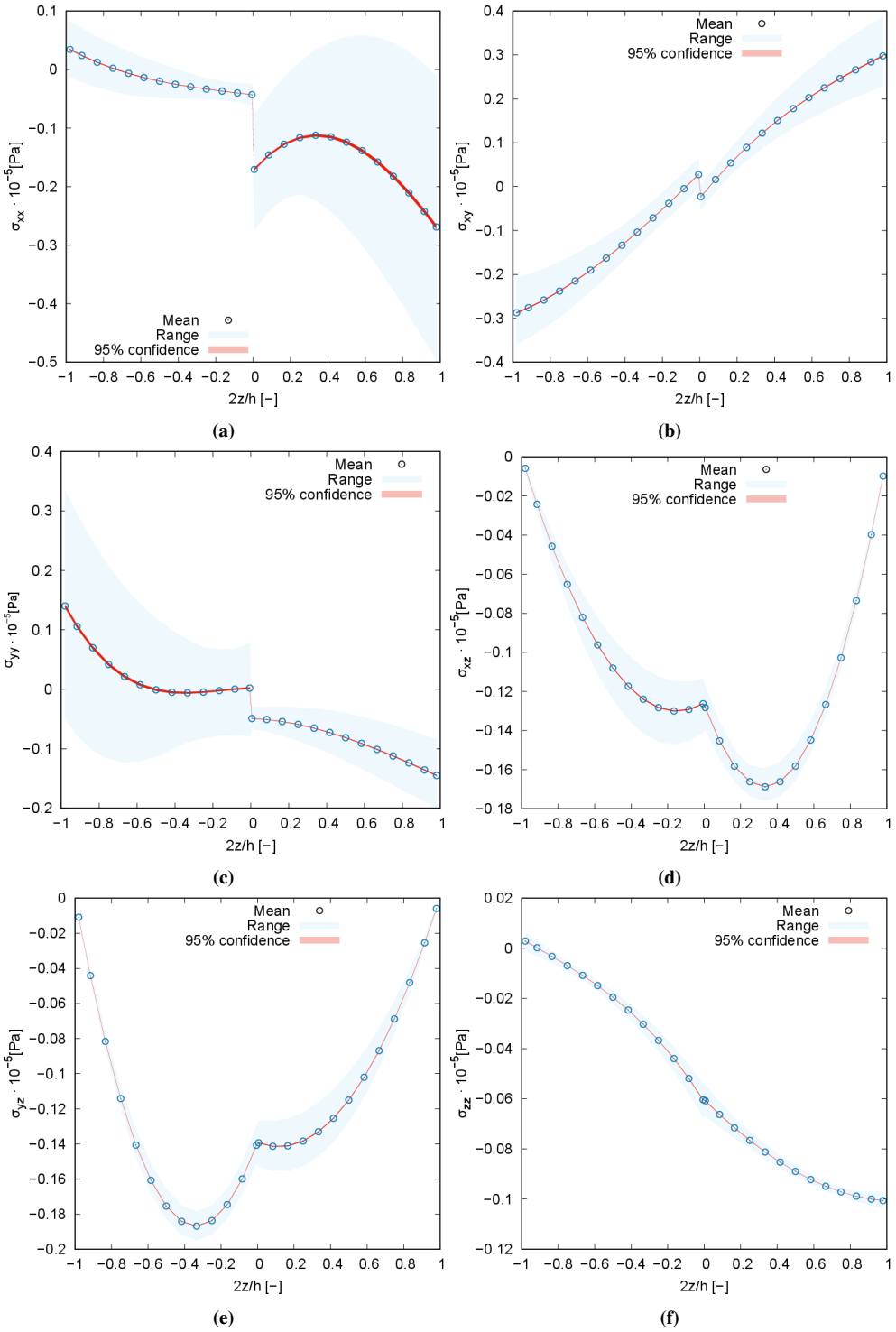

Figure 6.20 Through-the-thickness stress field, measured at point Q, for the pristine and flawed $[\langle 90,45\rangle, \langle 0,45\rangle]$ clamped plate. The fibre misalignment field has a null mean and standard deviation equal to $\sigma_\theta = 1.5°$.

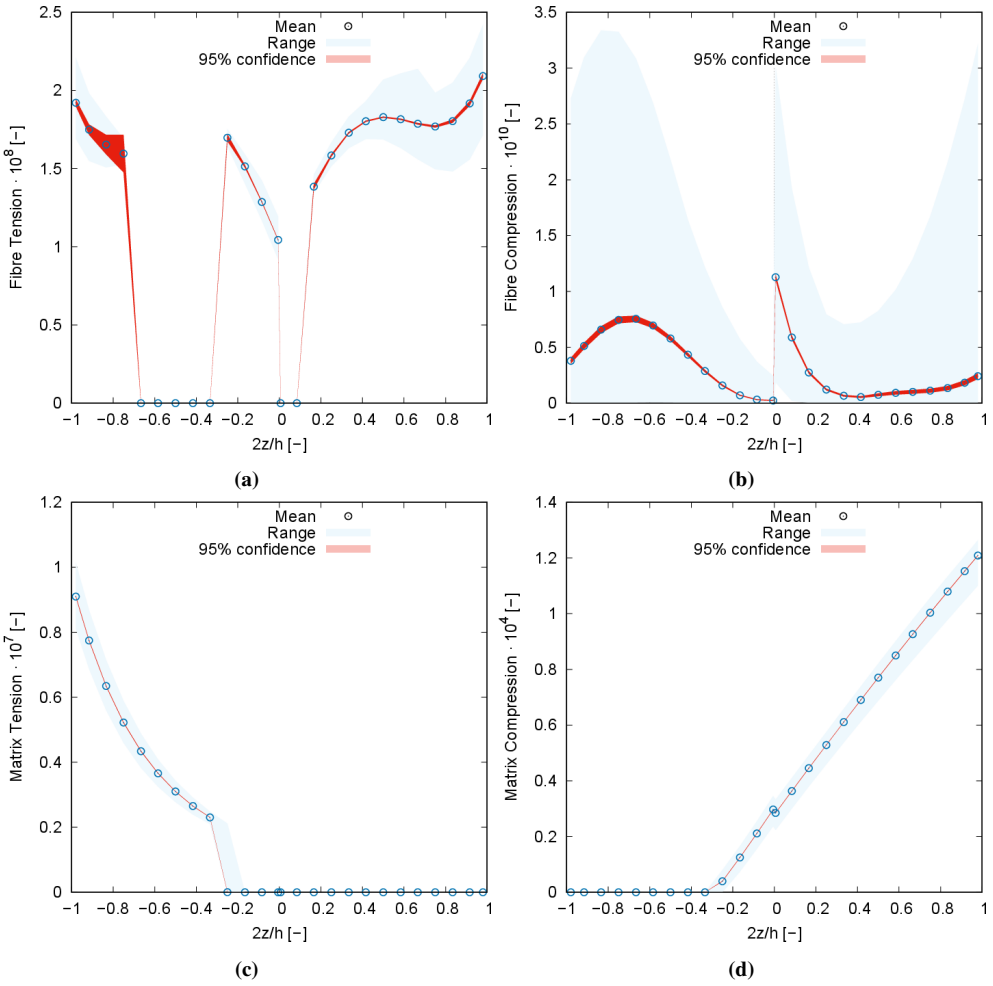

Figure 6.21 Through-the-thickness Hashin 3D failure indices, measured at $(-0.25, -0.25)$ m, for the pristine and flawed $[\langle 90,45\rangle, \langle 0,45\rangle]$ clamped plate. The fibre misalignment field has a null mean and standard deviation equal to $\sigma_\theta = 1.5°$.

6.21b, is first analysed. From Fig. 6.21a, and the expression to calculate the Fibre Tension failure index, reported in Appendix A, it is inferred that in $2z/h \in (-0.66, -0.40) \cup (0, 0.10)$, the σ_{11} stress component has a compression character. Furthermore, the lower ply is mainly subject to compression state in σ_{11} when the misalignments are modelled. The upper lamina is subject to compressive σ_{11}, although some outliers with $\sigma_{11} > 0$ are present, which leads to the data represented in Fig. 6.21a when $2z/h > 0.10$.

The matrix failure modes are represented in Figs. 6.21c and 6.21d. There is a clear differentiation between matrix tension and compression failure modes, as opposed to fibre failure. In case of matrix failure at point $(-0.25, -0.25)$ m, the structure will fail because of matrix compression in the upper ply, as this failure mode presents the largest value.

Stochastic buckling analysis

After studying how mesoscale flaws such as misalignments affect the 3D stress state and failure indices, it is time to understand how it may affect the buckling load. In detail, the effect of the selected structural theory on the buckling load prediction is addressed. As in the previous case, the CMD method is used to construct the stochastic fields that spread the waviness throughout the structure.

The object under consideration is a four-layered squared balanced and symmetric VAT plate with $\theta = [0 \pm \langle 45, 0 \rangle]_s$. The width and length are equal to $a = b = 0.254$ m, and ply thickness $t_{\text{ply}} = 0.127$ mm. The plate is clamped on the left edge, and a compression load is exerted on the right edge, whereas the top and bottom edges are free to deform. For the random field characterisation, a misalignment standard deviation $\sigma_\theta = 1^\circ$ is employed for this case.

The first five buckling loads, computed with LW and ESL models, are reported in Table 6.15. Furthermore, their respective buckling modes are illustrated in Figs. 6.22 to 6.24. It is inferred that low-order kinematics cannot accurately predict the buckling loads compared to LW models, especially in the higher modes. There are noticeable differences when observing the buckling modes. In detail, in those modes where the ESL-TE 1 cannot predict the bending-torsional couplings, since TE 1 corresponds to a Timoshenko beam model. In contrast, the ESL-TE 3 provides similar results for the first, second, third and fifth modes.

Table 6.15 Buckling loads N_{cr_i} of the $[0 \pm \langle 45, 0 \rangle]_s$ VAT structure computed with different beam models.

Model	DOF	N_{cr_1} [kN/m]	N_{cr_2} [kN/m]	N_{cr_3} [kN/m]	N_{cr_4} [kN/m]	N_{cr_5} [kN/m]
ESL-TE 1	288	0.55	1.14	2.11	3.27	4.81
ESL-TE 3	960	0.74	0.94	1.55	1.70	2.65
LW-L9	18144	0.73	0.88	1.22	1.58	1.75

The uncertainty study is conducted through a thousand Monte Carlo simulations. The resulting mean values and standard deviations of the first five buckling loads are available in Table 6.16. It is observed that the ESL-TE 3 model provides accurate results for the first buckling load yet still overestimates the remaining four if compared to the LW model. Nevertheless, it is remarkable that the ESL-TE 3 and LW standard deviations are similar for the first four buckling loads.

The Probability Density Function (PDF) of the buckling loads are displayed in Fig. 6.25. Note that the fifth buckling load's PDF is not shown because it does not show a normal distribution. In addition to the PDF of the buckling loads, the effect of misalignments on the buckling modes is addressed by computing the Modal Assurance Criterion (MAC) matrix. Each mode shape of each Monte Carlo sample is compared

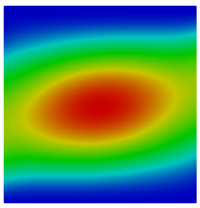

(a) First buckling mode

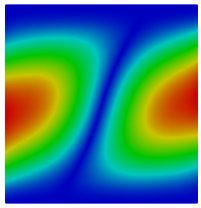

(b) Second buckling mode

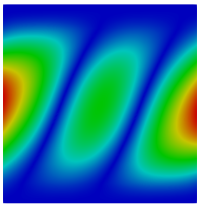

(c) Third buckling mode

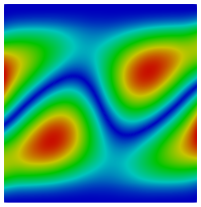

(d) Fourth buckling mode

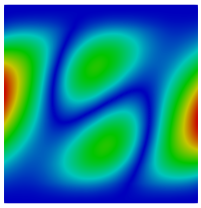

(e) Fifth buckling mode

Figure 6.22 Buckling modes of the pristine $[0 \quad \pm\langle 45,0\rangle]_s$ panel with clamped-free boundary conditions using an LW-L9 model.

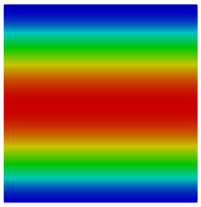

(a) First buckling mode

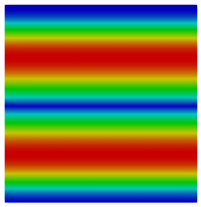

(b) Second buckling mode

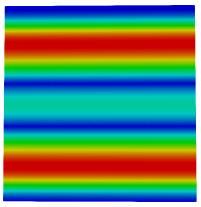

(c) Third buckling mode

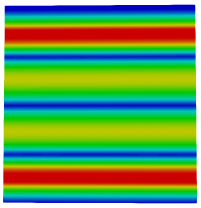

(d) Fourth buckling mode

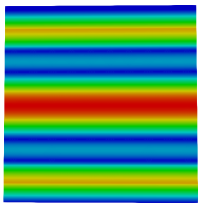

(e) Fifth buckling mode

Figure 6.23 Buckling modes of the pristine $[0 \quad \pm\langle 45,0\rangle]_s$ panel with clamped-free boundary conditions using an ESL-TE 1 model.

Table 6.16 Mean value and standard deviation of N_{cr_i} for the $[0 \quad \pm\langle 45,0\rangle]_s$ VAT panel using ESL-TE 1, ESL-TE 3 and LW-L9 structural theories.

Load	ESL-TE 1		ESL-TE 3		LW-L9	
	Mean [kN/m]	Std. Dev. [N/m]	Mean [kN/m]	Std. Dev. [N/m]	Mean [kN/m]	Std. Dev. [N/m]
N_{cr_1}	0.55	4.64	0.74	4.08	0.73	5.14
N_{cr_2}	1.14	14.35	0.95	5.03	0.88	4.96
N_{cr_3}	2.11	23.82	1.55	8.32	1.22	7.19
N_{cr_4}	3.27	37.76	1.70	9.01	1.58	10.68
N_{cr_5}	4.80	54.78	2.53	60.38	1.75	9.84

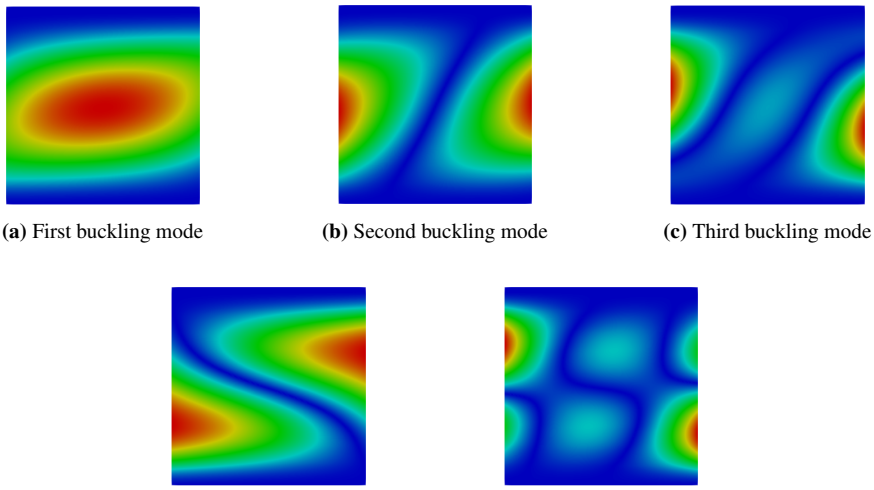

(a) First buckling mode **(b)** Second buckling mode **(c)** Third buckling mode

(d) Fourth buckling mode **(e)** Fifth buckling mode

Figure 6.24 Buckling modes of the pristine $[0 \ \pm\langle 45,0\rangle]_s$ VAT panel with clamped-free boundary conditions using an ESL-TE 3 model.

with its counterpart of the pristine structure using the following equation:

$$\mathrm{MAC}_{j,k}^{(i)} = \frac{|\phi_{i,j}^T \phi_{\mathrm{ref},k}|^2}{(\phi_{i,j}^T \phi_{i,j})(\phi_{\mathrm{ref},k}^T \phi_{\mathrm{ref},k})} \tag{6.1}$$

where $\mathrm{MAC}_{j,k}^{(i)}$ is the i^{th} sample of the j^{th} and k^{th} column of the MAC matrix; $\phi_{i,j}$ is the j^{th} eigenvector of the i^{th} sample, and $\phi_{\mathrm{ref},k}$ is the k^{th} eigenvector of the reference mode, i.e., the mode of the pristine structure. In this manner, the statistics of the MAC matrix are computed and available in Fig. 6.26. Figure 6.26c shows the mean value and standard deviation of each entry of the MAC matrix. In detail, the floor colour corresponds to the mean value of $\mathrm{MAC}_{i,j}$, and the height of the bar to its standard deviation. According to the statistics from the ESL-TE 1 case, one can say that this structural model cannot distinguish between the modes of a flawed and pristine structure as all the diagonal terms practically equal one and present a low standard deviation except the fifth buckling mode. Then, as one introduces higher-order kinematics, the variability in the modes due to the fibre misalignments can be appreciated; see Figs. 6.26b and 6.26c. In this manner, it is proven that LW models can catch eventual resemblances between the buckling modes of the flawed and pristine structures.

Concerning the fifth buckling load predicted by the ESL-TE 3 model, Fig. 6.26b shows that the mean value for $\mathrm{MAC}_{5,5}$ is nearly 0.2, while $\mathrm{MAC}_{2,5}$ and $\mathrm{MAC}_{4,5}$ mean values equal 0.6 and 0.35, respectively. PDF of $\mathrm{MAC}_{2,5}$ and $\mathrm{MAC}_{4,5}$ are available in Fig. 6.27a, while the statistics of $\mathrm{MAC}_{5,5}$ are illustrated as an histogram in Fig. 6.27b.

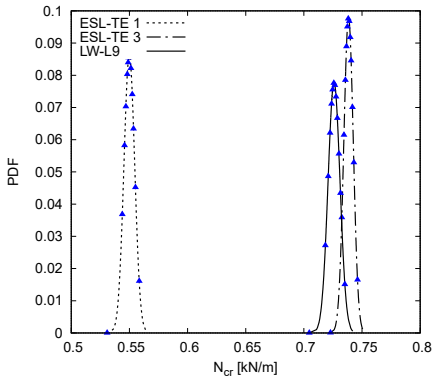

(a) PDF of first buckling load

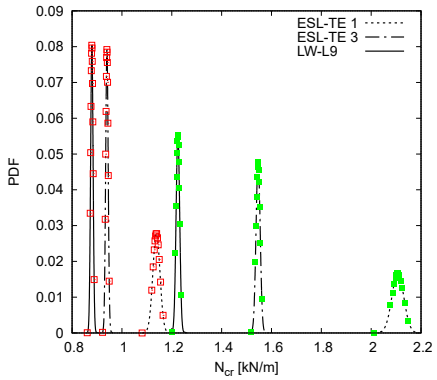

(b) PDF of second and third buckling load

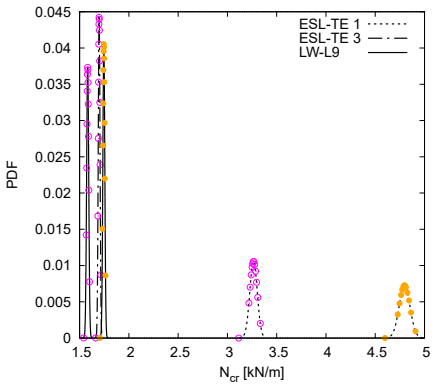

(c) PDF of fourth and fifth buckling load

Figure 6.25 PDF of buckling loads N_{cr_i} for the $[0 \ \pm\langle 45,0\rangle]_s$ VAT plate presenting fibre misalignment with standard deviation equal to $\sigma_\theta = 1^\circ$ employing ESL-TE 1, ESL-TE 3 and LW-L9 models. Mode 1 ▲, Mode 2 □, Mode 3 ■, Mode 4 ○, Mode 5 •

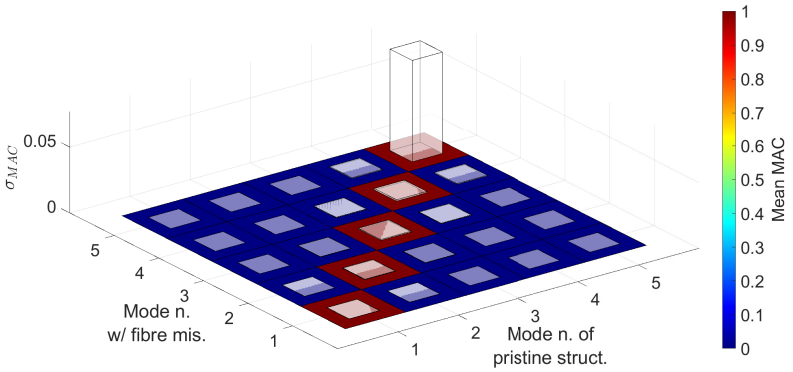

(a) MAC criterion using ESL-TE 1

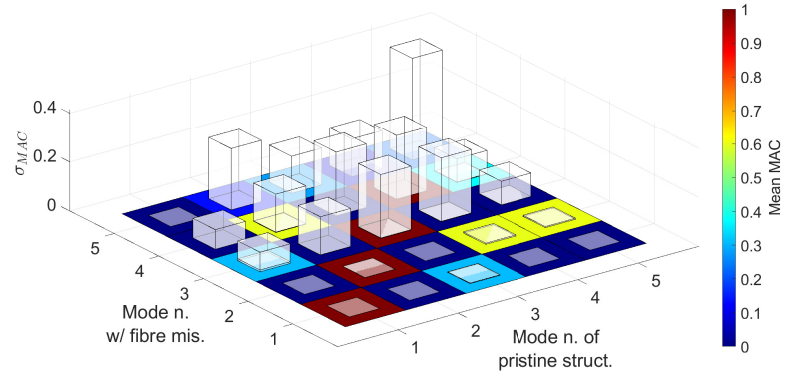

(b) MAC criterion using ESL-TE 3

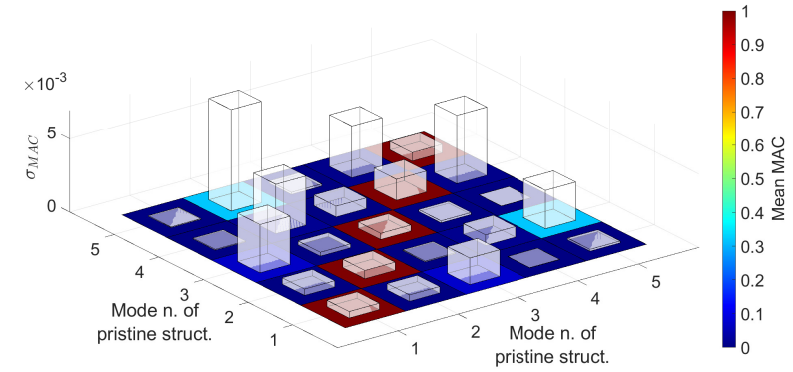

(c) MAC criterion using LW-L9

Figure 6.26 Mean MAC values and standard deviation between buckling modes of pristine $[0 \ \pm\langle 45,0\rangle]_s$ VAT panel and defected one employing ESL-TE 1, ESL-TE 3 and LW-L9 expansions. The fibre misalignment field has a null mean and standard deviation equal to $\sigma_\theta = 1^\circ$.

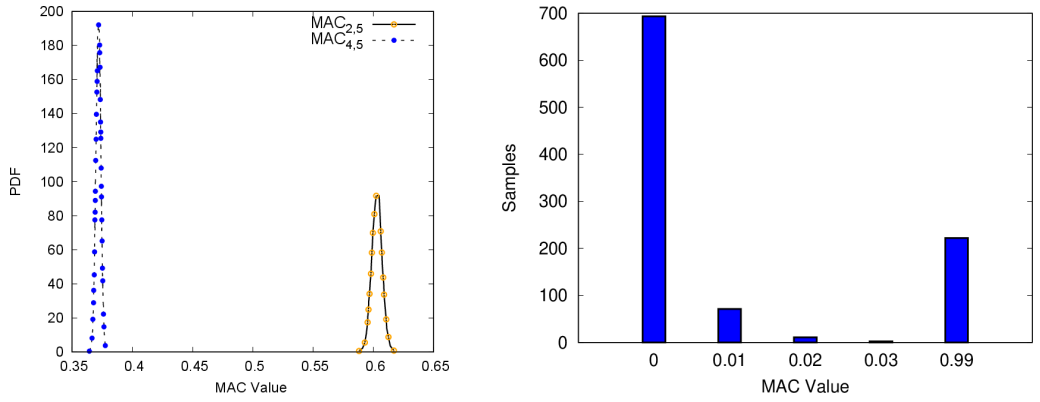

(a) $MAC_{2,5}$ and $MAC_{4,5}$ PDFs. **(b)** $MAC_{5,5}$ histogram.

Figure 6.27 (a) PDFs of $MAC_{2,5}$ and $MAC_{4,5}$ indices, and (b) $MAC_{5,5}$ histogram of the ESL-TE 3 analysis of the $[0 \pm \langle 0,45 \rangle]_s$ VAT plate.

This histogram tells that nearly 23% of the Monte Carlo samples are gathered around $MAC_{5,5} \approx 1$, corresponding to $N_{cr_5} \approx 2.65$ kN/m. The remaining 77% approximately equals 0, and its buckling load is around $N_{cr_5} \approx 2.50$ kN/m. This implies that when misalignments are considered, the ESL-TE 3 model overestimates the critical load and may alter its respective buckling mode.

6.4.2 Layer and fibre scale uncertainty

This part is devoted to analysing VAT structures subject to uncertain manufacturing defects that appear at both the layer and fibre scale. The layer scale defects were already discussed in Section 6.4.1, that is, fibre misalignments, while the fibre scale uncertainty is related to the fibre volume fraction variability within the laminate. These two defects are modelled as a stochastic field using the Karhunen-Loève expansion (KLE). A null mean and standard deviation $\sigma_\theta = 1.5^\circ$ are considered for the layer scale field, as shown in [148]. The fibre scale defect assumes a mean volume fraction $V_f = 0.60$ and standard deviation $\sigma_{V_f} = 0.05$, as considered in [64].

Stochastic buckling analysis

The defects mentioned above are included in two VAT plates with orientations $[0 \pm \langle 45,0 \rangle]_s$ and $[90 \pm \langle 0,45 \rangle]_s$, referred to as Case 1 and Case 2, respectively. The structures involved in this study are square plates with $a = b = 0.254$ m and single ply thickness $t_{ply} = 0.127$ mm. The plate is clamped on the left edge, a pressure $P = 7.75$ kPa is exerted on the right edge, and the top and bottom edges are free to deform. Since multiscale defects are considered in this research item, material properties for

Table 6.17 Elastic properties of the constituents of the composite material and the homogenised material properties for a fibre volume fraction $V_f = 0.60$.

Constituent	E_{11} [GPa]	E_{22} [GPa]	G_{12} [GPa]	G_{23} [GPa]	ν_{12} [-]	ν_{23} [-]
Fibre	235.0	14.0	28.0	5.60	0.20	0.25
Matrix	4.80	4.80	1.79	1.79	0.34	0.34
Homogenised V_f =0.60	143.17	9.64	6.09	3.12	0.252	0.349

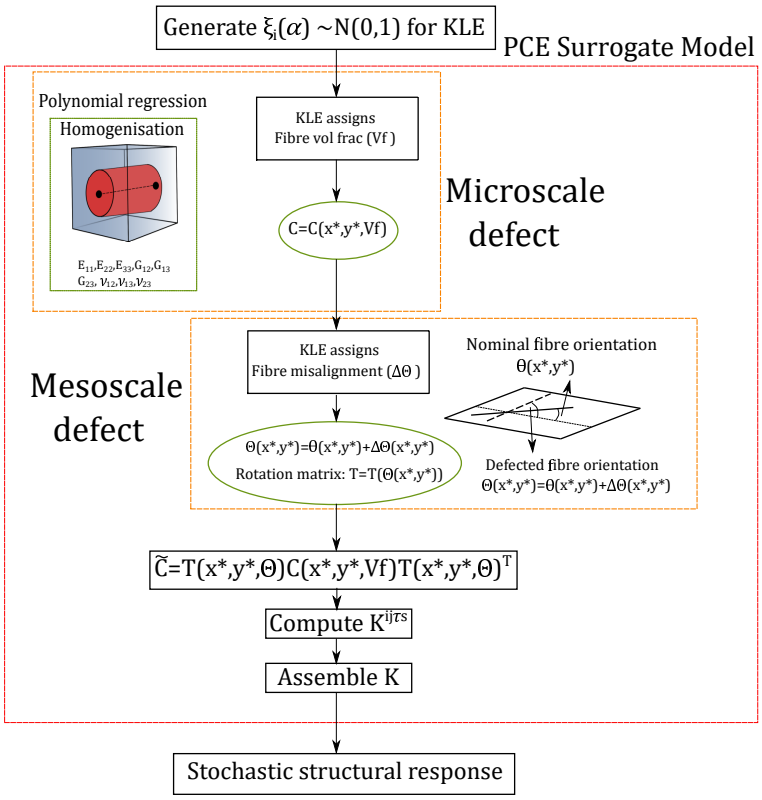

Figure 6.28 Flow-chart of the stochastic buckling analysis considering microscale and mesoscale defects.

both the fibre and matrix constituents are considered. These are available in Table 6.17 along with the homogenised properties when $V_f = 0.60$ are reported too.

The defects are included as depicted in Fig. 6.28 and explained in the following. First, $r = n_{\text{ply}} n_{def} n\ \xi_i(\omega)$ terms for the KLE are generated through Latin Hypercube Sampling (LHS) for each analysis, where n_{ply} stands for the number of plies in the VAT component, n_{def} is the number of defects considered, and n is the number of terms per each KLE. When the structural analysis begins, a fibre volume fraction and fibre misalignment field are generated with the KLE and are assigned to each integration point. In the first instance, the homogenised properties of the material are retrieved through a polynomial regression. The samples used to build such polynomials were obtained employing the MSG-CUF models established in Section 3.2. The polynomial

fitting is available in [136]. The homogenised material properties are then used to calculate the material stiffness matrix $\mathbf{C}$, which is then rotated into the structural reference frame, taking into account the misalignment $\Delta\Theta$ to obtain $\tilde{\mathbf{C}}$. Afterwards, the stiffness FN is computed for each FE, and the global stiffness matrix is assembled. Subsequently, the equilibrium state is calculated, and the internal stress state is utilised to calculate the geometrical stiffness matrix. Finally, the stochastic buckling response is retrieved.

As one can observe in Fig. 6.28, the multiscale defect propagation and generation of the assembled stiffness and geometrical stiffness matrices are contained in a module that is substituted by a Polynomial Chaos Expansion (PCE) surrogate model. The PCE is built with 300 Monte Carlo simulations and allows the computation of the first two statistical moments of the first six buckling loads. Those 300 samples were considered the minimum number of simulations necessary to achieve convergence in the computation of the mean value and standard deviation using PCE as shown in [136]. The deterministic buckling load, as well as the mean value and coefficient of variation (COV) computed with first- and second-order PCE for Case 1 and Case 2 laminations, are reported in Table 6.18. It is observed that first- and second-order PCE provided very similar mean and standard deviation values. Moreover, by using PCE, one can accelerate the calculation of statistical moments needed for reliability analyses. The PDFs of each buckling load are available in Fig. 6.29. Case 1 PDF shows some overlapping regions between the first and second loads and between the fourth, fifth and sixth. Indeed, the upper and lower tails of the fourth and sixth critical loads slightly overlap around 350 N. For Case 2, the overlapping tails appear between the second and third loads and the fourth, fifth and sixth loads. Despite the overlapping tails, it was found that no mode switching occurred and that the buckling loads increased altogether simultaneously.

Figure 6.30 provides the 3D MAC matrices. It is inferred that no swapping occurs between buckling modes. For the two fibre paths considered, the main diagonal components have a mean value close to one, while some other terms present values between 0.40 and 0.50. It means that the modes of the flawed structures are similar to those of the pristine ones. Regarding the standard deviations of the MAC terms, Case 1 presents similar values to those obtained when only fibre volume fraction variability is considered, see [136]. On the contrary, in Case 2, these standard deviations increased, which agrees with the behaviour of Case 2 COV of the buckling loads.

Table 6.18 Case 1 and 2 deterministic buckling loads, mean value and COV calculated by first- and second-order PCE accounting for spatially varying fibre volume fraction and fibre misalignments.

Case	Buckling Load	Deterministic Load [N]	1st order PCE mean [N]	2nd order PCE mean [N]	1st order PCE COV [%]	2nd order PCE COV [%]
Case 1	F_{cr_1}	143.59	143.30	143.34	4.52	4.42
	F_{cr_2}	159.07	159.29	159.26	3.91	3.79
	F_{cr_3}	216.77	217.22	217.23	3.61	3.41
	F_{cr_4}	310.21	309.82	309.76	3.59	3.39
	F_{cr_5}	366.45	366.75	366.76	5.02	4.88
	F_{cr_6}	407.53	407.09	406.99	4.05	3.93
Case 2	F_{cr_1}	26.05	26.13	26.14	3.96	3.88
	F_{cr_2}	48.64	48.65	48.65	3.57	3.46
	F_{cr_3}	60.27	60.42	60.41	5.32	5.22
	F_{cr_4}	81.31	81.32	81.32	3.72	3.63
	F_{cr_5}	109.30	109.67	109.66	4.08	4.05
	F_{cr_6}	134.89	135.11	135.11	3.75	3.68

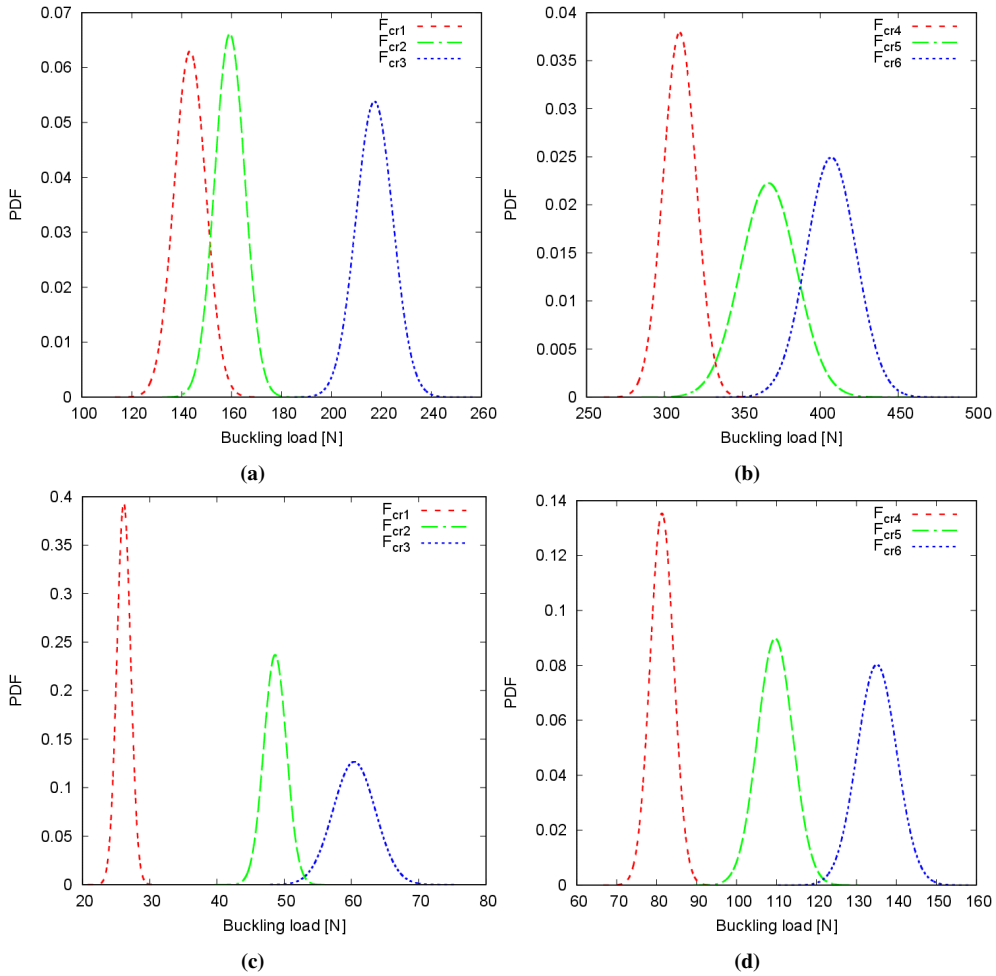

Figure 6.29 Case 1 buckling load PDFs: (a) F_{cr1}, F_{cr2} and F_{cr3}. (b) F_{cr4}, F_{cr5} and F_{cr6}. Case 2 buckling load PDFs: (c) F_{cr1}, F_{cr2} and F_{cr3}. (d) F_{cr4}, F_{cr5} and F_{cr6}. Spatially varying fibre volume fraction and fibre misalignments are accounted for.

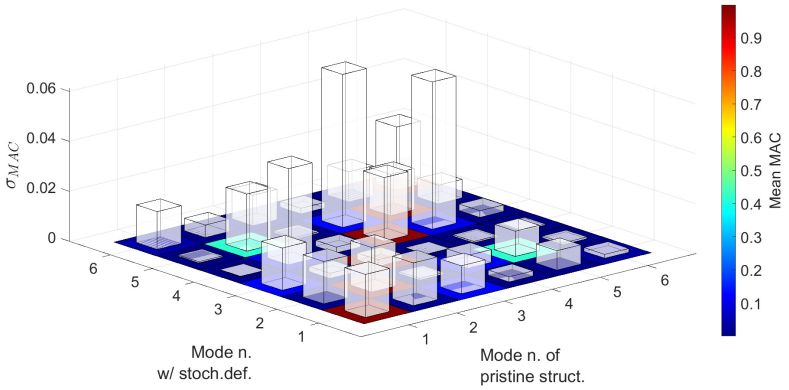

(a)

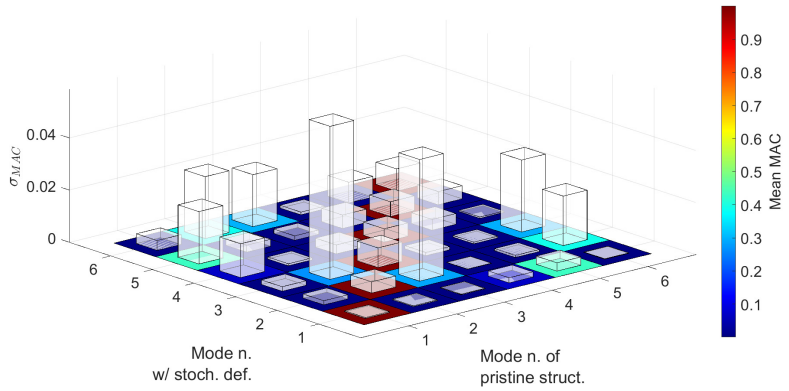

(b)

Figure 6.30 3D MAC matrices of (a) Case 1 (b) Case 2. Spatially varying fibre volume fraction and fibre misalignments are accounted for.

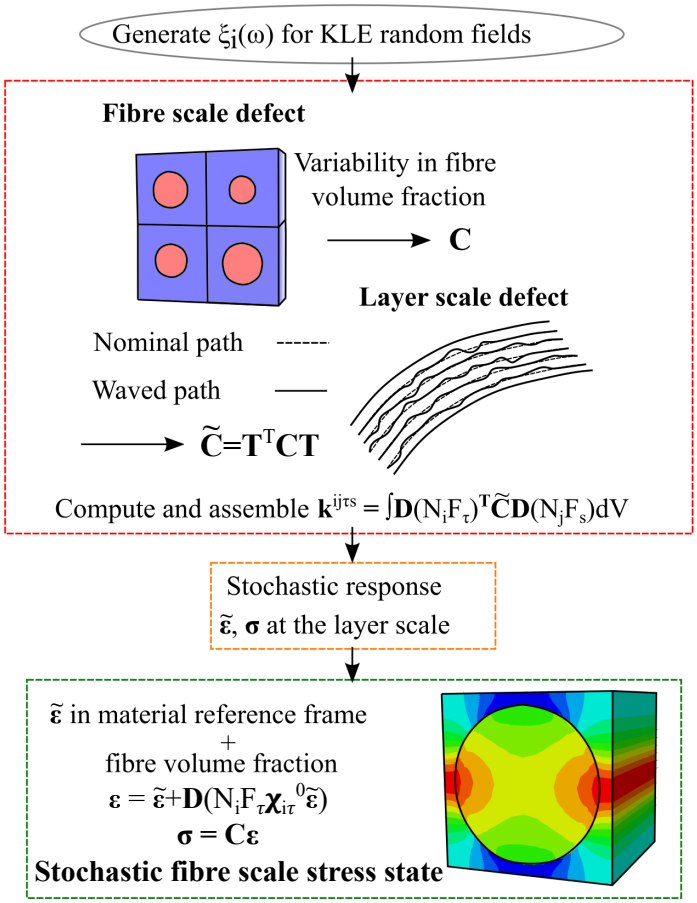

Figure 6.31 Flow-chart of the stochastic microscale stress analysis considering microscale and mesoscale defects.

Stochastic fibre scale stress analysis

The following study addresses the stochastic fibre-scale stresses that occur when fibre volume fraction and fibre misalignments are considered. The investigated structure consists of two layers with layup sequence $[\langle 90,45\rangle,\langle 0,45\rangle]$, simply-supported edges and a uniform pressure $p_z = 10$ kPa applied on top. Two width-to-thickness ratios are investigated: $a/h = 10$ and $a/h = 100$; the width and length are $a = b = 1$ m. The material properties used in this numerical study are reported in Table 6.17.

As in the stochastic buckling analysis considering multiscale uncertainty defects, the flow-chart in Fig. 6.31 depicts the defect propagation and microscale stress retrieval process. The propagation of defects and the computation of the stochastic structural response are conducted as in the previous study. The principal difference occurs after retrieving the strains and stresses at the layer scale. The strains in the material reference frame and the local fibre volume fraction are fed into the MSG-CUF method,

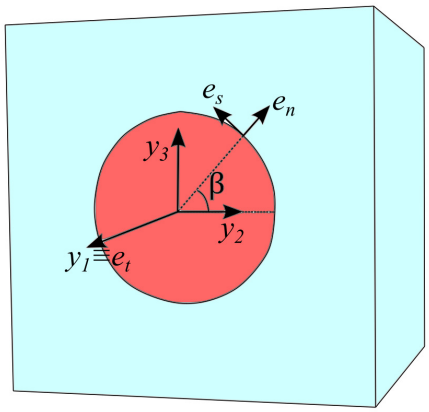

Figure 6.32 Micromechanics Cartesian and cylindrical reference frames used for the microscale stress tensor. Axis y_1 and e_t are coincident. β is defined as the angle between y_2 and the radial e_n.

see Section 3.2, to compute the stresses at the fibre-matrix level. The microscale stress sensitivity is performed with a total of a thousand Monte Carlo analyses. First- and second-order statistical moments of the stresses at the fibre-matrix interface are calculated. Note that the microscale stress components are transformed into the cylindrical reference frame shown in Fig. 6.32.

In the case of the thick plate ($a/h = 10$), the layer strain state at point (-0.25,-0.25,-0.02) m is used to retrieve the stress level at the fibre scale. The polar plots in Fig. 6.33 include the normal t_n and shear t_s, t_t stresses of both fibre and matrix constituents. The radial direction of the polar plots provides the magnitude, while the circumferential direction represents angle β from Fig. 6.32. Based on the data displayed in Fig. 6.33, the following comments are made:

- The circumferential stresses from Figs. 6.33a and 6.33b, present the largest differences between the nominal and mean value, especially in the ranges $\beta \in [45, 135]^\circ$ and $\beta \in [225, 315]^\circ$. As appreciated in Table 6.19, in those ranges, the pristine stresses are below the maximum-minimum range of the uncertainty analysis.

- The longitudinal stress of the fibre component in Fig. 6.33c has an oval shape, whose maximum is slightly lower than 15 kPa and its minimum is about 7 kPa. On the contrary, the matrix t_t has a two-lobed shape with peak values about 35 kPa at $\beta = 0^\circ$ and $\beta = 180^\circ$, see Fig. 6.33d.

- The radial stresses t_n in Figs. 6.33e and 6.33f are practically identical. This is because the continuity of radial stresses has to be guaranteed in the normal direction of the fibre-matrix interface.
- Overall, a small variability is observed. The 95% confidence intervals are very shallow, and the maximum-minimum ranges are not large, except for the fibre t_t.

Table 6.19 Normal and shear stresses statistics of the RUC constituents at $\beta = 75^\circ$ for the simply-supported $[\langle 90,45\rangle, \langle 0,45\rangle]$ thick ($a/h = 10$) laminate. Range indicates the minimum and maximum values registered in the Monte Carlo simulations.

Constituent	Magnitude	t_n [kPa]	t_s [kPa]	t_t [kPa]
Fibre	No defects	-4.08	41.96	5.55
	Mean	0.31	47.82	6.74
	95% interval	[0.27,0.35]	[47.72,47.93]	[6.54,6.94]
	Range	[-1.61,2.02]	[42.60,53.20]	[-1.52,18.93]
Matrix	No defects	-4.36	7.73	4.18
	Mean	0.03	14.43	6.53
	95% interval	[0,0.07]	[14.37,14.50]	[6.51,6.57]
	Range	[-2.04,1.76]	[11.67,17.42]	[4.95,7.88]

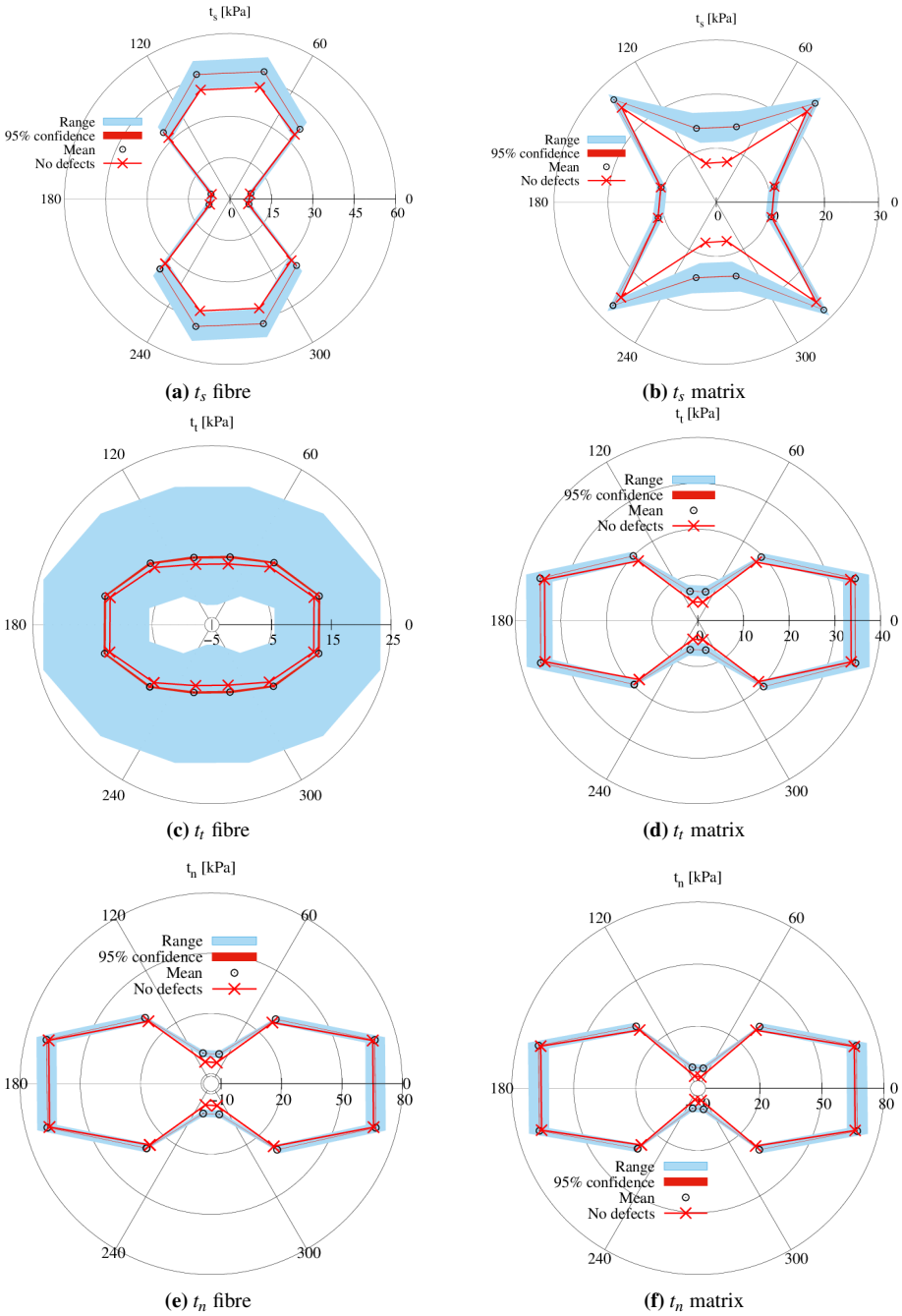

(a) t_s fibre **(b)** t_s matrix

(c) t_t fibre **(d)** t_t matrix

(e) t_n fibre **(f)** t_n matrix

Figure 6.33 Stress distribution of the fibre and matrix constituents at its interface, along with statistical data. Stresses are reported in a cylindrical reference frame. Data corresponds to the simply-supported $[\langle 90,45\rangle,\langle 0,45\rangle]$ thick $(a/h=10)$ laminate.

Concerning the thin plate $(a/h=100)$, the layer strain state at point (0,0,5) mm, where the minimum σ_{xx} is located. The multiscale defect Monte Carlo analysis yields the fibre scale stress state illustrated in Fig. 6.34. The following is appreciated:

- The circumferential stresses t_s are reported in Figs. 6.34a and 6.34b. For the fibre constituent, it presents an oval shape ranging from -5 MPa to -2 MPa in the non-defective case. The matrix presents a four-lobed distribution where the stresses vary between -3 MPa and -0.5 MPa. The highest compression stresses are observed at $\beta = 45, 135, 225, 315^\circ$.

- A constant value about -85 MPa is appreciated for the fibre in Fig. 6.34c. The matrix presents a two-lobed shape with peak compression values at $\beta = 0^\circ$ and $\beta = 180^\circ$, see Fig. 6.34d.

- The continuity of t_n is demonstrated in Figs. 6.34e and 6.34f, as well as in Table 6.20. In addition, it presents a peak value of about 0.50 MPa at $\beta = 90^\circ$ and $\beta = 270^\circ$.

- In general, there is no large variability when the pristine distributions are compared with their stochastic counterparts, except for Figs. 6.34a and 6.34b in the $\beta \in [75, 135]^\circ$ and $\beta \in [255, 295]^\circ$ ranges. In these ranges, differences of 1 MPa are observed.

- As in the case of the thick plate, the fibre longitudinal stress is undergoing more significant variability in terms of minimum-maximum range.

Table 6.20 Normal and shear stresses statistics of the RUC constituents at $\beta = 75^\circ$ for the thin laminate's minimum value of σ_{xx}. Range indicates the minimum and maximum values registered in the Monte Carlo simulations.

Constituent	Magnitude	t_n [MPa]	t_s [MPa]	t_t [MPa]
Fibre	No defects	0.52	-4.71	-85.01
	Mean	0.091	-5.23	-84.46
	95% interval	[0.087,0.094]	[-5.26,-5.21]	[-84.64,-84.28]
	Range	[0,0.18]	[-6.28,-4.58]	[-89.78,-79.54]
Matrix	No defects	0.54	-1.05	-2.27
	Mean	0.12	-1.68	-2.48
	95% interval	[0.11,0.12]	[-1.69,-1.67]	[-2.49,-2.47]
	Range	[0.02,0.21]	[-2.08,-1.44]	[-2.77,-2.27]

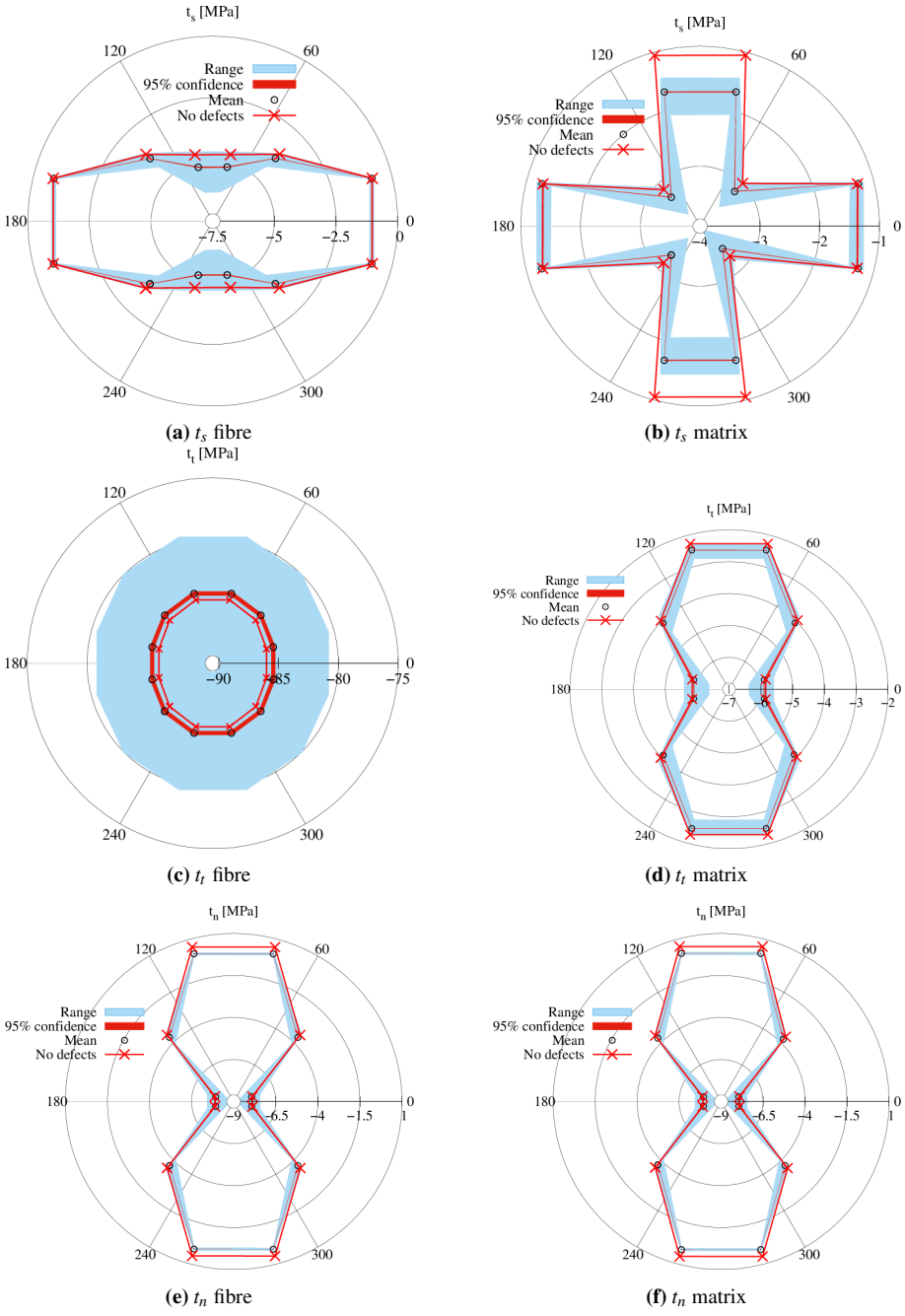

(a) t_s fibre **(b)** t_s matrix

(c) t_t fibre **(d)** t_t matrix

(e) t_n fibre **(f)** t_n matrix

Figure 6.34 Stress distribution of the fibre and matrix constituents at its interface, along with statistical data. Stresses are reported in a cylindrical reference frame. Data corresponds to the simply-supported $[\langle 90,45\rangle, \langle 0,45\rangle]$ thin ($a/h = 100$) laminate and minimum σ_{xx}.

6.5 Optimisation of VAT plates

This section gathers the optimisation of a series of mechanical properties of VAT plates. For the vast majority of results, uncertainty or deterministic manufacturing defects have not been considered. The mechanical features optimised are the fundamental frequency, buckling load, vertical deflection, strain concentration, strength maximisation, and fundamental frequency considering deterministic defects. A polynomial surrogate model coupled with a GA has been used for the first two optimisations. For the following three features, a solver from modeFrontier© [129] that combines global and local search and utilises the actual FE simulations has been chosen. The last optimisation uses the *surrogateopt* from MATLAB© [149], which presents a similar search strategy as the one from modeFrontier©. The main scope of this section is to understand the influence of structural theory on the retrieval of optimal design variables.

6.5.1 Fundamental frequency optimisation

Before proceeding with the optimisation, is mandatory to verify the numerical approach. For doing so, the free vibration problem from Akhavan and Ribeiro [150] is considered. This considers a three-layered squared plate with layup sequence $\theta = [\langle 0,45\rangle, \langle -45,-60\rangle, \langle 0,45\rangle]$. The plate has a width and length $a = b = 1$ m, and a width-to-thickness ratio $a/h = 10$, having each layer the same thickness. The structure is clamped on its four edges and the material properties are reported in Table 6.21.

Table 6.21 Material properties of the VAT plate considered for the free vibration analysis, from Akhavan and Ribeiro [150].

E_1 [GPa]	$E_2 = E_3$ [GPa]	G_{12} [GPa]	G_{23} [GPa]	$\nu_{12} = \nu_{23}$ [-]	ρ [kg/m^3]
173.00	7.20	3.76	3.76	0.29	1540.00

Different Taylor and Lagrange expansion functions have been considered for the verification. All the numerical models employ a 10×10 Q9 mesh. The FE mesh convergence is not included for the sake of brevity. The results are gathered in Table 6.22. First- and second-order TE provide higher natural frequencies than the reference model. Third- and fourth-order TE are closer to the reference but slightly higher than the LW models. The LW solutions present differences among them. LD1 results lay between ESL-TE 2 and LD2, while LD3 computes lower frequencies than LD2 with increased DOF and computational time. In this regard, a 10×10 Q9 FE mesh and 1 LD2 per layer are used in the optimisation problem.

Table 6.22 Convergence analysis of the first five natural frequencies for the fully-clamped $[\langle 0,45\rangle, \langle -45,-60\rangle, \langle 0,45\rangle]$ plate from Akhavan and Ribeiro [150]. Each model employs a 10×10 Q9 mesh. The relative difference between each model and the reference is reported in the superscript.

Model	DOF	f_1 [Hz]	f_2 [Hz]	f_3 [Hz]	f_4 [Hz]	f_5 [Hz]
Ref.[150]	-	613.79	909.04	1231.65	1337.69	1484.53
TE 1	2646	$638.87^{4.09\%}$	$955.51^{5.11\%}$	$1278.43^{3.80\%}$	$1419.71^{6.13\%}$	$1553.57^{4.65\%}$
TE 2	3969	$634.39^{3.36\%}$	$943.64^{3.81\%}$	$1273.88^{3.43\%}$	$1399.97^{4.66\%}$	$1542.34^{3.89\%}$
TE 3	5292	$611.17^{-0.43\%}$	$908.11^{-0.10\%}$	$1218.00^{-1.11\%}$	$1338.39^{0.05\%}$	$1473.10^{-0.70\%}$
TE 4	6615	$611.04^{-0.45\%}$	$907.83^{-0.13\%}$	$1217.56^{-1.14\%}$	$1337.69^{0\%}$	$1789.14^{20.52\%}$
TE 5	7938	$609.49^{-0.70\%}$	$903.63^{-0.60\%}$	$1214.24^{-1.41\%}$	$1328.60^{-0.68\%}$	$1467.81^{-1.13\%}$
TE 6	9261	$609.49^{-0.70\%}$	$903.63^{-0.60\%}$	$1214.24^{-1.41\%}$	$1328.59^{-0.68\%}$	$1774.46^{19.53\%}$
1 LD1	5292	$621.64^{1.28\%}$	$917.66^{0.95\%}$	$1244.85^{1.07\%}$	$1347.15^{0.71\%}$	$1499.66^{1.02\%}$
1 LD2	9261	$609.91^{-0.63\%}$	$903.93^{-0.56\%}$	$1216.18^{-1.26\%}$	$1328.88^{-0.66\%}$	$1469.58^{-1.01\%}$
1 LD3	13230	$608.60^{-0.85\%}$	$900.62^{-0.93\%}$	$1213.16^{-1.50\%}$	$1322.06^{-1.17\%}$	$1464.94^{-1.32\%}$

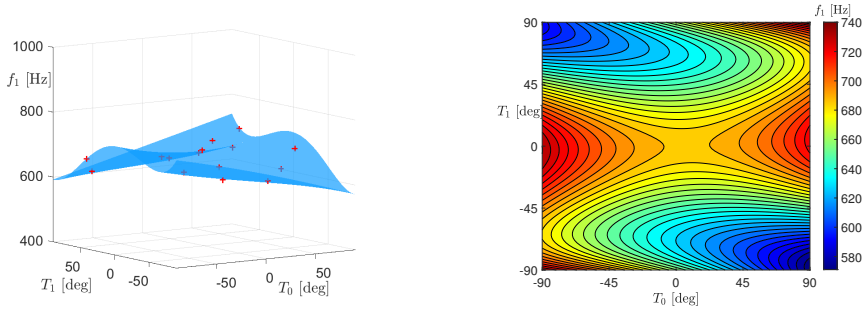

(a) LW-LD2 response surface.

(b) LW-LD2 contour plot.

Figure 6.35 Response surface and contour plot of the fully-clamped $[\langle T_0,T_1\rangle, \langle 90+T_0, 90+T_1\rangle]_s$ plate with width-to-thickness ratio $a/h = 10$. Red crosses in (a) indicate the sample points used to construct the surrogate models.

The fundamental frequency optimisation problem can be defined as follows:

$$\min_{\mathbf{x}} \quad -f_1(\mathbf{x}), \tag{6.2}$$

in which $\mathbf{x} = \{T_0, T_1\}$ is the vector containing the design variables. The considered structure is a fully-clamped plate with $\theta = [0\langle T_0,T_1\rangle, 0\langle 90+T_0, 90+T_1\rangle]_s$ as in [150]. The lower and upper boundaries are $\mathbf{x}_L = -90^\circ$ and $\mathbf{x}_U = 90^\circ$, respectively. The plate geometric dimensions are $a = b = 1$ m, and the material properties are enlisted in Table 6.21. Two width-to-thickness ratios are considered: $a/h = 10$ and $a/h = 100$, for thick and thin plates, respectively. Three theories of structures are considered for the optimisation process: ESL-TE 1, ESL-TE 3 and LW-LD2.

A polynomial surrogate model that mimics f_1 is used. In this context, f_1 is approximated by $\tilde{f}_1$, i.e.: $f_1 \approx \tilde{f}_1$, in Eq. (6.2). Fifteen samples were generated employing LHS to generate the training data, and a truncated fourth-order polynomial

was employed as the response surface. The surrogate model's 3D representation and contour plot are presented in Fig. 6.35. The GA used to solve the optimisation problem considers 40 individuals per generation, with an 80% crossover probability and 5% mutation probability.

Table 6.23 Optimal results of the unconstrained first fundamental frequency optimization problem for the fully-clamped $[\langle T_0, T_1\rangle, \langle 90+T_0, 90+T_1\rangle]_s$ plate, and comparison between surrogate model $\tilde{f}_1$ and direct analysis f_1 of the optimized stacking sequence.

	$a/h = 10$			$a/h = 100$		
	LW-LD2	ESL-TE 1	ESL-TE 3	LW-LD2	ESL-TE 1	ESL-TE 3
$\langle T_0,$	$\langle -90,$	$\langle -90,$	$\langle -90,$	$\langle -90,$	$\langle -90,$	$\langle -90,$
$T_1\rangle$ [°]	$-2.92\rangle$	$-2.30\rangle$	$-2.41\rangle$	$-1.15\rangle$	$-1.26\rangle$	$-1.15\rangle$
$\tilde{f}_1$ [Hz]	735.23	769.86	738.96	125.48	126.51	125.60
f_1 [Hz]	737.43	774.47	741.71	123.21	124.19	123.24
Error [%]	-0.29	-0.59	-0.37	1.84	1.87	1.91

Table 6.23 reports the design variables that maximise the fundamental frequency. The LW and ESL models provide similar solutions for both thick and thin laminates. It is observed that for all the optimum layups, T_1 is negative, as appreciated in Figs. 6.36. Fibres are pointing towards the $x = \pm a/2$ edges with constant T_1. In these edges, the local elastic modulus in the x direction is greater than the region with $x = 0$. Contrarily, at $x = 0$, the fibres point towards the $y = \pm b/2$ edges, presenting maximum transverse stiffness.

When a manufacturing constraint, as the maximum allowable curvature, is introduced in the optimisation problem, it can be written as:

$$\min_{\mathbf{x}} \; -f_1(\mathbf{x}) \;\text{ s.t. }\quad -1/r_{\min} \leq \kappa(\mathbf{x}) \leq 1/r_{\min}, \tag{6.3}$$

where $\kappa(\mathbf{x})$ is computed with Eq. (4.4). The solutions to the constrained problem are available in Table 6.24. Similarly to the unconstrained case, LW and ESL approaches provide close results for thick and thin laminates. The main discrepancy resides in predicting the fundamental frequency for thick plates, where ESL models overestimate f_1, especially ESL-TE 1. The optimal solutions lay on the constraint bound, meaning the curvature constraint is active. The fibre paths are illustrated in Fig. 6.37. A cluster of fibres is appreciated at the middle of the plates in Figs. 6.36 and 6.37 as the optimal $T_0 = -90°$. Although the maximum curvature manufacturing constraint is implemented, a defect-free design is foreseen. Thus, a varying fibre path that reaches a $\pm 90°$ local orientation is conceptually feasible. That is not the case in which not only manufacturing limitations but also fabrication defects are considered within the optimisation problem, as shown in Section 6.5.6.

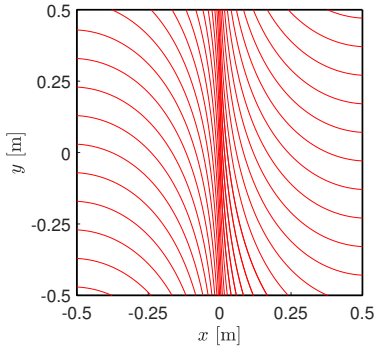

(a) $[0\langle -90, -2.92\rangle]$ ply.

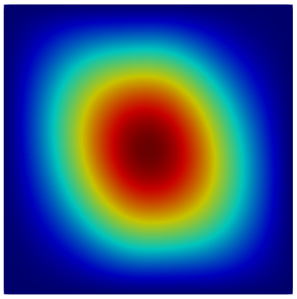

(b) First modal shape of optimum thick laminate.

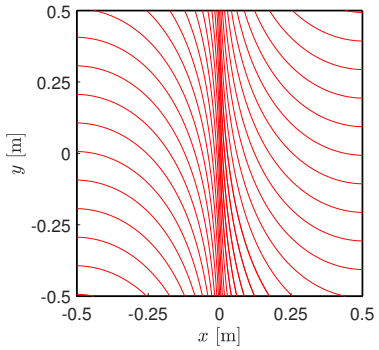

(c) $[0\langle -90, -1.15\rangle]$ ply.

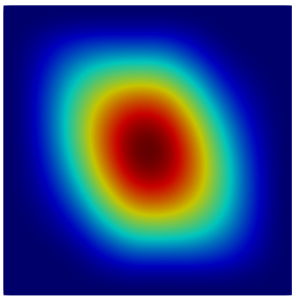

(d) First modal shape of optimum thin laminate.

Figure 6.36 Fibre paths and first modal shape of the LW optimum solution for the unconstrained free vibration optimisation of thick (a,b) and thin (c,d) laminates.

Table 6.24 Optimal results of the constrained first fundamental frequency optimization problem for the $[\langle T_0, T_1\rangle, \langle 90+T_0, 90+T_1\rangle]_s$ fully-clamped plate, comparison between surrogate model $\tilde{f}_1$ and direct analysis f_1 of the optimized stacking sequence, and maximum value of the steering curvature.

	$a/h = 10$			$a/h = 100$		
	LW-1LD2	ESL-TE 1	ESL-TE 3	LW-1LD2	ESL-TE 1	ESL-TE 3
$\langle T_0,$	$\langle -90,$	$\langle -84.68,$	$\langle -85.84,$	$\langle -89.73,$	$\langle -90,$	$\langle -90,$
$T_1\rangle$ [°]	$-34.96\rangle$	$-31.67\rangle$	$-32.41\rangle$	$-34.58\rangle$	$-34.96\rangle$	$-34.95\rangle$
$\tilde{f}_1$ [Hz]	710.63	739.16	713.76	117.25	118.36	117.40
f_1 [Hz]	717.03	751.76	720.08	118.01	118.96	118.07
Error [%]	-0.89	-1.67	-0.88	-0.64	-0.50	-0.57
κ_{max} [m^{-1}]	1.57	1.57	1.57	1.57	1.57	1.57

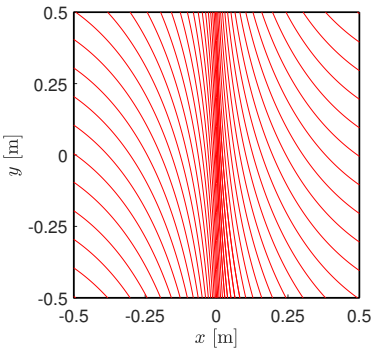

(a) $[\langle -90, -34.96 \rangle]$ ply.

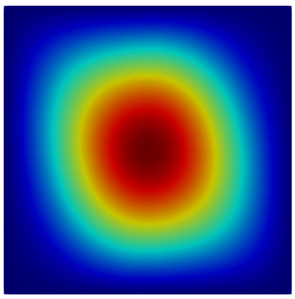

(b) First modal shape of optimum thick laminate.

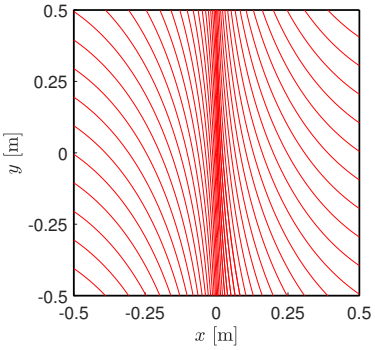

(c) $[\langle -89.73, -34.58 \rangle]$ ply.

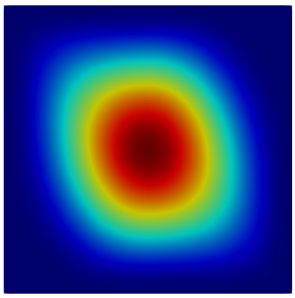

(d) First modal shape of optimum thin laminate.

Figure 6.37 Fibre paths and first modal shape of the LW optimum solution for the constrained free vibration optimisation of thick (a,b) and thin (c,d) laminates.

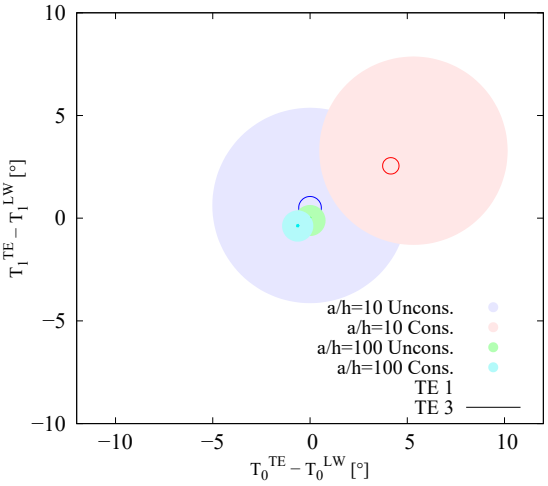

Figure 6.38 Absolute error between the optimal $\langle T_0, T_1 \rangle$ obtained by ESL models with respect to an LW approach. The radius of the circle represents the relative error between the actual simulations using an ESL approach with respect to LW.

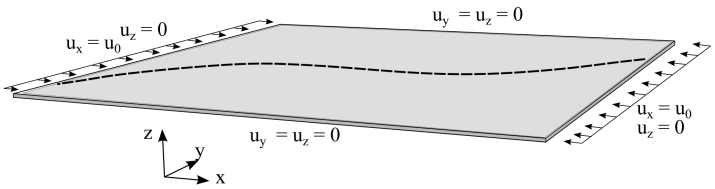

Figure 6.39 Boundary conditions of the twelve-layered $[0 \pm \langle T_0, T_1 \rangle]_{3s}$ plate.

Figure 6.38 summarises graphically the difference in the optimum design variables between the structural theories employed for the unconstrained and the constrained optimisation problems. It is appreciated that the absolute error between the optimum $\langle T_0, T_1 \rangle$ obtained with an ESL and an LW approach lies in the $\pm 5^\circ$ range. Moreover, it is observed that the largest relative error in the predicted fundamental frequency value is presented when the thick laminate is modelled using an ESL-TE 1 structural model. This error is much lower when an ESL-TE 3 is employed. In the case of thin plates, the error committed in the fundamental frequency prediction by the two ESL is much lower. Therefore, one can say that when maximising the fundamental frequency of VAT plates, ESL models provide optimum designs similar to an LW theory of structures.

6.5.2 Buckling optimisation

This section presents the optimal variable stiffness fibre paths to maximise the buckling load. A twelve-layered plate with $[0 \pm \langle T_0, T_1 \rangle]_{3s}$ stacking sequence is considered. The width a and length b of the plate are $a = b = 0.254$ m, and the thickness of each ply is

$t_{\text{ply}} = 0.127$ mm. The plate is subject to a uniform shortening $u_x = u_0$ along $x = \pm a/2$, while the transverse displacements are restrained at $y = \pm b/2$, as depicted in Fig. 6.39. The material properties are enlisted in Table 6.25.

Table 6.25 Material properties of the VAT plate considered for the analysis, from Gürdal *et al.* [11]. G_{23} was taken from Zhao and Kapania [89].

E_1 [GPa]	$E_2 = E_3$ [GPa]	G_{12} [GPa]	G_{23} [GPa]	$\nu_{12} = \nu_{23}$ [-]
181.00	10.27	7.17	4.00	0.28

Taylor and Lagrange expansions are used for the verification of the numerical model. The $[0 \pm \langle T_0, T_1 \rangle]_{3s}$ from [11] is considered for verification purposes. For the sake of brevity, the mesh convergence study is omitted. Convergence is reached with a 10×10 Q9 mesh. The comparison between the expansion functions and the reference is made in terms of the non-dimensional buckling load factor K_{cr}, defined as:

$$K_{cr} = \frac{F_{cr} a^2}{E_1 h^3 b}, \tag{6.4}$$

where h is the total thickness of the plate. The results are available in Table 6.26. It is observed that ESL models provide the closest solutions to the reference one, which uses CLPT and the Rayleigh-Ritz method. As the order of the TE increases, lower values of K_{cr} are obtained. Indeed, the ESL-TE 3 model provides the same value as 1LD2 with an 84% reduction in degrees of freedom. The buckling optimisation problem can be stated as follows:

$$\min_{\mathbf{x}} \quad -F_{cr}(\mathbf{x}), \tag{6.5}$$

in which $\mathbf{x} = \{T_0, T_1\}$ are the design variables of the $[0 \pm \langle T_0, T_1 \rangle]_{3s}$ stack. Again, the lower and upper bounds are $\mathbf{x}_L = -90^\circ$ and $\mathbf{x}_U = 90^\circ$. A polynomial surrogate

Table 6.26 Convergence analysis of K_{cr} for the $[0 \pm \langle 0, 50 \rangle]_{3s}$ plate from Gürdal *et al.* [11]. Each model uses a 10×10 Q9 mesh.

Model	DOF	K_{cr} [-]
Ref. [11]	–	1.44
ESL-TE 1	2646	1.42
ESL-TE 2	3969	1.40
ESL-TE 3	5292	1.39
ESL-TE 4	6615	1.39
LW-1LD1	17199	1.42
LW-1LD2	33075	1.39

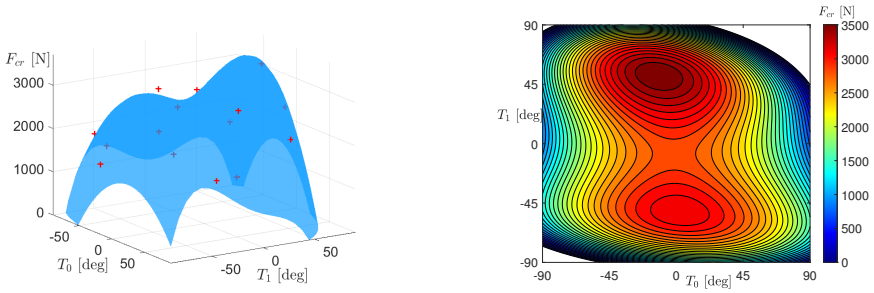

(a) LW-LD2 response surface.

(b) LW-LD2 contour plot.

Figure 6.40 Response surface and contour plot of the $[0 \pm \langle T_0, T_1 \rangle]_{3s}$ plate with width-to-thickness ratio $a/h = 167$ for the LW-1LD2 model. Red crosses in (a) indicate the sample points used to construct the surrogate models.

Table 6.27 Optimal results of the unconstrained buckling optimization problem for the $[0 \pm \langle T_0, T_1 \rangle]_{3s}$ plate, and comparison between surrogate model $\tilde{F}_{cr}$ and direct analysis F_{cr} of the optimized stacking sequence.

	$a/h = 10$			$a/h = 167$		
	LW-1LD2	ESL-TE 1	ESL-TE 3	LW-1LD2	ESL-TE 1	ESL-TE 3
$\langle T_0,$	$\langle -1.90,$	$\langle -3.38,$	$\langle -3.37,$	$\langle -17,$	$\langle -17,$	$\langle -11.77,$
$T_1\rangle$ [°]	$40.97\rangle$	$40.46\rangle$	$40.97\rangle$	$52\rangle$	$52\rangle$	$51.88\rangle$
$\tilde{F}_{cr}$ [N]	$8.24{\cdot}10^6$	$9.34{\cdot}10^6$	$8.73{\cdot}10^6$	$3.58{\cdot}10^3$	$3.58{\cdot}10^3$	$3.58{\cdot}10^3$
F_{cr} [N]	$8.28{\cdot}10^6$	$9.37{\cdot}10^6$	$8.73{\cdot}10^6$	$3.48{\cdot}10^3$	$3.56{\cdot}10^3$	$3.33{\cdot}10^3$
Error [%]	-0.51	-0.31	0.06	2.73	1.00	7.40

model that mimics F_{cr} is employed to solve the optimisation problem. LHS was used to generate the fifteen samples utilised to build the response surface. Two width-to-thickness ratios, $a/h = 10$ and $a/h = 167$ for thick and thin laminates, respectively, and three structural theories are investigated. The 3D visualisation and contour plot of the LW-1LD2 $a/h = 167$ plate are depicted in Fig. 6.40. A local and a global maximum are appreciated.

GA is employed to solve the optimisation problem. A total of 40 individuals per generation are considered. The crossover probability is set to 80%, while the mutation probability equals 5%. The optimal solutions are gathered in Table 6.27. In the case of thin plates, LW and ESL models lead to practically the same optimal fibre paths, the only difference being the T_0 predicted by ESL-TE 3. The results for the thin laminates are in agreement with those provided by Gürdal *et al.* [11], where the optimum was found for $\langle T_0, T_1 \rangle = \langle 0, 50 \rangle^\circ$. In their paper, Gürdal *et al.* allowed T_0 and T_1 to vary in the $T_0, T_1 \in [0, 90]^\circ$ range, while in this document $T_0, T_1 \in [-90, 90]^\circ$. LW and ESL provide similar solutions in the case of thick plates. The main difference is the predicted F_{cr} value, which is higher when ESL theories are employed.

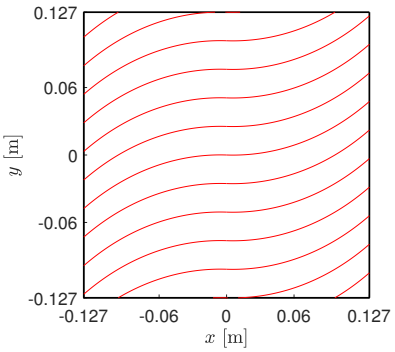

(a) $[\langle -1.90, 40.97 \rangle]$ ply.

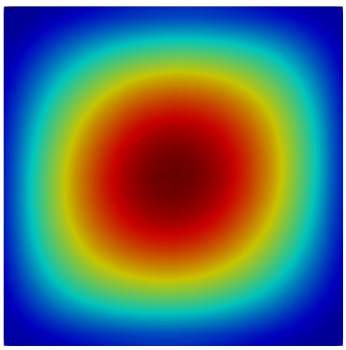

(b) First buckling mode of optimum thick laminate.

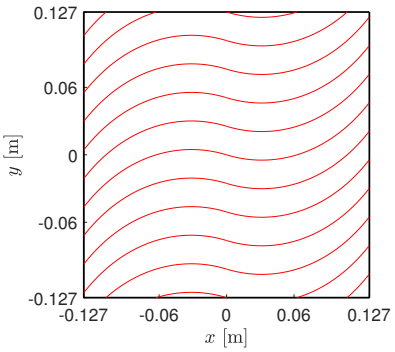

(c) $[\langle -17, 52 \rangle]$ ply.

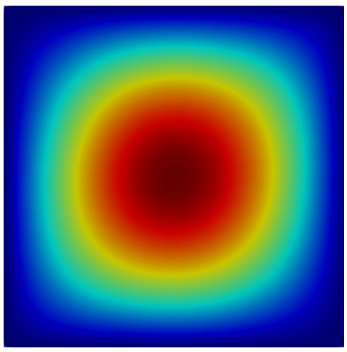

(d) First buckling mode of optimum thin laminate

Figure 6.41 Fibre paths and first buckling mode of the LW optimum solution for the unconstrained buckling load optimization problem for thick (a,b) and thin (c,d) laminates.

Although Olmedo and Gürdal [10] demonstrated that the buckling performance could be increased by steering fibres, they did not consider limitations on the turning radius of the AFP machine's head. Thus, constraints have to be incorporated into the optimisation problem. In this regard, the constrained buckling optimisation problem reads as follows:

$$\min_{\mathbf{x}} \quad -F_{cr}(\mathbf{x}) \;\; \text{s.t.} \quad -1/r_{\min} \leq \kappa(\mathbf{x}) \leq 1/r_{\min} \tag{6.6}$$

where $\kappa(\mathbf{x})$ is calculated through Eq. (4.4). The solutions to this problem are enlisted in Table 6.28. As for the unconstrained problem, LW and ESL provide close results when thin $a/h = 167$ plates are involved. The optimum is around $\langle T_0, T_1 \rangle = \langle 20, 32 \rangle^\circ$. The same occurs for the case of thick $a/h = 10$ plates, in which the optimal fibre path is around $\langle T_0, T_1 \rangle = \langle 12, 24 \rangle^\circ$. It is worth noting that constraints are active for all the retrieved solutions. That means that the optimal designs lay on the constraint boundary.

Table 6.28 Optimal results of the constrained buckling optimization problem for the $[0 \pm \langle T_0, T_1 \rangle]_{3s}$ plate subjected to uniform end shortening and restrained transverse edges, comparison between surrogate model $\tilde{F}_{cr}$ and direct analysis F_{cr} of the optimized stacking sequence, and maximum value of the steering curvature.

	$a/h = 10$			$a/h = 167$		
	LW-1LD2	ESL-TE 1	ESL-TE 3	LW-1LD2	ESL-TE 1	ESL-TE 3
$\langle T_0,$	$\langle 12.10,$	$\langle 9.57,$	$\langle 12.28,$	$\langle 20.81,$	$\langle 17.41,$	$\langle 18.93,$
$T_1\rangle$ [°]	$23.83\rangle$	$21.20\rangle$	$24.01\rangle$	$33.08\rangle$	$29.45\rangle$	$31.08\rangle$
$\tilde{F}_{cr}$ [N]	$8.08{\cdot}10^6$	$9.14{\cdot}10^6$	$8.51{\cdot}10^6$	$3.05{\cdot}10^3$	$3.05{\cdot}10^3$	$3.15{\cdot}10^3$
F_{cr} [N]	$8.08{\cdot}10^6$	$9.05 \cdot 10^6$	$8.47 \cdot 10^6$	$3.18{\cdot}10^3$	$3.20{\cdot}10^3$	$3.18{\cdot}10^3$
Error [%]	0.07	1.07	0.49	-3.97	-4.84	-0.59
κ_{max} [m^{-1}]	1.57	1.57	1.57	1.57	1.57	1.57

Figure 6.43 gathers the difference in the optimum design variables between the ESL and LW structural theories utilised for the unconstrained and constrained optimisation. The absolute error between the optimal solutions retrieved by ESL and LW is contained in the $\pm 5^\circ$ range. In addition, it is appreciated that the largest relative error in the predicted buckling load occurs when the thick laminate is modelled with an ESL-TE 1 model. This error diminishes when an ESL-TE 3 is considered. Contrariwise, the error committed is much lower when modelling thin laminates. In this context, ESL models lead to similar optimum designs to those retrieved by an LW approach when optimising the buckling load of a VAT plate.

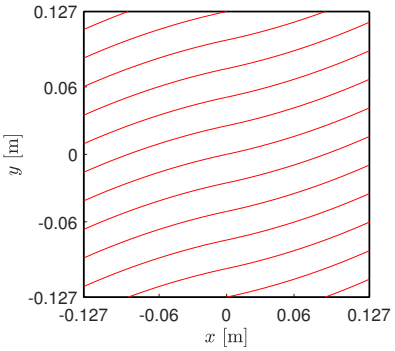

(a) $[0\langle 12.10, 23.83\rangle]$ ply.

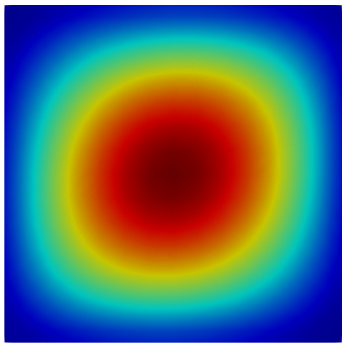

(b) First buckling mode of optimum thick laminate.

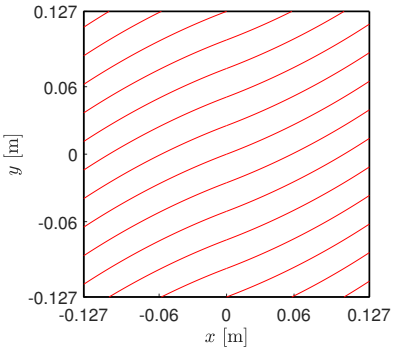

(c) $[0\langle 20.81, 33.08\rangle]$ ply.

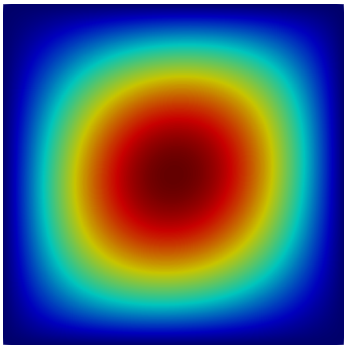

(d) First buckling mode of optimum thin laminate.

Figure 6.42 Fibre paths and first buckling mode of the LW optimum solution for the constrained buckling load optimization problem for thick (a,b) and thin (c,d) laminates.

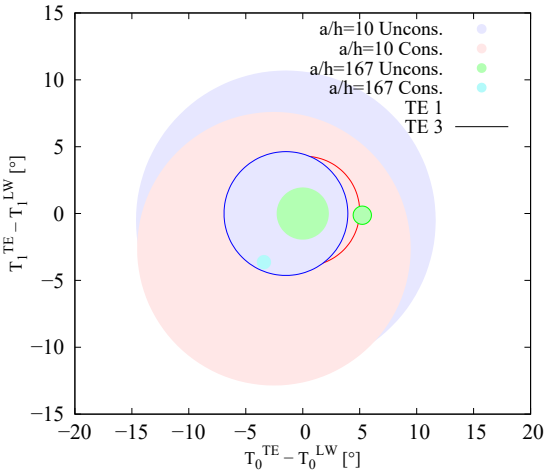

Figure 6.43 Absolute error between the optimal $\langle T_0, T_1\rangle$ obtained by ESL models with respect to an LW approach. The radius of the circle represents the relative error between the actual simulations using an ESL approach with respect to LW.

6.5.3 Vertical deflection optimisation

The minimisation of the deflection undergone from the plate presented in Section 6.1.1 is now addressed. The geometry, boundary and loading conditions, and material properties are already described in that section. The optimisation problem can be stated as follows:

$$\min_{\mathbf{x}} \quad -u_z(\mathbf{x}) \tag{6.7}$$

where $\mathbf{x} = \{T_0^1, T_1^1, T_0^2, T_1^2\}$ are the design variables of the $\theta = [\langle T_0^1, T_1^1 \rangle, \langle T_0^2, T_1^2 \rangle]$. For this problem, an optimisation algorithm that combines global and local search strategies is used to conduct the optimisation process. This algorithm is available in modeFrontier© and uses the actual FE simulation outcomes as the objective function.

Table 6.29 Optimal designs for the unconstrained deflection optimization problem.

	ESL-TE 1	ESL-TE 6	LW-1LD3
$\langle T_0^1,$	$\langle -90,$	$\langle -90,$	$\langle -90,$
$T_1^1\rangle$ [°]	$-5.36\rangle$	$-5.44\rangle$	$-5.44\rangle$
$\langle T_0^2,$	$\langle -90,$	$\langle -90,$	$\langle -90,$
$T_1^2\rangle$ [°]	$-5.32\rangle$	$-5.44\rangle$	$-5.44\rangle$
$-u_z \cdot 10^6$ [m]	3.74	4.16	4.16

The set of optimal solutions retrieved with the different structural theories is gathered in Table 6.29. It can be observed that ESL and LW models lead to similar fibre paths, ESL-TE 1 presenting slight differences in T_1^1 and T_1^2. It is appreciated that the three solutions have T_0^1 and T_0^2 equal to $-90°$. That implies that the structure is stiffer in the transverse direction at the centre of the plate, where the maximum deflection is observed. The $\langle -90, -5.44 \rangle^\circ$ fibre path of the LW optimal solution is displayed in Fig. 6.44. It is worth mentioning that the optimal fibre path is practically identical to the fundamental frequency optimisation shown in Section 6.5.1. This is because maximising the fundamental frequency is equivalent to maximising the flexural stiffness and, thus, minimising the vertical deflection.

As in the previous optimisation problems, the AFP machine's maximum turning radius is imposed as a constraint of the problem. In this regard, the constrained deflection minimisation problem reads as follows:

$$\min_{\mathbf{x}} \quad -u_z(\mathbf{x}) \;\; \text{s.t.} \quad -1/r_{\min} \leq \kappa^k(\mathbf{x}) \leq 1/r_{\min} \;\; k = 1,2 \tag{6.8}$$

in which the design variables are the same as in the unconstrained case, and κ^k denotes the curvature of the k^{th} layer fibre path.

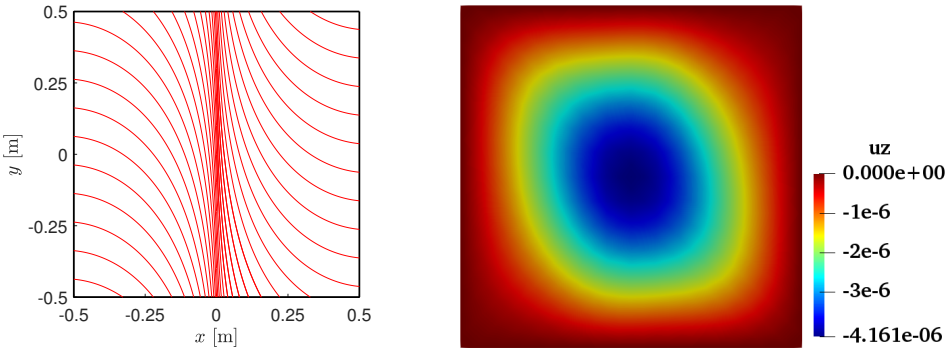

(a) $[\langle -90, -5.44 \rangle]$ ply.

(b) Deflection contour of the $[\langle -90, -5.44 \rangle]_2$ laminate.

Figure 6.44 Fibre paths and contour of the LW optimum solution for the unconstrained deflection optimization problem.

Table 6.30 Optimal designs for the constrained deflection optimization problem.

	ESL-TE 1	ESL-TE 6	LW-1LD3
$\langle T_0^1,$	$\langle 90,$	$\langle -90,$	$\langle 90,$
$T_1^1\rangle$ [°]	$34.95\rangle$	$-34.95\rangle$	$34.95\rangle$
$\langle T_0^2,$	$\langle 90,$	$\langle -90,$	$\langle 90,$
$T_1^2\rangle$ [°]	$34.95\rangle$	$-34.95\rangle$	$34.95\rangle$
$-u_z \cdot 10^6$ [m]	3.90	4.297	4.296
$\kappa^1_{max}/\kappa^2_{max}$ [m^{-1}]	1.57/1.57	1.57/1.57	1.57/1.57

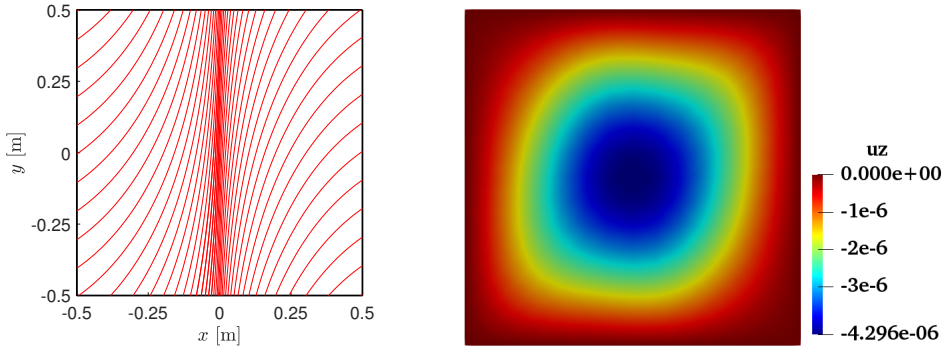

(a) $[\langle 90, 34.95 \rangle]$ ply. **(b)** Deflection contour of the $[\langle 90, 34.95 \rangle]_2$ laminate.

Figure 6.45 Fibre paths and contour of the LW optimum solution for the constrained deflection optimization problem.

Table 6.30 shows the optimal fibre path parameters of the constrained problem. As seen before, ESL and LW theories provide similar optimal designs. Indeed, ESL-TE 1 and LW-1LD3 designs are identical, while ESL-TE 6 shows the same laminate with opposite signs. This change in sign is due to the global and local search strategy and constraint handling of the optimisation algorithm. In any case, a symmetric response surface of u_z is foreseen as a very similar value of the deflection is observed for the $[\langle 90, 34.95 \rangle]_2$ and $[\langle -90, -34.95 \rangle]_2$ designs. The optimal LW-1LD3 design and the deflection contour are illustrated in Fig. 6.45.

Last, it is worth noting that the unconstrained and constrained solutions present the same fibre orientation at the plate centre, i.e., $T_0^1 = T_0^2 = \pm 90°$. This means these parameters are the most important, and the value of T_1^1 and T_1^2 depends on whether the problem is bounded. The influence of the design parameters on the objective function can be investigated before triggering the optimisation by performing a global sensitivity analysis [151].

Table 6.31 Material properties of the VAT plate considered for the SCF and strength optimization problems. Taken from Vijayachandran *et al.* [85].

E_1 [GPa]	$E_2 = E_3$ [GPa]	$G_{12} = G_{13}$ [GPa]	$\nu_{12} = \nu_{13}$ [-]
148.24	8.48	3.94	0.329

6.5.4 Strain concentration factor optimisation

The strain concentration factor (SCF) around the hole of a cutout VAT plate is studied in this section. The plate has a semi-width $a = 0.125$ m and a width-to-thickness ratio $2a/h = 10$. The material properties are reported in Table 6.31. Because of the symmetry of loading and geometry, only a quarter of the plate is considered, and

symmetry boundary conditions are imposed at planes $x = 0$ and $y = 0$. The boundary and loading conditions are illustrated in Fig. 6.46. The SCF is defined as follows:

$$\text{SCF} = \frac{\varepsilon_{xx}}{\varepsilon_0} \tag{6.9}$$

where ε_{xx} is the longitudinal strain component in the global reference frame, and ε_0 is the applied strain at $x = a$, which corresponds to a 1% of the plate semi-width.

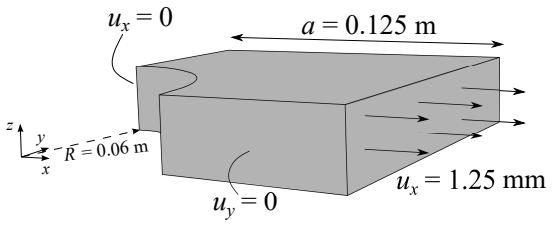

Figure 6.46 Geometry dimensions and boundary conditions of the notched plate considered in the SCF and strength optimisation problems.

The objective is minimising the SCF around the plate's hole. The unconstrained problem is stated as:

$$\min_{\mathbf{x}} \ \text{SCF}(\mathbf{x}), \tag{6.10}$$

in which $\mathbf{x} = \{T_0^1, T_1^1, T_0 T_1^2\}$ denotes the design variables vector. The layup sequence reads as $\theta = [\langle T_0^1, T_1^1 \rangle, \langle T_0^2, T_1^2 \rangle]_s$, and modeFrontier© is used to solve the optimisation problem.

Table 6.32 Optimal designs for the unconstrained SCF optimization problem.

	ESL-TE 1	ESL-TE 4	LW-1LD3
$\langle T_0^1,$	$\langle -47.53,$	$\langle -53.29,$	$\langle -55.18,$
$T_1^1\rangle$ [°]	$-78.99\rangle$	$-76.55\rangle$	$-75.39\rangle$
$\langle T_0^2,$	$\langle 11.04,$	$\langle 2.04,$	$\langle -0.62,$
$T_1^2\rangle$ [°]	$-90\rangle$	$-90\rangle$	$-90\rangle$
SCF [-]	0.60	0.74	0.76
SCF evaluated with an LW-LD3 model			
SCF [-]	1.06	0.78	0.76

Table 6.32 gathers the optimisation results of the unconstrained problem when different structural theories are employed. The outcomes of the optimisation process are compared against a quasi-isotropic (QI) $[90, \pm 45, 0]$ plate with the same dimensions and loading conditions as the VAT plate under investigation. The QI plate presents an SCF equal to 3.60. The optimal ESL-TE 1, ESL-TE 4, and LW-1LD3 designs result in an 83.3%, 79.4% and 78.9% drop in terms of SCF compared to the QI plate,

respectively. These reductions are obtained by considering the simulation outcome of each structural model used during the optimisation run. If the ESL-TE 1 and ESL-TE 4 optimal designs used an LW-1LD3 kinematic model, the SCF will differ, as pointed out in the last row of Table 6.32. This re-evaluation with an LW model is made because LW presents the highest fidelity. After this re-evaluation, the actual SCF diminishes by 70.5% and 78.3% for the ESL-TE 1 and ESL-TE 4 models, respectively. The resulting SCF optimal distributions, calculated with LW-1LD3 kinematics, are represented in Fig. (6.47). The ESL-TE 1 solution decreases steadily from the peak value. In contrast, ESL-TE 4 and LW-1LD3 show a slight increase in the cutout proximities and suddenly drop, subsequently reaching a plateau. Figure 6.48 illustrates the optimised fibre paths and SCF contours. As anticipated in Table 6.32, the retrieved optimal fibre paths are similar. Despite the similarities, it is remarkable the 39% difference between the optimal ESL-TE 1 and LW-1LD3, evaluated with the latter kinematics, in the predicted SCF, see Table 6.32.

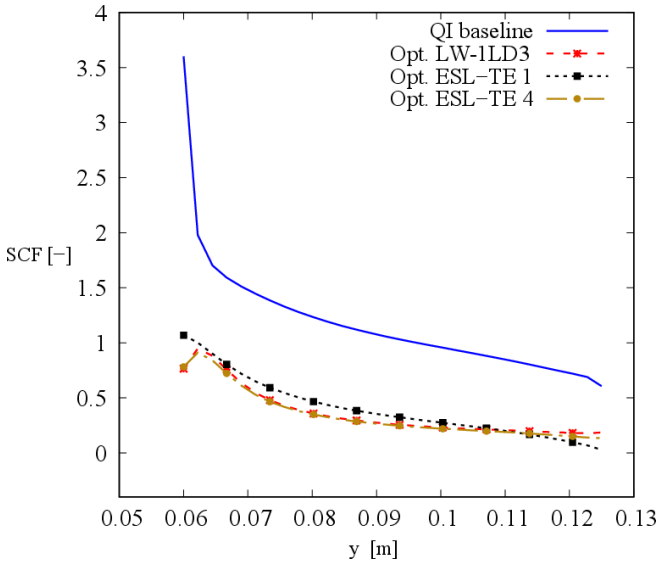

Figure 6.47 SCF distribution of the retrieved optimal solutions for the unconstrained optimisation problem. The distribution of the ESL optimal designs is computed with LW-1LD3 kinematics.

Although a significant SCF reduction, the previous optimal fibre paths cannot be manufactured because they exceed the maximum curvature of the AFP head. Thus, a constrained SCF optimisation problem is posed as follows:

$$\min_{\mathbf{x}} \ \mathrm{SCF}(\mathbf{x}) \ \text{ s.t. } \quad -1/r_{\min} \leq \kappa^k(\mathbf{x}) \leq 1/r_{\min} \ \ k = 1,2 \tag{6.11}$$

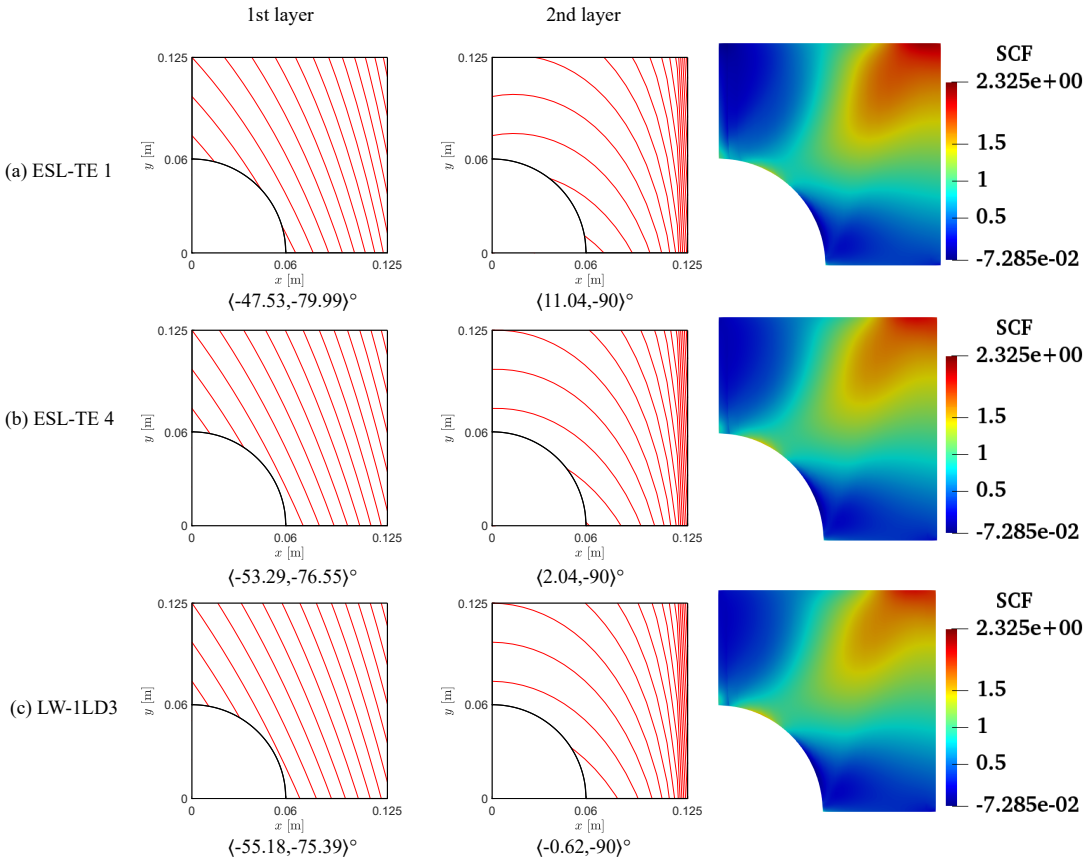

Figure 6.48 Fibre patterns and SCF contours of the retrieved solutions for the unconstrained optimisation problem. The contour of the ESL optimal designs is computed with LW-1LD3 kinematics.

Table 6.33 Optimal designs for the constrained SCF optimization problem.

	ESL-TE 1	ESL-TE 4	LW-1LD3
$\langle T_0^1,$ $T_1^1\rangle$ [°]	$\langle -50.63,$ $-68.56\rangle$	$\langle -69.60$ $-51.50\rangle$	$\langle 44.87,$ $60.83\rangle$
$\langle T_0^2,$ $T_1^2\rangle$ [°]	$\langle 19.52,$ $31.49\rangle$	$\langle -11.99,$ $-23.54\rangle$	$\langle -13.64,$ $-25.24\rangle$
SCF [-]	1.41	1.42	1.38
κ_1/κ_2 [m^{-1}]	1.56/1.57	1.57/1.57	1.57/1.57
SCF evaluated with an LW-LD3 model			
SCF [-]	3.60	1.47	1.38

The solutions to the constrained problem are available in Table 6.33. Compared to the QI plate, the SCF drop is lower than the unconstrained problem, as expected. The retrieved optimal solutions resulted in a 60.8%, 60.5% and 61.6% SCF reduction for the ESL-TE 1, ESL-TE 4 and LW-1LD3 models, respectively. Nonetheless, When the optimal ESL-TE 1 and ESL-TE 4 designs are evaluated with LW-1LD3 kinematics, their SCF equals 3.60 and 1.47, which means a 0% and 40.8% reduction, respectively. Figure 6.49 shows the SCF distributions calculated with an LW-1LD3 model. The SCF of the optimal ESL-TE 1 decreases steadily. In addition, it is larger than the QI distribution between $y = 0.06$ and $y = 0.0095$. The LW-1LD3 optimum presents a significant rise in SCF and a slow decrease. Last, the ESL-TE 4 solution shows a plateau around the hole and suddenly drops at a steeper rate than the LW-1LD3 optimal design. Figure 6.50 shows the fibre paths and SCF contours of the optimal solutions evaluated with an LW-1LD3 structural theory. Higher SCF values compared to the unconstrained problem are appreciated. The optimal ESL-TE 4 and LW-1LD3 present smoother SCF transitions around the hole than the optimal ESL-TE 1 design.

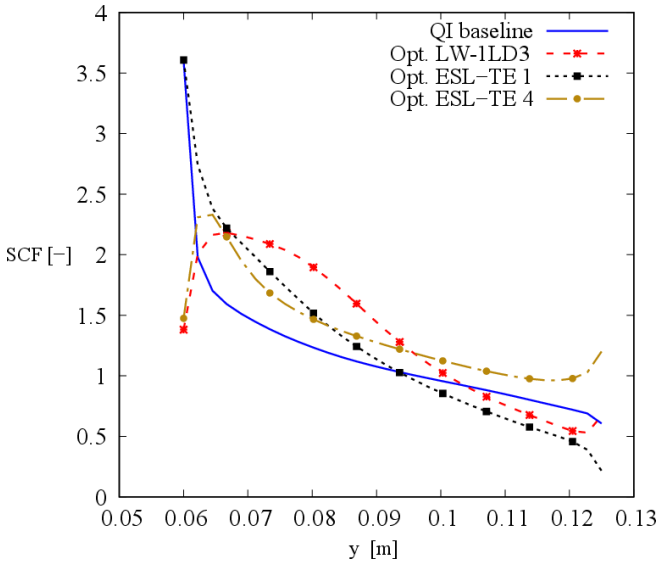

Figure 6.49 SCF distribution of the retrieved optimal solutions for the constrained optimisation problem. The distribution of the ESL optimal designs is computed with LW-1LD3 kinematics.

In the unconstrained problem, the optimum designs were similar for the considered structural models; contrariwise, the constrained problem leads to slight differences. They might be due to the constraints and how they subdivide the design space into feasible and unfeasible regions. The optimal results reported in Table 6.33 show that ESL-TE 1 and LW-1LD3 optimums share similar orientations with opposite signs. This is because the function $\mathrm{SCF}(\mathbf{x})$ is symmetric with respect to the constraint bounds. This symmetry is further demonstrated by observing the optimal $\langle T_0^2, T_1^2 \rangle$ from the

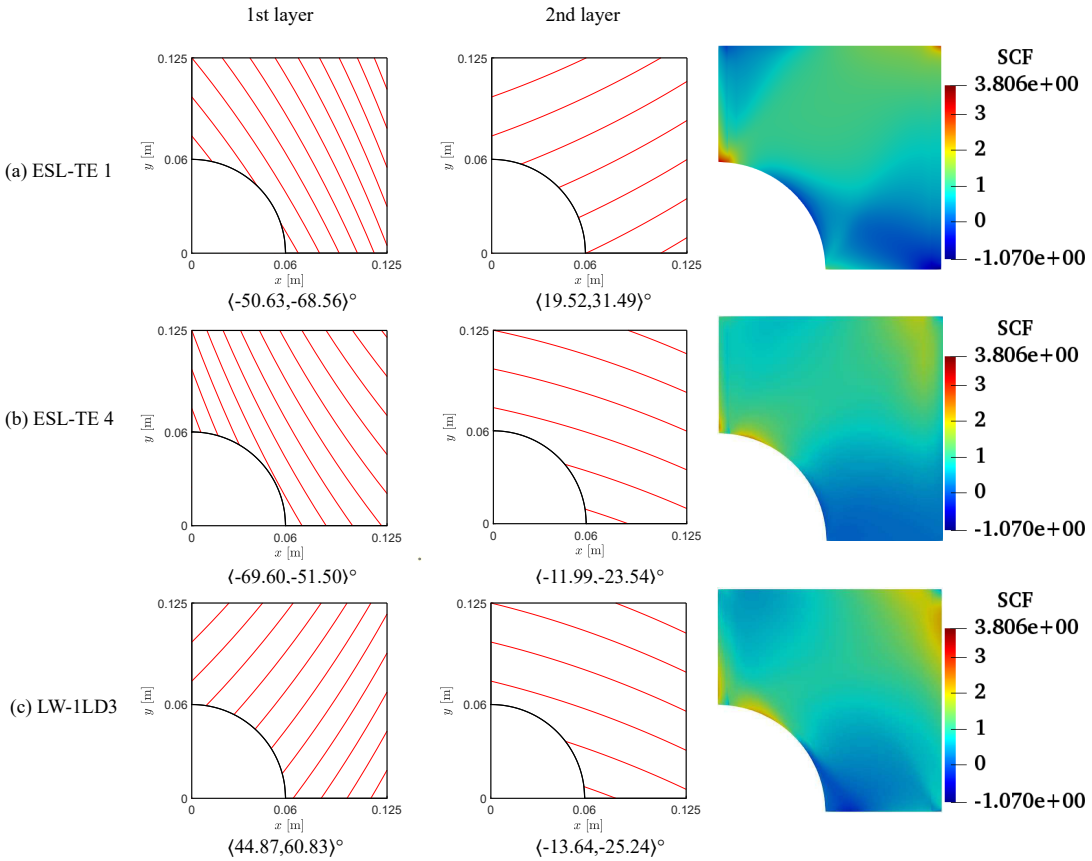

Figure 6.50 Fibre patterns and SCF contours of the retrieved solutions for the constrained optimisation problem. The contour of the ESL optimal designs is computed with LW-1LD3 kinematics.

ESL-TE 4 model, which differs by a couple of degrees from the LW-1LD3 optimal $\langle T_0^2, T_1^2 \rangle$. In addition, the optimisation algorithm combines global and local search capabilities. The former implies that the algorithm tries to explore design space. After finding a promising optimal candidate, it carries out a local search to converge to the local optimum. In this regard, the solver might have found the solution with the opposite sign during the global exploration phase. It is related to the nonconvexity of the optimisation problem, the multimodality, and the eventual noncontinuity of the objective function.

6.5.5 Strength optimisation

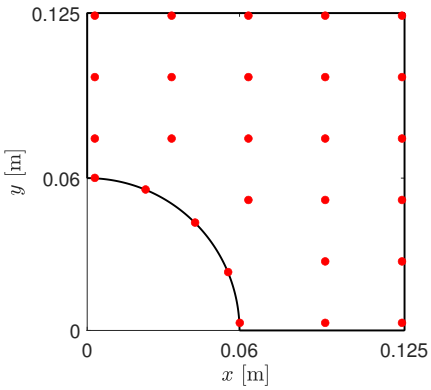

Figure 6.51 Control points in which the $\mathscr{FI}$ are evaluated through the thickness to perform the strength maximisation.

The strength of the cutout plate from Section 6.5.4 is maximised in this section. To do so, the safety factor $\mathscr{SF}$ is used as the objective function. The optimisation problem reads as follows:

$$\max_{\mathbf{x}} \ \min(\mathscr{SF}_j(\mathbf{x})) \quad j = 1, ..., n_s, \tag{6.12}$$

where n_s denotes the number of through-the-thickness sampling points where $\mathscr{SF}$ is measured. The optimisation problem is posed in terms of the safety factor as in the work by Groenwold and Haftka [152]. They state that minimising the maximum $\mathscr{FI}$ is equivalent to maximising the minimum $\mathscr{SF}$. The Hashin 3D failure criteria [153] is evaluated through the thickness at the control points highlighted in Fig. 6.51, and the safety factor is computed according to the procedure described in Appendix A.2. Recall that Hashin 3D comprises four failure modes, namely Fibre Tension (FT), Fibre Compression (FC), Matrix Tension (MT), and Matrix Compression (MC). The

material strengths were taken from Toray© T800S datasheet [154] and are gathered in Table 6.34.

Table 6.34 Strength properties of the material used for strength optimization. Taken from Toray© T800S datasheet [154].

X_T [MPa]	X_C [MPa]	Y_T [MPa]	Y_C [MPa]	S_{12} [MPa]	$S_{13} = S_{23}$ [MPa]
3290.0	1490.0	79.0	300.0	135.0	87.6

The optimal solutions to the unconstrained optimisation problem are gathered in Table 6.35. As in the previous optimisation, ESL-TE 1, ESL-TE 4, and LW-1LD3 kinematic models are used to solve the problem in Eq. (6.12). The optimal fibre paths and $\mathscr{FI}$ contours are illustrated in Fig. 6.52. From Table 6.35, it is inferred that various optimal solutions are achieved for the different structural theories. Likewise, the safety factors differ from each model. Notably, a lower $\mathscr{SF}$ is obtained when the optimal ESL designs are evaluated with an LW-1LD3 structural theory. Besides, the failure onset mode changes from FT to MT for the ESL-TE 1 design.

Table 6.35 Optimal designs for the unconstrained strength optimization problem.

	ESL-TE 1	ESL-TE 4	LW-1LD3
$\langle T_0^1,$	$\langle 2.31,$	$\langle 90,$	$\langle 4.10,$
$T_1^1\rangle$ [°]	$28.00\rangle$	$79.33\rangle$	$1.70\rangle$
$\langle T_0^2,$	$\langle 1.95,$	$\langle 9.25,$	$\langle -0.66,$
$T_1^2\rangle$ [°]	$-1.13\rangle$	$90\rangle$	$58.53\rangle$
$\mathscr{SF}$ [-]	0.862(FT)	0.627(MT)	0.824(FT)
$\mathscr{SF}$ evaluated with an LW-1LD3 model			
$\mathscr{SF}$ [-]	0.600(MT)	0.607(MT)	0.824(FT)

Figure 6.52 provides some $\mathscr{FI}$ contours and the location where failure is triggered. The point in which failure onset occurs can be retrieved by following the procedure depicted in Appendix A.2 for the n_s sampling points. The ESL-TE 1 optimum design is affected by FT at the cutout and the top of the layup. However, if this design is evaluated with LW-1LD3 kinematics, the failure onset is located at the rightmost edge and $z = -h/2$. Concerning ESL-TE 4, the first failure mode triggered is MT in the middle of the upper edge and $z = h/2$. Nonetheless, when the ESL-TE 4 optimal design uses the LW-1LD3 structural theory, the MT onset occurs at the cutout and bottom in the layup direction. The LW-1LD3 optimum fails due to FT at the hole at the laminate bottom.

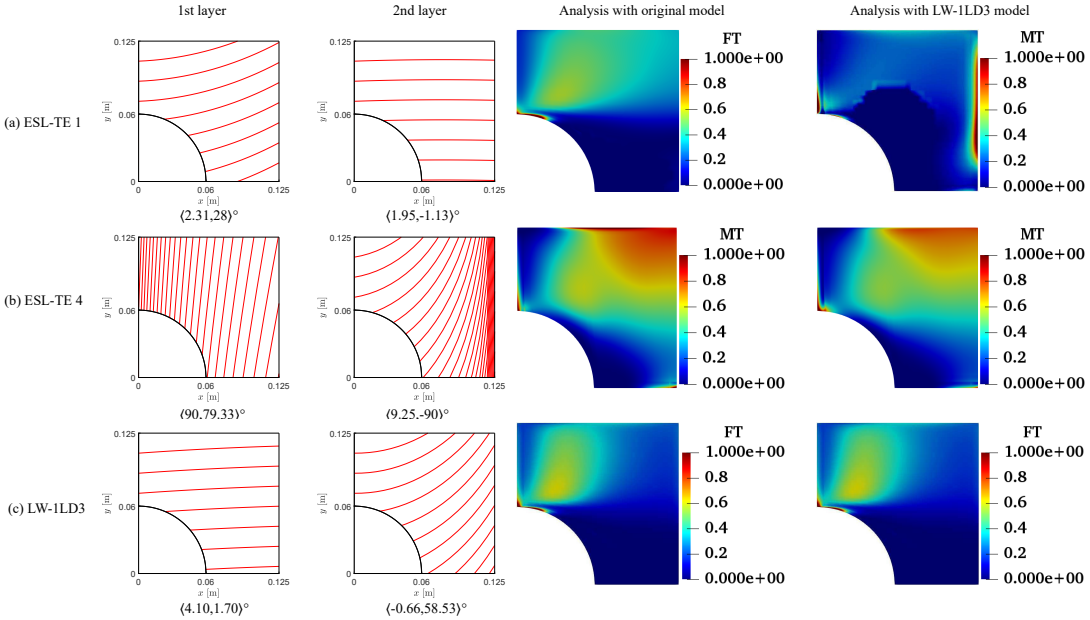

Figure 6.52 Fibre patterns and $\mathscr{FI}$ contours of the retrieved solutions for the unconstrained optimization problem. The contours of the ESL models are computed with the original ESL and the LW-1LD3 models. The failure mode that triggers the loss of strength is the only one represented.

The constrained strength maximisation problem, where the requirement is the maximum steering curvature, reads as follows:

$$\max_{\mathbf{x}} \ \min(\mathscr{SF}_j(\mathbf{x})) \quad j=1,\ldots,n_s, \ \text{ s.t.} \quad -1/r_{\min} \leq \kappa^k(\mathbf{x}) \leq 1/r_{\min} \quad k=1,2 \quad (6.13)$$

The solutions to the problem stated in Eq. (6.13) are available in Table 6.36. It is observed that nonidentical optimal solutions are retrieved for the different structural theories under consideration. Furthermore, it is remarkable that the constrained ESL-TE 4 and LW-1LD3 models provided higher safety factors than their unconstrained counterparts. Moreover, the three solutions present non-active constraint values. That is, the κ^1 and κ^2 requirements are not equal to the maximum allowable value of $\kappa_{max} = 1.5748\ \text{m}^{-1}$. From a mathematical point of view, it means that the maximum turning radius might not be considered a constraint when optimising the strength of VAT components. Of course, this assumption holds only in the present case, where manufacturing defects, such as gaps or overlaps, are not considered within the numerical model.

Concerning the failure onset modes, it is appreciated that ESL designs keep it from unconstrained optimisation. As seen before, the $\mathscr{SF}$ value drops when the optimal ESL are evaluated with an LW-1LD3 model. However, the mode failure mode does

Table 6.36 Optimal designs for the constrained strength optimization problem.

	ESL-TE 1	ESL-TE 4	LW-1LD3
$\langle T_0^1,$	$\langle 6.54,$	$\langle 2.27,$	$\langle 2.91,$
$T_1^1\rangle$ [°]	$0.70\rangle$	$7.24\rangle$	$-1.95\rangle$
$\langle T_0^2,$	$\langle -1.40,$	$\langle 2.27,$	$\langle 2.27,$
$T_1^2\rangle$ [°]	$7.85\rangle$	$-3.15\rangle$	$5.51\rangle$
$\mathscr{SF}$ [-]	0.777(FT)	0.912(MT)	1.08(MC)
κ_1/κ_2 [m^{-1}]	0.81/1.29	0.69/0.76	0.68/0.45
$\mathscr{SF}$ evaluated with an LW-1LD3 model			
$\mathscr{SF}$ [-]	0.401(FT)	0.644(MT)	1.08(MC)

not vary in the constrained ESL optimal designs. Contrariwise, the LW-1LD3 model reaches the onset due to MC, differing from the FT mode of the unconstrained solution.

The optimal fibre paths and the $\mathscr{FI}$ contours are available in Fig. 6.53. The ESL-TE 1 optimum fails in FT at the top layer and in the cutout proximities. Nevertheless, when this design is analysed with the LW-1LD3 kinematics, it fails due to FT at the same in-plane coordinates but at the interface between the second and third layers. The ESL-TE 4 optimum fails due to MT at the leftmost edge in the fourth layer. When this analysis is carried out with LW-1LD3 structural theory, failure happens at the right edge and $z = -h/2$. Last, the LW-1LD3 optimal design fails in MC at the right edge, close to the interface between the first and second plies.

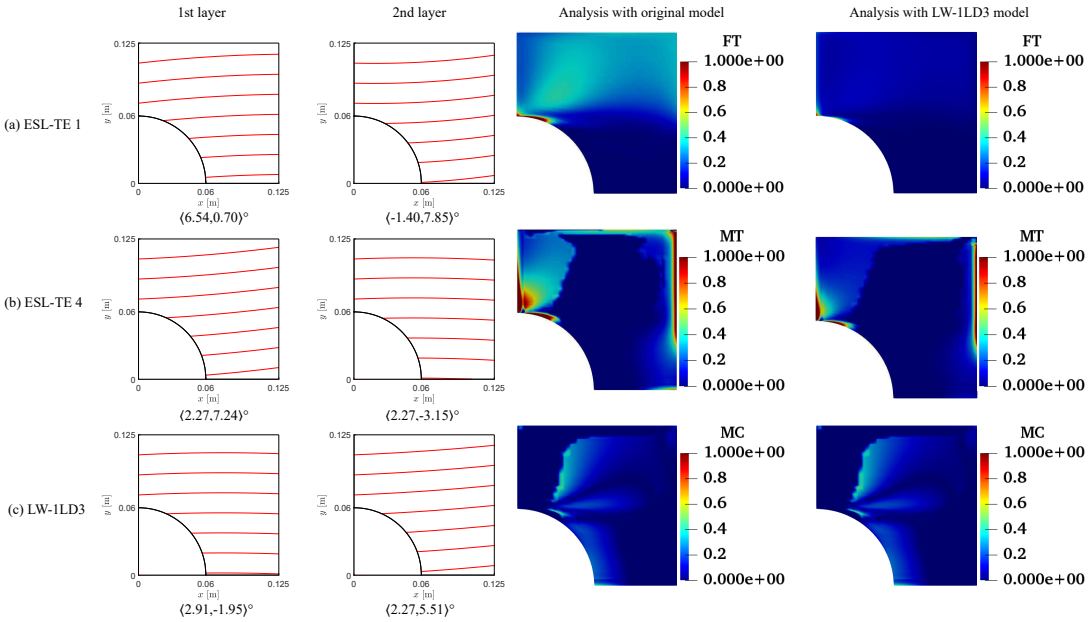

Figure 6.53 Fibre patterns and $\mathscr{FI}$ contours of the retrieved solutions for the constrained optimization problem. The contours of the ESL models are computed with the original ESL and the LW-1LD3 models. The failure mode that triggers the loss of strength is the only one represented.

6.5.6 Fundamental frequency optimisation considering gaps and overlaps

Table 6.37 Material properties of the pre-impregnated tows and resin used in Akbarzadeh *et al.* [46].

	E_1[GPa]	$E_2 = E_3$[GPa]	G_{12}[GPa]	$G_{13} = G_{23}$[GPa]	ν_{12} [-]	ρ [kg/m^3]
Tow	143	9.1	4.82	4.9	0.3	1500
Resin	3.72	3.72	1.43	1.43	0.3	1100

In this case, deterministic manufacturing defects are included within the numerical model used in the optimisation process. For doing so, the procedure depicted in Sections 4.4 and 4.5 is followed. This approach is verified against the optimum results found in [46]. In detail, a sixteen-layered symmetric and balanced $[\langle 58,39\rangle]_{4s}$ laminate and width-to-thickness ratio $a/h = 200$. The width and length of the plate are $a = b = 1$ m, and the individual ply thickness equals 0.159 mm. The plate is simply supported on all four sides. The mechanical properties of the pre-impregnated tows and the resin are listed in Table 6.37.

The effect of the structural theory on the predicted fundamental frequency is investigated first. A 6×6 Q9 mesh is employed because of the accuracy and computational time trade-off. Various ESL and LW models are tested for a complete gap and overlap

Table 6.38 Effect of the structural theory on the first fundamental frequencies. Both LD and TE expansions are considered along the thickness with a complete gap and overlap condition. Each model uses a 6×6 Q9 FE mesh.

Model	DOFs	f_1 [Hz]
Complete gap		
Ref [46]	-	30.95
ESL-TE 1	1041	32.17
ESL-TE 2	1521	31.91
ESL-TE 3	2028	31.90
LW-1LD1	8619	31.89
LW-1LD2	16731	31.89
LW-1LD3	24843	31.89
Complete overlap		
Ref [46]	-	36.19
ESL-TE 1	1014	37.00
ESL-TE 2	1521	36.65
ESL-TE 3	2028	36.64
ESL-TE 4	2535	36.64
ESL-TE 5	3042	36.64

manufacturing strategy. The results are enlisted in Table 6.38. A good agreement between the proposed method and the reference is appreciated. It is observed that, in the complete gap case, there is no significant difference between ESL and LW models in terms of the predicted f_1. Only ESL theories are employed to study the complete overlap strategy. This is because a local thickness increase needs to be associated with each FE, which would require a significant rise in computational burden. This issue has already been explained in Section 4.5. Again, no significant difference is observed as the order of the TE increases.

Table 6.39 Geometric and material properties of the VAT plate taken into account for the optimisation. Taken from Akhavan and Ribeiro [150].

Parameter	Value
$a = b$ [m]	1
h [m]	0.01
E_1 [GPa]	173
$E_2 = E_3$ [GPa]	7.2
$G_{12} = G_{13} = G_{23}$ [GPa]	3.76
$\nu_{12} = \nu_{13} = \nu_{23}$ [-]	0.29
ρ [kg/m^3]	1540

Once the model is verified, the optimisation problem can be posed. The objective is to maximise the first natural frequency of a three-layered laminate by adjusting the

lamination angles T_0 and T_1 for each ply. Table 6.39 reports the geometry dimensions and material properties. The optimal defect-free, complete gap and complete overlap conditions are investigated and a limitation on the curvature of the fibre path $\kappa_{max} = 1.5748\ \mathrm{m}^{-1}$ is incorporated. In this regard, the problem reads as follows:

$$\min_{\mathbf{x}} \quad -f_1(\mathbf{x}) \quad \text{s.t.} \quad -1/r_{\min} \leq \kappa^k(\mathbf{x}) \leq 1/r_{\min} \quad k = 1,2,3 \tag{6.14}$$

where $\mathbf{x} = \{T_0^1, T_1^1, T_0^2, T_1^2, T_0^3, T_1^3\}$. The workflow illustrated in Fig. 6.54 solves the constrained optimisation problem.

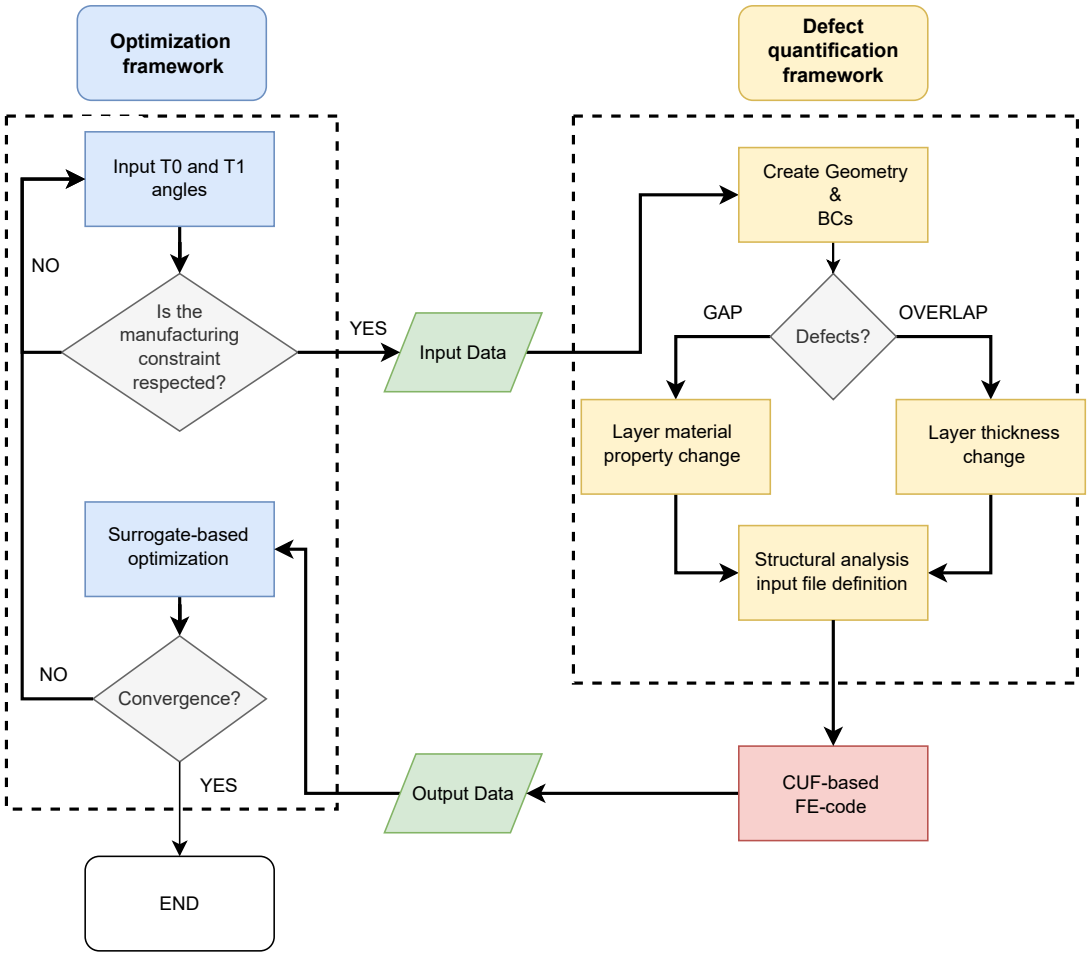

Figure 6.54 Flowchart of the surrogate-based optimisation framework considering manufacturing defects and constraints. CUF is used to solve the mechanical problem and DLM to map the fabrication flaws.

Table 6.40 provides the optimal results for the pristine and defected models and different structural theories. It is observed that the optimal fibre paths differ depending on the modelling condition, i.e., defect-free or with fabrication flaws. The fact that a quasi-symmetric layup is retrieved is remarkable. That is, $\langle T_0^1, T_1^1 \rangle \approx \langle T_0^3, T_1^3 \rangle$. In

addition, it is worth noting that for the complete gap strategy, the first and third layers present an almost unsteered design. As demonstrated in the previous optimisation results, very similar optimal stacking sequences are obtained regardless of the selected structural theory. A graphical representation of the design space for the three manufacturing conditions is available in Fig. 6.55. In these plots, it has been assumed $\langle T_0^1, T_1^1 \rangle = \langle T_0^3, T_1^3 \rangle$ while the fibre orientation of the second layer is equal to the optimal solution. The defect-free and complete overlap contour plots resemble each other. Contrariwise, the complete gap map presents higher fundamental frequency values at the centre of the design space.

Table 6.40 Optimal designs for the constrained fundamental frequency optimisation problem considering defect-free, complete gap and complete overlap condition.

	ESL-TE 1	ESL-TE 3	LW-1LD1
Defect-free			
$\langle T_0^1, T_1^1 \rangle$ [°]	$\langle 88.31, 43.35 \rangle$	$\langle 88.25, 43.29 \rangle$	$\langle 89.62, 44.71 \rangle$
$\langle T_0^2, T_1^2 \rangle$ [°]	$\langle -56.84, -15.69 \rangle$	$\langle -34.99, -17.86 \rangle$	$\langle -56.55, -42.80 \rangle$
$\langle T_0^3, T_1^3 \rangle$ [°]	$\langle 87.77, 42.95 \rangle$	$\langle 88.38, 43.40 \rangle$	$\langle 88.80, 43.98 \rangle$
f_1 [Hz]	120.74	119.57	119.35
Complete gap			
$\langle T_0^1, T_1^1 \rangle$ [°]	$\langle -1.28, 0.54 \rangle$	$\langle -0.38, -1.09 \rangle$	$\langle -1.42, 0.26 \rangle$
$\langle T_0^2, T_1^2 \rangle$ [°]	$\langle 48.89, 19.74 \rangle$	$\langle 53.76, 37.26 \rangle$	$\langle 46.66, 37.14 \rangle$
$\langle T_0^3, T_1^3 \rangle$ [°]	$\langle -0.65, 2.32 \rangle$	$\langle -2.28, 0.35 \rangle$	$\langle -1.21, -0.15 \rangle$
f_1 [Hz]	116.77	115.77	115.89
Complete overlap			
$\langle T_0^1, T_1^1 \rangle$ [°]	$\langle 35.36, -6.16 \rangle$	$\langle 35.49, -5.93 \rangle$	-
$\langle T_0^2, T_1^2 \rangle$ [°]	$\langle 65.25, 21.75 \rangle$	$\langle 64.64, 21.97 \rangle$	-
$\langle T_0^3, T_1^3 \rangle$ [°]	$\langle 33.37, -8.50 \rangle$	$\langle 34.29, -9.42 \rangle$	-
f_1 [Hz]	124.68	123.20	-

Last, the first modal shape of the optimised manufacturing conditions is available in Fig. 6.56. The defect-free and complete overlap designs present an ellipse-like lobe pointing towards the top left and bottom right corners, whereas the complete gap optimal design has a rounder shape. Because of the different mode shapes, one could optimise the modal shape for a particular application rather than the fundamental frequency in future investigations.

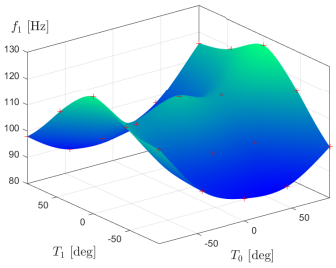

(a) LW-1LD2 defect-free response surface.

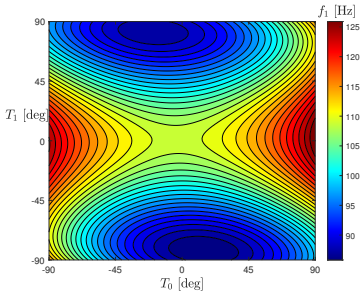

(b) LW-1LD2 defect-free contour plot.

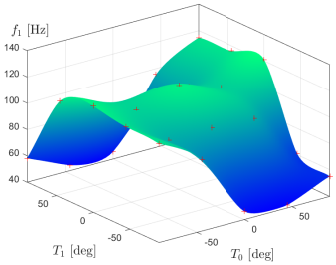

(c) LW-1LD2 complete gap response surface.

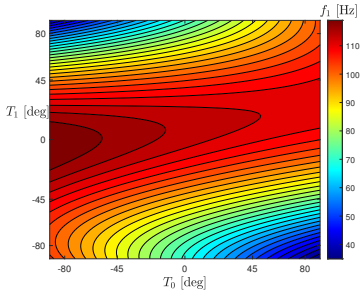

(d) LW-1LD2 complete gap contour plot.

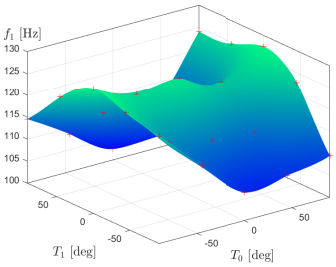

(e) ESL-TE 3 complete overlap response surface.

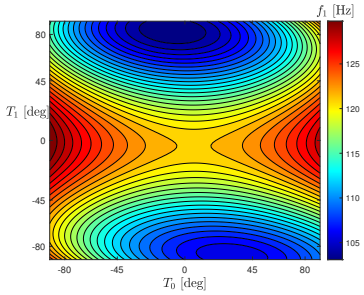

(f) ESL-TE 3 complete overlap contour plot.

Figure 6.55 Response surfaces and contour plots of the defect-free, complete gap and complete overlap condition. For each configuration, T_0^2 and T_1^2 are equal to those of the optimal solution and it is assumed $\langle T_0^1, T_1^1 \rangle = \langle T_0^3, T_1^3 \rangle = \langle T_0, T_1 \rangle$.

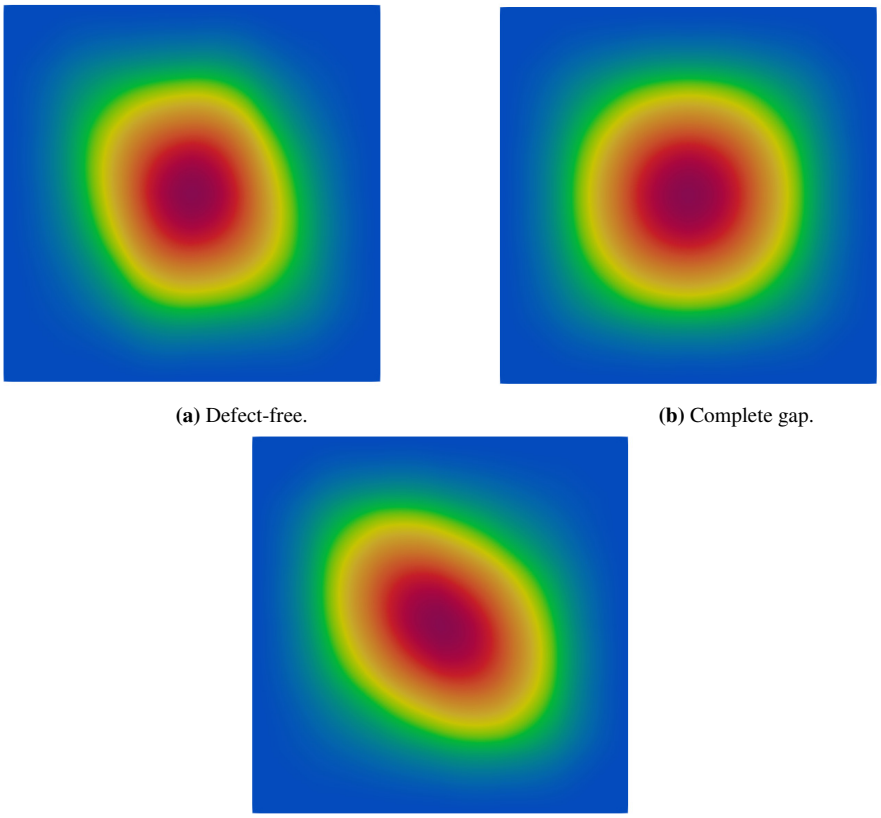

(a) Defect-free.

(b) Complete gap.

(c) Complete overlap

Figure 6.56 First mode shape of the optimal defect-free, complete gap and complete overlap configuration.

Chapter 7

Conclusions

7.1 Remarks

This thesis presented an efficient tool for the multiscale analysis of variable stiffness composites. The different scales have been modelled as beam, plate and shell structures. For instance, fibre-matrix unit cells have been considered as beams, while tow-steered components have been modelled as beams, plates and shells. These analyses were performed using the Carrera Unified Formulation (CUF) as a generator of refined one-dimensional and two-dimensional models. CUF allows the generation of low-to-high-order models straightforwardly and hierarchically. In the CUF framework, the governing equations and the associated Finite Element (FE) arrays of any model are formulated in terms of Fundamental Nuclei (FNs), whose dimensions are independent of the order of the structural theory and the strain approximation assumed. Taylor (TE), Lagrange (LE) and Hierarchical Legendre (HLE) expansions have been employed throughout the manuscript.

First, plate and shell models were presented and employed to carry out linear static analyses of VAT components. The models were validated against literature and commercial software Abaqus. Attention was paid to predicting deflections and 3D through-the-thickness stress distributions of structures subject to different loads and boundary conditions.

Second, beam models were devoted to the linear static analysis of straight-fibre composite structures. Layer- and fibre-scale studies were conducted in detail utilising the Component-Wise (CW) approach. The layer scale was simulated through the novel embedded CW method introduced in this thesis. Displacement and 3D stress distributions over laminated structures and textiles were obtained. On the other hand, the thermo-elastic behaviour at the fibre scale was modelled following the original CW method. Non-isoparametric HLE was used to describe the Unit Cell (UC) cross-

section. Homogenised material thermo-elastic properties and 3D stress distributions were predicted.

Subsequently, the effect of uncertainty manufacturing defects at the different structural scales is studied. Specifically, the influence of fibre waviness and fibre volume fraction on the buckling performance and the stress prediction at the layer and fibre scale is addressed.

The second set of results focuses on the optimisation of VAT plates. Global responses such as fundamental frequency and buckling loads are optimised by combining polynomial surrogate models and Genetic Algorithm (GA). Subsequently, the flexural and in-plane stiffness and the strength of VAT laminates are optimised through an optimisation algorithm, implemented in modeFrontier©, that combines global and local search capabilities. Last, manufacturing defects were also considered for the fundamental frequency optimisation. The effect of the structural theory on the optimum solution was investigated.

7.2 Main contributions

The main novelties and important results obtained during this doctoral research are summarised in the following:

- The proposed 1D and 2D models can accurately predict the 3D stress state of straight fibre and tow-steered composite beams, plates and shells.
- Displacements and in-plane stress components provided by equivalent-single-layer (ESL) and layer-wise (LW) models agree with those from literature or obtained using commercial software.
- The proposed CUF-based LW models can predict transverse stresses with unprecedented accuracy and a reduced fraction of degrees of freedom (DOFs) compared with reference 3D solid models. An accurate stress prediction is extremely useful for failure considerations.
- Classical theories, such as first-order shear deformation (FSDT), can bring wrong shear and stress distributions. This is not admissible when pursuing multiscale analysis, where information exchange between the scales is needed. High-order approximations, like TE 3 or TE 4, may be sufficient in some circumstances. However, LW is preferred when an accurate stress prediction is required.
- The introduced embedded CW method represents an efficient approach for the layer-scale, or mesoscale, analysis of composites. One of the main advantages

is the simple meshing procedure since the host and embedded components are meshed separately. In this regard, cumbersome meshing strategies are no longer needed. Additionally, fewer DOFs are required to simulate intricate geometries with no loss of accuracy.

- The MSG-CUF coupling allows retrieving homogenised thermo-elastic properties of heterogeneous fibre- and particle-reinforced materials. This framework foresees using HLE expansion functions based on a non-isoparametric description of the beam's cross-section kinematics. Second-to-fourth-order HLE models are enough to predict homogenised material properties well. At the same time, higher-order HLE are mandatory to account for the steep stress gradients that appear within the UC.

- The effect of layer-scale uncertainty defects such as fibre waviness on the 3D stress state affects especially the normal in-plane stress components σ_{xx} and σ_{yy}. A large variability was observed, which may affect the failure index prediction and eventually initiate the damage evolution unexpectedly.

- Fibre waviness affects the buckling load value. Low-order ESL-TE does not capture the mean value or the standard deviation of the buckling load, especially when accounting for higher buckling modes. Higher-order ESL theories provide similar buckling load mean values and standard deviations for the first modes.

- Regarding the buckling modes, low-order ESL theories cannot capture resemblances between the buckling modes of the pristine and flawed structure. Higher-order ESL models perform better. Nevertheless, LW theories are the ones that better predict the mode variability between the defect-free and the defective VAT components.

- An efficient multiscale defect propagation scheme was implemented. Fibre volume fraction at the fibre level and waviness at the layer scale were incorporated within the CUF framework utilising random fields generated with the Karhunen-Loève expansion (KLE).

- When accounting for multiple defects, the buckling loads present larger standard deviations than in the single-defected case. Therefore, Probability Density Functions (PDFs) are wider when flaws at different scales are considered.

- The uncertainty quantification analysis of buckling load can be accelerated using surrogate models. In this regard, Polynomial Chaos Expansion (PCE) metamodels are helpful for reliability analysis or reliability-based design optimisation.

The surrogate model is constructed with fewer numerical analyses, and the PDF is retrieved by simply evaluating the PCE model.

- Stochastic stress analyses at the fibre scale were carried out, in which fibre volume fraction and fibre waviness were propagated throughout the material scales. A significant difference was found between the nominal fibre scale circumferential stresses t_s and the mean value of the stochastic t_s. Moreover, fibre's longitudinal stress t_t presented larger variability in terms of maximum-minimum range.

- The normal stress t_n continuity between fibre and matrix was guaranteed using high-order HLE and non-isoparametric subdomains. In this context, a geometrically exact shape of the micromechanical model was generated.

- The effect of the structural theory on the retrieved optimal design variables for a series of mechanical performances was investigated. In the first instance, a polynomial surrogate model that mimicked the fundamental frequency and buckling load of VAT plates was built. The metamodel was combined with GA to optimise the fundamental frequency and buckling. Direct simulations were performed in a second series of analyses through modeFrontier© and MATLAB©. The selected optimisation algorithm combined global and local search capabilities.

- It has been demonstrated that ESL models lead to similar optimal solutions to those obtained by an LW approach. This was proven for unconstrained and constrained problems and different width-to-thickness ratios. However, in the case of low-order ESL theories, the fundamental frequency is overestimated, especially when thick plates are studied.

- In the buckling load optimisation of VAT plates, ESL models led to similar results in terms of buckling load and optimal design variables as those retrieved by an LW method. This has been proven to be valid for both thin and thick plates and unconstrained and constrained optimisation problems. Nonetheless, ESL theories overestimate the buckling load since they lead to stiffer models.

- Surrogate models are helpful in solving optimisation problems because of the quick evaluation of the objective function or constraints that they mimic. However, errors might be committed if few samples or a poor sampling strategy is followed. This might represent an essential issue if failure constraints or uncertainty are involved in the optimisation problem. Thus, direct simulations might be preferred in those cases.

- When minimising the vertical deflection, ESL and LW models provided equivalent results regarding optimal fibre paths. The only difference was the predicted value of u_z.
- Again, ESL and LW approaches led to similar results in optimising the strain concentration factor (SCF). Minor differences were observed in the unconstrained problem. On the other hand, for the manufacture-constraint optimisation, the optimal fibre orientations had opposite signs, but the fibre path trends were comparable.
- When optimising the strength of VAT components, different modelling strategies lead to diverse fibre paths in the unconstrained problem. Similar and practically non-steered solutions were retrieved in the constrained problem. Surprisingly, LW and high-order ESL theories yielded larger safety factors than the unconstrained problem. It means that maximum curvature constraint may not be necessary for strength optimisation.
- Considering the manufacturing defects in the optimisation loop, different solutions are obtained for the various fabrication strategies. The optimal defect-free layup sequence differs from those involving gaps and overlaps. Therefore, the modal shape *a priori* varies between the fabrication strategies. This has implications for optimising the modal shape rather than the fundamental frequency.
- In general, when optimising global continuous magnitudes such as fundamental frequency, buckling load, vertical deflection or SCF, which ultimately can be written as first-order derivatives of the displacement, ESL and LW models tend to provide similar optimal solutions. Contrariwise, when optimising a discontinuous magnitude like the minimum safety factor, which involves stress components for its prediction, ESL and LW approaches lead to different optimal designs.

7.3 Future activities

This thesis has provided the foundations for a plethora of future developments. In this research, CUF has demonstrated excellent performance for the multiscale analysis of tow-steered composites, modelled primarily as beams, plates, and shells. Subsequent research activities can be devoted to multifield problems, i.e., hygro-thermo-elasticity, heat transfer, and prediction of process-induced deformations and residual stresses, among others. Also, the fluid-structure interaction, i.e., static and dynamic aeroelasticity, can be investigated.

From the fibre-matrix and layer scale modelling perspective, new applications to multiphysics shall be derived. For instance, MSG-CUF could be extended to piezo-electric and magneto-static and their eventual coupling. On the other hand, the embedded component-wise approach can be exploited to conduct multiscale analysis by modifying the MSG governing equations according to the embedded formulation.

Concerning optimisation, future steps should focus on the mechanical performance, or least-weight minimisation of composite structures, and real-world applications like aerostructural optimisation of aircraft, spacecraft and wind turbines. Considering fluid-structure interaction, multidisciplinary optimisation can be tackled in future CUF-based research.

References

[1] C. Zweben. *Composite Materials*, chapter 10, pages 1–37. John Wiley & Sons, Ltd, 2015.

[2] M. N. Grimshaw, C. G. Grant, and J. M. L. Diaz. Advanced technology tape laying for affordable manufacturing of large composite structures. In *International Sampe Symposium and Exhibition*, volume 46, pages 2484–2494. Citeseer, 2001.

[3] G. B. Olson. Computational design of hierarchically structured materials. *Science*, 277(5330):1237–1242, 1997.

[4] J. LLorca, C. González, J. M. Molina-Aldareguía, J. Segurado, R. Seltzer, F. Sket, M. Rodríguez, S. Sádaba, R. Muñoz, and L. P. Canal. Multiscale modeling of composite materials: a roadmap towards virtual testing. *Advanced materials*, 23(44):5130–5147, 2011.

[5] B. G. Falzon and W. Tan. *Virtual Testing of Composite Structures: Progress and Challenges in Predicting Damage, Residual Strength and Crashworthiness*, pages 699–743. Springer International Publishing, Cham, 2017.

[6] A. W. Leissa and A. F. Martin. Vibration and buckling of rectangular composite plates with variable fiber spacing. *Composite Structures*, 14(4):339–357, 1990.

[7] C. M. Kuo, K. Takahashi, and T. W. Chou. Effect of fiber waviness on the non-linear elastic behavior of flexible composites. *Journal of Composite Materials*, 22(11):1004–1025, 1988.

[8] M. W. Hyer and H. H. Lee. The use of curvilinear fiber format to improve buckling resistance of composite plates with central circular holes. *Composite Structures*, 18(3):239–261, 1991.

[9] Z. Gürdal and R. Olmedo. In-plane response of laminates with spatially varying fiber orientations-variable stiffness concept. *AIAA Journal*, 31(4):751–758, 1993.

[10] R. Olmedo and Z. Gürdal. Buckling response of laminates with spatially varying fiber orientations. In *34th Structures, Structural Dynamics and Materials Conference*, page 1567, 1993.

[11] Z. Gürdal, B. F. Tatting, and C. K. Wu. Variable stiffness composite panels: effects of stiffness variation on the in-plane and buckling response. *Composites Part A: Applied Science and Manufacturing*, 39(5):911–922, 2008.

[12] J. N. Reddy. *Mechanics of laminated composite plates and shells: theory and analysis*. CRC press, 2003.

[13] G. Kirchhoff. Über das gleichgewicht und die bewegung einer elastischen scheibe. *Journal für die reine und angewandte Mathematik (Crelles Journal)*, 1850(40):51–88, 1850.

[14] E. Reissner. The effect of transverse shear deformation on the bending of elastic plates. *Journal of Applied Mechanics*, 12(2):69–77, 1945.

[15] R. D. Mindlin. Influence of rotary inertia and shear flexural motion of isotropic, elastic plates. *Journal of Applied Mechanics*, 18:31–38, 1951.

[16] J. N. Reddy. A simple higher-order theory for laminated composites. *Journal of Applied Mechanics*, 51:745–752, 1984.

[17] J. N. Reddy and C. F. Liu. A higher-order shear deformation theory of laminated elastic shells. *International Journal of Engineering Science*, 23(3):319–330, 1985.

[18] E. Carrera. Theories and finite elements for multilayered, anisotropic, composite plates and shells. *Archives of Computational Methods in Engineering*, 9(2):87–140, 2002.

[19] E. Carrera. Theories and finite elements for multilayered plates and shells: a unified compact formulation with numerical assessment and benchmarking. *Archives of Computational Methods in Engineering*, 10(3):215–296, 2003.

[20] M. Cinefra and E. Carrera. Shell finite elements with different through-the-thickness kinematics for the linear analysis of cylindrical multilayered structures. *International Journal for Numerical Methods in Engineering*, 93(2):160–182, 2013.

[21] Y. Huang, L. Xu, and S. Kyu Ha. Prediction of three-dimensional composite laminate response using micromechanics of failure. *Journal of Composite Materials*, 46(19-20):2431–2442, 2012.

[22] E. J. Pineda, B. A. Bednarcyk, A. M. Waas, and S. M. Arnold. Progressive failure of a unidirectional fiber-reinforced composite using the method of cells: Discretization objective computational results. *International Journal of Solids and Structures*, 50(9):1203–1216, 2013.

[23] R. Hill. The Elastic Behaviour of a Crystalline Aggregate. *Proceedings of the Physical Society. Section A*, 65(5):349, 1952.

[24] B. W. Rosen and Z. Hashin. Effective thermal expansion coefficients and specific heats of composite materials. *International Journal of Engineering Science*, 8(2):157–173, 1970.

[25] Z. Hashin and S. Shtrikman. A variational approach to the theory of the elastic behaviour of polycrystals. *Journal of the Mechanics and Physics of Solids*, 10(4):343–352, 1962.

[26] T. O. Williams. A three-dimensional, higher-order, elasticity-based micromechanics model. *International Journal of Solids and Structures*, 42(3-4):971–1007, 2005.

[27] T. Mori and K. Tanaka. Average stress in matrix and average elastic energy of materials with misfitting inclusions. *Acta Metallurgica*, 21(5):571–574, 1973.

[28] J. Aboudi. A continuum theory for fiber-reinforced elastic-viscoplastic composites. *International Journal of Engineering Science*, 20(5):605–621, 1982.

[29] M. Paley and J. Aboudi. Micromechanical analysis of composites by the generalized cells model. *Mechanics of materials*, 14(2):127–139, 1992.

[30] J. Aboudi, M. J. Pineda, and S. M. Arnold. Linear Thermoelastic Higher-Order Theory for Periodic Multiphase Materials. *Journal of Applied Mechanics*, 68(5):697–707, 2001.

[31] C. T. Sun and R. S. Vaidya. Prediction of composite properties from a representative volume element. *Composites Science and Technology*, 56(2):171–179, 1996.

[32] P. Sahu, N. Sharma, H. C. Dewangan, and S. K. Panda. Theoretical prediction and experimental validity of thermal frequency responses of laminated advanced fiber-reinforced epoxy hybrid composite panel. *International Journal of Structural Stability and Dynamics*, 22(08):2250088, 2022.

[33] B. A. Bednarcyk and S. M. Arnold. Micromechanics-based modeling of woven polymer matrix composites. *AIAA Journal*, 41(9):1788–1796, 2003.

[34] H. J. Kim and C. C. Swan. Voxel-based meshing and unit-cell analysis of textile composites. *International Journal for Numerical Methods in Engineering*, 56(7):977–1006, 2003.

[35] F. Heinecke and C. Willberg. Manufacturing-induced imperfections in composite parts manufactured via automated fiber placement. *Journal of Composites Science*, 3(2):56, 2019.

[36] A. W. Blom, C. S. Lopes, P. J. Kromwijk, Z. G$'$urdal, and P. P. Camanho. A theoretical model to study the influence of tow-drop areas on the stiffness and strength of variable-stiffness laminates. *Journal of Composite Materials*, 43(5):403–425, 2009.

[37] O. Falcó, J.A. Mayugo, C.S. Lopes, N. Gascons, A. Turon, and J. Costa. Variable-stiffness composite panels: As-manufactured modeling and its influence on the failure behavior. *Composites Part B: Engineering*, 56:660 – 669, 2014.

[38] O. Falcó, C.S. Lopes, F. Naya, F. Sket, P. Maimí, and J.A. Mayugo. Modelling and simulation of tow-drop effects arising from the manufacturing of steered-fibre composites. *Composites Part A: Applied Science and Manufacturing*, 93:59 – 71, 2017.

[39] B. C. Kim, K. Potter, and P. M. Weaver. Continuous tow shearing for manufacturing variable angle tow composites. *Composites Part A: Applied Science and Manufacturing*, 43(8):1347–1356, 2012.

[40] B. C. Kim, P. M. Weaver, and K. Potter. Computer aided modelling of variable angle tow composites manufactured by continuous tow shearing. *Composite Structures*, 129:256–267, 2015.

[41] R. L. Lincoln, P. M. Weaver, A. Pirrera, and R. M. J. Groh. Imperfection-insensitive continuous tow-sheared cylinders. *Composite Structures*, 260:113445, 2021.

[42] C. J. McInnes, R. L. Lincoln, A. Pirrera, B. C. Kim, and R. M. J. Groh. On the finite element discritization of continuous tow sheared structures. In *AIAA SCITECH 2022 Forum*, page 2598, 2022.

[43] C. Dill, S. Tipton, E. Glaessgen, and K. Branscum. Fatigue strength reduction imposed by porosity in a fiberglass composite. In *Damage Detection in Composite Materials*, pages 152–162, West Conshohocken, PA, USA, 1992. ASTM International.

[44] H. Huang and R. Talreja. Effects of void geometry on elastic properties of unidirectional fiber reinforced composites. *Composites Science and Technology*, 65(13):1964 – 1981, 2005.

[45] K. Fayazbakhsh, M. A. Nik, D. Pasini, and L. Lessard. Defect layer method to capture effect of gaps and overlaps in variable stiffness laminates made by automated fiber placement. *Composite Structures*, 97:245–251, 2013.

[46] A. H. Akbarzadeh, M. A. Nik, and D. Pasini. The role of shear deformation in laminated plates with curvilinear fiber paths and embedded defects. *Composite Structures*, 118:217 – 227, 2014.

[47] A. Noevere and C. Collier. Mapping manufacturing data for stress analysis of automated fiber placement structures. In *2018 AIAA/ASCE/AHS/ASC Structures, Structural Dynamics, and Materials Conference*, Kissimmee, Florida, USA, 2018.

[48] A. Marouene, R. Boukhili, J. Chen, and A. Yousefpour. Effects of gaps and overlaps on the buckling behavior of an optimally designed variable-stiffness composite laminates – a numerical and experimental study. *Composite Structures*, 140:556 – 566, 2016.

[49] R. Butler, T. J. Dodwell, R. T. Haftka, N. Ho Kim, T. Kim, S. Kynaston, and R. Scheichl. Uncertainty quantification of composite structures with defects using multilevel Monte Carlo simulations. In *17th AIAA Non-Deterministic Approaches Conference*, Kissimmee, Florida, USA, 5-9 January 2015. AIAA.

[50] M. B. Giles. Multilevel Monte Carlo path simulation. *Operations Research*, 56(3):981–986, 2008.

[51] L. M. Ferreira, E. Graciani, and F. París. Modelling the waviness of the fibres in non-crimp fabric composites using 3D finite element models with straight tows. *Composite Structures*, 107:79–87, 2014.

[52] A. Gonzalez, E. Graciani, and F. París. Prediction of in-plane stiffness properties of non-crimp fabric laminates by means of 3d finite element analysis. *Composites Science and Technology*, 68(1):121 – 131, 2008.

[53] B. Van Der Broucke, J. Hegemann, R. Das, R. Oster, K. Hackl, and R. Stobel. Modelling of textile reinforced composites using finite element tools and investigation of the influence of porosity on mechanical properties. In *Finite element modelling of textiles and textile composites*, pages 26–28, St. Petersburg, Russia, September 2007. ASTM International.

[54] R. S. Choudhry, K. A. Khan, S. Z. Khan, M. A. Khan, and A. Hassan. Micromechanical modeling of 8-harness satin weave glass fiber-reinforced composites. *Journal of Composite Materials*, 51(5):705–720, 2017.

[55] B. Sudret and A. Der Kiureghian. Stochastic finite element methods and reliability: a state-of-the-art report. Technical report, Department of Civil and Environmental Engineering, University of California, Berkeley, 2000.

[56] C. Scarth, S. Adhikari, P. Cabral, G. Silva, and A. Prado. Random field simulation over curved surfaces: Applications to computational structural mechanics. *Computer Methods in Applied Mechanics and Engineering*, 345:283–301, 2019.

[57] S. van den Broek, S. Minera, A. Pirrera, P. Weaver, E. Jansen, and R. Rolfes. Enhanced deterministic performance of panels using stochastic variations of geometric and material parameters. In *AIAA Scitech 2019 Forum*, San Diego, California, USA, 2019.

[58] S. Murugan, R. Chowdhury, S. Adhikari, and M.I. Friswell. Helicopter aeroelastic analysis with spatially uncertain rotor blade properties. *Aerospace Science and Technology*, 16(1):29–39, 2012.

[59] H. Choi, S. Jung, C. Zhang, and G.J. Yun. A three-dimensional stochastic progressive damage simulation model for polymer matrix-based laminate composites. *Mechanics of Advanced Materials and Structures*, 0(0):1–18, 2020.

[60] C. Scarth and S. Adhikari. Modeling spatially varying uncertainty in composite structures using lamination parameters. *AIAA Journal*, 55(11):3951–3965, 2017.

[61] G. Balokas, B. Kriegesmann, S. Czichon, and R. Rolfes. Stochastic modeling techniques for textile yarn distortion and waviness with 1d random fields. *Composites Part A: Applied Science and Manufacturing*, 127:105639, 2019.

[62] S. van den Broek, S. Minera, E. Jansen, and R. Rolfes. Robust improvement of the asymmetric post-buckling behavior of a composite panel by perturbing fiber paths. *Composite Structures*, 270:114011, 2021.

[63] S. Dey, T. Mukhopadhyay, and S. Adhikari. Stochastic free vibration analysis of angle-ply composite plates–a rs-hdmr approach. *Composite Structures*, 122:526–536, 2015.

[64] T. Guimarães, H. Silva, D. Rade, and C. Cesnik. Aeroelastic stability of conventional and tow-steered composite plates under stochastic fiber volume. *AIAA Journal*, 58(6):2748–2759, 2020.

[65] R. T. Haftka and Z. Gürdal. *Elements of structural optimization*, volume 11. Springer Science & Business Media, 2012.

[66] J. R. R. A. Martins and A. Ning. *Engineering design optimization*. Cambridge University Press, 2021.

[67] R. T. Haftka and J. L. Walsh. Stacking-sequence optimization for buckling of laminated plates by integer programming. *AIAA Journal*, 30(3):814–819, 1992.

[68] R. Le Riche and R. T. Haftka. Optimization of laminate stacking sequence for buckling load maximization by genetic algorithm. *AIAA Journal*, 31(5):951–956, 1993.

[69] R. Le Riche and R.T. Haftka. Improved genetic algorithm for minimum thickness composite laminate design. *Composites Engineering*, 5(2):143–161, 1995.

[70] F. X. Irisarri, A. Lasseigne, F. H. Leroy, and R. Le Riche. Optimal design of laminated composite structures with ply drops using stacking sequence tables. *Composite Structures*, 107:559–569, 2014.

[71] H. Fukunaga and H. Sekine. Stiffness design method of symmetric laminates using lamination parameters. *AIAA Journal*, 30(11):2791–2793, 1992.

[72] G. H. C. Silva, A. P. do Prado, P. H. Cabral, R. De Breuker, and J. K. S. Dillinger. Tailoring of a composite regional jet wing using the slice and swap method. *Journal of Aircraft*, 56(3):990–1004, 2019.

[73] T. Macquart, M. T. Bordogna, P. Lancelot, and R. De Breuker. Derivation and application of blending constraints in lamination parameter space for composite optimisation. *Composite Structures*, 135:224–235, 2016.

[74] T. Macquart, V. Maes, M. T. Bordogna, A. Pirrera, and P. M. Weaver. Optimisation of composite structures–enforcing the feasibility of lamination parameter constraints with computationally-efficient maps. *Composite Structures*, 192:605–615, 2018.

[75] G. Ntourmas, F. Glock, S. Deinert, F. Daoud, G. Schuhmacher, D. Chronopoulos, E. Özcan, and J. Ninić. Stacking sequence optimisation of an aircraft wing skin. *Structural and Multidisciplinary Optimization*, 66(2):31, 2023.

[76] A. Catapano and M. Montemurro. A multi-scale approach for the optimum design of sandwich plates with honeycomb core. Part II: the optimisation strategy. *Composite Structures*, 118:677–690, 2014.

[77] P. Vannucci. Plane anisotropy by the polar method. *Meccanica*, 40:437–454, 2005.

[78] G. Serhat and I. Basdogan. Lamination parameter interpolation method for design of manufacturable variable-stiffness composite panels. *AIAA Journal*, 57(7):3052–3065, 2019.

[79] A. Khani, S. T. IJsselmuiden, M. M. Abdalla, and Z. Gürdal. Design of variable stiffness panels for maximum strength using lamination parameters. *Composites Part B: Engineering*, 42(3):546–552, 2011.

[80] S. T. IJsselmuiden, M. M. Abdalla, and Z. Gürdal. Implementation of strength-based failure criteria in the lamination parameter design space. *AIAA Journal*, 46(7):1826–1834, 2008.

[81] I. M. Daniel and O. Ishai. *Engineering mechanics of composite materials*. Oxford university press, New York, New York, USA, 2006.

[82] A. Catapano, M. Montemurro, J.A. Balcou, and E. Panettieri. Rapid prototyping of variable angle-tow composites. *Aerotecnica Missili & Spazio*, 98(4):257–271, 2019.

[83] M. A. Nik, K. Fayazbakhsh, D. Pasini, and L. Lessard. Surrogate-based multi-objective optimization of a composite laminate with curvilinear fibers. *Composite Structures*, 94(8):2306–2313, 2012.

[84] M. A. Nik, K. Fayazbakhsh, D. Pasini, and L. Lessard. Optimization of variable stiffness composites with embedded defects induced by automated fiber placement. *Composite Structures*, 107:160–166, 2014.

[85] A. A. Vijayachandran, P. Davidson, and A. M. Waas. Optimal fiber paths for robotically manufactured composite structural panels. *International Journal of Non-Linear Mechanics*, 126:103567, 2020.

[86] A. A. Vijayachandran and A. M. Waas. Minimizing stress concentrations using steered fiberpaths and incorporating realistic manufacturing signatures. *International Journal of Non-Linear Mechanics*, 146:104160, 2022.

[87] R. M. Groh and P. Weaver. Mass optimisation of variable angle tow, variable thickness panels with static failure and buckling constraints. In *56th AIAA/ASCE/AHS/ASC Structures, Structural Dynamics, and Materials Conference*, page 0452, 2015.

[88] K. Singh and R. K. Kapania. Optimal design of tow-steered composite laminates with curvilinear stiffeners. In *2018 AIAA/ASCE/AHS/ASC Structures, Structural Dynamics, and Materials Conference*, page 2243, 2018.

[89] W. Zhao and R. K. Kapania. Buckling analysis and optimization of stiffened variable angle tow laminates with a cutout considering manufacturing constraints. *Journal of Composites Science*, 6(3):80, 2022.

[90] R. Vescovini, E. Spigarolo, E. L. Jansen, and L. Dozio. Efficient post-buckling analysis of variable-stiffness plates using a perturbation approach. *Thin-Walled Structures*, 143:106211, 2019.

[91] R. Vescovini, V. Oliveri, D. Pizzi, L. Dozio, and P. M. Weaver. Pre-buckling and buckling analysis of variable-stiffness, curvilinearly stiffened panels. *Aerotecnica Missili & Spazio*, 99:43–52, 2020.

[92] R. Vescovini, V. Oliveri, D. Pizzi, L. Dozio, and P. M. Weaver. A semi-analytical approach for the analysis of variable-stiffness panels with curvilinear stiffeners. *International Journal of Solids and Structures*, 188:244–260, 2020.

[93] L. Demasi, G. Biagini, F. Vannucci, E. Santarpia, and R. Cavallaro. Equivalent single layer, zig-zag, and layer wise theories for variable angle tow composites based on the generalized unified formulation. *Composite Structures*, 177:54–79, 2017.

[94] A. Viglietti, E. Zappino, and E. Carrera. Analysis of variable angle tow composites structures using variable kinematic models. *Composites Part B: Engineering*, 171:272–283, 2019.

[95] E. Carrera, M. Cinefra, M. Petrolo, and E. Zappino. *Finite Element Analysis of Structures through Unified Formulation*. Wiley & Sons, Hoboken, New Jersey, USA, 2014.

[96] E. Carrera and M. Petrolo. Refined one-dimensional formulations for laminated structure analysis. *AIAA Journal*, 50(1):176–189, 2012.

[97] E. Carrera and M. Petrolo. Refined beam elements with only displacement variables and plate/shell capabilities. *Meccanica*, 47:537–556, 2012.

[98] A. de Pagani, A. G. De Miguel, M. Petrolo, and E. Carrera. Analysis of laminated beams via unified formulation and legendre polynomial expansions. *Composite Structures*, 156:78–92, 2016.

[99] E. Carrera, G. Giunta, and M. Petrolo. *Beam structures: classical and advanced theories*. John Wiley & Sons, 2011.

[100] E. Carrera, G. Giunta, P. Nali, and M. Petrolo. Refined beam elements with arbitrary cross-section geometries. *Computers & Structures*, 88(5-6):283–293, 2010.

[101] B. Szabó and I. Babuška. *Finite Element Analysis: Method, Verification and Validation*. John Wiley & Sons, 2021.

[102] W. J. Gordon and C. A. Hall. Transfinite element methods: blending-function interpolation over arbitrary curved element domains. *Numerische Mathematik*, 21(2):109–129, 1973.

[103] E. Carrera. Historical review of zig-zag theories for multilayered plates and shells. *Applied Mechanics Reviews*, 56(3):287–308, 2003.

[104] E. Carrera. Cz0 requirements: models for the two dimensional analysis of multilayered structures. *Composite Structures*, 37(3-4):373–383, 1997.

[105] B. Wu, A. Pagani, W. Q. Chen, and E. Carrera. Geometrically nonlinear refined shell theories by carrera unified formulation. *Mechanics of Advanced Materials and Structures*, 28:1721–1741, 2019.

[106] E. Carrera, A. Pagani, and M. Petrolo. Classical, refined, and component-wise analysis of reinforced-shell wing structures. *AIAA Journal*, 51(5):1255–1268, 2013.

[107] V. A. Martin, R. H. Kraft, T. H. Hannah, and S. Ellis. An energy-based study of the embedded element method for explicit dynamics. *Advanced Modeling and Simulation in Engineering Sciences*, 9(1):1–18, 2022.

[108] W. Yu. A unified theory for constitutive modeling of composites. *Journal of Mechanics of Materials and Structures*, 11(4):379–411, 2016.

[109] T. R. Brooks and J. R. R. A. Martins. On manufacturing constraints for tow-steered composite design optimization. *Composite Structures*, 204:548–559, 2018.

[110] P. D. Spanos and B. A. Zeldin. Monte Carlo treatment of random fields: A broad perspective. *Applied Mechanics Reviews*, 51(3):219–237, 1998.

[111] M. W. Davis. Production of conditional simulations via the LU triangular decomposition of the covariance matrix. *Mathematical Geology*, 19:91–98, 1987.

[112] R. G. Ganhem and P. D. Spanos. *Stochastic finite elements: a spectral approach*. Springer-Verlag, Berlin, Germany, 1991.

[113] W. Betz, I. Papaioannou, and D. Straub. Numerical methods for the discretization of random fields by means of the karhunen–loève expansion. *Computer Methods in Applied Mechanics and Engineering*, 271:109–129, 2014.

[114] F. Yamazaki and M. Shinozuka. Digital generation of non-gaussian stochastic fields. *Journal of Engineering Mechanics*, 114(7):1183–1197, 1988.

[115] M. Grigoriu. Simulation of stationary non-gaussian translation processes. *Journal of Engineering Mechanics*, 124(2):121–126, 1998.

[116] N. Cressie. *Statistics for spatial data*. John Wiley & Sons, 2015.

[117] M. D. Buhmann. Radial basis functions. *Acta numerica*, 9:1–38, 2000.

[118] V. Vapnik. *The nature of statistical learning theory*. Springer science & business media, 1999.

[119] S. Marelli and B. Sudret. Uqlab user manual – polynomial chaos expansions. Technical report, Chair of Risk, Safety and Uncertainty Quantification, ETH Zurich, Switzerland, 2019. Report UQLab-V1.3-104.

[120] M. H. Nguyen, A. A. Vijayachandran, P. Davidson, D. Call, D. Lee, and A. M. Waas. Effect of automated fiber placement (AFP) manufacturing signature on mechanical performance of composite structures. *Composite Structures*, 228:111335, 2019.

[121] V. Oduguwa, A. Tiwari, and R. Roy. Evolutionary computing in manufacturing industry: an overview of recent applications. *Applied Soft Computing*, 5(3):281–299, 2005.

[122] J. McCall. Genetic algorithms for modelling and optimisation. *Journal of Computational and Applied Mathematics*, 184(1):205–222, 2005.

[123] J. Sacks, W. J. Welch, T. J. Mitchell, and H. P. Wynn. Design and analysis of computer experiments. *Statistical Science*, 4(4):409–423, 1989.

[124] T. Krishnamurthy. Response surface approximation with augmented and compactly supported radial basis functions. In *44th AIAA/ASME/ASCE/AHS/ASC Structures, Structural Dynamics, and Materials conference*, page 1748, 2003.

[125] A. I. J. Forrester and A. J. Keane. Recent advances in surrogate-based optimization. *Progress in Aerospace Sciences*, 45(1-3):50–79, 2009.

[126] W. Squire and G. Trapp. Using complex variables to estimate derivatives of real functions. *SIAM review*, 40(1):110–112, 1998.

[127] A. Griewank and A. Walther. *Evaluating derivatives: principles and techniques of algorithmic differentiation*. SIAM, Philadelphia, PA, USA, 2008.

[128] U. Naumann. *The art of differentiating computer programs: an introduction to algorithmic differentiation*. SIAM, Philadelphia, PA, USA, 2011.

[129] L. Nardin, K. Sørensen, S. Hitzel, and U. Tremel. modeFrontier©, a framework for the optimization of military aircraft configurations. In Norbert Kroll, Dieter Schwamborn, Klaus Becker, Herbert Rieger, and Frank Thiele, editors, *MEGADESIGN and MegaOpt - German Initiatives for Aerodynamic Simulation and Optimization in Aircraft Design*, pages 191–205, Berlin, Heidelberg, 2009. Springer Berlin Heidelberg.

[130] M. D. McKay, R. J. Beckman, and W. J. Conover. A comparison of three methods for selecting values of input variables in the analysis of output from a computer code. *Technometrics*, 42(1):55–61, 2000.

[131] A. R. Sánchez-Majano, R. Azzara, A. Pagani, and E. Carrera. Accurate Stress Analysis of Variable Angle Tow Shells by High-Order Equivalent-Single-Layer and Layer-Wise Finite Element Models. *Materials*, 14(21):6486, 2021.

[132] A. Racionero Sánchez-Majano and A. Pagani. High-order embedded finite elements for the component-wise analysis of composite laminated structures. In *Proceeding for the American Society for Composites-38th Technical Conference*, 2023.

[133] A. R. Sánchez-Majano, R. Masia, A. Pagani, and E. Carrera. Microscale thermoelastic analysis of composite materials by high-order geometrically accurate finite elements. *Composite Structures*, 300:116105, 2022.

[134] A. Pagani and A. R. Sánchez-Majano. Influence of fiber misalignments on buckling performance of variable stiffness composites using layerwise models and random fields. *Mechanics of Advanced Materials and Structures*, pages 1–16, 2020.

[135] A. Pagani and A. R. Sánchez-Majano. Stochastic stress analysis and failure onset of variable angle tow laminates affected by spatial fibre variations. *Composites Part C: Open Access*, 4:100091, 2021.

[136] A. R. Sánchez-Majano, A. Pagani, M. Petrolo, and C. Zhang. Buckling sensitivity of tow-steered plates subjected to multiscale defects by high-order finite elements and polynomial chaos expansion. *Materials*, 14(11):2706, 2021.

[137] A. Pagani, M. Petrolo, and A .R. Sánchez-Majano. Stochastic characterization of multiscale material uncertainties on the fibre-matrix interface stress state of composite variable stiffness plates. *International Journal of Engineering Science*, 183:103787, 2023.

[138] A. Racionero Sánchez-Majano and A. Pagani. Buckling and fundamental frequency optimization of tow-steered composites using layerwise structural models. *AIAA Journal*, 61(9):4149–4163, 2023.

[139] A. Pagani, A. Racionero Sánchez-Majano, and D. Zamani. Optimizaion of variable-stiffness composites considering manufacturing defects and unified structural theories. In *ASME 2024 Aerospace Structures, Structural Dynamics and Materials Conference*, 2024.

[140] M. Smith. *ABAQUS/Standard User's Manual, Version 6.9*. Dassault Systèmes Simulia Corp, United States, 2009.

[141] E. Carrera, A. G. de Miguel, and A. Pagani. Component-wise analysis of laminated structures by hierarchical refined models with mapping features and enhanced accuracy at layer to fiber-matrix scales. *Mechanics of Advanced Materials and Structures*, 25(14):1224–1238, 2018.

[142] E. Carrera, M. Maiarú, and M. Petrolo. Component-wise analysis of laminated anisotropic composites. *International Journal of Solids and Structures*, 49(13):1839–1851, 2012.

[143] I. Kaleel, A. Garcia de Miguel, M. Petrolo, A. Pagani, E. Carrera, T. M. Ricks, E. J. Pineda, B. A. Bednarcyk, and S. M. Arnold. Computationally-efficient structural models for analysis of woven composites. In *AIAA Scitech 2020 Forum*, page 2110, 2020.

[144] W. Yu and X. Liu. SwiftComp, January 2017.

[145] W. Voigt. Theoretische Studien über die Elasticitätsverhaltnisse der Krystalle. *Abhandlungen der Königlichen Gesellschaft der Wissenschaften in Göttingen*, 34:3–51, 1887.

[146] A. Reuß. Berechnung der fließgrenze von mischkristallen auf grund der plastizitätsbedingung für einkristalle. *ZAMM-Journal of Applied Mathematics and Mechanics/Zeitschrift für Angewandte Mathematik und Mechanik*, 9(1):49–58, 1929.

[147] K. K. Tamma and A. F. Avila. *An integrated micro/macro modeling and computational methodology for high temperature composites*. Lastran Corporation Rochester, NY, Rochester, NY., 1999.

[148] M. P. F. Sutcliffe, S. L. Lemanski, and A. E. Scott. Measurement of fibre waviness in industrial composite components. *Composites Science and Technology*, 72(16):2016–2023, 2012.

[149] Y. Wang and C. A. Shoemaker. A general stochastic algorithmic framework for minimizing expensive black box objective functions based on surrogate models and sensitivity analysis. *arXiv preprint arXiv:1410.6271*, 2014.

[150] H. Akhavan and P. Ribeiro. Natural modes of vibration of variable stiffness composite laminates with curvilinear fibers. *Composite Structures*, 93(11):3040–3047, 2011.

[151] I. M. Sobol. Global sensitivity indices for nonlinear mathematical models and their monte carlo estimates. *Mathematics and Computers in Simulation*, 55(1):271–280, 2001.

[152] A. A. Groenwold and R. T. Haftka. Optimization with non-homogeneous failure criteria like Tsai-Wu for composite laminates. *Structural and Multidisciplinary Optimization*, 32:183–190, 2006.

[153] Z. Hashin. Failure criteria for unidirectional fiber composites. *Journal of Applied Mechanics*, 47(2):329–334, 1980.

[154] Toray Composite Materials America, Inc. *Toray T800S Intermediate Modulus Carbon Fiber*, April 2018.

Appendix A

Computation of Failure Indices

A.1 Three-dimensional Hashin failure criteria

The three-dimensional Hashin failure criteria [153], also referred to as Hashin 3D, establishes four failure mechanisms, namely fibre and matrix tension and compression. The expressions that allow to compute them are gathered in the following:

1. Fiber tension:
$$\mathscr{F}\mathscr{I} := \left(\frac{\sigma_{11}}{X_T}\right)^2 + \frac{\sigma_{12}^2 + \sigma_{13}^2}{S_{12}^2} \tag{A.1}$$

2. Fiber compression
$$\mathscr{F}\mathscr{I} := \left(\frac{\sigma_{11}}{X_C}\right)^2 \tag{A.2}$$

3. Matrix tension:
$$\mathscr{F}\mathscr{I} := \frac{(\sigma_{22} + \sigma_{33})^2}{Y_T^2} + \frac{\sigma_{23}^2 - \sigma_{22}\sigma_{33}}{S_{23}^2} + \frac{\sigma_{12}^2 + \sigma_{13}^2}{S_{12}^2} \tag{A.3}$$

4. Matrix compression:
$$\mathscr{F}\mathscr{I} := \left[\left(\frac{Y_C}{2S_{23}}\right)^2 - 1\right]\left(\frac{\sigma_{22} + \sigma_{33}}{Y_C}\right) + \frac{(\sigma_{22} + \sigma_{33})^2}{4S_{23}^2} + \frac{\sigma_{23}^2 - \sigma_{22}\sigma_{33}}{S_{23}^2} + \frac{\sigma_{12}^2 + \sigma_{13}^2}{S_{12}^2} \tag{A.4}$$

where σ_{ij} are the stress tensor components in the material reference frame, see Fig. A.1. In addition, X and Y are the material strengths, in tension T and compression C, and S_{ij} are the material shear strengths. Failure starts when any of the above $\mathscr{F}\mathscr{I} \geq 1$.

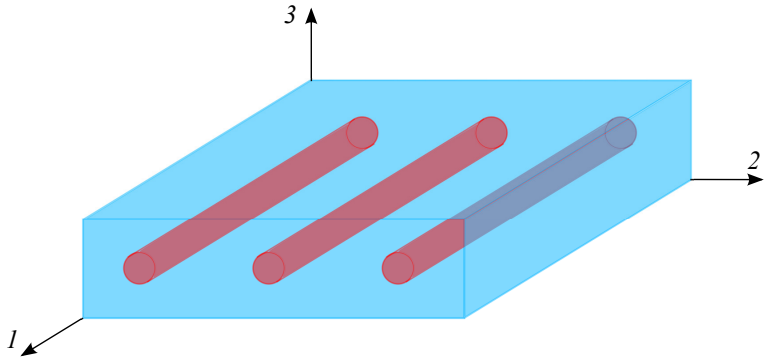

Figure A.1 Material coordinate system. Direction 1 corresponds to the fibre direction while 2 and 3 represent the transverse directions.

A.2 Safety factor and strength constraint formulation

This appendix depicts the procedure of retrieving the safety factor for the strength maximisation problem in Section 6.5.5. Recall that Hashin 3D failure criteria, described in Appendix A.1, is used. Hashin 3D computes the individual $\mathscr{FI}$ through different mathematical operations involving the stress components in the material coordinate system. Since linear analyses are considered, these components can be expressed in terms of a safety factor $\mathscr{SF}$, which is equal to the scalar load multiplier λ that results in the failure onset. In this context, the stress tensor at which any of the Hashin 3D $\mathscr{FI}$ equals one can be expressed as follows:

$$\boldsymbol{\sigma} = \lambda \tilde{\boldsymbol{\sigma}} \tag{A.5}$$

Equations (A.1) to (A.4) can be rewritten at failure onset as:

1. Fiber tension:

$$\mathscr{FI} = \lambda^2 \left[\left(\frac{\tilde{\sigma}_{11}}{X_T} \right)^2 + \frac{\tilde{\sigma}_{12}^2 + \tilde{\sigma}_{13}^2}{S_{12}^2} \right] = a\lambda^2 = 1 \tag{A.6}$$

2. Fiber compression:

$$\mathscr{FI} = \lambda^2 \left(\frac{\tilde{\sigma}_{11}}{X_C} \right)^2 = a\lambda^2 = 1 \tag{A.7}$$

3. Matrix tension:

$$\mathscr{FI} = \lambda^2 \left[\frac{(\tilde{\sigma}_{22} + \tilde{\sigma}_{33})^2}{Y_T^2} + \frac{\tilde{\sigma}_{23}^2 - \tilde{\sigma}_{22}\tilde{\sigma}_{33}}{S_{23}^2} + \frac{\tilde{\sigma}_{12}^2 + \tilde{\sigma}_{13}^2}{S_{12}^2} \right] = a\lambda^2 = 1 \tag{A.8}$$

4. Matrix compression:

$$\begin{aligned}\mathscr{FI} =& \lambda^2 \left[\frac{(\tilde{\sigma}_{22}+\tilde{\sigma}_{33})^2}{4S_{23}^2} + \frac{\tilde{\sigma}_{23}^2 - \tilde{\sigma}_{22}\tilde{\sigma}_{33}}{S_{23}^2} + \frac{\tilde{\sigma}_{12}^2+\tilde{\sigma}_{13}^2}{S_{12}^2} \right] + \\ & \lambda \left[\left(\frac{Y_C}{2S_{23}} \right)^2 - 1 \right] \left(\frac{\sigma_{22}+\sigma_{33}}{Y_C} \right) = a\lambda^2 + b\lambda = 1\end{aligned} \tag{A.9}$$

The quadratic equations above can be easily solved, and the safety factor $\mathscr{SF}$ corresponds with the smallest positive root of λ.